CONTROLLING SELF-ASSEMBLY AND ORDERING OF BLOCK POLYMER NANOSTRUCTURES IN THIN FILMS

by

Ming Luo

A dissertation submitted to the Faculty of the University of Delaware in partial fulfillment of the requirements for the degree of Doctor of Philosophy in Chemical Engineering

Summer 2016

CONTROLLING SELF-ASSEMBLY AND ORDERING OF BLOCK POLYMER NANOSTRUCTURES IN THIN FILMS

by

Ming Luo

Approved: _____
Abraham M. Lenhoff, Ph.D.
Chair of the Department of Chemical and Biomolecular Engineering

Approved: _____
Babatunde A. Ogunnaike, Ph.D.
Dean of the College of Engineering

Approved: _____
Ann L. Ardis, Ph.D.
Senior Vice Provost for Graduate and Professional Education

I certify that I have read this dissertation and that in my opinion it meets the academic and professional standard required by the University as a dissertation for the degree of Doctor of Philosophy.

Signed: _____

Thomas H. Epps, III, Ph.D.
Professor in charge of dissertation

I certify that I have read this dissertation and that in my opinion it meets the academic and professional standard required by the University as a dissertation for the degree of Doctor of Philosophy.

Signed: _____

Norman J. Wagner, Ph.D.
Member of dissertation committee

I certify that I have read this dissertation and that in my opinion it meets the academic and professional standard required by the University as a dissertation for the degree of Doctor of Philosophy.

Signed: _____

Eric M. Furst, Ph.D.
Member of dissertation committee

I certify that I have read this dissertation and that in my opinion it meets the academic and professional standard required by the University as a dissertation for the degree of Doctor of Philosophy.

Signed: _____

Michael E. Mackay, Ph.D.
Member of dissertation committee

ACKNOWLEDGMENTS

I first would like to thank my advisor, Thomas Epps, for his support and guidance throughout my research work. He sets high standards for himself and cultivates the same to others. He showed great patience and understanding to me during my development of researching, writing, and presenting skills. He has inspired me to not only grow as an experimentalist but as an independent thinker. Without him this thesis work would not have been possible.

I also would like to thank my committee members: Norman Wagner, Eric Furst, and Michael Mackay, for their helpful suggestions on my research. Prof. Wagner has always been an amazing support for my wife Jingsi and me. We often seek his advice when making a life decision. I am grateful that Prof. Furst was willing to talk to Jingsi when she came to the United States first time. I remembered how joyful we were when she learned out from him that she was admitted to UD. I also am very appreciative of Prof. Mackay for serving on my committee and his insightful suggestions on my thesis work.

Next, I would like to thank my group members who have provided me with support every step of the way, especially Julie Albert, my mentor when I began my graduate school, Jillian Emerson and Angela Holmberg, my comrades in arms for the past five years. Many thanks to Maeva Tureau, Wen-Shiue Young, Elizabeth Kelley, Sarah Mastroianni, Michael Mayeda, Wei-Fan Kuan, Jonathan Seppala, Thomas Smart, Bin Wei, Cameron Shelton, Melody Morris, for their help and discussion in my experiments. Thank you to the rest of the Epps group, especially Kaleigh Reno, Shu

Wang, Tiffany Suekama, Chad Greco Thomas Gartner, Rashida Ruddock, Ryan Murphy, Matthew Green, Sung Hyun Han, Raghunath Roy, and undergraduate students Joey Kim, Ronald Lewis, Douglas Scott, John McCarron, Kevin Hutter, Eddie Sangern, and Jack Saltwick, I have had a pleasure working with all of you over the years.

I also would like to thank a number of people and collaborators: Nikhila Mahadevapuram and Prof. Stein (GISAXS), Jonathan Gilbert, Prof. Rubner, and Prof Cohen (XPS depth profiling), Jonathan Brown and Prof. Hall (fDFT simulations), Roddel Remy (XRR and DSC), Ngoc Nguyen (DMA), Frank Kriss, Prof. Chaoying Ni, Jennifer Sloppy, and Fei Deng (SEM, TEM, FIB), Tamas Prileszky (PDMS), Gerald Poirier (XRR and Nano IR), Alfred Lance and Jeffrey Ricketts (slit nozzle), George Whitmyre (*in situ* thermal annealing system), Douglas Nixon (glassware), Kathleen Young, Megan Argoe, Chil Alba, Mary Walsh, and Cinda Younce (Coburn staff). Moreover, I must thank the funding sources National Science Foundation DMR-0645586 and DMR-1207041.

I owe a debt of gratitude to Prof. Jingguang Chen who helped me during my first year. I also am indebted to my friends at UD, Jinlin Jiang, Dongcui Li, Ke Xiong, Chia-Hung Tsai, Qian Gou, Weiting Yu, Fang Liu, Qing Sun, Ke Gong, Qi Chen, Yan Zhang, Huibo Sheng, Long Chen, Hongton Lin, Lan Li, Jinlin Liu, Xuan Yu, Wenjuan Zheng, Chen Guo, Lei Chen, and Shu Wang. Thank you all for offering me help, bringing happiness, and fulfilling my life at Delaware.

Finally, I cannot thank my parents enough for their continued love, support, and encouragement. Thank you to Mom for coming to the United States over and over again to help take care of my daughter. Thank you to my wonderful daughter

Sophia for brightening up my life. This last word of acknowledgment I have saved for my beloved wife Jingsi Gao, who has been with me all the years for better, for worse, for sickness and health.

TABLE OF CONTENTS

LIST OF TABLES

LIST OF FIGURES

ABSTRACT

Block polymers have garnered significant attention in the past few decades due to their ability to self-assemble into a boundless array of structures such as spheres, cylinders, gyroid, and lamellae. The sizes of the periodical structures typically are ~5 – 100 nm, making them ideal for emerging nanotechnologies, such as nanolithography, nanotemplating, nanoporous membranes, and photonics devices. Many of these applications require thin film geometries, in which the block polymers form well-ordered nanostructures and precisely controlled domain orientations. Understanding the factors that affect thin film phase behavior and being able to control the nanostructures, domain orientation, and domain ordering in thin film is essential to realizing the full potential of these unique materials. In this dissertation, I describe significant efforts to manipulate the block polymer thin film structures, direct the nanostructure ordering, and understand the connection between the macromolecular molecular structures and the block polymer properties. First, substrate surface modification with chlorosilane was employed to manipulate the nanostructure of poly(styrene-*b*-isoprene-*b*-styrene) (SIS) thin films. A morphological transformation from parallel cylinders to hexagonally perforated lamellae (HPL) was identified, in a high-throughput fashion, using gradient methods. The gradient methods are highly adaptable for the possible universal manipulation of thin film nanostructures. Second, rastering solvent vapor annealing – soft shear method was developed and demonstrated as a simple, yet highly effective method to achieve macroscopic alignment of SIS cylinders. This method substantially improves on previous

approaches by using simple instrumentation to unlock an array of alignment patterns with a variety of self-assembling polymers and provides feasibility and flexibility for practical industrial production. Next, the interfacial mixing characteristics of tapered block polymer were explored quantitatively for the first time, and the tapered interfacial modification has led to unique and diverse self-assembly behavior and properties. Finally, XPS depth profiling with C_{60}^{+} sputtering was used to determine the lithium ion distribution in a lamellae-forming block polymer electrolyte film. The results provide useful insights for the future design and optimization of block polymer structures for high efficiency energy storage devices. Additionally, the unique capabilities of C_{60}^{+} depth profiling XPS are demonstrated as a method to determine the nanoscale distributions of molecules in a myriad of polymer thin film systems.

Chapter 1

SELF-ASSEMBLING BLOCK POLYMER THIN FILMS

1.1 Introduction to Block Polymers

Block polymers (BPs) have garnered significant interest in the past few decades due to their unique and diverse self-assembly behavior and properties. BP consists of chemically distinct polymer blocks that are bonded covalently. The different polymer blocks may be thermodynamically incompatible and can lead to phase segregation (like oil and water). Unlike mixtures of immiscible polymer blends that can phase separate on macroscopic length scale, covalently bonded BPs self-assemble on the nanoscale.[1, 2] There are a myriad of nanostructures BP can form such as body-centered cubic spheres, hexagonally-packed cylinders, lamellae, and gyroid networks (Figure 1.1). The functionality, shape, and size of the self-assembled BP nanostructures are tunable by changing their components, compositions, molecular weights, and molecular architecture, all of which make BPs ideal for cost-effective nanoscale fabrication technologies.[3-9]

Numerous studies have provided a solid foundation for understanding bulk BP self-assembly behavior.[2, 10-12] The phase behavior of bulk BPs primarily depends on the Flory-Huggins interaction parameter (χ), degree of polymerization (N), block volume fractions (f_i), and chain architecture (*e.g.*, linear, branched, star, and cyclic). Secondary factors include block flexibility (*e.g.*, flexible *versus* stiff chains), dispersity of the BP, and monomer segment distribution such as alternating, random, or tapered sequences of the repeat units.[13] Linear AB diblock polymers have been

investigated most extensively, leading to a comprehensive experimental and theoretical understanding of their bulk phase behavior.[1, 10, 14] A typical theoretical phase diagram of a linear AB diblock polymer is shown in Figure 1.1. The product χN dictates the degree to which the A and B blocks segregate. Conceptually, χ is a dimensionless measure of the energetic cost of exchanging a repeat unit of polymer A for an equal volume unit of polymer B:

$$\chi = \frac{1}{k_B T}[\varepsilon_{AB} - \frac{1}{2}(\varepsilon_{AA} + \varepsilon_{BB})] \qquad 1\text{-}1$$

in which ε_{ij} represents the contact energy between i and j segments, and k_B is the Boltzmann constant. The most commonly used equation for χ includes both enthalpic and entropic contributions:

$$\chi = \chi_H + \chi_S \qquad 1\text{-}2$$

For typical dissimilar monomer pairs in which there are no strong specific interactions (*e.g.*, hydrogen bonding), χ is positive and small in comparison with unity (*e.g.*, χ between polystyrene and polyisoprene is ≈ 0.1 at room temperature). When χN is below a critical value, entropy dominates the energetic penalty of mixing A and B segments, resulting in a disordered phase. As the segregation strength χN increases, the BP microphase segregates into spheres, cylinders, gyroid, and lamellae depending on the block composition. The transition from disordered phase to ordered phase is called order-disorder transition (ODT). It has been shown by self-consistent field theory that for a symmetric BP ($f_A = f_B = 0.5$), $(\chi N)_{ODT} = 10.495$.[15] Additionally, the BP may undergo order-order transitions (OOT's) between ordered morphologies by changing χN. In practice, the equation for χ often takes the following form:[16]

$$\chi = \frac{\alpha}{T} + \beta \qquad 1\text{-}3$$

in which α and β are experimentally determined enthalpy and entropy coefficients for a particular BP. Thus, OOT and ODT can be assessed by varying temperature.[17]

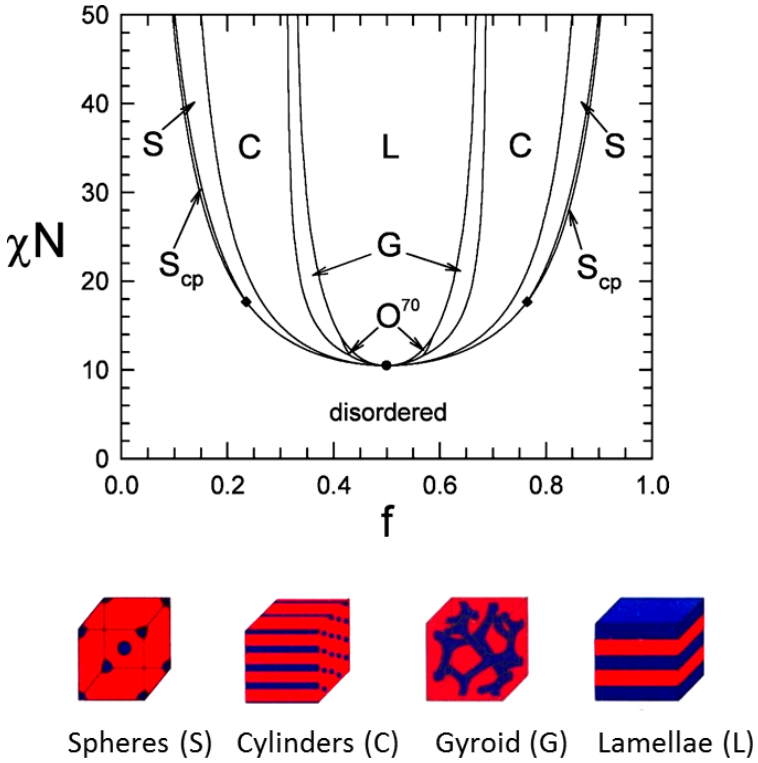

Figure 1.1: Theoretical linear AB diblock polymer phase diagram showing the BP nanostructures formed as a function of segregation strength, χN, and block volume fraction f: disordered, spheres (S), cylinders (C), gyroid network (G), and lamellae (L). Adapted with permission from Cochran, E. W., *et al. Macromolecules*. 2006, 39, (7), 2449-2451. Copyright 2006 American Chemical Society.

1.2 Block Polymer Thin Film and Applications

BPs often are cast down in thin films and have important applications in nanolithography,[18, 19] nanotemplating,[20, 21] nanoporous membranes,[22, 23] and photonic band gap materials (Figure 1.2).[24, 25] BP films with thickness less than *ca.* 200 nm are considered to be thin films, whereas BP films with thickness greater than *ca.* 2 μm are considered to exhibit bulk behavior.[26] BP thin films for nanolithography have received great attention in the last decade.[8, 27, 28] The microelectronics industry constantly strives to increase the speed of microprocessors and the storage density of hard disk drives. The well-known Moore's law suggests the number of transistors in a dense integrated circuit to be doubled approximately every two years, which means the size of transistors needs to be shrunk by half every two years. However, optical lithography technology has reached a limit in pattern resolution (≈10 nm). BP lithography has evolved into a viable tool to overcome the intrinsic resolution limit of conventional photolithography as BPs self-assemble to form highly ordered and densely packed features at scales as small as 3 to 10 nm.[6, 29] By using self-assembled BPs for nanolithography, the overall resolution may be increased by three to four-fold or more. Recently, BP lithography has shown significant promise in high value industrial processing. For example, IBM announced the first manufacturing application of BP self-assembly in a conventional chip fabrication line with the introduction of the "Airgap" insulator.[30] This technology could lead to 35% higher current speed or 15% lower power consumption. HGST has examined dense bit-patterned media using BP self-assembly that could allow the doubling of hard disk drive densities.[31] More recently, IMEC demonstrated the implementation of directed self-assembly of BP for viable patterning at the 7 nm node technology and beyond.[32]

BP thin films for nanotemplating and nanoporous membranes also have been developed with remarkable efficiency. Thurn-Albrecht *et al.* demonstrated the fabrication of ultrahigh-density nanowire arrays in self-assembled BP templates (> 1.9×10^{11} wires per square centimeter).[33] The dense arrays of ferromagnetic cobalt nanowires had marked enhanced ability to withstand external magnetic field without becoming demagnetized. Yang *et al.* fabricated a nanoporous membrane from BP suitable for virus filtration.[23] The BP membrane had cylindrical pores with diameters of 15 nm and a narrow pore size distribution. This membrane completely blocked human rhinovirus type 14 from penetrating into pores, while proteins such as bovine serum albumin could freely passed through the pores (Figure 1.2).

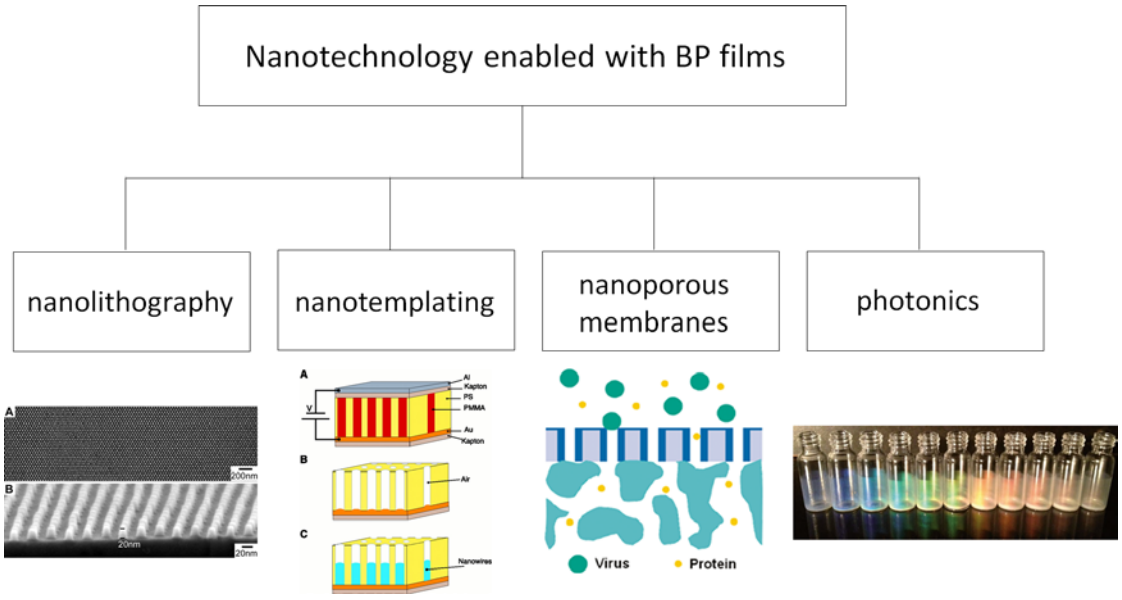

Figure 1.2: Nanotechnologies enabled with BP films. Image for nanolithography adapted with permission from Ruiz, R., *et al. Science* 2008, 321,(5891), 936-939. Copyright 2008 AAAS; Image for nanotemplating adapted with permission from Thurn-Albrecht, T., *et al. Science* 2000, 290, (5499), 2126-2129. Copyright 2000 AAAS; Image for nanoporous membranes adapted with permission from Yang, S. Y., *et al. Adv. Mater.* 2006, 18, (6), 709-712. Copyright 2006 John Wiley and Sons; Image for photonics adapted with permission from Miyake, G. M., *et al. Angew. Chem. Int. Ed*. 2012, 51, (45), 11246-11248. Copyright 2012 John Wiley and Sons.

Control of BP thin film nanostructures, domain orientation, and domain ordering are crucial for the aforementioned applications. For example, a perpendicular orientation of lamellae (relative to the plane of the substrate) with well-controlled directional ordering is desirable for nanolithography. Parallel lamellae are utilized to develop photonic band gap material with varying the lamellar periodicity can lead to tunability of the photonic band gap across the entire visible spectrum (Figure 1.2).[34] Cylindrical structures oriented parallel to the substrate also are useful for nanolithography applications, but require perpendicular orientation for nanoporous

membrane applications. Thus, a comprehensive understanding of factors dictating BP thin film nanostructures, domain orientation, and domain ordering is a significant research focus.[4, 9, 35]

1.3 Control of Self-Assembled Nanostructures in Thin Film

BP thin films are influenced strongly by the confinement and interactions subjected by the confining surfaces. There are three major categories of confinements defined for BP thin films: 1. free-standing or self-sustaining films; 2. "soft" confinement refers to a film that one interface is in direct contact with the atmosphere and the other interface is in contact with rigid interfaces (*i.e.*, substrate); 3. "hard" confinement describes a film that is confined between two rigid interfaces (*i.e.*, substrates).[4] The second category "soft" confinement is much more widely used in the aforementioned applications and is therefore the focus of the work in this thesis.

BP thin films cast from solution form poorly ordered and non-equilibrium structures due to fast evaporation of solvent upon casting. Therefore, films often are thermally annealed above the glass transition temperature of all the constituent blocks to promote chain mobility to adopt thermodynamically favorable structures. The equilibrium morphologies of BP thin film are governed by minimization of free energy of the system, and researchers need to consider all the factors that contribute to the overall free energy of the system. Edwards *et al.* provided a simple phenomenological model for the total free surface energy per polymer chain expressed as the sum of four terms:[36]

$$F = F_{elastic} + F_{block} + F_{free\ surface} + F_{substrate\ surface} \qquad 1\text{-}4$$

in which $F_{elastic}$ is an entropic term includes the elastic energy associated with chain stretching or compressing; F_{block} describes the interaction energy between blocks of the

copolymer; $F_{free\ surface}$ and $F_{substrate\ surface}$ refer to the surface energy at the free surface and the substrate surface.[36] It requires full knowledge of all the energetic contributions to the free energy of the system to achieve desired domain structure and orientation.

1.3.1 Confinement Effects

The confinement imposed by the film thickness can affect the thin film morphology because stretching or compression of chains to accommodate a specific film thickness is energetically unfavorable. Consider a lamellar-forming AB diblock copolymer thin film and the lamellae are parallel to the substrate, commensurate film thickness condition is achieved when the film thickness (t) is at integer multiples of the periodical spacing (L_0) for symmetric wetting conditions (the same block wets both surfaces) and at half-integer thicknesses for asymmetric wetting conditions (different blocks wet free and substrate surfaces). In these cases, the lamellae acquire their preferred layer spacing. When the film thickness is incommensurate with these values, BP form island/hole structures at the film surface (Figure 1.3) because the energetic penalty for creating more film surface area is less than the penalty of the lamellae taken a frustrated domain spacing (chain stretching or compression) or by putting an energetically disfavored block in contact with one or both surfaces. When the surface preferences are weak, perpendicular morphologies are possible to accommodate incommensurate film thickness.[37] The same principle applies to cylinder-forming BPs. Manipulation of film thickness have been shown to lead changes in packing symmetries,[38] domain structure,[39] and orientations of BP thin films.[37]

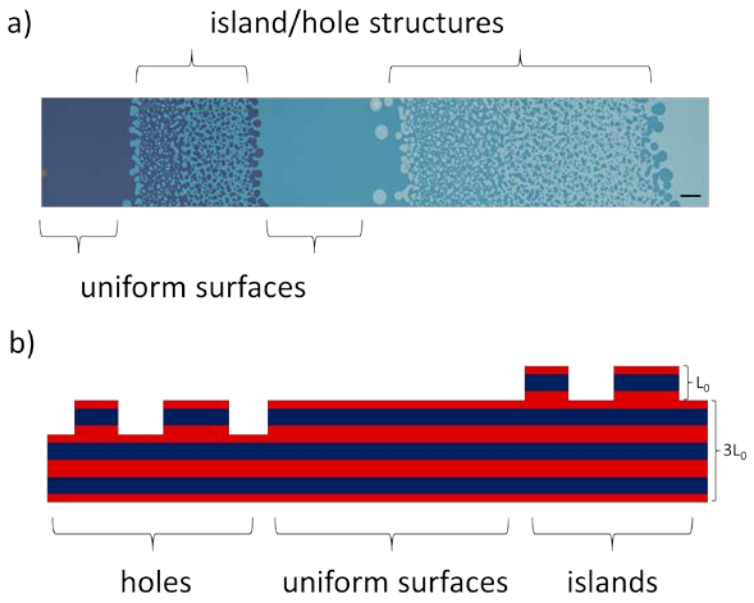

Figure 1.3: a) Optical microscopic graph of a gradient thickness lamellar-forming poly(isoprene-*b*-styrene) film. Close to the commensurability condition, films appeared featureless; with increasing film thickness, the morphology progressed from islands to bicontinuous island/hole structures to holes to featureless at the next commensurate thickness. The scale bar represents 40 μm. b) Side view schematic of a lamellar-forming BP thin film with a gradient film thickness. For symmetric wetting conditions (the same block wets both surfaces), commensurate film thickness condition is achieved when the film thickness is at integer multiples of the periodical spacing ($t = nL_0$, n = 1, 2, 3...). The height (depth) of the island (hole) structure is equal to the lamellar domain spacing (L_0).

1.3.2 Substrate Surface Effects

The BP domain structures and orientation are influenced strongly by the interfacial interactions between the BP and the surfaces (air and substrate). Each of the surfaces usually has a preferential affinity for one block of the BP, such that after annealing that block will segregate to that particular surface to minimize the enthalpic contributions $F_{free\ surface}$ and $F_{substrate\ surface}$. Generally, preferential surface interactions

drive BP to form parallel-oriented microdomains, while non-preferential (or neutral) surfaces encourage the presence of all blocks at surface and formation of perpendicular-oriented microdomains. As vertical lamellar and cylindrical morphologies are desirable technologically, researchers have been engaged in the development of surface modification methods to achieve neutral surface for BP thin film.[36, 40-42]

The substrate surface usually is modified by grafting random copolymer brushes or depositing chlorosilane monolayers. Random copolymer brushes with hydroxyl groups are used widely to modify hydroxyl-rich surfaces (*e.g.*, silicon oxide surfaces) through condensation reactions between two hydroxyl groups.[43] In a seminal work, Mansky *et al.* synthesized hydroxyl-terminated random copolymers of polystyrene-*r*-poly(methyl methacrylate) (PS-*r*-PMMA) with the styrene fraction varied from 0 to 1.[43] The random copolymer was end-grafted onto a silicon wafer by heating at 140 °C under vacuum, allowing the terminal OH groups to react with the native oxide layer. The thickness of the grafted brushes was ~5 nm after washing off the unattached materials. They demonstrated the polymer-surface interactions could be well-controlled by changing the composition of the random copolymers. For substrate surfaces that do not have a sufficient surface hydroxyl groups (*e.g.*, metals or polymers), random copolymers containing cross-linking components are employed to generate an insoluble cross-linked mat that may or may not be attached covalently to the surface.[44] For example, Han *et al.* synthesized PS-*r*-PMMA random copolymers with a third cross-linking component poly(glycidyl methacrylate), and the cross-linked mats (~ 8 nm thick) formed on the silicon wafer effectively induced the vertical orientation of domains in lamellae- and cylinder-forming PS-PMMA BPs.[41] Other

cross-linking polymers containing acryloyl, epoxide, or azide groups also are selected to modify surfaces depending on the surface material.[44-46]

Although the approach of random copolymer is efficient in modifying substrate surface, the compositions of the copolymer brushes need to be screened for balancing the interfacial energetics of the substrate with the BPs. Han *et al.* systematically investigated the composition window of random copolymer brushes and cross-linked mats to induce perpendicular orientation of domains in lamellae- and cylinder-forming PS-PMMA BPs.[41] They found the "perpendicular window" for each BP on a given brush was unique due to the individual energetic characteristics of each BP (Figure 1.4). Tuning the random copolymer composition is a tedious and time-consuming undertaking and requires an understanding of polymer synthesis and the associated kinetic processes in order to achieve the desired compositions.

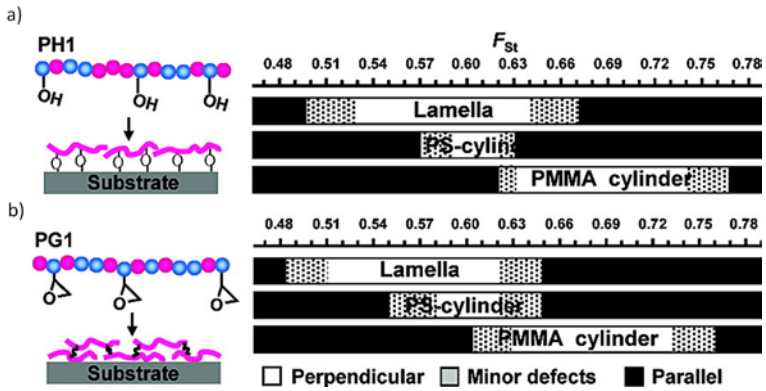

Figure 1.4: a) Side-chain hydroxy-containing PS/PMMA random copolymer and "perpendicular windows" of random copolymer composition (F_{st}) for lamellae-forming PS-PMMA and cylinder-forming PS-PMMA BPs. b) Side-chain epoxy-containing PS/PMMA random copolymer for cross-linking mats and its corresponding composition window for perpendicular domain structures. Adapted with permission from Han, E., *et al. Macromolecules*. 2008, 41, (23), 9090-9097. Copyright 2008 American Chemical Society.

Chlorosilane monolayer deposition method is a viable alternative to copolymer brushes for BP morphology manipulation.[47-49] The commercial availability of chlorosilane agents for deposition onto silicon oxide surfaces, along with the simplicity of the coating process, makes this approach highly attractive.[50] Furthermore, surface energy and surface chemistry can be tuned easily by selecting chlorosilane functionalities according to the BP of interest. For example, 3-(*p*-methoxyphenyl)propyltrichlorosilane is considered neutral for the PS and PMMA block, and it has been used to generate neutral substrate surfaces for lamellae- and cylinder-forming PS-PMMA BPs.[51, 52] The PS-PMMA domain structures were oriented perpendicular to the surface due to the balanced interfacial interactions of the blocks with the surface. Several other alkylchlorosilanes such as octadecyltrichlorosilane and octadecyldimethyl have been employed to control the wetting behavior of PS-PMMA BPs. By controlling the grafting densities of the alkylchlorosilanes or partially oxidizing the monolayers, neutral surface compositions can be achieved.[49, 53, 54] Unfortunately, the aforementioned examples utilize single chlorosilane and provide a limited tunability of substrate surface chemistry/energy. Recently, Albert *et al.* introduced a controlled vapor deposition method that is highly adaptable for two-chlorosilane systems. This method generates well-controlled gradient monolayers, allowing a high throughput examination of substrate surface effect on BP thin film phase behavior.[55]

1.3.3 Free Surface Effects

BP thin films often are thermally annealed above the glass transition temperature of the constituent bocks to impart mobility to the polymers chains such that morphology with the minimum energy state is reached. When the BP is annealed

in air or vacuum, the low surface energy block segregates to the free surface and forms a wetting layer to minimize the free energy of the film. This wetting layer behavior can lead the BP domain orient parallel in the vicinity of the free surface or, in some cases, through the entire film thickness. Numerous studies have demonstrated perpendicular orientations of PS-PMMA domain structures by modification of substrate surface alone because the interfacial energies of the two blocks at the free surface are balanced naturally at ~225 °C.[56] However, for BP systems have disparate interfacial energies, the perpendicular orientation of domain structures has been more challenging. A neutral free surface needs to be established.

Solvent vapor annealing (SVA) has been considered a viable method to control the free surface interactions. In general, the solvent vapor molecules swell the BP film and dilute the polymer. This dilution effectively lowers the glass transition temperatures (T_g's) of the polymer blocks, reduces the viscosity, and increases the chain mobility. If a selective solvent is in use, the relative composition of the blocks can be altered due to the preferentially swelling of specific blocks, leading to changes in BP morphologies.[57, 58] Furthermore, the solvent vapor in the film can mitigate the interactions between polymer blocks and both surfaces. By using selective solvents, the preferential segregation of the lower surface energy block to the free surface can be mitigated. With careful selection of solvents, surface neutrality can be achieved. However, finding a single solvent to create neutral surface is difficult. The use of solvent mixtures provides an avenue for tuning solvent selectivity.[59, 60] However, the screening process is a time consuming task and the nonidealities in cosolvent mixtures may limit the available solvent compositions. Recently, Albert *et al.* demonstrated using a microfluidic mixing device that produces discrete gradients in solvent vapor

composition and/or solvent vapor concentration to explore SVA parameter in a high-throughput fashion (Figure 1.5).[61]

Top coats for BP orientation control is an emerging research area offering enormous scientific and technological promise as industrial SVA tools are commercially unavailable. Top coats can be spin-coated onto the BP film and thus are highly compatible with existing manufacturing infrastructure. The seminal work of Bates *et al.* demonstrated the application of top coats to create perpendicular oriented lamellae-forming poly(styrene-*b*-trimethylsilylstyrene-*b*-styrene) and poly(trimethylsilylstyrene-*b*-lactide) BPs that otherwise orient parallel due to strongly surface preferred Si-containing block.[42] In their study, the polymeric coats were composed of maleic anhydride and two other components and were spin-coated from basic aqueous solution onto the BP film without damaging the underlying film. Subsequent thermal annealing induced anhydride reformation from ring-opened form to ring-closed form, and switched the polarity of the top coats to create a neutral layer for the BP. Finally, the top coats were stripped by washing with an aqueous base. The schematic of this process is shown in Figure 1.5.

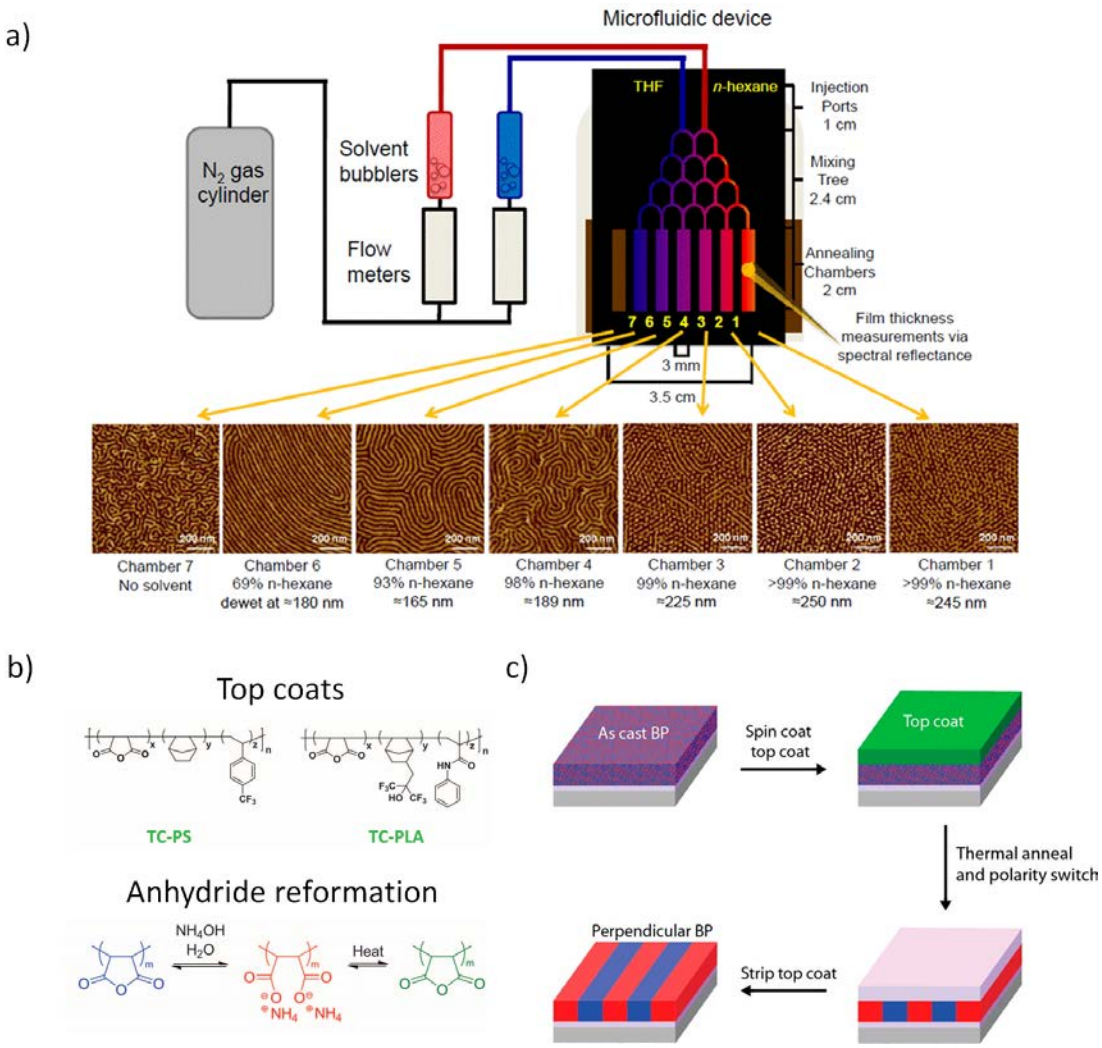

Figure 1.5: a) Schematic of SVA setup with the microfluidic device and its use as a screening tool to explore the phase behavior of a poly(styrene-*b*-isoprene-*b*-styrene) (SIS) triblock copolymer as a function of solvent composition and swollen film thickness. Adapted with permission from Albert, J. N. L., *et al. Nano Lett.* 2011, 11, (3), 1351-1357. Copyright 2011 American Chemical Society. b) The chemical structures of two top coats. TC-PS was applied to PS-PTMSS-PS and TC-PLA was applied to PTMSS-PLA. Ring-opening and -closing reactions that switch the polarity of the top coats. Adapted with permission from Bates, C. M., *et al. Science* 2012, 338, (6108), 775-779. Copyright 2012 AAAS. c) Schematic of the top coat process used to produce a perpendicular orientation of BP domains. Adapted with permission from Bates, C. M., *et al. Macromolecules* 2014, 47, (1), 2-12. Copyright 2014 American Chemical Society.

1.4 Directed Self-Assembly (DSA) of Block Polymer Thin Film

Portions of Section 1.4 is adapted with permission from Luo, M., *et al.* *Macromolecules* 2013, 46(19), 7567- 7579. Copyright 2013 American Chemical Society.

The control of BP nanostructures and domain orientation can be achieved through thin film confinement and film/surface interactions. However, many nanotechnology applications require the ability of fabricating BP nanostructures with high precision and in well-defined geometries as BPs typically self-assemble in an isotropic manner in the absence of surface forces and external fields[62, 63] (Figure 1.6). Many methods have been employed to direct the self-assembly of BP films, including graphoepitaxy,[20, 64] chemical prepatterning,[36, 65] electric, magnetic and mechanical (shear) fields, thermal gradients, nanoimprinting, and molecular transfer printing(REF).

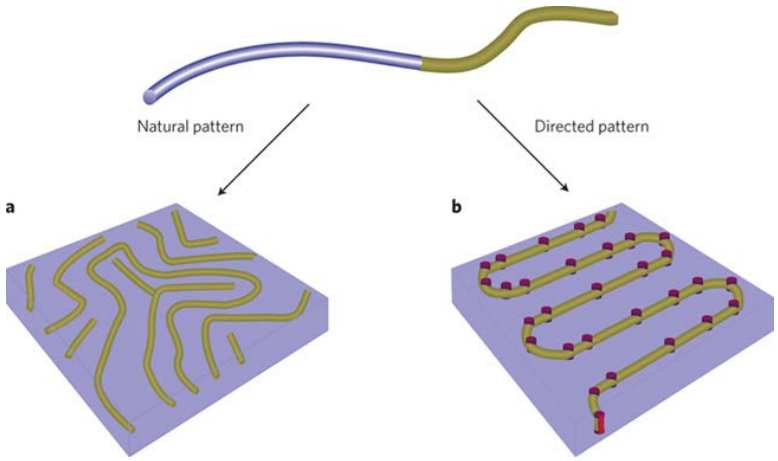

Figure 1.6: Directed self-assembly of a BP. The natural self-assembly of a BP thin film leads to a fingerprint pattern. However, nanotechnology applications require well-defined features. Adapted with permission from Poelma, *et al. Nat. Nanotechnol*. 2010, 5, (4), 243-244. Copyright 2010 Nature Publishing Group.

1.4.1 Graphoepitaxy and Chemical Prepatterning

Graphoepitaxy is a common approach to direct BP self-assembly in an attempt to overcome this inherent deficiency of copolymer assembly.[27, 66-71] Previous research efforts have demonstrated the generation of periodic patterns of parallel lines (perpendicular lamellae, parallel cylinders)[72-74] and close-packed dots (perpendicular cylinders, spheres)[64, 75, 76] using topographic guiding patterns. More complex structures such as concentric rings, "yin-yang" shape lines, and bent lines also were fabricated through the deliberate design of pre-patterned geometries or the induction of defects at the substrate walls.[20, 77, 78] In many of these cases, circular, triangular, rectangular and hexagonal patterns with varying dimensions usually were fabricated by optical lithography or e-beam lithography (Figure 1.7).[20, 76, 79] The underlying ordering mechanism is well understood with regard to commensurability and interactions of each block with substrates and walls.[63, 80-82] Two key drawbacks to graphoepitaxy are that valuable substrate area is lost due to patterning and precisely controlled lithographic writing instruments are costly.

In comparison to graphoepitaxy, chemical prepatterning does not sacrifice substrate area and allows for guidance of the BP self-assembling and control over nanostructure shapes and dimensions.[27, 28, 83] Many of the essential features required for manufacturing integrated circuits including dense and isolated bends, jogs, spots and T-junctions have been demonstrated in BP thin films through chemical prepatterning.[67, 70] However, this prepatterning method is somewhat disadvantageous as it involves a lithographic writing step, nominally at similar feature densities to those achieved by BPs (Figure 1.7).[71, 84] Even though BP assembly permits quality pattern rectification with respect to the chemical prepattern, creating a template in which every feature is written by e-beam lithography is prohibitive due to the long writing

times required for patterning large-areas at high densities. As a viable alternative, density multiplication recently was shown to improve resolution and reduce lithographic writing times for templating BPs.[19]

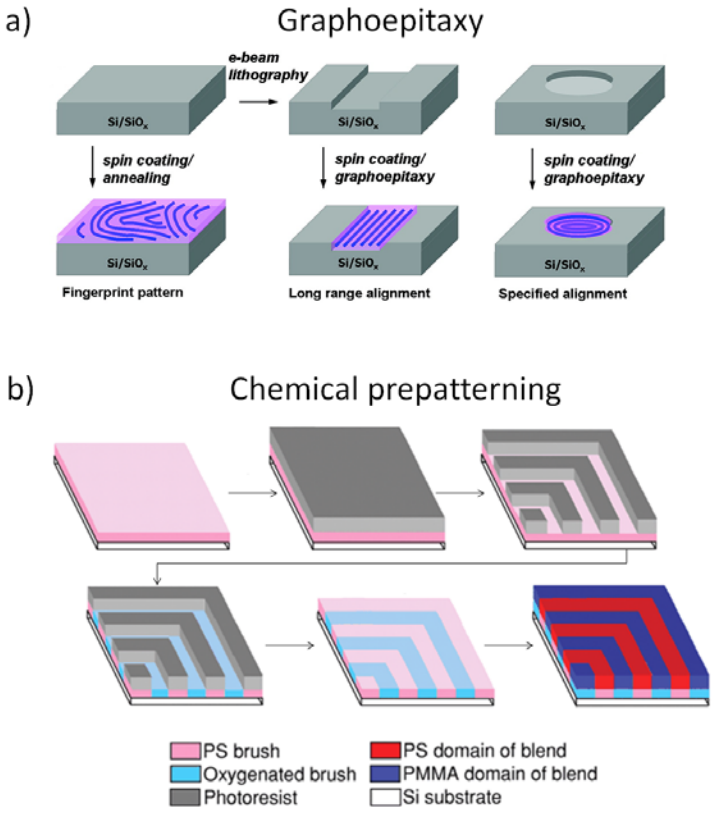

Figure 1.7: Schematic illustrations of (a) graphoepitaxy and (b) chemical prepatterning processes. Graphoepitaxy uses topographic patterns to guide the BP self-assembly. Chemical prepatterning uses lithographic tools to prepattern the substrate first, and then the BP was able to mimic the prepatterns. Part (a) adapted with permission from Chai, *et al. ACS Nano.* 2008, 2, (3), 489-501. Copyright 2008 American Chemical Society. Part (b) adapted with permission from Stoykovich, *et al. Science* 2005, 308, (5727), 1442-1446. Copyright 2005 AAAS.

1.4.2 Electric, Magnetic and Mechanical (Shear) Fields

Alignment by electric, magnetic and mechanical (shear) fields are well-established means to achieve directional ordering of BP structures. The electric field alignment of BPs is driven by the minimization of the orientation dependent electrostatic energy, which arises from the difference in dielectric permittivity between constituent blocks. BPs with high dielectric contrast between the constituent blocks (*e.g.*, PS-PMMA, PS-poly[ethylene oxide], PS-polylactide) have been used widely in electric field alignment.[85, 86] The alignment process must be performed above the T_g of all the blocks, and enhanced alignment process has been demonstrated when the BP samples were cooled across T_{ODT} in the electric field, as opposed to isothermal annealing at temperature below T_{ODT}.[26] Thus, electrical field alignment may not be desirable for high molecular weight polymers as their T_{ODT}'s may not be accessible without degradation. Additionally, at the electrode-film surface, the BPs may be subjected to a strong polymer-surface interaction and withstand the electrical field aligning.[87] Magnetic field alignment, which is similar to electric field alignment, induces BP alignment to minimize the orientation dependent magnetostatic energy originated from anisotropy in the magnetic susceptibility. Magnetic field alignment is applicable only to select polymer systems with large magnetic susceptibility. BP systems for magnetic field alignment often involve liquid crystalline or semi crystalline materials. For an overview of detailed topics and developments in electric and magnetic field alignment, the readers are directed elsewhere.[26]

Shear fields have been used widely to align BPs in bulk and is in principle not limited to any particular BP systems.[88, 89] Shear alignment can be conducted using a variety of simple tools and shear alignment of spheres, cylinders, gyroid, and lamellae have been documented in the literature.[90-93] Recently, shear field has been employed

to align single layer BP thin films (~30 nm) as demonstrated by Register and Chaikin (Figure 1.8).[94, 95] In these works, shear stress was applied by the deformation and displacement of a cross-linked poly(dimethylsiloxane) (PDMS) pad placed on top of a cylinder-forming poly[styrene-*b*-(ethylene-*alt*-propylene)] [PS-PEP] thin film, and the cylinder domain orientation was correlated strongly with the shear direction after thermal annealing under shear for an hour.[94] This technique could be modified easily for larger or smaller areas by changing the size of the elastomer pad. However, the alignment quality degraded quickly as the BP film thickness deviated from a single domain spacing.[94] Additionally, this batch processing method is potentially slow in comparison to the few minutes ideal for alignment for many applications. Recent studies of creative combinations of shear with thermal annealing or solvent vapor annealing have offered a promise way toward practical industrial utilization.[96-98]

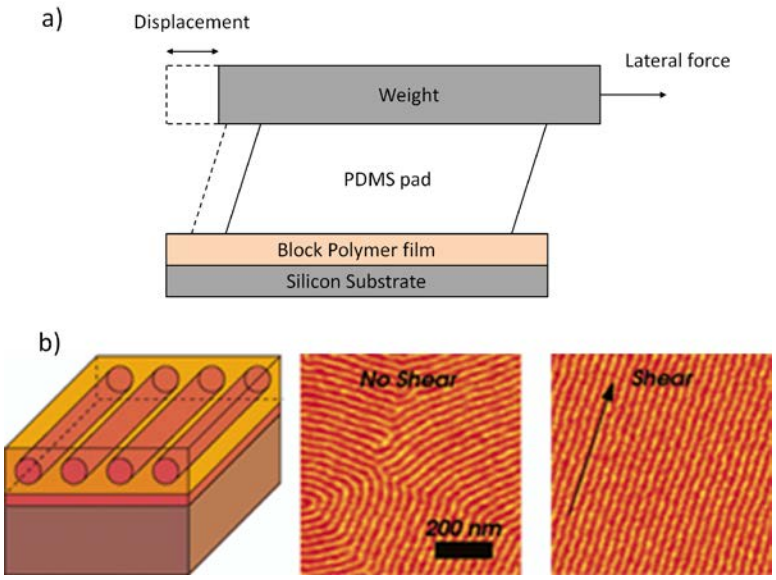

Figure 1.8: (a) Schematic of shear alignment setup. Shear force is imposed onto the BP film by a PDMS pad. (b) Atomic force microscopy (AFM) micrographs of PS-PEP BP thin film aligned by shear. The arrow indicates the shearing direction. Adapted with permission from Angelescu, *et al.* Adv. Mater. 2004, 16, (19), 1736-1740. Copyright 2004 John Wiley & Sons, Inc.

1.4.3 Thermal Gradients

Thermal annealing is one of the most broadly applicable techniques to improve long-range order of nanostructures in BP thin films. Thermal annealing the film above the glass transition temperature of all the constituent blocks imparts mobility to the polymer chains, facilitates BP to adopt equilibrium morphology and annihilates energetically unfavorable defects. However, directional self-assembled patterns are difficult to accomplish with uniform annealing. Seminal work on hot zone annealing (HZA) was performed by Hashimoto and his coworkers, in which a BP specimen (bulk) was swept through a sharp temperature gradient.[99] As the BP was heated above the T_{ODT} and then quickly cooled below T_{ODT}, ordered lamellae were found to align

normal to the direction of the moving gradient. Jones and coworkers developed a processing platform, termed "cold zone annealing" (CZA), in which the BP thin films were annealed using a thermal gradient with T_{max} below the T_{ODT} of the copolymer film.[100, 101] This CZA process affords additional advantages over conventional HZA by allowing the processing of thermally-sensitive materials and high-molecular weight BPs that possess a high T_{ODT}. Enhanced ordering kinetics was found (5 – 30 μm^2 grains of parallel cylinders in less than 5 h) due to the in-plane temperature gradient, and an orientation bias was noted due to the motion of a thermal zone and/or directional heat flux. Furthermore, Singh *et al.* combined the thermal gradient with a soft-shear process (CZA-SS, Figure 1.9), to rapidly fabricate unidirectional aligned BP nanopatterns over large length scales.[97] In the case of CZA-SS, an elastomeric PDMS layer is placed on top of the BP film and undergoes directional expansion and contraction due to a dynamic thermal field, thus imposes an oscillatory shear to the underlying BP film. Using this process, arrays of hexagonally-packed and horizontally-aligned BP cylinders could be fabricated in films over a thickness range of 40 – 1000 nm, with greater than 99% cylinder alignment in CZA-SS direction. Furthermore, this process can be accomplished at relatively high velocities for BP ordering ($V \approx 0.2$ mm/s). This technique is particularly attractive because it is amenable to roll-to-roll processing lines.

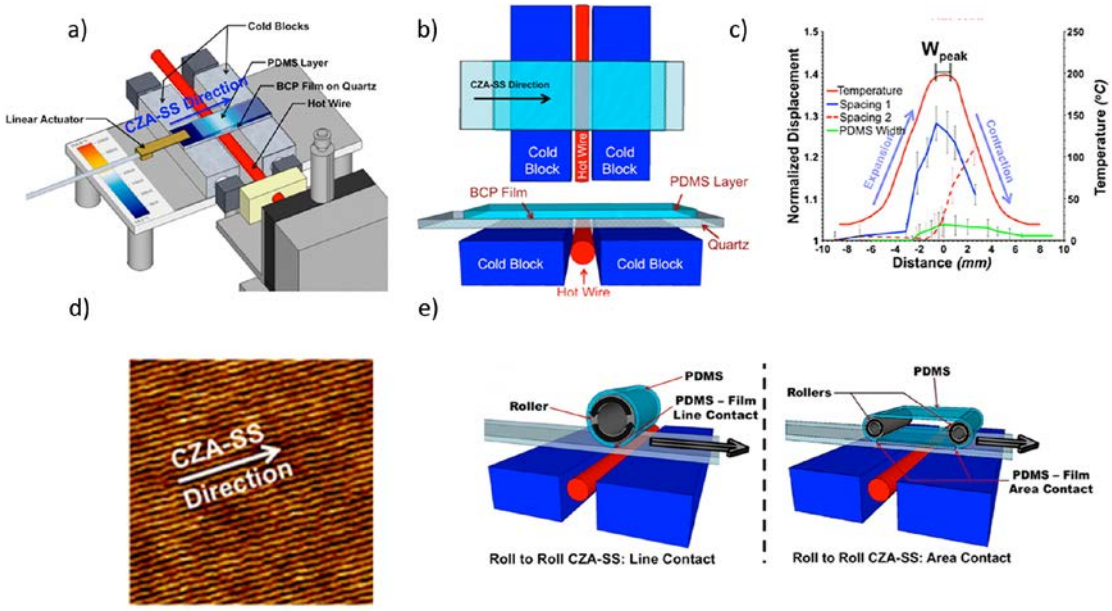

Figure 1.9: (a) Schematic of the CZA–SS apparatus. (b) In-plane and out-of-plane view of the CZA–SS process. (c) Temperature gradient curve. (d) AFM image of PS-PMMA after CZA-SS process. (e) CZA-SS amenable to roll-to-roll process. Adapted with permission from Singh, *et al. ACS Nano.* 2012, 6, (11), 10335-10342. Copyright 2012 American Chemical Society.

1.4.4 Nanoimprinting and Molecular Transfer Printing

Nanoimprint lithography (NIL) is a relatively recent lithographic technique useful for the high-throughput patterning of nanoscale structures in soft materials at great precision and relatively low cost.[102-105] In NIL, the patterning of polymers is accomplished by pressing a hard mold into softened thermoplastic resists (for example, PMMA) or liquid polymer precursors (for example, UV-curable epoxysilicone), and then fixing the pattern by either cooling or UV-photocuring the resists, as shown in Figure 1.10. Unlike traditional lithographic approaches that define patterns using photons or electrons to modify the resist layer, NIL creates patterns by direct mechanical deformation of the soft material. In this manner, NIL can achieve

resolutions beyond the limitations inherent to light diffraction. When combined with self-assembled BP materials, NIL has proved a facile and cost-effective way to generate ultra-high-density arrays of ordered, sub-10 nm nanopatterns.[102, 106] However, the successful demonstration of directed self-assembly of BPs *via* NIL are scarce in part because of mold release issues. The high interfacial adhesion between the mold and the imprinted polymer film often leads to poor mold release, leaving behind damaged, deformed, or delaminated features in addition to contaminating the mold for future usage.

Molecular transfer printing (MTP) is an alternative patterning technique for creating and replicating patterns to direct BP self-assembly over macroscopic areas with feature dimensions of order 10 nm.[107] MTP resembles the "copy-print" process, as it "copies" the domain structure pattern at the surface of BP films, and "prints" onto either rigid or flexible substrates with high fidelity. In MTP, "inks" are stored in the copolymer domains and transferred to the replica surface. A schematic of the MTP process is shown in Figure 1.10 and outlined below. MTP starts with a deposited thin film that is a blend of BP and inks. During annealing, the BP self-assembles into an ordered structure, and ink molecules segregate into their respective copolymer domains. Then, a replica substrate is brought into contact with the surface of the assembled film, and the ink molecules are transferred to the replica substrate by reaction, creating a pattern of ink molecules that resembles the domain structure of the BP film surface. After MTP, the BP thin film is dissolved, allowing recovery of the original master surface and the patterned replica surface. The MTP process can create multiple replicas in an efficient manner. However, a major limitation of MTP lays in

the geometries of patterns that can be replicated, which may hinder industrial production.

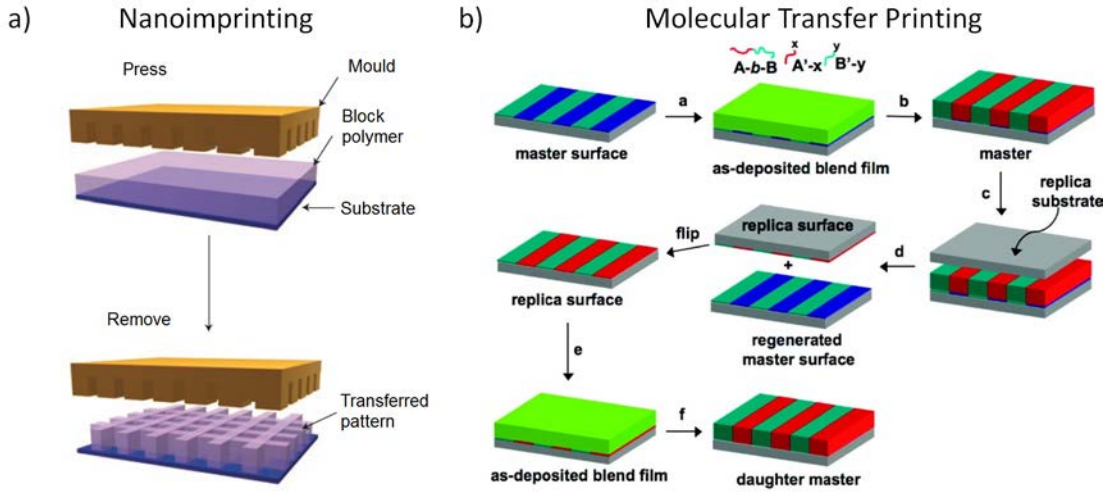

Figure 1.10: Schematic of (a) nanoimprinting and (b) molecular transfer printing techniques. Part (a) adapted with permission from Nie, *et al. Nat. Mater.* 2008, 7, (4), 277-290. Copyright 2008 Nature Publishing Group. Part (b) adapted with permission from Ji, *et al. ACS Nano* 2009, 4, (2), 599-609. Copyright 2009 American Chemical Society.

In summary, the ability to precisely control the spatial organization of structures in a plethora of soft materials is of crucial importance to the advancement of nanotechnology. Many techniques have been developed to guide the BP self-assembly, with varying degrees of success. Especially, defectivity and patterning reliability is one of the main hurdles for DSA process to becoming an industrially viable patterning method.[8] Future work will continue on many of the aforementioned techniques to reduce residual defects and defect densities to achieve near-perfect crystalline order, to enhance the resolution of soft materials nanopatterning into the

sub-10 nm range, to increase the speed of orientation and alignment processes, to simplify or reduce processing steps such that manufacturing times are less than minutes, and to increase the patternable areas of the oriented structures.

1.5 Thesis Overview

This thesis describes efforts to control the self-assembling and ordering of BP nanostructure in thin films. Specifically, a gradient approach was employed to examine the effects of substrate surface chemistry and film thickness on a cylinder-forming SIS triblock thin film. The substrate and thickness conditions for a phase transformation from cylinder to perforated lamellar were identified using a combination of techniques, including film etching, cross-sectional transmission electron microscopy (TEM) and grazing-incidence small-angle X-ray scattering (GISAXS). The use of high-throughput gradient tool facilitates the examination of new materials and furthers the understanding of BP thin film self-assembly.

Next, an incredibly simple, yet highly effective method was developed to achieve macroscopic alignment of nanostructures in BP thin films through the application of rastering solvent vapor annealing combined with a soft shear field (RSVA-SS). This method substantially improves on previous approaches by using simple SVA apparatus and a PDMS elastomer pad to unlock an array of alignment patterns with a variety of self-assembling polymers and provides feasibility and flexibility for practical industrial production.

Additionally, the influence of tapered interfaces in BPs on their thermodynamic properties and free surface morphologies in thin films were investigated. Tapered Block Polymers (TBPs) are an emerging class of macromolecules, and the interfacial manipulation of these polymers has led to unique

and diverse self-assembly behavior and properties. The quantitative measurement of interfacial mixing in these tapered materials allows us to connect macroscopic physical properties to microscopic molecular structures, and it furthers our understanding of interfacial modifications as a valuable tool for materials design.

Finally, XPS depth profiling with C_{60}^{+} sputtering was used to determine the lithium ion distribution in a lamellae-forming block polymer electrolyte film. The results provide useful insights for the future design and optimization of block polymer structures for high efficiency energy storage devices. Additionally, the unique capabilities of C_{60}^{+} depth profiling XPS are potentially applicable to investigations of nanoscale distributions of molecules in a myriad of polymer thin film systems.

The surface and thin film characterization techniques are provided in Chapter 2. The manipulation of nanoscale morphology of SIS thin films are presented in Chapter 3. The macroscopic alignment of SIS cylinders is described in Chapter 4. In Chapter 5, the influence of tapered interfaces in BPs with respect to their thermodynamic properties and free surface morphologies in thin films were examined. In Chapter 6, the application of XPS with C_{60}^{+} depth profiling for determination of lithium ion distribution in BP electrolyte thin films was demonstrated. Finally, Chapter 7 concludes with an outlook for future studies.

REFERENCES

1. Bates, F. S. *Science* **1991,** 251, (4996), 898-905.
2. Bates, F. S.; Fredrickson, G. H. *Physics Today* **1999,** 52, (2), 32-38.
3. Segalman, R. A. *Materials Science and Engineering: R: Reports* **2005,** 48, (6), 191-226.
4. Fasolka, M. J.; Mayes, A. M. *Annu. Rev. Mater. Res.* **2001,** 31, (1), 323-355.
5. Marencic, A. P.; Register, R. A. *Annual Review of Chemical and Biomolecular Engineering* **2010,** 1, 277-297.
6. Bates, C. M.; Maher, M. J.; Janes, D. W.; Ellison, C. J.; Willson, C. G. *Macromolecules* **2014,** 47, (1), 2-12.
7. Park, C.; Yoon, J.; Thomas, E. L. *Polymer* **2003,** 44, (22), 6725-6760.
8. Luo, M.; Epps, T. H., III. *Macromolecules* **2013,** 46, (19), 7567-7579.
9. Albert, J. N. L.; Epps, T. H., III. *Materials Today* **2010,** 13, (6), 24-33.
10. Cochran, E. W.; Garcia-Cervera, C. J.; Fredrickson, G. H. *Macromolecules* **2006,** 39, (7), 2449-2451.
11. Matsen, M. W.; Bates, F. S. *Macromolecules* **1996,** 29, (4), 1091-1098.
12. Matsen, M. W.; Thompson, R. B. *J. Chem. Phys.* **1999,** 111, (15), 7139-7146.
13. Bates, F. S.; Hillmyer, M. A.; Lodge, T. P.; Bates, C. M.; Delaney, K. T.; Fredrickson, G. H. *Science* **2012,** 336, (6080), 434-440.
14. Matsen, M. W. *Macromolecules* **2012,** 45, (4), 2161-2165.
15. Glaser, J.; Medapuram, P.; Beardsley, T. M.; Matsen, M. W.; Morse, D. C. *Phys. Rev. Lett.* **2014,** 113, (6), 068302.

16. Brandrup, J.; Immergut, E. H.; Grulke, E. A., *Polymer Handbook*. 4th ed.; Wiley: New York, 1999.

17. Khandpur, A. K.; Foerster, S.; Bates, F. S.; Hamley, I. W.; Ryan, A. J.; Bras, W.; Almdal, K.; Mortensen, K. *Macromolecules* **1995,** 28, (26), 8796-8806.

18. Zschech, D.; Kim, D. H.; Milenin, A. P.; Scholz, R.; Hillebrand, R.; Hawker, C. J.; Russell, T. P.; Steinhart, M.; Gösele, U. *Nano Lett.* **2007,** 7, (6), 1516-1520.

19. Ruiz, R.; Kang, H.; Detcheverry, F. A.; Dobisz, E.; Kercher, D. S.; Albrecht, T. R.; de Pablo, J. J.; Nealey, P. F. *Science* **2008,** 321, (5891), 936-939.

20. Chai, J.; Buriak, J. M. *ACS Nano* **2008,** 2, (3), 489-501.

21. Jung, Y. S.; Jung, W.; Tuller, H. L.; Ross, C. A. *Nano Lett.* **2008,** 8, (11), 3776-3780.

22. Bang, J.; Kim, S. H.; Drockenmuller, E.; Misner, M. J.; Russell, T. P.; Hawker, C. J. *J. Am. Chem. Soc.* **2006,** 128, (23), 7622-7629.

23. Yang, S. Y.; Ryu, I.; Kim, H. Y.; Kim, J. K.; Jang, S. K.; Russell, T. P. *Adv. Mater.* **2006,** 18, (6), 709-712.

24. Fink, Y.; Urbas, A. M.; Bawendi, M. G.; Joannopoulos, J. D.; Thomas, E. L. *Lightwave Technology, Journal of* **1999,** 17, (11), 1963-1969.

25. Deng, T.; Chen, C.; Honeker, C.; Thomas, E. L. *Polymer* **2003,** 44, (21), 6549-6553.

26. Hu, H.; Gopinadhan, M.; Osuji, C. O. *Soft Matter* **2014,** 10, (22), 3867-3889.

27. Bang, J.; Jeong, U.; Ryu, D. Y.; Russell, T. P.; Hawker, C. J. *Adv. Mater.* **2009,** 21, (47), 4769-4792.

28. Stoykovich, M. P.; Kang, H.; Daoulas, K. C.; Liu, G.; Liu, C.-C.; de Pablo, J. J.; Müller, M.; Nealey, P. F. *ACS Nano* **2007,** 1, (3), 168-175.

29. Sinturel, C.; Bates, F. S.; Hillmyer, M. A. *ACS Macro Letters* **2015,** 4, (9), 1044-1050.

30. IBM Brings Nature to Computer Chip Manufacturing. *IBM Press Release* May 3, 2007.

31. HGST Reaches 10-Nanometer Patterned-bit Milestone, Nanotechnology Process Will Double Today's Disk Drive Data Density. *HGST Press Release* February 28, 2013.

32. IMEC Announces World-first 300mm-Fab Compatible Directed Self-assembly Process Line. *IMEC News* February 10, 2012.

33. Thurn-Albrecht, T.; Schotter, J.; Kästle, G. A.; Emley, N.; Shibauchi, T.; Krusin-Elbaum, L.; Guarini, K.; Black, C. T.; Tuominen, M. T.; Russell, T. P. *Science* **2000,** 290, (5499), 2126-2129.

34. Miyake, G. M.; Piunova, V. A.; Weitekamp, R. A.; Grubbs, R. H. *Angew. Chem. Int. Ed.* **2012,** 51, (45), 11246-11248.

35. Kim, J. K.; Lee, J. I.; Lee, D. H. *Macromol. Res.* **2008,** 16, (4), 267-292.

36. Edwards, E. W.; Montague, M. F.; Solak, H. H.; Hawker, C. J.; Nealey, P. F. *Adv. Mater.* **2004,** 16, (15), 1315-1319.

37. Matsen, M. *J. Chem. Phys.* **1997,** 106, (18), 7781-7791.

38. Stein, G. E.; Kramer, E. J.; Li, X.; Wang, J. *Macromolecules* **2007,** 40, (7), 2453-2460.

39. Luo, M.; Seppala, J. E.; Albert, J. N. L.; Lewis, R. L.; Mahadevapuram, N.; Stein, G. E.; Epps, T. H., III. *Macromolecules* **2013,** 46, (5), 1803-1811.

40. Huang, E.; Pruzinsky, S.; Russell, T. P.; Mays, J.; Hawker, C. J. *Macromolecules* **1999,** 32, (16), 5299-5303.

41. Han, E.; Stuen, K. O.; La, Y.-H.; Nealey, P. F.; Gopalan, P. *Macromolecules* **2008,** 41, (23), 9090-9097.

42. Bates, C. M.; Seshimo, T.; Maher, M. J.; Durand, W. J.; Cushen, J. D.; Dean, L. M.; Blachut, G.; Ellison, C. J.; Willson, C. G. *Science* **2012,** 338, (6108), 775-779.

43. Mansky, P.; Liu, Y.; Huang, E.; Russell, T.; Hawker, C. *Science* **1997,** 275, (5305), 1458-1460.

44. Ryu, D. Y.; Shin, K.; Drockenmuller, E.; Hawker, C. J.; Russell, T. P. *Science* **2005,** 308, (5719), 236-239.

45. Bang, J.; Bae, J.; Löwenhielm, P.; Spiessberger, C.; Given‐Beck, S. A.; Russell, T. P.; Hawker, C. J. *Adv. Mater.* **2007,** 19, (24), 4552-4557.

46. Han, E.; In, I.; Park, S. M.; La, Y. H.; Wang, Y.; Nealey, P. F.; Gopalan, P. *Adv. Mater.* **2007,** 19, (24), 4448-4452.

47. Albert, J. N. L.; Baney, M. J.; Stafford, C. M.; Kelly, J. Y.; Epps, T. H., III. *ACS Nano* **2009,** 3, (12), 3977-3986.

48. Xu, J.; Russell, T. P.; Ocko, B. M.; Checco, A. *Soft Matter* **2011,** 7, (8), 3915-3919.

49. Peters, R. D.; Yang, X. M.; Kim, T. K.; Nealey, P. F. *Langmuir* **2000,** 16, (24), 9620-9626.

50. Gelest. *http://www.gelest.com/goods/pdf/couplingagents.pdf.*

51. Park, D.-H. *Nanotechnology* **2007,** 18, (35), 355304.

52. Sohn, B.; Yun, S. *Polymer* **2002,** 43, (8), 2507-2512.

53. Niemz, A.; Bandyopadhyay, K.; Tan, E.; Cha, K.; Baker, S. M. *Langmuir* **2006,** 22, (26), 11092-11096.

54. Liu, P.-H.; Thébault, P.; Guenoun, P.; Daillant, J. *Macromolecules* **2009,** 42, (24), 9609-9612.

55. Albert, J. N. L.; Kim, J. D.; Stafford, C. M.; Epps, T. H., III. *Rev. Sci. Instrum.* **2011,** 82, (6), 065103.

56. Mansky, P.; Russell, T. P.; Hawker, C. J.; Mays, J.; Cook, D. C.; Satija, S. K. *Phys. Rev. Lett.* **1997,** 79, (2), 237-240.

57. Hsieh, I. F.; Sun, H.-J.; Fu, Q.; Lotz, B.; Cavicchi, K. A.; Cheng, S. Z. D. *Soft Matter* **2012,** 8, (30), 7937-7944.

58. Paik, M. Y.; Bosworth, J. K.; Smilges, D.-M.; Schwartz, E. L.; Andre, X.; Ober, C. K. *Macromolecules* **2010,** 43, (9), 4253-4260.

59. Jung, Y. S.; Ross, C. A. *Adv. Mater.* **2009,** 21, (24), 2540-2545.

60. Kim, S. H.; Misner, M. J.; Xu, T.; Kimura, M.; Russell, T. P. *Adv. Mater.* **2004,** 16, (3), 226-231.

61. Albert, J. N. L.; Bogart, T. D.; Lewis, R. L.; Beers, K. L.; Fasolka, M. J.; Hutchison, J. B.; Vogt, B. D.; Epps, T. H., III. *Nano Lett.* **2011,** 11, (3), 1351-1357.

62. Bita, I.; Yang, J. K. W.; Jung, Y. S.; Ross, C. A.; Thomas, E. L.; Berggren, K. K. *Science* **2008,** 321, (5891), 939-943.

63. Mishra, V.; Fredrickson, G. H.; Kramer, E. J. *ACS Nano* **2012,** 6, (3), 2629-2641.

64. Cheng, J. Y.; Mayes, A. M.; Ross, C. A. *Nat. Mater.* **2004,** 3, (11), 823-828.

65. Han, E.; Leolukman, M.; Kim, M.; Gopalan, P. *ACS Nano* **2010,** 4, (11), 6527-6534.

66. Moon, H.-S.; Shin, D. O.; Kim, B. H.; Jin, H. M.; Lee, S.; Lee, M. G.; Kim, S. O. *J. Mater. Chem.* **2012,** 22, (13), 6307-6310.

67. Stoykovich, M. P.; Nealey, P. F. *Materials Today* **2006,** 9, (9), 20-29.

68. Cheng, J. Y.; Ross, C. A.; Smith, H. I.; Thomas, E. L. *Adv. Mater.* **2006,** 18, (19), 2505-2521.

69. Segalman, R. A.; Yokoyama, H.; Kramer, E. J. *Adv. Mater.* **2001,** 13, (15), 1152-1155.

70. Stoykovich, M. P.; Müller, M.; Kim, S. O.; Solak, H. H.; Edwards, E. W.; de Pablo, J. J.; Nealey, P. F. *Science* **2005,** 308, (5727), 1442-1446.

71. Kim, S. O.; Solak, H. H.; Stoykovich, M. P.; Ferrier, N. J.; de Pablo, J. J.; Nealey, P. F. *Nature* **2003,** 424, (6947), 411-414.

72. Park, S. M.; Stoykovich, M. P.; Ruiz, R.; Zhang, Y.; Black, C. T.; Nealey, P. F. *Adv. Mater.* **2007,** 19, (4), 607-611.

73. Sundrani, D.; Darling, S. B.; Sibener, S. J. *Nano Lett.* **2003,** 4, (2), 273-276.

74. Sundrani, D.; Darling, S. B.; Sibener, S. J. *Langmuir* **2004,** 20, (12), 5091-5099.

75. Fitzgerald, T. G.; Borsetto, F.; O'Callaghan, J. M.; Kosmala, B.; Holmes, J. D.; Morris, M. A. *Soft Matter* **2007,** 3, (7), 916-921.

76. Stein, G. E.; Kramer, E. J.; Li, X.; Wang, J. *Phys. Rev. Lett.* **2007,** 98, (8), 086101.

77. Yamaguchi, T.; Yamaguchi, H. *Adv. Mater.* **2008,** 20, (9), 1684-1689.

78. Sang-Min, P.; Oun-Ho, P.; Joy, Y. C.; Charles, T. R.; Ho-Cheol, K. *Nanotechnology* **2008,** 19, (45), 455304.

79. Kim, W. S.; Jia, L.; Thomas, E. L. *Adv. Mater.* **2009,** 21, (19), 1921-1926.

80. Han, E.; Kang, H.; Liu, C.-C.; Nealey, P. F.; Gopalan, P. *Adv. Mater.* **2010,** 22, (38), 4325-4329.

81. Detcheverry, F. o. A.; Nealey, P. F.; de Pablo, J. J. *Macromolecules* **2010,** 43, (15), 6495-6504.

82. Park, S.-M.; Rettner, C. T.; Pitera, J. W.; Kim, H.-C. *Macromolecules* **2009,** 42, (15), 5895-5899.

83. Wilmes, G. M.; Durkee, D. A.; Balsara, N. P.; Liddle, J. A. *Macromolecules* **2006,** 39, (7), 2435-2437.

84. Welander, A. M.; Kang, H.; Stuen, K. O.; Solak, H. H.; Müller, M.; de Pablo, J. J.; Nealey, P. F. *Macromolecules* **2008,** 41, (8), 2759-2761.

85. Amundson, K.; Helfand, E.; Davis, D. D.; Quan, X.; Patel, S. S.; Smith, S. D. *Macromolecules* **1991,** 24, (24), 6546-6548.

86. Ruppel, M.; Pester, C. W.; Langner, K. M.; Sevink, G. J.; Schoberth, H. G.; Schmidt, K.; Urban, V. S.; Mays, J. W.; Böker, A. *ACS Nano* **2013,** 7, (5), 3854-3867.

87. Thurn-Albrecht, T.; DeRouchey, J.; Russell, T. P.; Kolb, R. *Macromolecules* **2002,** 35, (21), 8106-8110.

88. Winey, K. I.; Patel, S. S.; Larson, R. G.; Watanabe, H. *Macromolecules* **1993,** 26, (16), 4373-4375.

89. Young, W. S.; Epps, T. H., III. *Macromolecules* **2012,** 45, (11), 4689-4697.

90. Lee, W.-K.; Kim, H. D.; Kim, E. Y. *Current Applied Physics* **2006,** 6, (4), 718-722.

91. Scott, D. B.; Waddon, A. J.; Lin, Y. G.; Karasz, F. E.; Winter, H. H. *Macromolecules* **1992,** 25, (16), 4175-4181.

92. Dair, B. J.; Honeker, C. C.; Alward, D. B.; Avgeropoulos, A.; Hadjichristidis, N.; Fetters, L. J.; Capel, M.; Thomas, E. L. *Macromolecules* **1999,** 32, (24), 8145-8152.

93. Gupta, V. K.; Krishnamoorti, R.; Chen, Z. R.; Kornfield, J. A.; Smith, S. D.; Satkowski, M. M.; Grothaus, J. T. *Macromolecules* **1996,** 29, (3), 875-884.

94. Angelescu, D. E.; Waller, J. H.; Adamson, D. H.; Deshpande, P.; Chou, S. Y.; Register, R. A.; Chaikin, P. M. *Adv. Mater.* **2004,** 16, (19), 1736-1740.

95. Kim, S. Y.; Nunns, A.; Gwyther, J.; Davis, R. L.; Manners, I.; Chaikin, P. M.; Register, R. A. *Nano Lett.* **2014,** 14, (10), 5698-5705.

96. Qiang, Z.; Zhang, L.; Stein, G. E.; Cavicchi, K. A.; Vogt, B. D. *Macromolecules* **2014,** 47, (3), 1109-1116.

97. Singh, G.; Yager, K. G.; Berry, B.; Kim, H.-C.; Karim, A. *ACS Nano* **2012,** 6, (11), 10335-10342.

98. Majewski, P. W.; Yager, K. G. *ACS Nano* **2015,** 9, (4), 3896-3906.

99. Hashimoto, T.; Bodycomb, J.; Funaki, Y.; Kimishima, K. *Macromolecules* **1999,** 32, (3), 952-954.

100. Berry, B. C.; Bosse, A. W.; Douglas, J. F.; Jones, R. L.; Karim, A. *Nano Lett.* **2007,** 7, (9), 2789-2794.

101. Yager, K. G.; Fredin, N. J.; Zhang, X.; Berry, B. C.; Karim, A.; Jones, R. L. *Soft Matter* **2010,** 6, (1), 92-99.

102. Ahn, S. H.; Guo, L. J. *ACS Nano* **2009,** 3, (8), 2304-2310.

103. Ofir, Y.; Moran, I. W.; Subramani, C.; Carter, K. R.; Rotello, V. M. *Adv. Mater.* **2010,** 22, (32), 3608-3614.

104. Park, J. Y.; Hendricks, N. R.; Carter, K. R. *Langmuir* **2011,** 27, (17), 11251-11258.

105. Hu, Z.; Jonas, A. M. *Soft Matter* **2010,** 6, (1), 21-28.

106. Park, S.-M.; Liang, X.; Harteneck, B. D.; Pick, T. E.; Hiroshiba, N.; Wu, Y.; Helms, B. A.; Olynick, D. L. *ACS Nano* **2011,** 5, (11), 8523-8531.

107. Ji, S.; Liu, C.-C.; Liao, W.; Fenske, A. L.; Craig, G. S. W.; Nealey, P. F. *Macromolecules* **2011,** 44, (11), 4291-4300.

Chapter 2

EXPERIMENTAL METHODS AND CHARACTERIZATION TECHNIQUES

The experimental methods for substrate modification, block polymer (BP) thin film fabrication and processing are described in this chapter. The characterization techniques used to determine the surface properties, BP thermal and morphological behaviors also are discussed in this chapter, whereas specific experimental results are provided in later chapters.

2.1 Substrate Modification with Chlorosilanes

The chlorosilane monolayer deposition method is a viable alternative to copolymer brushes for the BP morphology manipulation (see discussion in Chapter 1 Section 1.3.2).[1-3] Chlorosilanes are a group of chemicals that contain at least one hydrolytically sensitive silicon-chlorine bond that can react with oxide substrates such as silicon wafers to form stable covalent silicon-oxygen bonds, and an organic functional group that alters the surface chemistry/energy of treated substrates (Figure 2.1). Surface chemistry/energy can be tuned by selecting appropriate functionalized chlorosilanes. Common chlorosilanes include alkyl-, aromatic-, and fluorinated alkyl-chlorosilanes. Chlorosilanes with multiple silicon-chlorine groups form siloxane polymers after deposition, bonding both with each other as well as the substrate. Thus, only monochlorosilanes are used in this thesis work, and the deposited layer is likely one molecule thick.

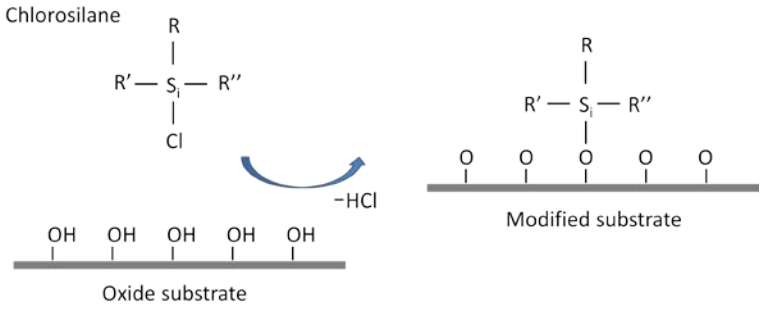

Figure 2.1: Scheme of chlorosilane deposition on oxide substrate.

The bare silicon substrates are placed in a UV-ozone cleaner for 1 h. The UV light excites/cleaves contaminant molecules on the substrate, and dissociates O_2 into atomic oxygen and ozone. The contaminant molecules react with atomic oxygen to form simpler volatile molecules such as CO_2, H_2O, N_2, *etc.*, and the substrate forms more hydroxyl groups on the surface. Then, chlorosilanes are deposited onto the silicon substrates by liquid or vapor phase deposition processes. The liquid deposition is accomplished by dropping pure chlorosilane or mixture of chlorosilanes (0.2 mL) onto a 1 in. × 2.5 in. silicon substrate to form a completely covered thin liquid layer, and allowing the chlorosilanes to react with the substrate for 2 h in a sealed petri dish. After liquid deposition, modified substrates are rinsed with dry toluene multiple times and ready for use. The vapor deposition relies on vaporization of the chlorosilane molecules, those with vapor pressures > 5 torr at 100 °C are suitable for the vapor deposition process. The chlorosilane vapors are generated by heating the liquid reservoir or applying a vacuum to the system. The vapor deposition reaction usually is extended to 4 – 6 h. The vapor deposition process eliminates direct contact of chlorosilane liquids to the substrates, making this technique amenable to polymeric substrates. For this thesis work, the liquid deposition is used for ease of processing,

while vapor deposition is used for creating controlled gradient monolayers on silicon wafers.[1, 3, 4]

Gradient chlorosilane monolayers are fabricated through a custom-built vapor deposition device designed by a previous group member Prof. Julie Albert.[1, 4] The device consists of a Teflon assembly and a vacuum chamber, as illustrated in Figure 2.2. Two liquid reservoirs containing different chlorosilanes are placed on either side of the silicon substrate. The chlorosilane reservoirs and silicon substrate are enclosed in a small compartment and allow for cross-deposition of chlorosilanes under vacuum condition. The gradient profiles are tunable by adjusting the size (reservoir surface area) and positions of the reservoirs.

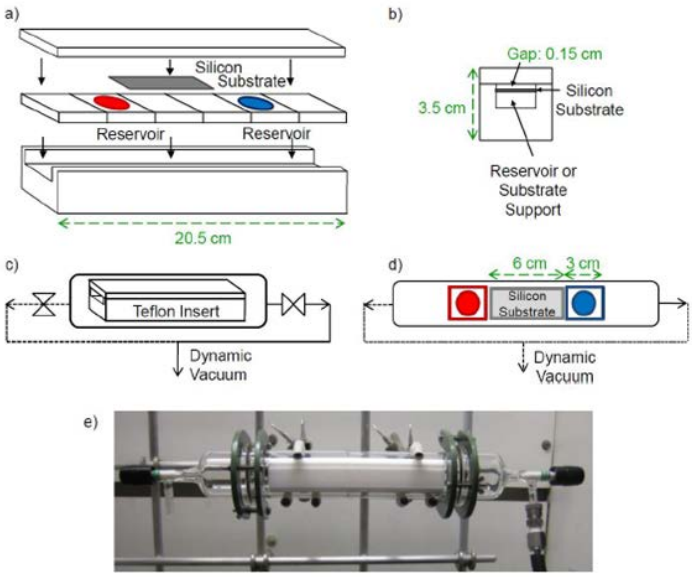

Figure 2.2: a) Teflon assembly consists of covered trough, chlorosilane reservoirs, and substrate supports. b) The small gap compartment enables cross-diffusion of the chlorosilane vapor molecules. c) and d) Schematic representation of vapor deposition chamber. Dynamic vacuum is applied at one or both sides of the chamber. e) Photography of the vapor deposition device setup. Adapted with permission from Albert, J. N. L., *et al. ACS Nano.* 2009, 3, (12), 3977-3986. Copyright 2009 American Chemical Society and Albert, J. N. L., *et al. Rev. Sci. Instrum.*2011, 82, (6), 065103. Copyright 2011 American Institute of Physics.

2.2 Block Polymer Thin Film Fabrication

BP thin films are cast on silicon wafers through spin coating or flow coating techniques. Spin coating is shown schematically in Figure 2.3. A typical spin coating process involves depositing a small amount of polymer solution onto the center of a substrate, and then spinning the substrate at high speeds to spread the coating solution (typically around 2000 – 3000 rpm). The majority of the polymer solution is spun off the edge of the substrate, leaving a very thin liquid layer on the substrate. Then, the

solvent evaporates, and produces a uniform thin film on the substrate. In general, the final film thickness is proportional to the inverse square root of the spin speed:

$$t \propto \frac{1}{\sqrt{\omega}} \qquad 2.1$$

in which t is the film thickness and ω is the angular velocity.[5, 6] The advantages of spin coating are the simplicity and relative ease with which thin and uniform film can be created. The disadvantage of spin coating is that it is a batch process and therefore relatively low throughput in comparison to the flow coating process. Additionally, the majority of the solution is spun off the side of the substrate and wasted.

Flow coating is a popular technique for generating both uniform and gradient thickness films.[7, 8] The unique ability to produce gradient thickness films allows for the rapid investigation of film thickness effects on BP behaviors. The flow coating process is depicted in Figure 2.3. Polymer solution is injected between a fixed blade and a substrate which rests upon a programmable motorized stage. Once the stage moves, the polymer solution is drawn onto the substrate by the blade. The resulting wet films dries, leaving behind a dry polymer film. The key factor governing the thickness profile is the casting velocity. Constant velocity produces a uniform film, and accelerating the substrate generates a film with a thickness gradient (Figure 2.3). In general, high velocity will result in a thick film, and low velocity will result in a thin film; low acceleration values will create shallow thickness gradients, and high acceleration values will produce steep gradients.

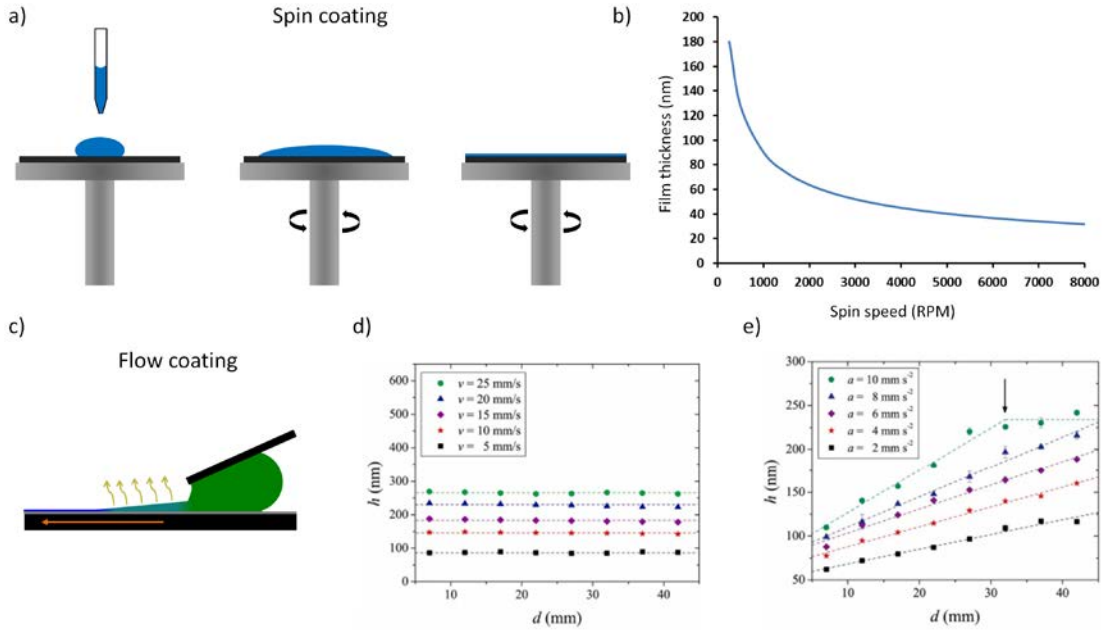

Figure 2.3: a) Schematic illustration of the spin coating process. b) Film thickness as a function of spin speeds. The final film thickness is proportional to the inverse square root of the spin speed. c) Schematic illustration of the flow coating process. d) Representative film thickness profiles produced at different casting speeds. Constant velocity can produce uniform thickness films. e) Gradient thickness films produced with different acceleration values. Note: the stage reaches the maximum velocity at d = 32 mm with a = 10 mm s^{-2} (marked by the arrow), therefore the film thickness reaches a plateau. Parts d) and e) are adapted with permission from Stafford, C. M., *et al. Rev. Sci. Instrum.* 2006, 77, (2), 023908.

2.3 Block Polymer Thin Film Processing

The nanostructures of as cast BP thin films often are poorly ordered due to the fast evaporation of solvent upon casting. Thermal annealing and solvent vapor annealing (SVA) are the two most commonly used processes to promote long-range ordering of nanostructures for the BP thin films.[9-12] Thermal annealing often is more preferred in industry because it is compatible with the current processing platforms.[13] Traditionally, thermal annealing is accomplished by using a vacuum oven heated at a

temperature above the glass transition temperature of all the constituent blocks but well below the decomposition temperature of the BPs, which imparts mobility to the polymer chains, facilitates BP to adopt equilibrium morphology, improves the order of the nanostructures, and annihilates energetically unfavorable defects. The annealing process typically takes hours to days. Harrison *et al.* studied the ordering dynamics of a cylinder-forming polystyrene-*b*-poly(ethylene-*alt*-propylene) (PS-PEP) thin film and showed that the orientational correlation length (ξ) increased as a function of time ($\xi \sim t^{1/4}$).[14, 15] While increasing the temperature expedites the ordering kinetics, defect density may increase as the annealing temperature approaches the bulk order-disorder temperature.[16] Thus, uniform thermal annealing is not a practical avenue to achieve perfect crystalline order in these materials. Recently, Jones and several others employed thermal gradients to anneal the BP thin films with enhanced ordering kinetics and controlled alignment direction (see Chapter 1 Section 1.4.3 for more details on thermal gradients).[17, 18] Yager and coworkers utilized highly localized laser heating to generate intense thermal gradients, and this processing method significantly reduce the annealing time to milliseconds.[12]

(*Parts of this section are adapted with permission from Luo, M., et al. Macromolecules 2013, 46, (19), 7567- 7579. Copyright 2013 American Chemical Society*) SVA is a valuable alternative to thermal annealing to impart mobility to the polymer chains without elevated temperature.[19, 20] Thus, SVA affords the advantage of annealing thermally sensitive or thermally responsive polymers. In a typical SVA setup (*i.e.*, bell jar annealing), the BP film is enclosed in a chamber with a solvent reservoir. The solvent evaporates and creates a solvent vapor environment. The solvent vapor molecules swell the BP film and dilute the polymer. This dilution

effectively lowers the glass transition temperatures (T_g's) of the polymer blocks, reduces the viscosity, and increases the chain mobility.[21] Kim *et al.* demonstrated that an ultrahigh molecular weight (1,000,000 g/mol) PS-*b*-poly(methyl methacrylate) (PS-PMMA) thin film with a large period of 200 nm could be directed into well-controlled nanoscale patterns using trench confinement combined with solvent vapor annealing.[21] Processing these high molecular weight BPs is challenging by thermal annealing due to their low chain mobility.

Furthermore, solvent in the film can mitigate the interactions between the polymer blocks, and selective solvents can swell specific blocks preferentially, leading to shifts in morphology.[22, 23] Jeong *et al.* found that different morphologies such as spheres, cylinders, hexagonally perforated lamellae, and lamellae could be generated from a single lamellar-forming poly(2-vinylpyridine)-*b*-poly(dimethylsiloxane) (P2VP-PDMS) copolymer by tuning the solvent selectivity towards the P2VP block. Moreover, the solvent vapor in the film can mitigate the interactions between the polymer blocks and both surfaces (free and substrate surfaces). By using selective solvents, the preferential segregation of the lower surface energy block to the free surface can be mitigated. With careful selection of solvents, surface neutrality can be achieved.[24, 25] [24] Recently, Ho and coworkers have demonstrated stable gyroid network structures in thin films by SVA using neutral solvents and neutral substrate modification.[24]

Finally, the swelling and deswelling (solvent evaporation) processes can affect the commensurability between the polymer periods and the film thickness, and induce changes in the orientation of the BP nanostructures.[26, 27] Early work by Kim and Libera showed that the orientation of cylindrical domains strongly depends on solvent

evaporation rate.[26] Cylinders oriented normal to the substrate were switched to parallel to the substrate as the solvent evaporation rate was decreased in a swollen thin film. In another work, Albert *et al.* found that parallel cylinders transitioning to perpendicular cylinders with decreasing solvent evaporation rate.[28]

Although SVA has been applied to different BP systems, a comprehensive understanding of the phenomena involved in SVA has not been established. According to Sinturel *et al.*, "two principal reasons for the lack of understanding of this important process are that (i) the connection between the nanostructure formed in the swollen film and the final dried film has not been rigorously established in most cases and (ii) no standardized SVA method has been developed."[19]

Flow system annealing is developed on the basis of "bell jar" annealing. An example of flow system is depicted in Figure 2.4. Solvent vapor streams are produced by bubbling inert gas through the solvent bubblers and continuously flowing through the SVA chamber. Thus, the solvent vapor pressure, solvent composition, and solvent flow rates can be controlled accurately and independently by the mass flow controllers. The swollen film thickness can be monitored *in-situ* by reflectance spectral or ellipsometry, providing spatial-temporal information of the SVA effect. In one example, Gotrik *et al.* systematically studied the effects of varying solvent compositions on the phase behavior of a PS-PDMS BP film using two streams of nitrogen gas flow containing heptane (PDMS-selective) and toluene (PS-selective) and one stream of pure nitrogen gas flow.[29] The morphologies of the PS-PDMS BP film were manipulated as a function of the partial pressure of the solvents and the swelling ratio of the film thickness. The results showed that the flow SVA approach produced a much richer array of BP structures than the bell jar SVA. Because the bell jar

approach used mixed liquid solvents, and the nonidealities in cosolvent mixtures may limit the available partial pressures of the solvents.

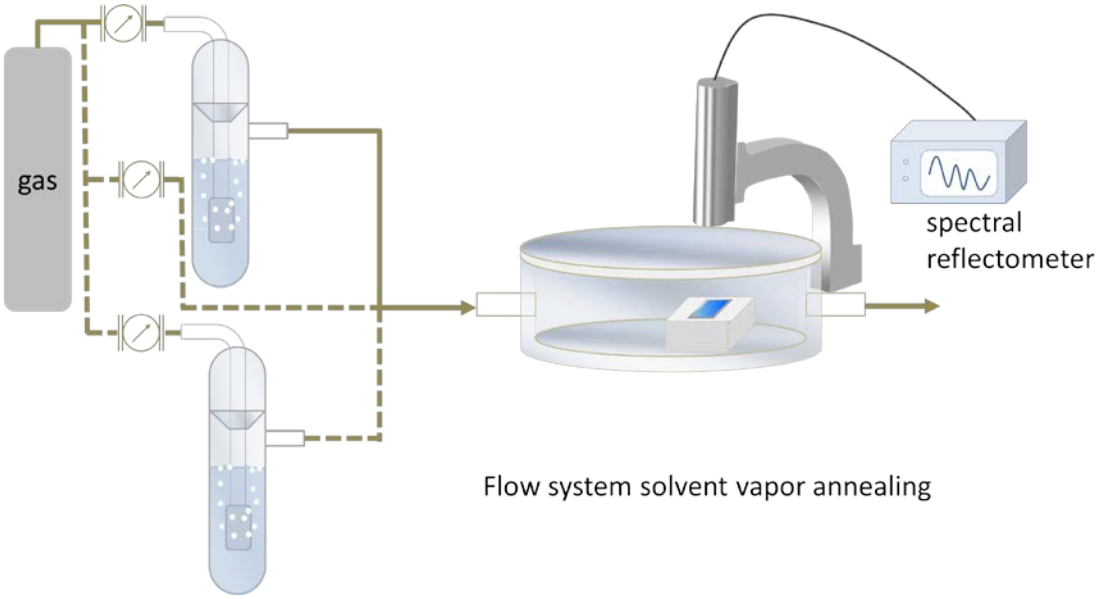

Figure 2.4: Schematic of flow system annealing setup. Solvent vapor streams are produced by bubbling inert gas through the solvent bubblers. The solvent vapor streams can be either single or multiple, and the pure inert gas stream can be added according to specific studies. Thus, the solvent vapor pressure, solvent composition, and solvent flow rates can be controlled accurately and independently by the mass flow controllers. Spectral reflectometer enables real-time monitoring of the film thickness for measuring solvent uptake by the film.

Raster solvent vapor annealing (RSVA) is another variation of flow system annealing recently developed by our group.[30] In RSVA system, the solvent vapor is directed onto the surface of a BP film using a nozzle, creating a localized annealing zone. Spatial control of the annealing zone is achieved through a motorized x-y stage. Seppala *et al*. employed this RSVA process to manipulate the nanoscale ordering and

nanostructure orientation of poly(styrene-*b*-isoprene-*b*-styrene) (SIS) BP thin films using tetrahydrofuran (THF) as a solvent.[30] Nearly instantaneous film swelling and enhanced ordering kinetics were achieved. It is important to note that macroscopic patterns of nanoscale features could be "written" in a controllable fashion into a soft materials system by RSVA process. Tunable parameters investigated in the above work included, solvent flux, raster area, and raster speed;[30] however, the modular nature of the RSVA method is amenable to additional modifications such as solvent composition, nozzle shape (*e.g.* slit geometries), substrate temperature, and substrate surface chemistry.

2.4 Contact Angle

The polymer−substrate interactions typically are quantified by the surface energy difference ($\Delta\gamma$) between the individual polymer block (γ_i) and the substrate (γ_S) surface energies:

$$\Delta\gamma = |\gamma_i - \gamma_S| \qquad 2.2$$

Contact angle measurements are used to characterize the substrate surface energy. The static sessile drop method is one of the most commonly used measuring methods and is used in this thesis work for ease of conducting experiments. As illustrated in Figure 2.5, a droplet of liquid with a known surface energy is placed on a solid surface; the contact angle is defined as the angle between the solid substrate surface and the tangent of the droplet's ovate shape after the size of the droplet reaches equilibrium. It is important to note that the existence of metastable "non-equilibrium" contact angles may result in experimental values between the maximum observable advancing angle and the minimum observable receding angle. The advancing contact angle and receding contact angle are measured by adding or removing liquid volume to the

droplet, and the difference between those two measured contact angles is called contact angle hysteresis. Thus, multiple measurements are needed to minimize the experimental error associated with the measurement of contact angle and we seek to use dynamic contact angle *(i.e.*, advancing and receding contact angles) in the future.

The contact angle and the known surface energy of the probe liquid are used to calculate the surface energy of the solid surface. Young's equation provides a simple mathematical expression that describes the equilibrium state of the droplet at the three-phase contact point *(i.e.*, intersection between the solid, liquid, and vapor phase) (Figure 2.5):

$$\gamma_{SV} - \gamma_{SL} = \gamma_{LV} \cos\theta \qquad 2.3$$

in which γ_{SV} is the surface tension of the solid in equilibrium with the saturated vapor of the liquid (*i.e.*, the surface energy of the substrate γ_S), γ_{SL} is the interfacial tension between the solid and liquid, γ_{LV} is the surface tension of the liquid in equilibrium with its saturated vapor, and θ is the contact angle.

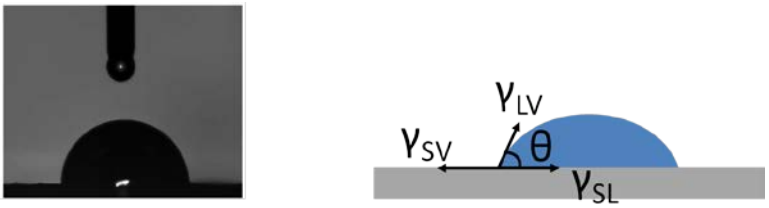

Figure 2.5: Static sessile droplet method and a schematic showing the surface energy components in the Young's equation.

Young's equation has two unknowns in one equation (γ_{SV} and γ_{SL}). Thus, the solution for the solid surface energy γ_{SV} cannot be resolved from a direct measurement.

Many methods have been developed on the basis of the Young's equation to calculate γ_{SV} from the contact angle measurements. The Young-Good-Girifalco-Fowkes method assumes the interfacial tension between two phases to be the geometric mean of the surface tension of each phase,[31, 32] and yields

$$\gamma_{LV}(\cos\theta + 1) = 2\sqrt{\gamma_{LV}\gamma_{SV}} \qquad 2.4$$

The Owens and Wendt method follows the geometric mean concept and decomposes the surface energy into dispersive and polar components:

$$\gamma_{LV}(\cos\theta + 1) = 2(\sqrt{\gamma_{LV}^{D}\gamma_{SV}^{D}} + \sqrt{\gamma_{LV}^{P}\gamma_{SV}^{P}}) \qquad 2.5$$

in which the superscripts D and P represent the dispersive and polar components, respectively.[33] This method requires contact angle measurements from two probe liquids with known surface tension components. The individual dispersive and polar components of the solid surface can be determined directly. It is important to choose probe liquid pairs that have very different polarities. If the polarities of the probe liquids are too similar, it has been shown that even small errors in the contact angle measurements can cause severe errors in the calculation.[34] Therefore, diiodomethane (non-polar) and water (highly polar) often are selected for contact angle experiments when the Owens and Wendt method is employed.

Another method developed by Wu uses a different approach, called harmonic mean or reciprocal mean equation:

$$\gamma_{LV}(\cos\theta + 1) = 4\left(\frac{\gamma_{LV}^{D}\gamma_{SV}^{D}}{\gamma_{LV}^{D} + \gamma_{SV}^{D}} + \frac{\gamma_{LV}^{P}\gamma_{SV}^{P}}{\gamma_{LV}^{P} + \gamma_{SV}^{P}}\right) \qquad 2.6$$

Wu demonstrated this method possibly was more suitable than the geometric mean in calculating the polar components of the polymers.[35, 36] However, both the Owens and Wendt method and the Wu method are used extensively in surface energy analysis.

In this work, the Owns-Wendt equation was used to calculate the surface energy of the silicon substrate with or without chlorosilane modification. Diiodomethane (99%, stabilized, Acros Organics) and water (purified with a Milli-Q reagent water purification system) contact angles were measured using a contact angle goniometer (First Ten Ångstroms FTÅ 125). Probe liquid drops (2 μL) were dispensed onto the substrate surface with a Distriman pipet, and static contact angle measurements were taken after the drop shape stabilized (0.3 s for diiodomethane, 0.1 s for water). Note: the dispersive components (γ^D) and polar components (γ^P) of the contact angle probe liquids used in these calculations are $\gamma^D_{diiodomethane} = 50.8$ mJ/m^2, $\gamma^P_{diiodomethane} = 0$ mJ/m^2, $\gamma^D_{water} = 21.8$ mJ/m^2, and $\gamma^P_{water} = 51.0$ mJ/m^2.

2.5 Spectral Reflectance

Spectral reflectance (SR) is used to determine the thickness and refractive index of the BP thin films. SR measures the intensity of light reflected from a thin film over a range of wavelengths, with the incident light beam normal to the film surface (Figure 2.6). Ellipsometry is similar except the light is incident at an angle and the two different polarizations of the reflected light are analyzed as well. Both techniques are non-destructive. SR is suitable to measure non-metal films that are 1 nm – 1 mm thick (for metal film: 0.5 nm – 50 nm), and the measurement speed is typically ~0.1 – 5 seconds per location (for ellipsometry the speed is ~1 – 300 seconds per location).[37] For thinner film less than 10 nm, ellipsometry provides more accurate results as the polarization measurements provide twice as much information for the

analysis. In comparison to ellipsometry, SR is much easier to operate, and the instrumentation is simper and lower cost; however, SR is restricted to measuring less complex structures.

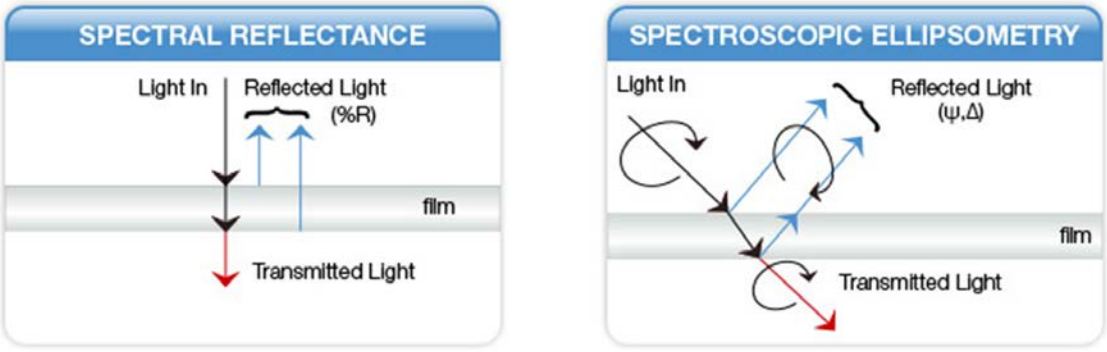

Figure 2.6: Illustrations of spectral reflectance and ellipsometry. Images from *http://www.filmetrics.com/ellipsometry*.

Reflection occurs when the light travels across the interface between two different mediums. The fraction of light that is reflected from an interface is determined by the refractive index (n) and the extinction coefficient (k) of the two mediums, in which n is defined as the ratio of the speed of the light in vacuum to the speed of light in the medium, and k describes how much light is absorbed in the medium. Considering a thin film on top of a substrate, the light is reflected from both of the air-film surface and the film-substrate surface, experiencing constructive interference (intensities add) or destructive interference (intensities subtract) depending on the phase relationship. The constructive interference occurs when $2nd = i\lambda$, and the destructive interference happens when $2nd = (i+1/2)\lambda$, in which d is the

thickness of the film and *i* is an integer. In general, the total reflectance spectrum was modeled using

$$R = A + B\cos(\frac{4\pi}{\lambda}nt) \qquad 2.7$$

in which A and B are constants that account for the roughness and extinction coefficient parameters.[37] From this equation, the periodicity and amplitude of the reflectance spectrum is determined by the film thickness, optical constant, and other properties such as interface roughness.

The thicknesses of the BP thin films studied in this thesis work were measured using a reflectance spectrometer (Filmetrics F20-UV). The reflectometer measured the intensity of light reflected from a sample surface over a range of wavelengths (400 – 1000 nm) when the incident light beam was placed normal to the surface. The initial value *n* for the BP film was estimated by the volume fraction weighted average of the homopolymer refractive indexes obtained from the literature. The Filmetrics software then was allowed to fit both *t* and *n*, and the goodness of fit was usually > 0.99 for the BP films.[38] The accuracy of the film thickness was within 1 nm.

2.6 Microscopic Techniques

2.6.1 Optical Microscopy

Optical microscopy involves visible lights reflected from or transmitted through the sample and uses one or more lenses to allow a magnified view of the sample. The resolution of optical microscopy is limited by the diffraction to approximately 0.2 μm. Thus, optical microscopy is suitable for examining the island/hole structures of BP films as these structures are typically at micrometer scale.

Optical microscope has been employed widely to study the effects of film thickness,[39] substrate surface energy,[2] and molecular weight of the BPs[40] on the surface pattern formation in BP thin films. Optical microscopy also has served as a quick screening tool for identifying phase transformation from parallel domain structures to perpendicular domain structures as the island/hole structure disappeared.[1, 2] Additionally, *in-situ* optical microscopy could provide useful information on the kinetics of island/hole formation. [40, 41]

The BP thin films studied in this thesis were supported on silicon substrates, thus optical microscopy images were taken in reflectance mode using a Nikon microscope equipped with a 5 MP CCD camera (Nikon Eclipse LV100). The BP thin films formed island/hole structure during thermal annealing when the film thickness was incommensurate with the polymer domain spacing. The films were quenched by placing the films on a cold aluminum plate immediately after thermal annealing. Therefore, the microstructures of the BPs were kinetically trapped.

In situ optical microscopy was conducted using a Linkam thermal stage with a glass window. The system was maintained under an argon environment throughout the annealing process (Figure 2.7). The stage was heated at a rate of 3 °C min^{-1}, similar to the heating rate of the vacuum oven. The growth of island/hole structures was monitored by capturing images every 5 – 15 min at the initial stage and every 30 min once the rate of island/hole growth decelerated. The optical microscopy images were converted to binary images in ImageJ software, and the size of the island/hole structures were analyzed using Analyze Particles functional.

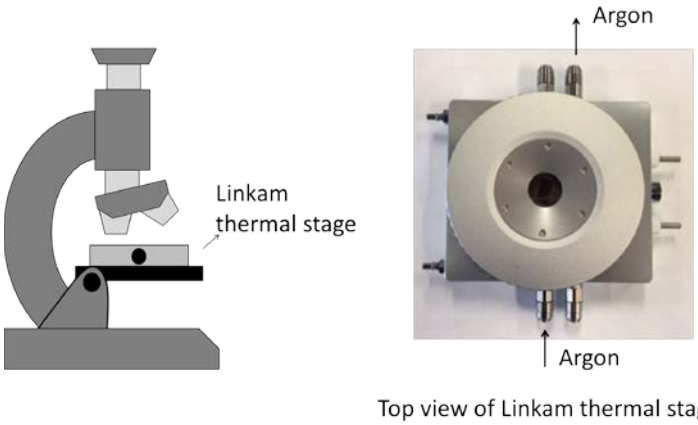

Figure 2.7: Schematic of *in situ* optical microscopy with a Linkam thermal stage. The inert gas can flow in and out through the cell chamber. Image courtesy of Cameron K. Shelton.

2.6.2 Atomic Force Microscopy

Atomic force microscopy (AFM), also known as scanning force microscopy (SFM), is one of the most commonly used techniques to study the surface properties of a sample.[42] In AFM, a sharp tip (usually made of silicon or silicon nitride) is interacting with the sample surface. The intermolecular force is detected by the deflection of the tip cantilever and amplified by a laser beam system. As the sample is raster scanned in the x-y plane, height variations in the sample will change the deflection of the cantilever. The feedback system adjusts the distance between the tip and the sample to maintain a constant force between the tip and the sample (Figure 2.8). Thus, the topography of the surface can be imaged. Additionally, the variations of softness, elasticity and stickiness on sample surface will cause a phase lag in the signal, and produce a phase image. Other useful information such as friction, adhesion and conductivity properties can be gained through AFM as well. There are three operating modes: contact mode, non-contact mode and tapping mode. In contact

mode, the tip is heavily influenced by frictional and adhesive forces as the tip is "dragged" across the surface of the sample. Contact mode AFM can damage the sample and usually is applied to hard surfaces. In non-contact mode, the tip is oscillated at the resonance frequency above the sample surface and interacts with the surface through the van der Waals forces. The non-contact mode AFM does not suffer from tip or sample degradation effects; however, the resolution is relatively low and can be hampered by the contaminant layer (*e.g.*, water) that interferes with the oscillation. Tapping mode takes advantages of the two above. The tip oscillates with sufficient amplitude and intermittently contacts with the sample surface. Therefore, it eliminates frictional forces and prevents the tip from being trapped by the adhesive meniscus forces from the contaminant layer.[43]

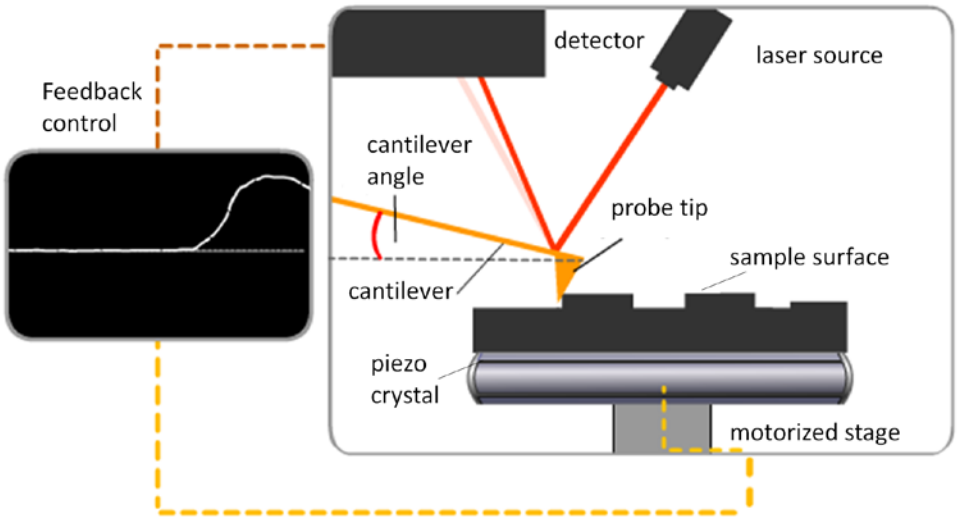

Figure 2.8: Schematic illustration of AFM components and feedback system. Image from *http://virtual.itg.uiuc.edu/training/AFM_tutorial/*

Tapping mode AFM has been a standard technique to study the surface of soft materials. Its spatial nanometer resolution together with the ability to distinguish different BP domains on the basis of elastic modulus difference between the constituent blocks has made tapping mode AFM an attractive method for studying the surface morphologies of the BPs.[44-47] Even with BPs that have a low modulus contrast between individual domains such as PS-PMMA, tapping mode AFM has revealed excellent image resolution.[48] Tapping mode AFM affords additional advantages over scanning electron microscopy (SEM) or transmission electron microscopy (TEM) as it does not require staining or etching of the BP samples. Further, tapping mode AFM can defect sub-surface structures by tapping through the thin surface layer, useful for study BPs that form wetting layer on the sample surface.[43] Tapping mode AFM also has been combined with etching methods to construct 3D through-film morphologies of the BP thin films.[27]

The surface morphologies of BPs studies in this thesis were acquired in a Veeco Dimension 3100 AFM. Silicon probes (Tap 150G, BudgetSensors) were used in tapping mode and a typical amplitude set point ratio was 0.9.

The through-film morphologies of a SIS film was assessed by AFM combined with UV ozone etching steps. UV ozone etching was conducted in a UVO cleaner (model 342, Jelight Co., Inc.) in 15 s increments with the samples placed $\approx$1 cm from the lamp. In one single UVO step, 20 – 30 nm polymer film was removed. The polymer film then was soaked in an isopropyl alcohol bath (Fisher Scientific, ACS grade) for $\approx$10 min between exposures to wash off polymer fragments. Film thickness measurements and AFM images were collected after drying the sample

under a stream of nitrogen. The AFM and UVO etching step was repeated to probe the full depth of the film.

2.6.3 Focus Ion Beam Milling/Cross-Sectional Transmission Electron Microscopy

Focused ion beam milling technique is used to prepare electron transparent sections from the BP thin film for cross-sectional TEM examination. When the BP film is deposited on a silicon substrate, preparing sample sections for cross-sectional TEM analysis has proved challenging because it is not possible to section hard silicon crystals directly.[49] Some studies relied on floating the film off the silicon substrate with hazardous HF solution or extremely basic KOH solution,[50, 51] and the polymer film then was transferred to embedded media and subsequently microtomed. This approach may destroy the first layers of the films near the substrate surface from the "floating" process, and it only works for a few polymers due to the acid and base degradation. Several other researchers used adhesive to peel off the film from the substrate.[27] However, this peeling process may cause incomplete removal of the polymer from the substrate, as well as distorting the polymer structures.

Focused ion beaming milling technique employs a focused beam of Ga^+ ions to mill out sections from the specimen for the cross-sectional TEM analysis. This method has several advantages that make it useful for BP thin film studies.[49] First, the polymer films do not need to be removed from the substrate and the film structures remain intact. Second, this method precludes some artifacts that could be induced during the microtome step due to the differences in hardness between the BP components. Third, the focused ion beam milling section can be controlled with high

spatial resolution; hence local structural information can be achieved on inhomogeneous films.

In this thesis, the BP thin film sections for the cross-sectional TEM experiment were prepared in an Auriga 60 CrossBeam instrument at room temperature. The instrument has a scanning electron microscopy (SEM) detector for *in-situ* imaging of the sample surface. The working procedures are as follows: a) a gold layer was sputtered onto the BP film to provide conductivity and reduce electron build-up on the sample surface; b) a rectangle shape of platinum (Pt) protective layer (about 2 μm × 15 μm in size, 1 μm in thickness) was deposited onto the BP film to protect the film from the milling step; c) low beam current (1 nA) of the Ga^+ ion gun was used to mill out two trapezoid trenches (10 μm in depth) next to the rectangle to make a film bridge (Figure 2.9); d) the bottom side of the film bridge was cut from the silicon substrate, and one side of the film bridge was cut from the polymer film; e) a hydraulic micromanipulator with a sharp glass tip was brought close to the film bridge, and the glass tip was attached to the film bridge using Pt deposition; f) the film bridge was lifted out from the BP film after cutting off the other side of the film bridge and attached to a TEM carbon grid using Pt deposition again; g) a lower beam current (100 pA) was applied to fine milling the thin sample from 2 μm to about 50 nm in thickness (thickness suitable for TEM examination); h) the thin sample was stained with osmium tetroxide (OsO_4) vapor for 20 min, providing electron density contrast between the BP domains for TEM examination; i) TEM studies were carried out on a JEM-2010F TEM at an acceleration voltage of 200 keV.

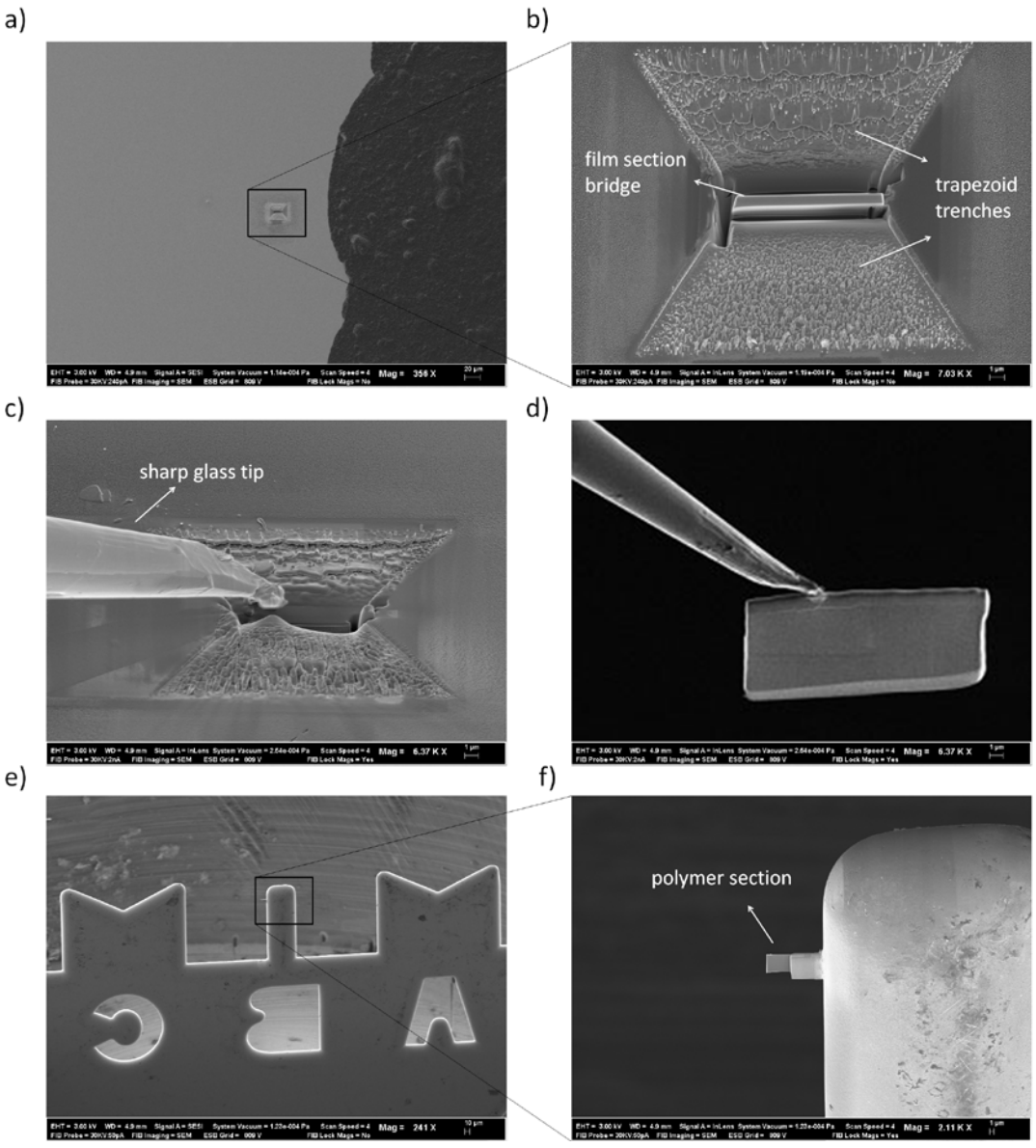

Figure 2.9: a) SEM image of a BP thin film after FIB processing. b) Zoom-in image of (a). Two trapezoid trenches were milled out by the FIB beam, and a film section bridge was demonstrated. c) A hydraulic micromanipulator with a sharp glass tip was brought close to the film section. However, the electrostatic repulsion force blew away the film section. d) The film section was lifted out by the glass tip successfully. Image courtesy Dr. Fei Deng. e) The film section was transferred and attached to a carbon grid. f) Zoom-in image of (e). The film section (~2 μm thick) was fine milled on both sides to reduce the thickness to ~50 nm. The film further was examined by TEM.

2.7 Scattering Techniques

2.7.1 Small-Angle X-ray Scattering

Small-angle X-ray scattering (SAXS) has been one of the most powerful tools for morphological characterization in bulk BPs (Figure 2.10).[52-54] When an incident X-ray beam passed through a sample, the X-rays are scattered at the electrons of the atomic shell. The scattering waves of all atoms interact with each other, creating either incoherent scattering (destructive interferences) or coherent scattering (constructive interferences). For destructive interferences, the scattering waves cancel out one another and do not produce diffractions. For constructive interferences, the relationship between the order of diffraction (n), the wavelength of X-ray (λ), the scattering angle (2θ), and the interplanar spacing (d) follows Bragg's law:

$$n\lambda = 2d\sin\theta \tag{2.8}$$

A detector records the intensity of X-rays collected over time in a 2-D diffraction pattern. For a single-crystalline material, a dot-pattern is seen on the 2-D detector, while a polycrystalline material produces a powder-ring pattern. The scattering pattern then can be integrated azimuthally to generate a 1-D plot of intensity *versus* the magnitude of scattering vector (**q**), in which **q** is the difference between the incident beam wavevector ($\mathbf{k_I}$) and the scattered beam wavevector ($\mathbf{k_S}$), and

$$q = |\mathbf{q}| = \frac{4\pi}{\lambda}\sin\theta \tag{2.9}$$

Combining Equation 2.8 and Equation 2.9, the interplanar spacing d can be directly correlated with q:

$$q = \frac{2\pi n}{d} \tag{2.10}$$

As the plane within the unit cell can be represented by a set of Miller indices (*hkl*), a more general equation is derived:

$$q_{hkl} = \frac{2\pi n}{d_{hkl}} \tag{2.11}$$

The interplanar spacing d_{hkl} between two (*hkl*) planes is given by:

$$\frac{1}{d_{hkl}} = \sqrt{\frac{h^2}{a^2} + \frac{k^2}{b^2} + \frac{l^2}{c^2} + \frac{2hk}{ab}\cos\gamma^* + \frac{2hl}{ac}\cos\beta^* + \frac{2kl}{bc}\cos\alpha^*} \tag{2.12}$$

in which a, b , and c are lattice constants of the unit cell, and α^*, β^*, and γ^* are the unit cell angles in reciprocal space.

Depending on the morphology of the unit cell, Equation 2.12 can be simplified significantly. For example of hexagonally-packed cylinders, $a = b$, $c = \infty$, $\alpha^* = \beta^* = 90^\circ$, and $\gamma^* = 60^\circ$, Equation 2.12 further simplifies as

$$\frac{1}{d_{hkl}} = \frac{1}{a}\sqrt{h^2 + k^2 + hk} \tag{2.13}$$

The characteristic spacings for hexagonally-packed cylinders are d_{100}, d_{110}, d_{200}, d_{210}, d_{300}, …, leading to possible intensity peaks at q_{100}, q_{110}, q_{200}, q_{210}, q_{300}, … These peaks often are normalized by the smallest scattering vector q^* (q_{100} in this case), and the peak ratios are useful for the morphology assignment (Figure 2.10). Some examples of peak ratios for common BP structures are provided in Table 2.1.

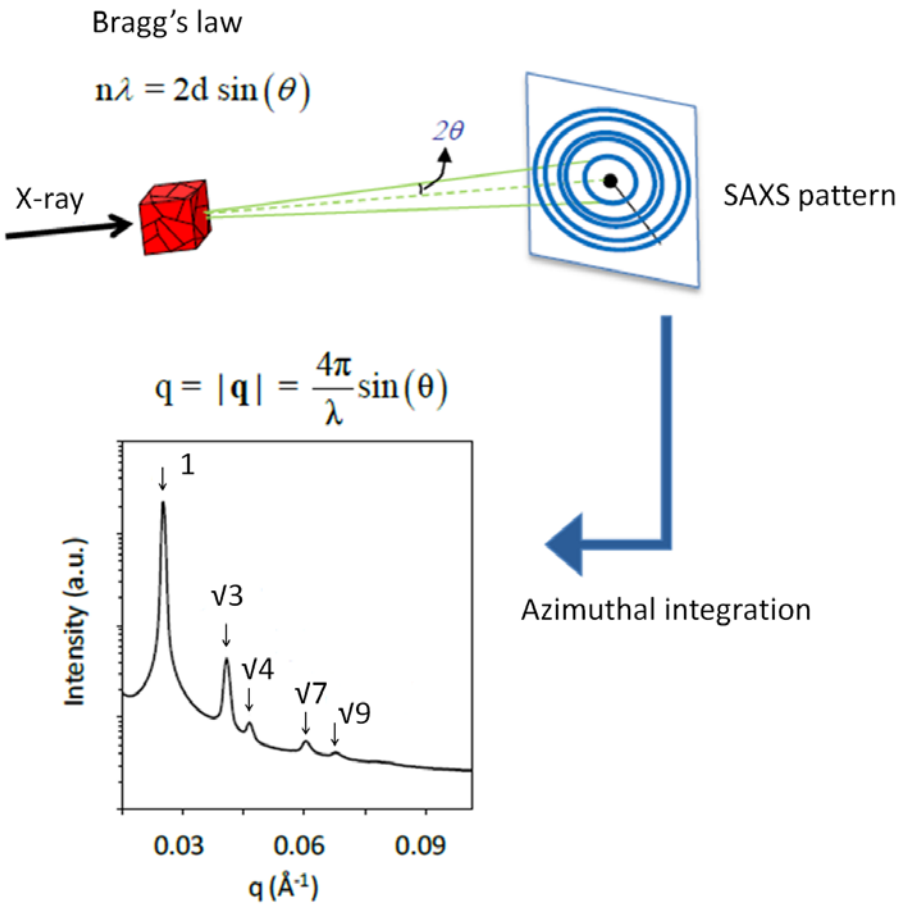

Figure 2.10: Schematic illustration of small-angle X-ray scattering. For a polycrystalline structures, a ring pattern is seen on the 2-D detector. The 2-D intensity data can be integrated azimuthally to a 1-D plot of intensity *versus q*, in which *q* is the magnitude of the scattering vector. The peaks ratios of 1, √3, √4, √7, √9 were assigned to a hexagonally-packed cylindrical structure. Adapted with permission from Young, W. S., PhD dissertation, University of Delaware, 2012.

Table 2.1: BP morphologies and corresponding SAXS peak locations.

Morphology	**Peak ratios**
Lamellae	1, 2, 3, 4, 5, 6…
Hexagonally-packed cylinders	1, √3, √4, √7, √9, √12…
Body-centered cubic spheres	1, √2, √3, √4, √5, √6…
Gyroid network	√6, √8, √14, √16, √20…

In this thesis work, SAXS was used to characterize the BP morphology in the bulk sample. The morphology and domain spacing determined from SAXS were compared with results in thin films. The experiments were conducted using a Rigaku SAXS instrument with 2.2 kW sealed-tube X-ray source (Cu Kα, λ = 1.54 Å) and a 2000 mm sample-to-detector distance. The BP samples were sealed between two Kapton films in a stainless steel cell, and the temperature of the sample was controlled using a Linkam HFS91 CAP stage while acquiring *in-situ* scattering data under vacuum. Two-dimensional scattering data were recorded using a Rigaku Multi-wire detector. The data were integrated azimuthally for a one-dimensional plot of intensity *versus* the magnitude of the scattering vector.

2.7.2 X-ray Reflectivity

The X-ray reflectivity (XRR) or X-ray reflectometry is a non-destructive technique used to examine thin film parameters such as density, thickness, and surface/interface roughness. XRR measurement analyzes the intensity of the reflection when an X-ray beam impinges on a flat film at a grazing incident angle. The X-rays undergo total reflection when the incident angle is below the critical angle (θ_c). As the incident angle slowly increases from θ_c, the X-ray beams penetrate into the sample, and the reflectivity intensity rapidly decreases in proportion to θ^4 (Figure 2.11). The X-ray beams reflected on the film surface, internal thin film interface, and substrate surface will interfere either constructively or destructively with each other, resulting in an oscillation pattern. These oscillations were first found by Kiessig in 1931 and are called Kiessig fringes.[55] The reflective curve (reflectivity intensity *versus* incident angle) contains structure information of the thin film in the resolution of an angstrom level, which is the X-ray wavelength. The thickness of the film/layer

can be obtained by Fourier transformation of the extracted oscillation curves. A reflectivity profile on the basis of a layer structure model is created in the software (*e.g.*, GlobalFit) and the parameters values (*e.g.*, thickness, electron density, roughness of the surface or interface) are optimized to minimize the residual between the measured data and calculated data.[56] The basic interpretation of XRR pattern is summarized inFigure 2.12. Specifically, the film thickness and layer thickness can be determined from the periodicity of the oscillation. The amplitude of the oscillation and the critical angle for total reflection provide information on the density of the film. The oscillation and intensity decaying rates at high angles indicate surface or interface roughness.

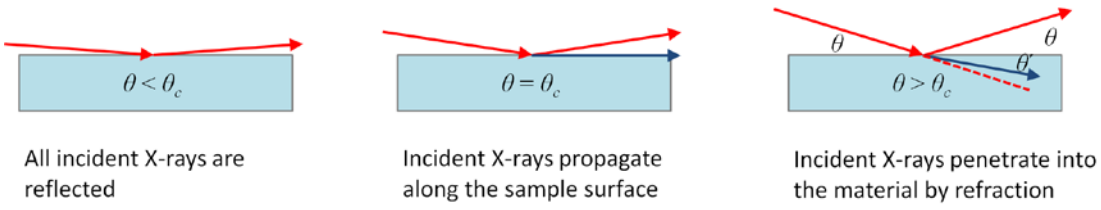

Figure 2.11: Reflection and refraction of X-rays at sample surface with changes in incident angle.

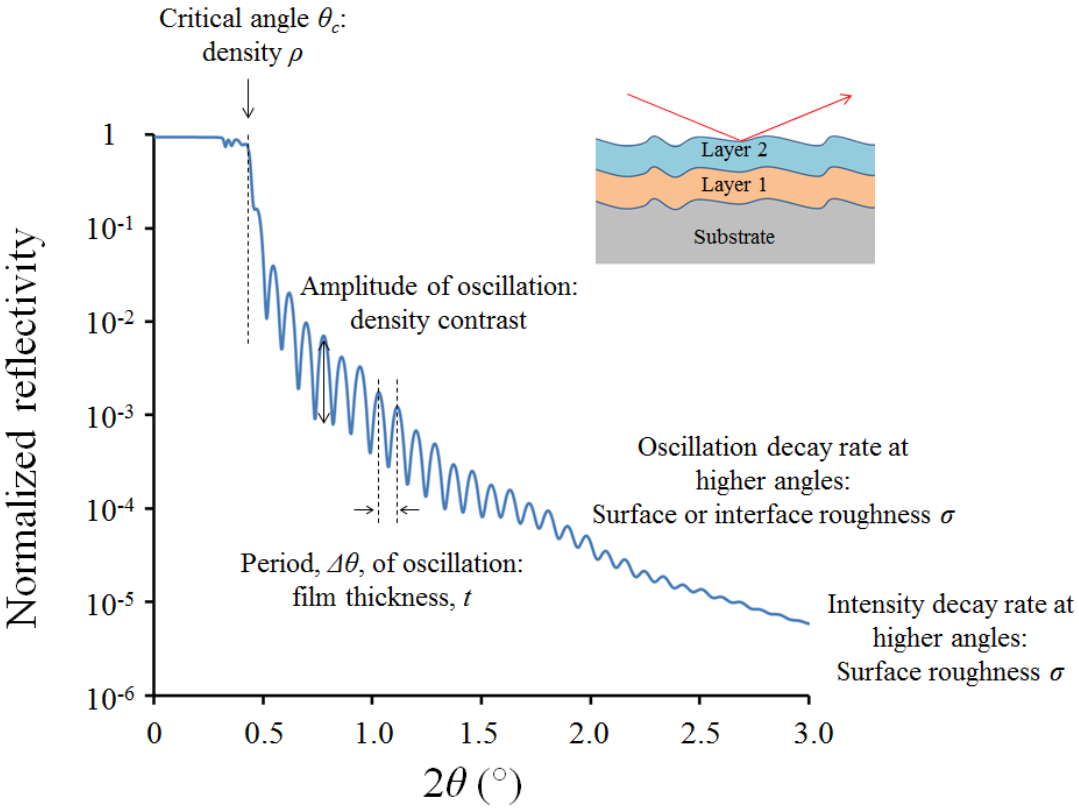

Figure 2.12: Information provided by the X-ray reflectivity profile.

XRR has been employed successfully to study the structures, interfacial mixing, and distribution of nanoparticles in BP thin films.[57-60] In this thesis work, the BPs for XRR experiments are lamellae-forming BPs. The films were thermally annealed in a vacuum oven to promote parallel lamellar structures, which are ideal for the XRR experiments. XRR was performed on an Ultima IV instrument (Rigaku). A thin, parallel beam of Cu-Kα radiation, λ = 0.154 nm, was incident on the samples. The beam was sized to capture the critical edge of the samples for the best results and fit accuracy. XRR profiles were collected by scanning a small incident angle (θ) of X-

rays from the source and a detection angle (2θ) of reflected X-rays ($0° < 2\theta < 4°$). The fit profiles across the film thicknesses were calculated using the GlobalFit software.

2.7.3 Grazing-Incidence Small-Angle X-ray Scattering

Grazing-incidence small-angle X-ray scattering (GISAXS) combines features from SAXS and diffuse X-ray reflectivity (X-rays diffusely scattered in any direction on a rough surface), is a versatile tool for characterizing nanoscale structures at the surfaces, or in the thin films. A schematic illustration of GISAXS is shown in Figure 2.13. The X-ray beam is directed onto the sample surface at a grazing incidence angle typically around 0.05° to 0.50°. If the incident angle is in-between the critical angles of the film and the substrate, the X-rays can penetrate the sample up to several 100 nm. The area detector records the scattering intensity of the scattered beams, the scattering along the 2θ and α axes relates to the in-plane (lateral) and out-of-plane (normal) domain symmetry, respectively, in which the in-plane scattering vector is $q_{xy} \approx \frac{4\pi\theta}{\lambda}$ and the out-of-plane scattering vector is $q_z = \frac{2\pi(\sin\alpha_f + \sin\alpha_i)}{\lambda}$.

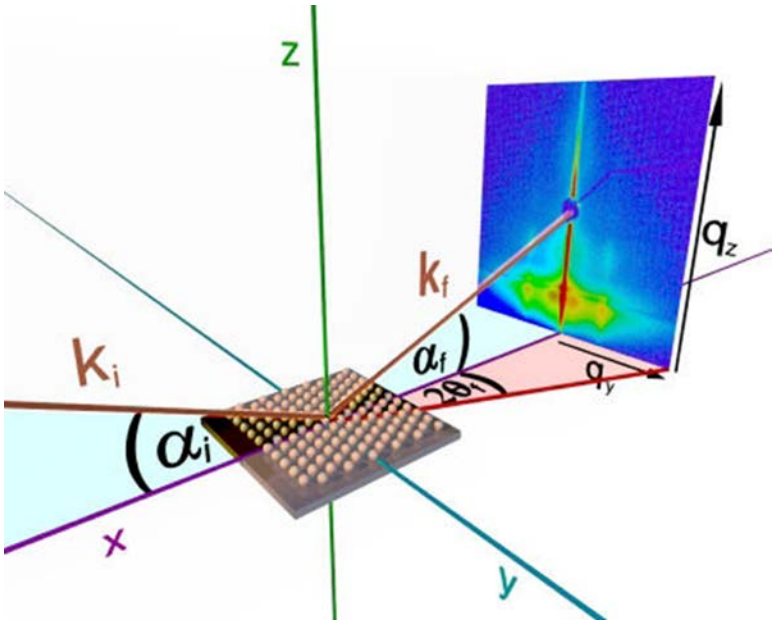

Figure 2.13: Schematic illustration of GISAXS. Image from *www.gisaxs.de.*

For a parallel lamellar film, the GISAXS pattern exhibits stripes of intensity at specific spacing along the q_z axis, while for a perpendicular lamellar film, the GISAXS pattern displays peaks parallel to the interface along the q_{xy} axis (Figure 2.14). Each of these in-plane peaks is elongated along the q_z axis, which is typical of surface scattering from a monolayer. The in-plane line cut generates a 1-D plot of intensity *versus* q_{xy}, which shows the ratio of the peak positions are 1, 2, 3…, corresponding to a lamellar symmetry. In another case, if the lamellar structures are tilted or random in the film, the GISAXS will have rings or partial rings in the intensity maps (Figure 2.14).

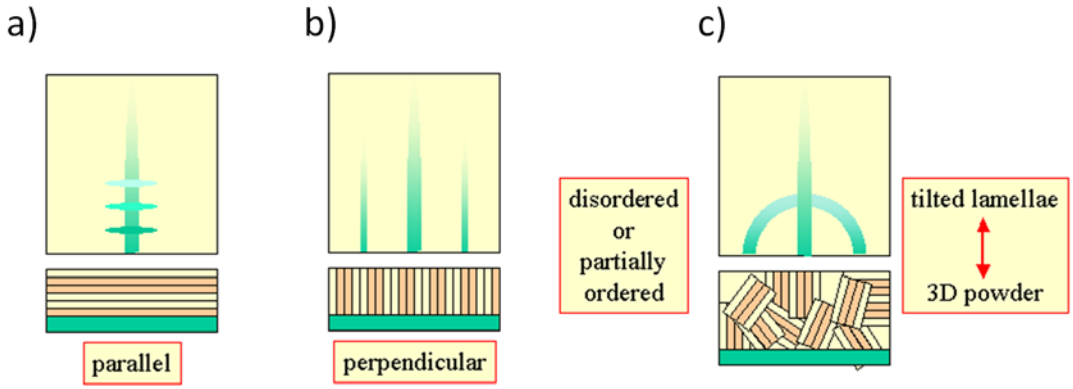

Figure 2.14: Representative GISAXS patterns on a) parallel, b) perpendicular, and c) random oriented lamellar films. Images from *http://staff.chess.cornell.edu/~smilgies/gisaxs/GISAXS.php*

The perpendicular cylinder phase is characterized by in-plane hexagonal symmetry (Figure 2.15), thus GISAXS will generate in-plane Bragg peaks at q_{xy}^*, $\sqrt{3}q_{xy}^*$, $2q_{xy}^*$, *etc*, with $q_{xy}^* = 2\pi/d$, d is the spacing of (100) plane. The parallel cylinder phase exhibits one-dimensional in-plane symmetry with hexagonal layering along the out-of-plane axis. GISAXS from parallel cylinders will produce Bragg peaks at in-plane positions q_{xy}^*, $2q_{xy}^*$, $3q_{xy*}$, *etc*., with $q_{xy}^* = 2\pi/d$. Additionally, the strong layering will generate Bragg peaks along the q_z axis that correspond to different crystallographic planes, where the positions of these peaks are very sensitive to the incident angle α_i. Examples of simulated GISAXS patterns for perpendicular and parallel cylinders are shown in Figure 2.16. Details of the models for calculating Bragg peak positions and simulating the full GISAXS patterns are discussed elsewhere.[61-65]

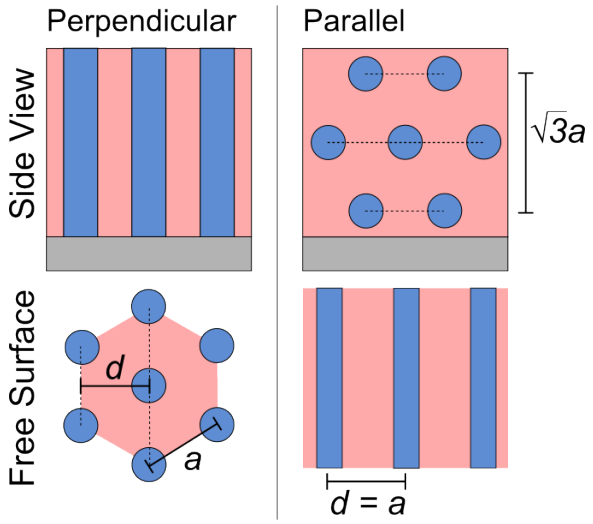

Figure 2.15: Illustration of perpendicular and parallel cylinders in thin films, *d* is the domain spacing of plane (100), and *a* is the nearest neighbor distance of the cylinders.

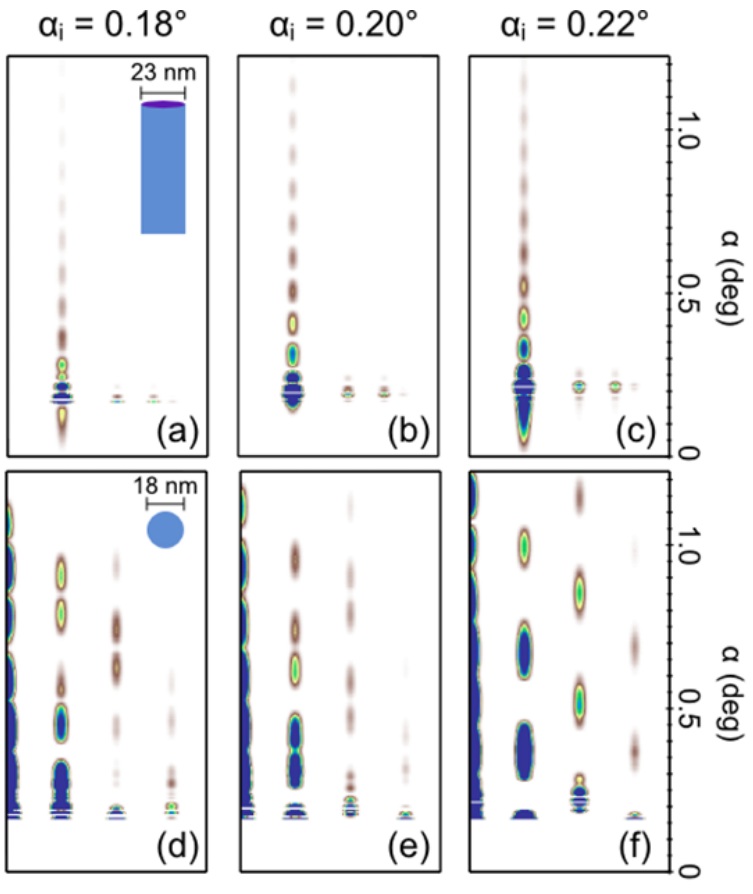

Figure 2.16: GISAXS simulations on the basis of the distorted-wave Born approximation (DWBA): (a-c) Perpendicular cylinders; (d-f) Parallel cylinders at incident angle 0.18°, 0.20°, and 0.22°. For this particular case, when the cylinder diameter is 23 nm, the form factor of perpendicular cylinders has a minima near the $\sqrt{3}q_{xy}$* Bragg peak. Therefore, the $\sqrt{3}q_{xy}$* Bragg peak is not shown in figures (a-c).

GISAXS has recently been applied to the BP thin films exploring their near-surface and internal nanostructures.[45, 64, 66] The GISAXS method has several advantages. First, it is a non-destructive technique and requires no special sample preparations. Second, a highly intense scattering pattern can be obtained even for monolayer films, because the X-ray beam path length through the film plane is

sufficiently long. Third, as a large sample area (a few mm^2) is illuminated, high throughput examination of the sample with statistically averaged information are allowed. Fourth, the high temporal resolution of 10^{-3} - 1 s makes GISAXS particularly suitable for studying dynamic ordering processes.[67] Several research groups have employed time-resolved GISAXS to investigate the BP thin film phase behavior under solvent vapor annealing.[23, 68-70] Recently, microbeam GISAXS (μGISAXS) has been exploited to obtain local structural information in thin films.[68] As opposed to conventional GISAXS that has an X-ray beam of diameter 100 - 500 μm and probes large areas of the film surface due to the low incident angle, μGISAXS reduces the sampling size down to a few micrometers (even submicrometer in some cases) to capture more localized behavior. This technique may be employed in a variety of systems for the position-sensitive mapping of 2D and 3D morphologies as a function of film thickness, surface roughness, substrate heterogeneity, *etc*.[20]

In collaboration with the Stein Group at University of Huston, GISAXS measurements of the BPs studied in this thesis were performed by Nikhila Mahadevapuram at beamline 8-ID-E at the Advanced Photon Source of Argonne National Laboratory. Samples were placed in a vacuum chamber and illuminated with 7.35 keV radiation at incident angles in the range of 0.1° – 0.24°. The off-specular scattering was recorded with a Pilatus 1MF pixel array detector (pixel size = 172 μm) positioned 2185 mm from the sample. Acquisition times were ≈20 s per frame. Each data set was stored as a 981 × 1043 32-bit tiff image (with 20-bit dynamic range). All data are displayed as intensity maps $I(2\theta,\alpha)$, in which 2θ and α denote in-plane and out-of-plane scattering angles, respectively.

2.8 X-ray Photoelectron Spectroscopy Depth Profiling with C_{60}^+ Cluster Ion Sputtering

X-ray Photoelectron Spectroscopy (XPS), also known as Electron Spectroscopy for Chemical Analysis (ESCA), is the most extensively used surface analysis technique for a broad range of materials (*e.g.*, metals, polymers, and organic silane monolayers), providing valuable quantitative chemical composition and chemical state information of the material surface. XPS typically is accomplished by exciting a samples surface with monochromatic X-rays and causing electrons to be emitted from the sample surface. The emitted electrons (*i.e.*, photoelectrons) are captured by an electron energy analyzer and their kinetic energies are detected (Figure 2.17). Because the energy of an X-ray with a particular wavelength is known, the electron binding energy of each of the emitted electrons can be determined by the following equation:[71]

$$E_b = h\upsilon - E_k - \varphi \qquad 2.14$$

in which E_b is the binding energy of the electron, h is Plank's constant, υ is the frequency of the X-ray beam, E_k is the kinetic energy of the photoelectron measured by the analyzer, and φ is the work function dependent on both the spectrometer and the material.

Each element has its own characteristic binding energy values and produces a characteristic set of XPS peaks corresponding to different electron configuration within the atom (*e.g.*, 1s, 2s, 2p, 3s,…). For example, the binding energy for C1s electron is ~285 eV, O1s electron is ~530 eV, F1s electron is ~685 eV and S2p electron is ~165 eV. These elements commonly are selected for analysis in the polymeric materials. Additionally, the binding energies of the elements will have slight shifts due to a change in the chemical bonding of that element. For example, a

C1s electron ejected from a C-C or C-H bond has a binding energy of 284.8 eV; the binding energy shifts to ~288.5 eV from a C=O bond, and ~286.0 eV from a C-O-C bond. Thus, from the binding energy and intensity of a photoelectron peak, the elemental composition, chemical state and electron state of the elements can be determined. The XPS is a high resolution technique which can detect the element at low concentrations ~0.1 – 1%. A typical survey scan of a polymer sample and peak analysis of a carbon signal is shown in Figure 2.18.

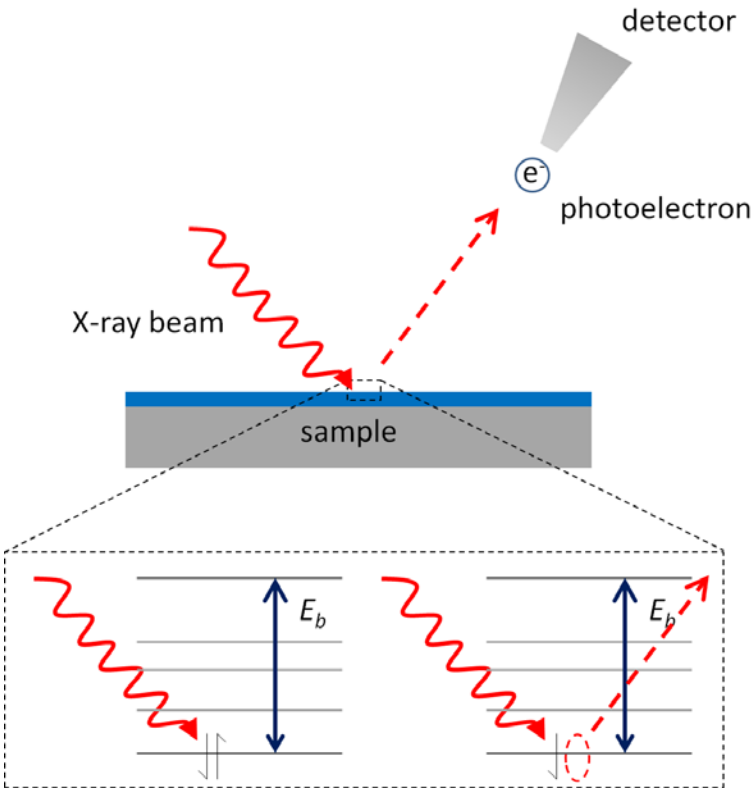

Figure 2.17: Cartoon of XPS. The electrons of the atoms at the sample surface are excited by the incident X-ray beams and ejected from the surface as photoelectrons. The photoelectrons are captured by the detected, and their kinetics energies are measured.

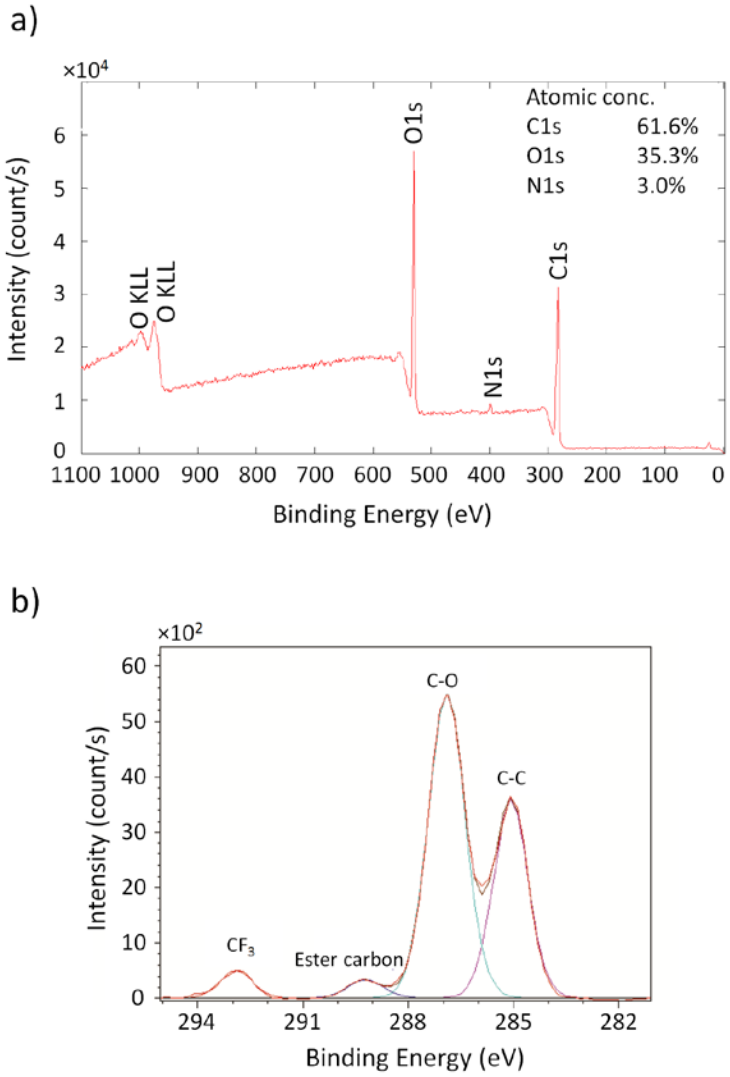

Figure 2.18: a) Sample survey of XPS spectra from a polymer film. b) Peak analysis associated with the C1s signal.

The typically sample probe area is 100 – 200 μm^2; however, the spatial resolution can be improved by using synchrotron X-ray sources. The average depth of analysis for an XPS measurement is approximately 3 – 10 nm, as determined by the attenuation function of the emitted electrons. Depth distribution analysis can be

achieved by angle-resolved XPS (non-destructive method) or combing ion sputtering etching methods (destructive method).[72] The angle-resolved XPS is accomplished by tilting the specimen away or towards the analyzer, *i.e.*, by changing the take-off angle (θ) between the analyzer and the sample. The average sampling depth is giving by

$$d_{avg} = d \sin\theta \qquad 2.15$$

Therefore, higher take-off angle results in more sampling depth.[73] However, the sampling depth still is limited by the inelastic mean free path of the photoelectrons (IMFP) as about 65% of the signal emanates from a depth of less than λ, 85% from a depth of less than 2λ, and 95% from a depth of less than 3λ.

XPS depth profiling with ion sputtering etching is a destructive method which uses an ion beam to remove layers of the sample surface. Combining a sequence of ion etch cycles interleaved with XPS measurements provides quantitative depth distribution information (Figure 2.19). Single-ion sputtering sources like Ar^+ or Cs^+ cause severe damage to soft materials that can alter the chemical composition and confound analysis.[74, 75] In contrast, cluster-ion sputtering sources like C_{60}^+ result in much less damage, as the energy transfer from the ion to the material occurs primarily at the film surface, minimizing the propagation of damage into the depth of the film.[76]

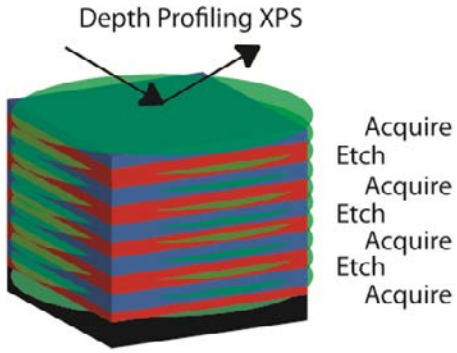

Figure 2.19: Schematic illustration of XPS depth profiling. A sequence of ion etch cycles with XPS measurements allows quantitative depth distribution information. Adapted with permission from Gilbert, J. B.; Luo, M.; Shelton, C. K.; Rubner, M. F.; Cohen, R. E.; Epps III, T. H. *ACS Nano* 2014, 9, (1), 512-520.

In this thesis work, XPS depth profiling with $C60^+$ sputtering was employed to resolve the lithium-ion distribution in the nanometer-scale domain structures of block polymer electrolyte thin films. In collaboration with the Rubner Group and Cohen Group at MIT, the XPS depth profiling experiment was performed by Jonathan Gilbert at MIT using a PHI Versaprobe II X-ray photoelectron spectrometer with a scanning monochromated Al source (1486.6 eV, 100 W, spot size 200 μm). Depth profiling was accomplished using the instrument's $C60^+$ ion source. The takeoff angle between the sample surface and analyzer was 45°, and the X-ray beam collected C1s, O1s, F1s, Li1s, and Si2p elemental information while rastering over a 200 × 1400 μm^2 area. Sputtering occurred in 1 min intervals, while the sample was moved using concentric Zalar rotation at 1 rpm. The $C60^+$ source was operated at 10 kV and 10 nA and rastered over a 4×4 mm^2 area at an angle 70° to the surface normal. Atomic composition was determined on the basis of photoelectron peak areas corrected with

the relative sensitivity factors. All data were background-subtracted and smoothed using a five-point quadratic Savitzky-Golay algorithm. Data also were charge-corrected so that the C-C bond has a binding energy of 285.0 eV. No significant increase in temperature occurred (<1 °C) as measured by the temperature of the stage. The surface of the silicon substrate was defined as the point at which the atomic concentration of silicon reached 5% in the depth profiling data. Spectra peaks were fit in CasaXPS software.

2.9 Differential Scanning Calorimetry

Differential scanning calorimetry (DSC) has been utilized to measure the phase transitions and heat capacities for a broad range of materials, including polymers, composites and drugs.[77, 78] DSC measures the difference in heat flow between a sample pan and a reference pan as both are subjected to a controlled thermal profile. The reference pan usually is empty, and the sample pan usually contains 3 – 5 mg of samples. The heat flow (Q) that needed for increasing the temperature of the sample is:

$$Q = C_p \Delta T \tag{2.16}$$

in which C_p is the heat capacity of the sample, and ΔT is the temperature change. For polymer samples, when the sample undergoes phase transition such as glass transition, the heat flow curve will rise as the heat capacity of the sample increases (Figure 2.20). After the glass transition temperature, the polymer may form crystalline structures. This process is exothermic, and the corresponding heat flow curve will drop. If the temperature continues to increase, those crystals start to melt and absorb heat, resulted in a peak in the heat flow curve. Therefore, DSC can be used to measure properties such as the glass transition temperature (T_g), crystallization temperature (T_c), and/or

melting temperature (T_m) of the polymer. This method also is useful for determining the extent of mixing between polymer domains in BPs, as the location and breadth of the T_g's, as well as the change of heat capacity (ΔC_P) values, provides quantitative information on the extent of microphase separation.[79-81] For example, Prud'homme *et al.* studied the domain mixing in a series of low molecular weight non-tapered poly(isoprene-*b*-styrene) (I-S) BPs through DSC.[79] They noted the $T_{g\text{-}PS}$ shifted significantly toward lower temperatures with decreasing molecular weight, suggesting there was enhanced mixing of the PI and PS domains at low molecular weight systems. The thicknesses of interfacial regions were estimated from the analysis of ΔC_P, and the results of interfacial width (δ_{DSC}) agreed well with values derived from SAXS (δ_{SAXS}) realizing $\delta_{SAXS} \approx 2\ \delta_{DSC}$.[79]

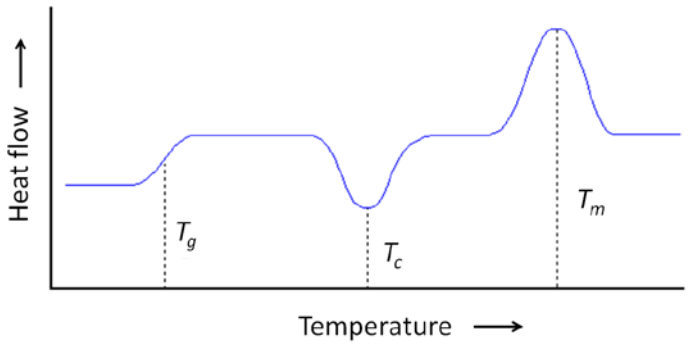

Figure 2.20: Example of DSC plot showing phase transitions at glass transition temperature (T_g), crystallization temperature (T_c), and melting temperature (T_m).

DSC measurements for the BPs studied in this thesis work were performed on a Discovery DSC (TA Instruments) using a temperature range from -90 °C to 150 °C.

Samples were treated through three heating/cooling cycles at 10 °C min^{-1} with a continuous N_2 purge (50 mL min^{-1}). The first cycle typically removes the thermal history of the sample. The second and third heating/cooling cycles were nearly identical, and the T_gs were determined from the midpoint of the inflections in the second heating trace. The ΔC_P for individual polymer phases was evaluated by measuring the difference in height between the extrapolated base lines recorded above and below the T_g of the respective block. The values of ΔC_P for each phase are normalized by the weight of the respective block in the particular sample for comparison with homopolymers.

REFERENCES

1. Albert, J. N. L.; Baney, M. J.; Stafford, C. M.; Kelly, J. Y.; Epps, T. H., III. *ACS Nano* **2009,** 3, (12), 3977-3986.

2. Peters, R. D.; Yang, X. M.; Kim, T. K.; Nealey, P. F. *Langmuir* **2000,** 16, (24), 9620-9626.

3. Luo, M.; Seppala, J. E.; Albert, J. N. L.; Lewis, R. L.; Mahadevapuram, N.; Stein, G. E.; Epps, T. H., III. *Macromolecules* **2013,** 46, (5), 1803-1811.

4. Albert, J. N. L.; Kim, J. D.; Stafford, C. M.; Epps, T. H., III. *Rev. Sci. Instrum.* **2011,** 82, (6), 065103.

5. Bornside, D.; Macosko, C.; Scriven, L. *J. Appl. Phys.* **1989,** 66, (11), 5185-5193.

6. Bornside, D. E.; Macosko, C. W.; Scriven, L. E. *Journal of Imaging Technology* **1987,** 13, (4), 122-130.

7. Stafford, C. M.; Roskov, K. E.; Epps, T. H., III; Fasolka, M. J. *Rev. Sci. Instrum.* **2006,** 77, (2), 023908.

8. Davis, R. L.; Jayaraman, S.; Chaikin, P. M.; Register, R. A. *Langmuir* **2014,** 30, (19), 5637-5644.

9. Bang, J.; Kim, B. J.; Stein, G. E.; Russell, T. P.; Li, X.; Wang, J.; Kramer, E. J.; Hawker, C. J. *Macromolecules* **2007,** 40, (19), 7019-7025.

10. Hamley, I. W. *Prog. Polym. Sci.* **2009,** 34, (11), 1161-1210.

11. Harrison, C.; Adamson, D. H.; Cheng, Z.; Sebastian, J. M.; Sethuraman, S.; Huse, D. A.; Register, R. A.; Chaikin, P. M. *Science* **2000,** 290, (5496), 1558-1560.

12. Majewski, P. W.; Yager, K. G. *ACS Nano* **2015,** 9, (4), 3896-3906.

13. Bates, C. M.; Maher, M. J.; Janes, D. W.; Ellison, C. J.; Willson, C. G. *Macromolecules* **2014,** 47, (1), 2-12.

14. Harrison, C.; Adamson, D. H.; Cheng, Z.; Sebastian, J. M.; Sethuraman, S.; Huse, D. A.; Register, R. A.; Chaikin, P. *Science* **2000,** 290, (5496), 1558-1560.

15. Harrison, C.; Cheng, Z.; Sethuraman, S.; Huse, D. A.; Chaikin, P. M.; Vega, D. A.; Sebastian, J. M.; Register, R. A.; Adamson, D. H. *Physical Review E* **2002,** 66, (1), 011706.

16. Mishra, V.; Fredrickson, G. H.; Kramer, E. J. *ACS Nano* **2012,** 6, (3), 2629-2641.

17. Berry, B. C.; Bosse, A. W.; Douglas, J. F.; Jones, R. L.; Karim, A. *Nano Lett.* **2007,** 7, (9), 2789-2794.

18. Yager, K. G.; Forrey, C.; Singh, G.; Satija, S. K.; Page, K. A.; Patton, D. L.; Douglas, J. F.; Jones, R. L.; Karim, A. *Soft Matter* **2015,** 11, (25), 5154-5167.

19. Sinturel, C.; Vayer, M.; Morris, M.; Hillmyer, M. A. *Macromolecules* **2013,** 46, (14), 5399-5415.

20. Luo, M.; Epps, T. H., III. *Macromolecules* **2013,** 46, (19), 7567-7579.

21. Kim, E.; Ahn, H.; Park, S.; Lee, H.; Lee, M.; Lee, S.; Kim, T.; Kwak, E.-A.; Lee, J. H.; Lei, X.; Huh, J.; Bang, J.; Lee, B.; Ryu, D. Y. *ACS Nano* **2013**, 1952-1960.

22. Hsieh, I. F.; Sun, H.-J.; Fu, Q.; Lotz, B.; Cavicchi, K. A.; Cheng, S. Z. D. *Soft Matter* **2012,** 8, (30), 7937-7944.

23. Paik, M. Y.; Bosworth, J. K.; Smilges, D.-M.; Schwartz, E. L.; Andre, X.; Ober, C. K. *Macromolecules* **2010,** 43, (9), 4253-4260.

24. She, M.-S.; Lo, T.-Y.; Ho, R.-M. *Macromolecules* **2013,** 47, (1), 175-182.

25. Wu, Y.-H.; Lo, T.-Y.; She, M.-S.; Ho, R.-M. *ACS Appl. Mater. Interfaces* **2015,** 7, (30), 16536-16547.

26. Kim, G.; Libera, M. *Macromolecules* **1998,** 31, (8), 2569-2577.

27. Albert, J. N. L.; Young, W.-S.; Lewis, R. L., III; Bogart, T. D.; Smith, J. R.; Epps, T. H., III. *ACS Nano* **2012,** 6, (1), 459-466.

28. Albert, J. N. L.; Young, W. S.; Lewis, R. L.; Bogart, T. D.; Smith, J. R.; Epps, T. H. *ACS Nano* **2012,** 6, (1), 459-466.

29. Gotrik, K. W.; Hannon, A. F.; Son, J. G.; Keller, B.; Alexander-Katz, A.; Ross, C. A. *ACS Nano* **2012,** 6, (9), 8052-8059.

30. Seppala, J. E.; Lewis, R. L., III; Epps, T. H., III. *ACS Nano* **2012,** 6, (11), 9855-9862.

31. Girifalco, L.; Good, R. *The Journal of Physical Chemistry* **1957,** 61, (7), 904-909.

32. Fowkes, F. M. *The Journal of Physical Chemistry* **1962,** 66, (2), 382-382.

33. Owens, D. K.; Wendt, R. C. *J. Appl. Polym. Sci.* **1969,** 13, (8), 1741-1747.

34. *Application note: Solid surface energy analysis yesterday and today* Thermo Fisher Scientific.

35. Wu, S. In *Calculation of interfacial tension in polymer systems*, Journal of Polymer Science Part C: Polymer Symposia, 1971; Wiley Online Library: 1971; pp 19-30.

36. Wu, S., *Polymer Interface and Adhesion*. M. Dekker: 1982.

37. *Taking the Mystery Out of Thin Film Measurement* **2006,** Filmetrics, Inc.

38. *FILMeasure, 4.12.0* **2008,** Filmetrics, Inc.

39. Smith, A. P.; Douglas, J. F.; Meredith, J. C.; Amis, E. J.; Karim, A. *Phys. Rev. Lett.* **2001,** 87, (1), 015503.

40. Smith, A. P.; Douglas, J. F.; Meredith, J. C.; Amis, E. J.; Karim, A. *J. Polym. Sci. Part B: Polym. Phys.* **2001,** 39, (18), 2141-2158.

41. Coulon, G.; Collin, B.; Ausserre, D.; Chatenay, D.; Russell, T. *Journal de physique* **1990,** 51, (24), 2801-2811.

42. Magonov, S. N.; Reneker, D. H. *Annual Review of Materials Science* **1997,** 27, (1), 175-222.

43. Knoll, A.; Magerle, R.; Krausch, G. *Macromolecules* **2001,** 34, (12), 4159-4165.

44. Lammertink, R. G. H.; Hempenius, M. A.; Vancso, G. J.; Shin, K.; Rafailovich, M. H.; Sokolov, J. *Macromolecules* **2001,** 34, (4), 942-950.

45. Qiang, Z.; Zhang, L.; Stein, G. E.; Cavicchi, K. A.; Vogt, B. D. *Macromolecules* **2014,** 47, (3), 1109-1116.

46. Albert, J. N. L.; Bogart, T. D.; Lewis, R. L.; Beers, K. L.; Fasolka, M. J.; Hutchison, J. B.; Vogt, B. D.; Epps, T. H., III. *Nano Lett.* **2011,** 11, (3), 1351-1357.

47. Singh, G.; Yager, K. G.; Berry, B.; Kim, H.-C.; Karim, A. *ACS Nano* **2012,** 6, (11), 10335-10342.

48. Zhang, X.; Berry, B. C.; Yager, K. G.; Kim, S.; Jones, R. L.; Satija, S.; Pickel, D. L.; Douglas, J. F.; Karim, A. *ACS Nano* **2008,** 2, (11), 2331-2341.

49. White, H.; Pu, Y.; Rafailovich, M.; Sokolov, J.; King, A.; Giannuzzi, L.; Urbanik-Shannon, C.; Kempshall, B.; Eisenberg, A.; Schwarz, S. *Polymer* **2001,** 42, (4), 1613-1619.

50. Kim, S. H.; Misner, M. J.; Russell, T. P. *Adv. Mater.* **2004,** 16, (23 - 24), 2119-2123.

51. Koneripalli, N.; Singh, N.; Levicky, R.; Bates, F. S.; Gallagher, P. D.; Satija, S. K. *Macromolecules* **1995,** 28, (8), 2897-2904.

52. Young, W. S.; Epps, T. H., III. *Macromolecules* **2012,** 45, (11), 4689-4697.

53. Tureau, M. S.; Epps, T. H., III. *Macromol. Rapid Commun.* **2009,** 30, (20), 1751-1755.

54. Epps, T. H., III; Cochran, E. W.; Bailey, T. S.; Waletzko, R. S.; Hardy, C. M.; Bates, F. S. *Macromolecules* **2004,** 37, (22), 8325-8341.

55. Kiessig, H. *Annalen der Physik* **1931,** 402, (6), 715-768.

56. *Integrated Thin Film Analysis Software GlobalFit (Reflectivity Analysis) User's manual* Rigaku Corporation.

57. Lin, B.; Morkved, T. L.; Meron, M.; Huang, Z.; Viccaro, P. J.; Jaeger, H. M.; Williams, S. M.; Schlossman, M. L. *J. Appl. Phys.* **1999,** 85, (6), 3180-3184.

58. Russell, T. *Materials science reports* **1990,** 5, (4), 171-271.

59. Mayes, A.; Russell, T.; Bassereau, P.; Baker, S.; Smith, G. *Macromolecules* **1994,** 27, (3), 749-755.

60. Liu, Y.; Zhao, W.; Zheng, X.; King, A.; Singh, A.; Rafailovich, M.; Sokolov, J.; Dai, K.; Kramer, E. *Macromolecules* **1994,** 27, (14), 4000-4010.

61. Babonneau, D. *J. Appl. Crystallogr.* **2010,** 43, (4), 929-936.

62. Busch, P.; Rauscher, M.; Smilgies, D.-M.; Posselt, D.; Papadakis, C. M. *J. Appl. Crystallogr.* **2006,** 39, (3), 433-442.

63. Busch, P.; Posselt, D.; Smilgies, D.-M.; Rauscher, M.; Papadakis, C. M. *Macromolecules* **2007,** 40, (3), 630-640.

64. Lee, B.; Park, I.; Yoon, J.; Park, S.; Kim, J.; Kim, K.-W.; Chang, T.; Ree, M. *Macromolecules* **2005,** 38, (10), 4311-4323.

65. Lee, B.; Park, I.; Park, H.; Lo, C.-T.; Chang, T.; Winans, R. E. *J. Appl. Crystallogr.* **2007,** 40, (3), 496-504.

66. Vu, T.; Mahadevapuram, N.; Perera, G. M.; Stein, G. E. *Macromolecules* **2011,** 44, (15), 6121-6127.

67. Jiang, Z.; Li, X.; Strzalka, J.; Sprung, M.; Sun, T.; Sandy, A. R.; Narayanan, S.; Lee, D. R.; Wang, J. *Journal of Synchrotron Radiation* **2012,** 19, (4), 627-636.

68. Körstgens, V.; Wiedersich, J.; Meier, R.; Perlich, J.; Roth, S.; Gehrke, R.; Müller-Buschbaum, P. *Anal. Bioanal. Chem.* **2010,** 396, (1), 139-149.

69. Gowd, E. B.; Marcus, B.; Manfred, S. *IOP Conference Series: Materials Science and Engineering* **2010,** 14, (1), 012015.

70. Bai, W.; Yager, K. G.; Ross, C. A. *Macromolecules* **2015,** 48, (23), 8574-8584.

71. Brune, D.; Hellborg, R.; Whitlow, H. J.; Hunderi, O., *Surface characterization: a user's sourcebook*. John Wiley & Sons: 2008.

72. Merzlikin, S. *Fakultät für Chemie* **2007**.

73. Moulder, J. F.; Chastain, J.; King, R. C., *Handbook of X-ray photoelectron spectroscopy: a reference book of standard spectra for identification and interpretation of XPS data*. Physical Electronics Eden Prairie, MN: 1995.

74. Sanada, N.; Yamamoto, A.; Oiwa, R.; Ohashi, Y. *Surf. Interface Anal.* **2004,** 36, (3), 280-282.

75. Tanaka, K.; Sanada, N.; Hikita, M.; Nakamura, T.; Kajiyama, T.; Takahara, A. *Appl. Surf. Sci.* **2008,** 254, (17), 5435-5438.

76. Shard, A. G.; Brewer, P. J.; Green, F. M.; Gilmore, I. S. *Surf. Interface Anal.* **2007,** 39, (4), 294-298.

77. Young, W. S.; Brigandi, P. J.; Epps, T. H., III. *Macromolecules* **2008,** 41, (17), 6276-6279.

78. Kuan, W.-F.; Remy, R.; Mackay, M. E.; Epps III, T. H. *RSC Advances* **2015,** 5, (17), 12597-12604.

79. Morèse-Séguéla, B.; St-Jacques, M.; Renaud, J. M.; Prud'homme, J. *Macromolecules* **1980,** 13, (1), 100-106.

80. Kim, J.; Mok, M. M.; Sandoval, R. W.; Woo, D. J.; Torkelson, J. M. *Macromolecules* **2006,** 39, (18), 6152-6160.

81. Wong, C. L.; Kim, J.; Torkelson, J. M. *J. Polym. Sci. Part B: Polym. Phys.* **2007,** 45, (20), 2842-2849.

Chapter 3

MANIPULATION OF NANOSCALE MORPHOLOGY IN BLOCK POLYMER THIN FILMS

This chapter describes the manipulation of block polymer (BP) nanostructure in thin films using substrate modification. High throughput methods were employed to examine the effects of substrate surface chemistry and film thickness on the self-assembly of cylinder-forming poly(styrene-*b*-isoprene-*b*-styrene) (SIS) thin films. The conditions for a morphological transformation from parallel cylinders to hexagonally perforated lamellae (HPL) were identified. The HPL structures were revealed by a combination of techniques, including film etching/atomic force microscopy (AFM), focused ion beam (FIB) milling/cross-sectional transmission electron microscopy (TEM) and grazing-incidence small-angle X-ray scattering (GISAXS). This chapter presents a significant expansion of designer surface modification methods for the possible universal manipulation of thin film nanostructures. Text and figures are reproduced and adapted with permission from Luo M., *et al. Macromolecules* 2013, 46, (5), 1803-1811.

3.1 Introduction

Controlling the self-assembled nanostructures is crucial for the widespread adoption of BP thin films for emerging nanotechnologies such as nanolithographic masks,[1, 2] nanotemplates,[3, 4] and nanoporous membranes.[5, 6] While the phase behavior of the bulk BPs depends primarily on the block interactions (interaction parameter, χ), degree of polymerization (N), and block volume fractions (f_i), the thin film self-

assembly is influenced strongly by the commensurability considerations (*i.e.* film thickness) and surface interactions.[7-10] Numerous researchers have studied AB-type lamellar forming BP thin films, and the nanoscale behavior of these systems is fairly well understood, particularly with respect to the surface interactions and commensurability effects (also discussed in Chapter 1, Section 1.3).[2, 7-9, 11-19]

The thin film phase behavior of BPs that form cylinders in the bulk is more complex and less understood. The interplay between the confinement and the surface effects (*e.g.*, wetting layer formation of minor component[20, 21] and surface reconstruction[9, 22-24]) is complicated by the system asymmetry.[9, 25-27] Both theoretical and experimental investigations have demonstrated changes in morphology through the manipulations of the substrate surface interactions.[18, 28-31] For example, Huinink and coworkers applied dynamic density functional theory (DDFT) to simulate thermally-annealed cylinder-forming poly(styrene-*b*-butadiene) (PS-PB) thin films and suggested that the surfaces may initiate transformations from cylinders to HPL, and to lamellae in the case of sufficiently strong surface interactions.[32] To study these trends experimentally, Tsarkova *et al.* examined cylinder-forming PS-PB thin films on two chemically different substrates (SiO_x/Si and carbon/SiO_x/Si).[33] They noted that HPL and lamellar morphologies developed on piranha-treated SiO_x/Si surfaces due to strong interactions between the substrate surface and PB block, while parallel cylinders formed on the carbon/SiO_x/Si substrates. Additionally, several research groups have employed random copolymer brushes or chlorosilane monolayers to investigate the effect of substrate surface chemistry/energy on BP thin film orientation; however, the focus mostly has been concerned with creating "neutral" substrate surfaces to generate perpendicularly-oriented cylinders.[16, 18, 28-31, 34-38] In this

chapter, chlorosilane monolayers were employed to study the phase behavior of a cylinder-forming SIS triblock copolymer thin film in response to a preferential substrate surface field.

Although the similarities between AB diblock copolymer and ABA triblock copolymer bulk phase behavior are well established,[39] the phase behavior of ABA triblock copolymers in thin films, though investigated in several studies as discussed below, still has many open questions. For example, Khanna and coworkers studied the effect of chain architecture on the domain orientation of lamellar and cylinder forming BPs.[17] They found "spontaneously" perpendicular oriented domains for lamellae- and cylinder-forming poly(cyclohexylethylene-*b*-ethylene-*b*-cyclohexylethylene) (CEC) triblock films, while the diblock analogues prefer a parallel orientation to the surface. Using self-consistent-field theory (SCFT) calculations of the excess free energy for different orientations in AB and ABA BPs, Khanna predicted that the perpendicular orientation is favorable when the middle block has a lower surface energy, and the difference in surface energies between the two blocks is small ($\Delta\gamma < 3$ mJ/m^2). Similarly, Vu *et al.* found the domain orientations of poly(styrene-*b*-methyl methacrylate) (PS-PMMA) diblock ($\Delta\gamma < 1$ mJ/m^2) were very sensitive to film thickness, annealing temperature, and substrate coating conditions, and parallel or mixed parallel/perpendicular domain orientations are detected for most film thicknesses studied. While ABA triblocks were more tolerate to the processing conditions and perpendicular domain orientation were stable across all the film thicknesses studied. Furthermore, using Monte Carlo simulations of cylinder-forming asymmetric ABA thin films, Szamel *et al.* predicted a sequence of perpendicular cylinder to parallel cylinder to perforated lamellar morphologies upon

increasing the film thickness for cases in which the film surfaces were slightly attractive to the majority block.[40] Thus, the nanoscale orientation and assembly of BP structures depends not only on the energetics between the copolymer and the surfaces but also on the film thickness and chain architecture.

To gain further insight into these effects on the phase behavior of cylindrical BP thin films, the nanoscale morphologies of the SIS thin films were investigated systematically, in a high-throughput fashion, using the substrate surface chemistry and film thickness gradients. Though cylinder-forming SIS triblock copolymer thin film orientations have been manipulated in a controlled fashion using solvent vapor annealing techniques,[41-43] thin films of these triblock materials, whose blocks possess significantly different surface energies,[44] have not been studied using systematic substrate surface modifications. This surface energy difference also differentiates the studies herein from those on copolymers such as PS-PMMA whose blocks possess similar surface energies.[30, 31] Thus, the work presented in this chapter, where the SIS thin films were deposited onto chlorosilane-modified substrates, highlights an expansion of designer surface modification methods for the manipulation of thin film nanostructures.

3.2 Materials and Methods

3.2.1 Substrate Surface Modification and Characterization

Benzyldimethylchlorosilane (benzyl silane) and *n*-butyldimethylchlorosilane (*n*-butyl silane) (Gelest, Inc.) were used as received. Pure component monolayers were deposited onto silicon wafers using liquid deposition, and gradient monolayers were created by controlled vapor deposition as discussed in Chapter 2 Section 2.1.

The surface energies of the modified substrate were characterized by contact angle measurements using diiodomethane and water as probe liquids. Surface energies of the modified substrates were calculated using the Owens-Wendt geometric mean method.[45] The dispersive components (γ^D) and polar components (γ^P) of the contact angle probe liquids used in these calculations are $\gamma^D_{Diiodomethane} = 50.8$ mJ/m^2, $\gamma^P_{Diiodomethane} = 0$ mJ/m^2, $\gamma^D_{Water} = 21.8$ mJ/m^2, and $\gamma^P_{Water} = 51.0$ mJ/m^2.[46] The liquid deposition and vapor deposition techniques offered consistent contact angle results, indicating that the liquid depositions likely are homogeneous and reproducible.

3.2.2 Polymer Film Preparation and Characterization

An SIS triblock copolymer was obtained from DEXCO (V4211) and used as received. The SIS polymer had an overall molecular mass of 118 kg/mol, block volume fractions of $f_S = 0.134$, $f_I = 0.732$, $f_S = 0.134$, a dispersity of 1.09, and a bulk nearest-neighbor spacing of $L_0 = 33$ nm ($d_{bulk} = 2\pi/q^* = 29$ nm, q^* is the primary peak in small angle X-ray scattering and d is the distance between (100) planes). SIS films were cast on the modified substrates by flow coating[47] from a 2.3 wt % solution of SIS in tetrahydrofuran (THF, Fisher Scientific, ACS Optima grade). A 50 µL volume of polymer solution, a gap height of 200 µm, and a constant velocity of $v = 12$ mm/s were used to produce films with uniform thickness of 90 ± 1 nm. Gradient thickness SIS films were cast in a similar manner but with an initial velocity of $v = 7$ mm/s and an acceleration of $a = 4$ mm/s^2, to achieve a film thickness range of 85-120 nm over a 32 mm distance on the substrate. In addition, an initial velocity of $v = 9$ mm/s and an acceleration of $a = 1.8$ mm/s^2 was used to produce a thickness range from 80-100 nm to investigate the film thickness effect close to 90 nm. Film thickness was measured using a reflectance spectrometer (Filmetrics F20-UV). Thickness profiles are

provided in Appendix A. The films were stored under vacuum overnight and subsequently annealed under vacuum (20 mTorr) at 135 °C for 24 h.

Optical microscopy images were collected on a Nikon microscope equipped with a 5 MP CCD camera (Nikon Eclipse LV100). The free surface morphologies of polymer films were assessed by tapping-mode atomic force microscopy (AFM) (Veeco Dimension 3100).

Ultraviolet ozone etching was conducted in the UVO cleaner in 15 s increments with the samples placed ≈1 cm from the lamp.[42] In one single UVO step, 20 – 30 nm polymer film was removed. The polymer film then was soaked in an isopropyl alcohol bath (Fisher Scientific, ACS grade) for ≈10 min between exposures to wash off polymer fragments. Film thickness measurements and AFM images were collected after drying the sample under a stream of nitrogen. The AFM and UVO etching step was repeated to probe the full depth of the film.

In collaboration with the Stein group in the Department of Chemical and Biomolecular Engineering of University of Huston, grazing-incidence small angle X-ray scattering (GISAXS) measurements were performed by Nikhila Mahadevapuram at beamline 8-ID-E at the Advanced Photon Source of Argonne National Laboratory. Samples were placed in a vacuum chamber and illuminated with 7.35 keV radiation at incident angles in the range of 0.1° - 0.24°. All data are displayed as intensity maps $I(2\Theta, \alpha)$, where 2Θ and α denote in-plane and out-of-plane scattering angles, respectively.

Thin film sections for the cross-sectional TEM experiment were prepared in an Auriga 60 CrossBeam instrument (Auriga 60 FIB/SEM) at room temperature. The detailed procedures are discussed in Chapter 2 Section 2.6.3.

3.3 Results and Discussion

3.3.1 Gradient Thickness Films on Pure Component Monolayer Substrates

Modified substrates were fabricated by liquid deposition of pure chlorosilanes onto UVO-cleaned silicon substrates. The chlorosilane functionalities were chosen to mimic the molecular structures of the BP components, with benzyl silane being chemically similar to the PS block and *n*-butyl silane resembling the polyisoprene (PI) block. The diiodomethane and water contact angles of the modified surfaces are given in Table 3.1. Surface energies, calculated using the Owens-Wendt method,[45] were 42.0 ± 0.4 mJ/m^2 for the benzyl silane surface and 29.9 ± 0.6 mJ/m^2 for the *n*-butyl silane surface. The surface energies of these modified surfaces correlated well with those of the polymer components, 40.7 mJ/m^2 for PS and 32.0 mJ/m^2 for PI.[48]

Table 3.1: Contact Angle Measurements of Pure Component Monolayers*

Contact angle liquid	Benzyl silane monolayer	*n*-Butyl silane monolayer
Diiodomethane	$42.4 \pm 0.5°$	$61.5 \pm 0.6°$
Water	$80.4 \pm 1.2°$	$92.1 \pm 1.4°$

* The reported contact angles were averaged over five samples with six spots on each sample; the uncertainty represents one standard deviation of the data obtained from the repeated measurements.

The optical microscopy images of gradient thickness SIS films on bare silicon, benzyl silane, and *n*-butyl silane surfaces after thermal annealing are shown in Figure 3.1. The film thicknesses spanned 85 nm to 120 nm, which corresponds to 3.15 *d* to 4.44 *d* (interlayer spacing, *i.e.*, (100) plane, *d* was 27 nm as discussed in the later section). At $t = 87$ nm (3.22 *d*), polymer chains could stretch to accommodate small deviations from commensurability,[49-51] thus, smooth featureless films formed. As the film thickness incommensurability increased, the island structures (light blue areas)

emerged at a film thickness of 91 nm (3.37 *d*), they continued to grow into a labyrinthine-like surface morphology (also known as "spinodal patterns" by analogy with phase separation[11]) at a film thickness of 94 nm (3.48 *d*), and finally the hole structures formed (navy blue areas) at a film thickness of 101 nm (3.74 *d*). At t = 108 nm (4.00 *d*), commensurability was achieved and a uniform film was recovered. At t = 116 nm (4.30 *d*), the film exhibited a similar surface pattern with t = 89 nm (3.30 *d*), and the cyclical changes in morphology with further increases in film thickness are expected.[11]

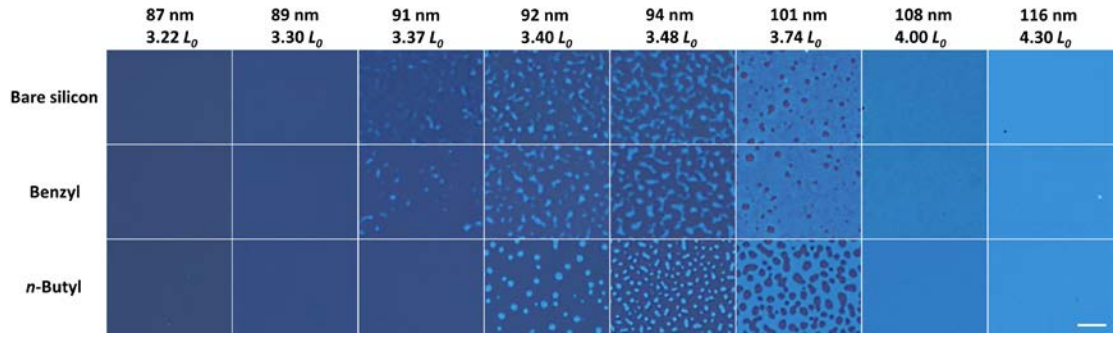

Figure 3.1: Optical images of gradient thickness SIS films annealed at 135 °C for 24 h. Close to the commensurability condition t/d = 3 or 4, the films appear featureless; with increasing thickness, the morphology progresses from islands to spinodal island/hole structures to holes to featureless at the next commensurate thickness. The scale bar represents 10 μm and applies to all images. Reprinted with permission from Luo M., *et al.* *Macromolecules* 2013, 46, (5), 1803-1811.

The effects of substrate surface energy/chemistry and film thickness on SIS film morphology are highlighted by the AFM images of gradient thickness films as shown in Figure 3.2. Parallel cylinders were found in the SIS films on both bare silicon and benzyl silane surfaces regardless of film thickness, whereas a higher

number density of "dots" (indicative of perpendicular cylinders or HPL) was found at the free surface of the films on *n*-butyl silane coated substrates. Films exhibiting only surface dot patterns were found at narrow thickness ranges t = 89 – 91 nm (3.30 d – 3.37 d) and t = 116 nm (4.30 d) on the *n*-butyl silane surface, whereas mixed nanostructure regions (with a preference for perpendicular cylinders or HPL) were noted at all other film thicknesses. The thickness difference between regions with solely surface dot patterns was ≈27 nm, which was slightly less than the bulk domain spacing (d_{bulk}) of 29 nm. The small reduction of the repeat thickness of the dot patterns relative to the bulk domain spacing is a known phenomenon in BP thin films.[50, 52-57]

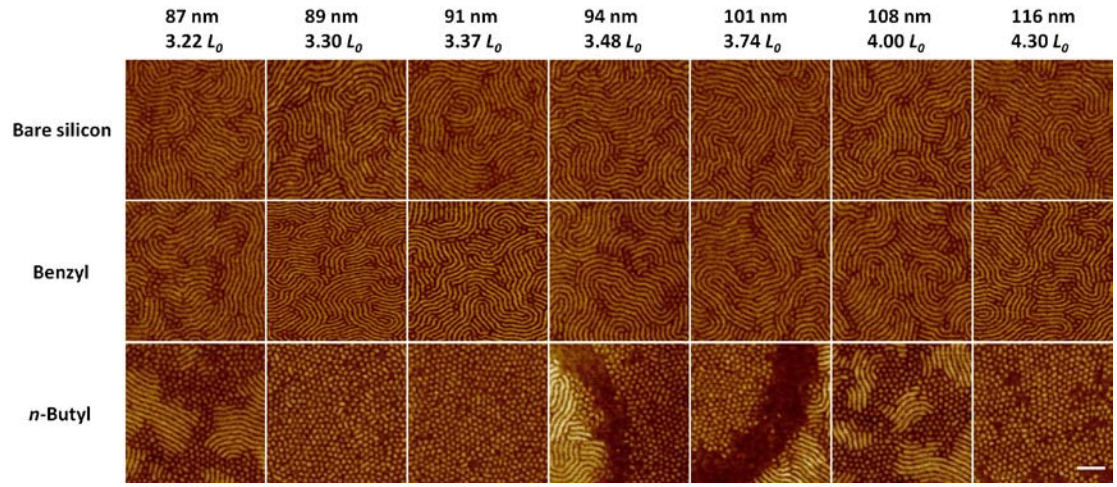

Figure 3.2: AFM phase images of SIS gradient thickness films on bare silicon, benzyl silane, and *n*-butyl silane surfaces, where the thickness increases from 3.22 d to 4.30 d. Parallel cylinders were noted for films on bare silicon and benzyl silane surfaces, while dot patterns were noted for films on *n*-butyl silane surfaces. The scale bar represents 200 nm and applies to all images. Reprinted with permission from Luo M., *et al.* *Macromolecules* 2013, 46, (5), 1803-1811.

For the thickness gradient films, the benzyl substrate surface was preferential for the PS end-blocks, which leads to parallel cylinder structure at all film thicknesses. This result is consistent with the conceptual description of thin film free energy proposed by Han *et al*., which suggested that favorable interactions between the hard wall and the short end blocks promote parallel domains.[18] A similar hypothesis could hold for the bare silicon substrate as well. The PI block had a lower surface energy (32.0 mJ/m^2) than the PS block (40.7 mJ/m^2), and thus was preferred to segregate to the free air and substrate surfaces, leading to a parallel cylinder domain orientation. It is possible that the surface energy difference was significant enough to overcome the entropic penalties for looping the mid-block (PI)[17] and loss of free chain ends (PS) at the surfaces.[58] The silicon substrate effect was not strong enough to promote any lamellar-like morphology in this SIS system, in contrast to Tsarkova *et al*.[33]

By examining the films across a variety of thicknesses, the substrate surface energy/chemistry effect on nanostructure was clearest at a thickness of ≈90 nm (3.33 *d*), where the film on the *n*-butyl surface exhibited surface dot patterns (HPL, as will be detailed later in this discussion), and the films on the benzyl and bare silicon surfaces displayed parallel cylinders. To verify this HPL region for films on the *n*-butyl surface, uniform thickness SIS films (90 ± 1 nm) were cast on pure *n*-butyl silane substrates, and the featureless optical micrograph and dot patterns were reproduced on a 1" × 2.5" substrate. Thus, the gradient thickness allowed us to identify the thickness region of interest for further detailed analysis.

In the following section, the detailed internal structure of 90 nm thick SIS thin films on the *n*-butyl silane substrates was investigated using UVO etching/AFM, FIB/TEM, and GISAXS. Initially, successive UVO etching steps were followed by

AFM imaging of the SIS films were employed to examine the propagation of the free surface morphology towards the substrate surface.[59] The results of the successive etching steps, shown in Figure 3.3, reveal that the dot pattern persisted through the film thickness, indicating that the free surface nanostructure was likely influenced (and templated) by interactions at the substrate. Typically, the substrate surface field propagates ~6 *d* from the substrate interface;[30, 31] this scenario also applied to the films herein, which spanned ~3-4 *d* in thickness, and thus displayed a noticeable substrate surface effect. I also fabricated an SIS film with thickness of ~ 6.8 – 8.9 *d* on *n*-butyl silane coated substrate, parallel cylinders were revealed on the film surface, indicating the propagation distance substrate surface may be less than 6 *d*.

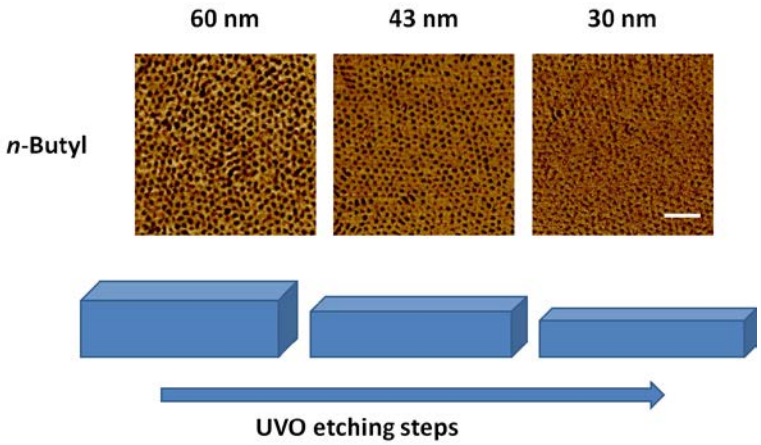

Figure 3.3: Through-film morphology of an SIS film on an *n*-butyl silane substrate, revealed by UVO etching followed by AFM imaging. AFM phase images corresponding to the residual film thickness (60 nm, 43 nm, and 30 nm) after each etching step. The scale bar indicates 200 nm and applies to all images. Reprinted with permission from Luo M., *et al.* *Macromolecules* 2013, 46, (5), 1803-1811.

Further, a lift-out technique was employed to prepare a specimen for cross-sectional processing and imaging through a combination of FIB and TEM. Although a hexagonal array pattern (not highly ordered, see Appendix A) was noted on the film surface, the cross-sectional TEM image, shown in Figure 3.4, clearly displayed layered structures stacked parallel to the substrate.[60] The sample was stained with OsO_4, which was selective for the PI block, thus the dark regions represented the PI domains, and the light regions corresponded to PS domains. The TEM image indicated that the PS layers were perforated by PI domains, forming an HPL structure. Non-cylindrical phases like HPL or lamellae have been found in thin film BP samples that show cylindrical nanostructures in the bulk.[33, 61] In this system, the *n*-butyl silane substrate was preferential for the PI block, which led to a preferred affinity of the PI block to the substrate. This hypothesis is supported by the cross-sectional TEM image (Figure 3.4), where a wetting layer of PI block was noted close to the silicon substrate, possibly suggesting that the phase transition of cylinder to HPL was triggered by a volume fraction change due to the substrate surface interactions.[32, 62]

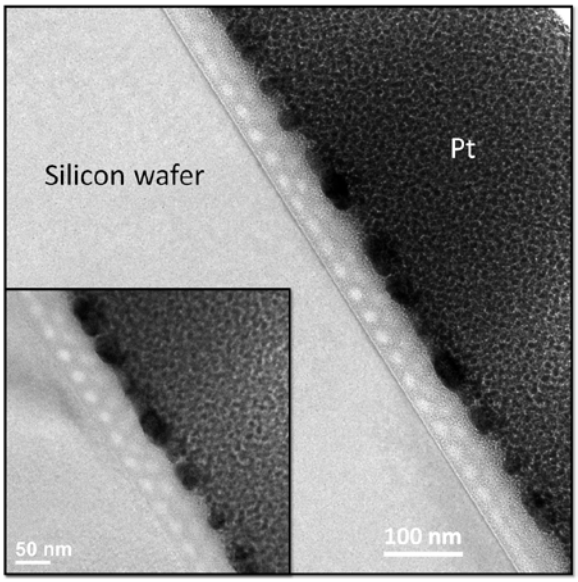

Figure 3.4: Cross-sectional TEM images of 90 nm thick SIS film on an *n*-butyl silane substrate. The film section was stained with OsO_4. Reprinted with permission from Luo M., *et al. Macromolecules* 2013, 46, (5), 1803-1811.

Because the cross-sectional TEM only revealed two-dimensional features, the three-dimensional stacking type of the hexagonal perforations (on the *n*-butyl surface) was further investigated by GISAXS. These data were compared with measurements for parallel cylinders (benzyl surfaces), which highlights the change in symmetry versus substrate surface chemistry. Figures 3.5 (a) and (c) shows the GISAXS patterns of SIS films annealed at 135 °C for 12 h on benzyl and *n*-butyl surfaces, respectively. The film thickness was ≈90 nm. The critical angle for total external reflection was approximately 0.16° for this SIS copolymer; thus, higher incident angles (0.18°, 0.20°, and 0.22°) were used to probe the full film thickness (0.18° shown here, and data for additional angles are included in the Appendix A). Furthermore, to facilitate interpretation of experimental data, simulations of the

GISAXS intensity on the basis of the distorted-wave Born approximation (DWBA) were performed. These simulations were implemented using an algorithm described elsewhere,[63] and outcomes are reported in Figures 3.5 (b) and (d) for the parallel cylinder and HPL phases, respectively.

The GISAXS data reveal changes in the in-plane symmetry on each surface. Films prepared on benzyl surfaces exhibit in-plane peak positions of 1:2:3, while films prepared on *n*-butyl surfaces exhibit in-plane peak positions of 1:√3:2. The √3 peak is denoted by the black arrow in Figure 3.5 (c) and (d), while the "2" peak is marked by the orange dashed arrow. Line cuts at $\alpha = 0.75°$ are reported in Figure 3.6, and the √3 peak is visible only on the *n*-butyl surface (black arrow). The appearance of a scattering peak at this position is significant, as it indicates a transition from the in-plane "striped" symmetry of parallel cylinders to in-plane hexagonal symmetry. The peak at the "2" position for *n*-butyl surfaces could be the expected √4 peak from hexagonal symmetry, or it could be associated with coexisting parallel cylinders.

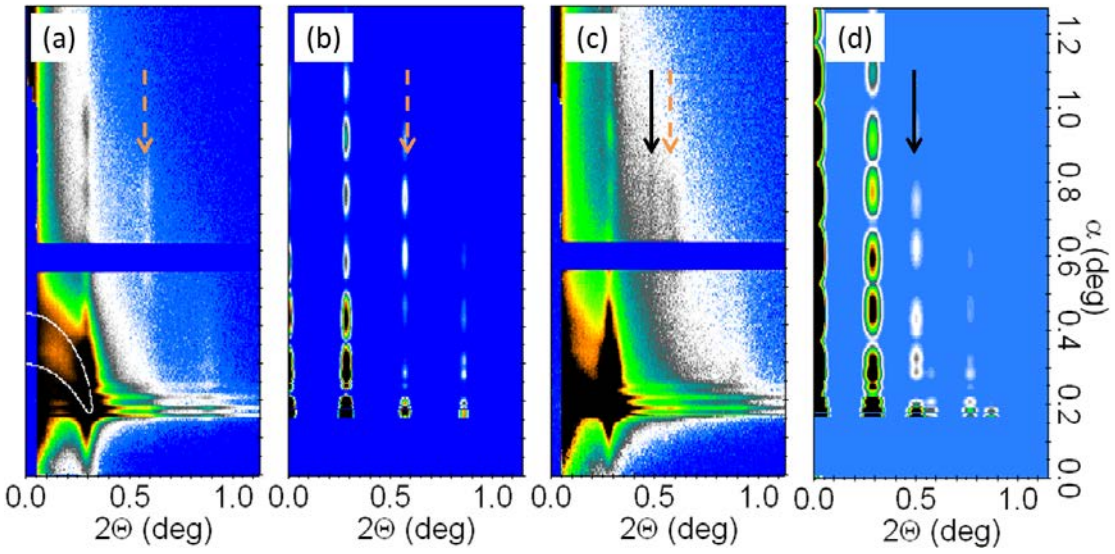

Figure 3.5: (a) Measured GISAXS pattern on benzyl surface; (b) DWBA simulation from ABA stacking of parallel cylinders; (c) Measured GISAXS pattern on *n*-butyl surface; (d) DWBA simulation from ABA stacking of hexagonal perforations. Film thickness was 90 nm, and incidence angle was 0.18° for all cases. Peaks positions corresponding to $\sqrt{3}q^*$ and $2q^*$are marked with black and orange arrows, respectively. Reprinted with permission from Luo M., *et al. Macromolecules* 2013, 46, (5), 1803-1811.

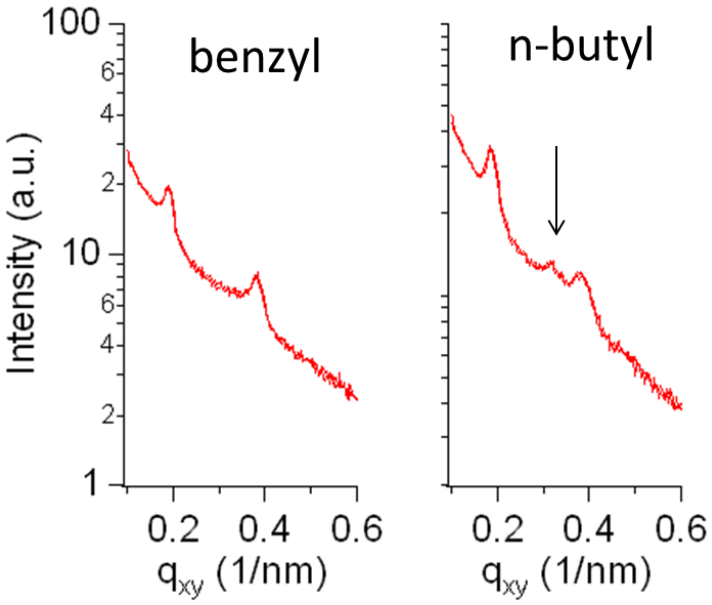

Figure 3.6: In-plane line cuts for films on benzyl and *n*-butyl surfaces (taken at α = 0.75°); q_{xy} denotes the in-plane scattering vector. Arrow denotes the √3 peak for hexagonal symmetry. Reprinted with permission from Luo M., *et al. Macromolecules* 2013, 46, (5), 1803-1811.

The GISAXS data for both systems exhibit elongated Bragg peaks along the q_z axis (or α-axis), typical of scattering from a thin crystal.[63] The fact that out-of-plane Bragg peaks are found indicates that the sample is characterized by a layered morphology, such as ABA or ABC stacking of in-plane hexagonal perforations. Debye-Scherrer rings are detected for films on benzyl surfaces (white contour in Figure 3.5a), but they are less pronounced for films on *n*-butyl surfaces, indicating the latter system has better out-of-plane order. [64] (See Appendix A for comparison at other angles of incidence.) Similar behavior has been reported in other studies that compare GISAXS data for parallel cylinders and HPL phases.[65] The *d*-spacing for the *n*-butyl sample (HPL) was found ≈4% larger than that for the benzyl sample (parallel

cylinder), which is consistent with other literature studies on the transformation from cylinders to HPL.[66]

The positions of the Bragg peaks along the q_z axis (or α-axis) are very sensitive to the incident angle α_i and the stacking sequence normal to the substrate.[63] Thus, the experimental GISAXS patterns were compared with the DWBA simulations for ABA stacking of parallel cylinders and hexagonal perforations. Figure 3.5 reports the comparison at an incident angle of 0.18°, and the Appendix A includes the comparison for incident angles of 0.16°, 0.20°, and 0.22°. For parallel cylinders, the DWBA simulation assumes L_0 = 33 nm, cylinder radius of 9 nm, and layer thickness of d = 30 nm. For the HPL phase, the DWBA simulation describes the perforations as vertical cylinders with height and radius of 7 nm and 9 nm, respectively, with L_0 = 38 nm and d = 30 nm.[67] The experimental and simulated scattering patterns were in reasonable agreement for both parallel cylinders and HPL phases, and the layering thickness was preserved through the transition. From these simulations, the "2" peak on *n*-butyl surfaces likely was associated with ABA stacking of cylinders (the second-order peak for this structure). While the predicted scattering intensity for the √4 HPL peak is weak due to a minimum in the form factor, the predicted location along the α-axis does not match the experimental data. Considering what is known about the order-order transition from cylinders to HPL, it is not surprising that the scattering from HPL symmetry is weak and reflects a "residual" ABA cylindrical symmetry: The cylinder-to-HPL transformation is driven by fluctuations that merge the (10) cylinders into perforated sheets, thus the process does not directly generate ordered hexagonal domains.[66, 68] Therefore, compared to other order-order transitions, the formation of a HPL phase with long-range in-plane hexagonal symmetry and a well-defined out-of-

plane stacking sequence is very slow.[66] Additionally, the GISAXS data for the HPL samples were compared to the simulations of an ABC stacking sequence, and no agreement was found between the experiments and simulations. These data are included in Appendix A.

3.3.2 Uniform Thickness Films on Gradient Monolayer Substrates

Gradient monolayers were created using a vapor deposition device as described by Albert *et al*.[28, 69] The specific setup employed in this work consisted of one benzyl silane reservoir (19.0 mm in diameter) and one *n*-butyl silane reservoir (3.2 mm in diameter) on either end of a cleaned silicon wafer (60 mm in length). Following deposition for 4 h, the gradient monolayer showed the expected changes in diiodomethane and water contact angles with position (Figure 3.7a-b). The combined contact angle measurements indicated that a surface gradient had been successfully generated with primarily benzyl silane on one end and primarily *n*-butyl silane at the other (note: the reported contact angles for the gradient monolayer were averaged over five gradient substrates with eleven spots spaced every 5 mm on each substrate). The surface energy, calculated using the Owens-Wendt method,[45] decreased across the substrate from the benzyl silane end to the *n*-butyl silane end (40 mJ/m^2 to 32 mJ/m^2). Additionally, surface chemistry composition was deduced from a correlation between diiomethane contact angle and *n*-butyl silane molar composition, utilizing Albert and coworkers' X-ray photoelectron spectroscopy (XPS) studies on gradient substrates.[69] (Note: the data were shifted -2° to account for systematic differences in diiodomethane contact angle measurements on the pure component monolayer surfaces.) The gradient monolayer showed a nearly linear profile in composition, spanning approximately 20 mol % to 80 mol % *n*-butyl silane as shown in Figure 3.7.

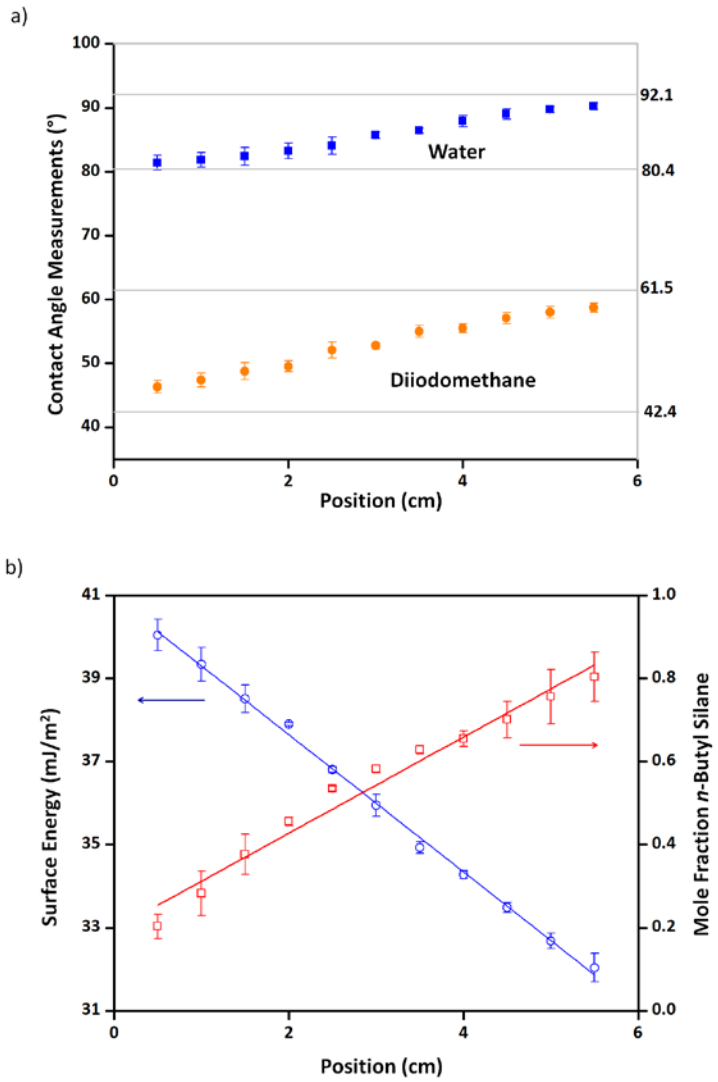

Figure 3.7: (a) Contact angle measurements of diiodomethane (orange circles) and water (blue squares) for gradient monolayer. Contact angle measurements for pure component surfaces are provided as a baseline. (b) Surface energy (blue circles) and surface composition (red squares) across the gradient substrate. The error bars in (a) and (b) represent the standard deviations of the measurements. Reprinted with permission from Luo M., *et al. Macromolecules* 2013, 46, (5), 1803-1811.

A uniform thickness film (90 nm, 3.33 *d*) was flow coated onto the gradient monolayer surface described in Figure 3.7. The film was thermally annealed and then examined using optical microscopy and AFM. The optical images showed a featureless surface, as the film thickness was only moderately incommensurate with *d*. The substrate effect on the nanostructures of SIS films is shown in the AFM images in Figure 3.8. The morphology transitioned from parallel cylinders on the benzyl silane end to HPL on the *n*-butyl silane end, in agreement with the single-component substrate experiments. An in-house JAVA program (see more detail in Appendix A) was utilized to quantify the ratio of HPL to parallel cylinders across the gradient, which showed an increasing degree of HPL structure as one moves from the benzyl silane end to the *n*-butyl silane end (Figure 3.8). Using this gradient monolayer allows for quick examination of the substrate surface effects on the film morphology. A HPL window was identified from ≈76% *n*-butyl silane to pure *n*-butyl silane, a parallel cylinder window was identified from (0% *n*-butyl silane) pure benzyl silane to ≈28% *n*-butyl silane, whereas mixed nanostructures were noted between these substrate surface composition windows. These results highlight the use of monolayer substrate surface chemistry gradients to manipulate nanostructure in the SIS system.

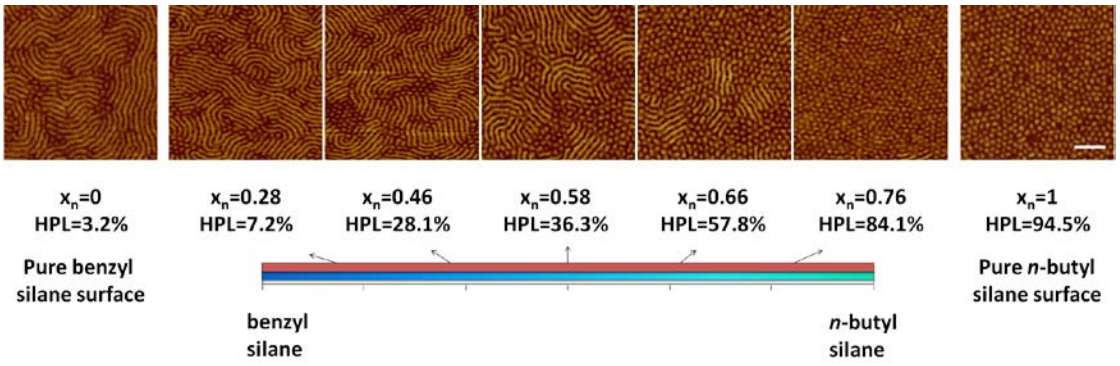

Figure 3.8: AFM phase images of an SIS film coated on top of the gradient monolayer following thermal annealing; the film thickness is 90 ± 1 nm. AFM phase images of SIS films on pure benzyl silane and pure *n*-butyl silane surfaces also are included for comparison. Parallel cylinders were found near the benzyl silane end with a transition to HPL noted as the *n*-butyl silane composition on the substrate increases. The molar surface composition of *n*-butyl silane (x_n) and the ratio of HPL to parallel cylinders (given as percentage of HPL) are provided for reference at the bottom of each image. Scale bar is 200 nm and applies to all images. Reprinted with permission from Luo M., *et al. Macromolecules* 2013, 46, (5), 1803-1811.

3.4 Conclusions

This chapter demonstrates the ability to control the SIS thin film nanostructures using substrate surface energy/chemistry and film thickness gradients. This combinatorial approach with film thickness and monolayer surface chemistry gradients is feasible for screening new materials and identifying conditions to obtain the desired morphologies in a myriad of systems, as the substrate surface chemistry and film thickness gradients are easily tuned. One major endeavor in our research group is developing interfacially-modified (tapered) diblock and triblock copolymer systems, with a specific focus on network-forming materials. The stabilization of network structures strongly depends on the surface conditions and film thickness commensurability. These gradient tools will facilitate the nanoscale network

formation in tapered diblock and triblock copolymer thin film systems. Control of nanostructure ordering is further discussed in Chapter 4.

REFERENCES

1. Segalman, R. A.; Yokoyama, H.; Kramer, E. J. *Adv. Mater.* **2001,** 13, (15), 1152-1155.

2. Yang, X. M.; Peters, R. D.; Nealey, P. F.; Solak, H. H.; Cerrina, F. *Macromolecules* **2000,** 33, (26), 9575-9582.

3. Urade, V. N.; Wei, T.-C.; Tate, M. P.; Kowalski, J. D.; Hillhouse, H. W. *Chem. Mater.* **2007,** 19, (4), 768-777.

4. Crossland, E. J. W.; Kamperman, M.; Nedelcu, M.; Ducati, C.; Wiesner, U.; Smilgies, D. M.; Toombes, G. E. S.; Hillmyer, M. A.; Ludwigs, S.; Steiner, U.; Snaith, H. J. *Nano Lett.* **2008,** 9, (8), 2807-2812.

5. Olson, D. A.; Chen, L.; Hillmyer, M. A. *Chem. Mater.* **2007,** 20, (3), 869-890.

6. Yang, S. Y.; Ryu, I.; Kim, H. Y.; Kim, J. K.; Jang, S. K.; Russell, T. P. *Adv. Mater.* **2006,** 18, (6), 709-712.

7. Albert, J. N. L.; Epps, T. H., III. *Materials Today* **2010,** 13, (6), 24-33.

8. Segalman, R. A. *Materials Science and Engineering: R: Reports* **2005,** 48, (6), 191-226.

9. Fasolka, M. J.; Mayes, A. M. *Annu. Rev. Mater. Res.* **2001,** 31, (1), 323-355.

10. Epps, T. H., III; DeLongchamp, D. M.; Fasolka, M. J.; Fischer, D. A.; Jablonski, E. L. *Langmuir* **2007,** 23, (6), 3355-3362.

11. Smith, A. P.; Douglas, J. F.; Meredith, J. C.; Amis, E. J.; Karim, A. *Phys. Rev. Lett.* **2001,** 87, (1), 015503.

12. Smith, A. P.; Sehgal, A.; Douglas, J. F.; Karim, A.; Amis, E. J. *Macromol. Rapid Commun.* **2003,** 24, (1), 131-135.

13. Matsen, M. W. *J. Chem. Phys.* **1997,** 106, (18), 7781-7791.

14. Mansky, P.; Russell, T. P.; Hawker, C. J.; Pitsikalis, M.; Mays, J. *Macromolecules* **1997,** 30, (22), 6810-6813.

15. Forrey, C.; Yager, K. G.; Broadaway, S. P. *ACS Nano* **2011,** 5, (4), 2895-2907.

16. Peters, R. D.; Yang, X. M.; Kim, T. K.; Nealey, P. F. *Langmuir* **2000,** 16, (24), 9620-9626.

17. Khanna, V.; Cochran, E. W.; Hexemer, A.; Stein, G. E.; Fredrickson, G. H.; Kramer, E. J.; Li, X.; Wang, J.; Hahn, S. F. *Macromolecules* **2006,** 39, (26), 9346-9356.

18. Han, E.; Stuen, K. O.; La, Y.-H.; Nealey, P. F.; Gopalan, P. *Macromolecules* **2008,** 41, (23), 9090-9097.

19. Ji, S.; Liu, C.-C.; Son, J. G.; Gotrik, K.; Craig, G. S. W.; Gopalan, P.; Himpsel, F. J.; Char, K.; Nealey, P. F. *Macromolecules* **2008,** 41, (23), 9098-9103.

20. Karim, A.; Singh, N.; Sikka, M.; Bates, F. S.; Dozier, W. D.; Felcher, G. P. *J. Chem. Phys.* **1994,** 100, (2), 1620-1629.

21. Radzilowski, L. H.; Carvalho, B. L.; Thomas, E. L. *J. Polym. Sci., Part B: Polym. Phys.* **1996,** 34, (17), 3081-3093.

22. Cavicchi, K. A.; Russell, T. P. *Macromolecules* **2007,** 40, (4), 1181-1186.

23. Konrad, M.; Knoll, A.; Krausch, G.; Magerle, R. *Macromolecules* **2000,** 33, (15), 5518-5523.

24. Zhang, Q.; Tsui, O. K. C.; Du, B.; Zhang, F.; Tang, T.; He, T. *Macromolecules* **2000,** 33, (26), 9561-9567.

25. Niihara, K.; Sugimori, H.; Matsuwaki, U.; Hirato, F.; Morita, H.; Doi, M.; Masunaga, H.; Sasaki, S.; Jinnai, H. *Macromolecules* **2008,** 41, (23), 9318-9325.

26. Knoll, A.; Horvat, A.; Lyakhova, K. S.; Krausch, G.; Sevink, G. J. A.; Zvelindovsky, A. V.; Magerle, R. *Phys. Rev. Lett.* **2002,** 89, (3), 035501.

27. Knoll, A.; Magerle, R.; Krausch, G. *J. Chem. Phys.* **2004,** 120, (2), 1105-1116.

28. Albert, J. N. L.; Baney, M. J.; Stafford, C. M.; Kelly, J. Y.; Epps, T. H., III. *ACS Nano* **2009,** 3, (12), 3977-3986.

29. Xu, J.; Russell, T. P.; Ocko, B. M.; Checco, A. *Soft Matter* **2011,** 7, (8), 3915-3919.

30. Han, E.; Stuen, K. O.; Leolukman, M.; Liu, C.-C.; Nealey, P. F.; Gopalan, P. *Macromolecules* **2009,** 42, (13), 4896-4901.

31. Ji, S.; Liu, C.-C.; Liao, W.; Fenske, A. L.; Craig, G. S. W.; Nealey, P. F. *Macromolecules* **2011,** 44, (11), 4291-4300.

32. Huinink, H. P.; van Dijk, M. A.; Brokken-Zijp, J. C. M.; Sevink, G. J. A. *Macromolecules* **2001,** 34, (15), 5325-5330.

33. Tsarkova, L.; Knoll, A.; Krausch, G.; Magerle, R. *Macromolecules* **2006,** 39, (10), 3608-3615.

34. Ryu, D. Y.; Shin, K.; Drockenmuller, E.; Hawker, C. J.; Russell, T. P. *Science* **2005,** 308, (5719), 236-239.

35. Park, D.-H. *Nanotechnology* **2007,** 18, (35), 355304.

36. Sohn, B.; Yun, S. *Polymer* **2002,** 43, (8), 2507-2512.

37. Niemz, A.; Bandyopadhyay, K.; Tan, E.; Cha, K.; Baker, S. M. *Langmuir* **2006,** 22, (26), 11092-11096.

38. Liu, P.-H.; Thébault, P.; Guenoun, P.; Daillant, J. *Macromolecules* **2009,** 42, (24), 9609-9612.

39. Matsen, M. W.; Thompson, R. B. *J. Chem. Phys.* **1999,** 111, (15), 7139-7146.

40. Szamel, G.; Muller, M. *J. Chem. Phys.* **2003,** 118, (2), 905-913.

41. Albert, J. N. L.; Bogart, T. D.; Lewis, R. L.; Beers, K. L.; Fasolka, M. J.; Hutchison, J. B.; Vogt, B. D.; Epps, T. H., III. *Nano Lett.* **2011,** 11, (3), 1351-1357.

42. Albert, J. N. L.; Young, W.-S.; Lewis, R. L.; Bogart, T. D.; Smith, J. R.; Epps, T. H., III. *ACS Nano* **2011,** 6, (1), 459-466.

43. Seppala, J. E.; Lewis, R. L., III; Epps, T. H., III. *ACS Nano* **2012,** 6, (11), 9855-9862.

44. Brandrup, J.; Immergut, E. H.; Grulke, E. A., *Polymer Handbook*. 4th ed.; Wiley: New York, 1999.

45. Owens, D. K.; Wendt, R. C. *J. Appl. Polym. Sci.* **1969,** 13, (8), 1741-1747.

46. Clint, J. H.; Wicks, A. C. *Int. J. Adhes. Adhes.* **2001,** 21, (4), 267-273.

47. Stafford, C. M.; Roskov, K. E.; Epps, T. H., III; Fasolka, M. J. *Rev. Sci. Instrum.* **2006,** 77, (2), 023908.

48. Brandrup, J. I., E. H.; Grulke, E. A., *Polymer Handbook*. Wiley: 1999.

49. Tsui, O. K. C.; Russell, T. P., *Polymer Thin Films*. World Scientific: 2008.

50. Mansky, P.; Russell, T. P. *Macromolecules* **1995,** 28, (24), 8092-8095.

51. Mansky, P.; Russell, T. P.; Hawker, C. J.; Mays, J.; Cook, D. C.; Satija, S. K. *Phys. Rev. Lett.* **1997,** 79, (2), 237-240.

52. Lammertink, R. G. H.; Hempenius, M. A.; Vancso, G. J.; Shin, K.; Rafailovich, M. H.; Sokolov, J. *Macromolecules* **2001,** 34, (4), 942-950.

53. Jeong, U.; Ryu, D. Y.; Kho, D. H.; Lee, D. H.; Kim, J. K.; Russell, T. P. *Macromolecules* **2003,** 36, (10), 3626-3634.

54. Knoll, A.; Tsarkova, L.; Krausch, G. *Nano Lett.* **2007,** 7, (3), 843-846.

55. Tsarkova, L.; Sevink, G.; Krausch, G. *Adv. Polym. Sci.* **2010,** 227, 33-73.

56. Koneripalli, N.; Singh, N.; Levicky, R.; Bates, F. S.; Gallagher, P. D.; Satija, S. K. *Macromolecules* **1995,** 28, (8), 2897-2904.

57. Lambooy, P.; Russell, T. P.; Kellogg, G. J.; Mayes, A. M.; Gallagher, P. D.; Satija, S. K. *Phys. Rev. Lett.* **1994,** 72, (18), 2899-2902.

58. Matsen, M. W. *Macromolecules* **2010,** 43, (3), 1671-1674.

59. Note: UVO etching experiment also was performed on an 87 nm thick SIS film on *n*-butyl silane substrate. The results show that the parallel cylinder structures existed throughout the thickness of the film, eliminating the possibility of an underlying HPL structure.

60. Two PS perforated layers are noted in the TEM image. The first layer close to the substrate was clearest, but the contrast decreased as the film approached to the air surface. The loss of contrast likely was from the shadowing of the Pt protection layer. The smaller cross sectional film thickness (≈60 nm) also suggests that part of the film was hidden under the Pt layer.

61. Park, I.; Park, S.; Park, H.-W.; Chang, T.; Yang, H.; Ryu, C. Y. *Macromolecules* **2006,** 39, (1), 315-318.

62. Huinink, H. P.; Brokken-Zijp, J. C. M.; van Dijk, M. A.; Sevink, G. J. A. *J. Chem. Phys.* **2000,** 112, (5), 2452-2462.

63. Stein, G. E.; Kramer, E. J.; Li, X.; Wang, J. *Macromolecules* **2007,** 40, (7), 2453-2460.

64. Vu, T.; Mahadevapuram, N.; Perera, G. M.; Stein, G. E. *Macromolecules* **2011,** 44, (15), 6121-6127.

65. Lee, B.; Park, I.; Yoon, J.; Park, S.; Kim, J.; Kim, K.-W.; Chang, T.; Ree, M. *Macromolecules* **2005,** 38, (10), 4311-4323.

66. Lai, C.; Loo, Y.-L.; Register, R. A.; Adamson, D. H. *Macromolecules* **2005,** 38, (16), 7098-7104.

67. Note: the interlayer spacing for GISAXS simulation was slightly different from the value determined by AFM (Figure 3.2). This difference was attributed to the distortion of unit cell in thin film geometry (reference 54), as the AFM only revealed the layer at the free surface.

68. Laradji, M.; Shi, A.-C.; Noolandi, J.; Desai, R. C. *Macromolecules* **1997,** 30, (11), 3242-3255.

69. Albert, J. N. L.; Kim, J. D.; Stafford, C. M.; Epps, T. H., III. *Rev. Sci. Instrum.* **2011,** 82, (6), 065103.

70. Lewis, R. The Effect of Morphology in Block Copolymer Thin Films on Stem Cell Differentiation and Fate. University of Delaware, 2013.

Chapter 4

MACROSCOPIC ALIGNMENT OF CYLINDRICAL BLOCK POLYMER THIN FILMS

In this chapter, an incredibly simple, yet highly effective method to achieve macroscopic alignment of nanostructures in block polymer (BP) thin films was demonstrated through the application of raster solvent vapor annealing combined with a soft shear field (RSVA-SS). This method substantially improves on previous alignment approaches by using simple solvent vapor annealing apparatus and a PDMS elastomer pad to unlock an array of alignment patterns with a variety of self-assembling polymers and provides feasibility and flexibility for practical industrial production. The unique ability to directly write macroscopic patterns with microscopically aligned BP nanostructures will open new avenues of applied research in nanotechnology. Text and figures are reproduced and adapted with permission from Luo, M.; Scott, D. M.; Epps, T. H. *ACS Macro Letters* 2015, 4, (5), 516-520.

4.1 Introduction

Control of the BP thin film nanostructures, domain orientation, and domain ordering are crucial when realizing their great potential applicability in various fields of materials chemistry and nanotechnology such as patterning semiconductors, fabricating ultra-dense arrays of metal nanowires, and templating magnetic storage media.[1-13] As discussed in chapter 3, the BP thin film nanostructures can be manipulated by modifying the substrate interaction and changing the film thickness. However, the progress in the widespread adoption of BPs for emerging

nanotechnologies has been impeded by the lack of a versatile and efficient technique for inducing the long-range order and orientation of nanostructures in a predetermined direction, as the BPs tend to self-assemble in an isotropic manner in the absence of surface forces and external fields.[14-16] Chapter 1 Section 1.4 describes some of the most commonly used techniques to direct the self-assembly in BP thin films with different degrees of success. For example, graphoepitaxy creates single-crystalline ordered structures, but the required substrate prepatterning can limit the size of the arrays that can be fabricated.[17, 18] Additionally, valuable substrate area is lost due to patterning. Chemical prepatterning can direct BP alignment over large areas, but it requires substrate modification at the nanometer scale; this process can be prohibitively slow.[19, 20] Electric fields, magnetic fields, and polarized light also have been explored but are limited to specialized polymer systems.[21-23] To address these above limitations, researchers are devoted to developing new and more universal methods to efficiently direct BP self-assembly on template-free substrates through cost-effective means.

Shear fields are an established means of aligning BPs in bulk and is in principle not limited to any particular BP systems and morphologies.[24-29] Shear process could be performed in various forms such as elongation flow, oscillatory shear, and roll-casting. The response to shear originates from differences in the mechanical properties or viscoelasticity of the BP domains, and microstructure alignment under shear tends to minimize viscous dissipation and chain mixing. In other words, the polymer chains orient to a direction that minimizes the work done during shear flow and reduces chain mixing due to deformation of the microstructures. Thus, lamellae and cylinders often are found to align parallel to the shear flow

direction. However, alignment in other directions also was reported in the literatures depending on shear parameters (shear rate, amplitude, and frequency) and polymer properties (see Appendix B for schematic representation of possible orientations of lamellae and cylinders).

Register and Chaikin first employed shear fields to align single layer BP thin films (~30 nm).[30, 31] In these works, shear stress was applied by the deformation and displacement of a cross-linked poly(dimethylsiloxane) (PDMS) pad placed on top of a cylinder-forming BP thin film, and the BP domain orientation was correlated strongly with the shear direction after thermal annealing under shear for an hour.[30] This technique could be modified easily for larger or smaller areas by changing the size of the elastomer pad. However, the alignment quality degraded quickly as the BP film thickness deviated from a single domain spacing.[30] Additionally, this batch processing method is potentially slow in comparison to the few minutes ideal for alignment for many applications.

Recently, other techniques have been combined with shear fields to facilitate alignment in BP thin films.[32-34] Karim *et al.* employed a moving temperature gradient in conjunction with shear, termed cold zone annealing-soft shear (CZA-SS).[32] In the case of CZA-SS, an elastomeric PDMS layer was placed on top of the BP film and undergoes directional expansion and contraction due to a dynamic thermal field, thereby imposing an oscillatory shear field on the underlying BP film. Using this process, horizontally-aligned BP cylinders were fabricated continuously in films over a wide thickness range of 40-1000 nm at industrially relevant speeds of v = 12 mm/min (*i.e.*, 200 μm/s). However, this process required high annealing temperatures, well above the glass transition temperature (T_g) of the BP to enable chain mobility,

and only was applicable to BPs with an accessible $T_g << T_{ODT}$ (order-disorder transition temperature). More recently, Jung and co-workers demonstrated that unidirectional alignment of BP cylinders could be produced by solvent vapor annealing (SVA) partnered with shear.[35] A solvent–containing PDMS pad was placed on top of a BP film, and shear alignment was accomplished by the movement of the PDMS pad across the film surface. The solvent vapor effectively decreases the T_g of the BP and imparts mobility to the polymer chains, thus making this approach readily applicable to a vast array of BPs.[36] Cavicchi, Vogt, and co-workers further showed alignment of BP thin films using a flow chamber annealing method (solvent flow in/out a chamber).[33, 37, 38] The nanostructure alignment was found to be induced primarily by contraction of the PDMS pad during solvent removal. However, the resulting alignment depended strongly on the shape and placement of the PDMS pad, and this method is not directly amenable to continuous processing.

Herein, raster solvent vapor annealing with soft shear (RSVA-SS) was developed to achieve macroscopic alignment of BP cylinders. Spatial control over nanoscale structures was accomplished through the implementation of a solvent vapor delivery nozzle and motorized stage. In this manner, macroscopic patterns of nanoscale features could be "written" in a controlled fashion into the BP thin film. Some complex patterns such as dashes, crossed lines, and curves can be imparted easily to thin films on featureless and untreated substrates. This method significantly improves on previous approaches by eliminating the correlation between the BP alignment and PDMS shape, allowing continuous fabrication of highly ordered BP cylinder patterns in a two-dimensional manner. This advance makes the RSVA-SS

approach more attractive for the industrial production of hierarchically-patterned BP nanostructures.

4.2 Materials and Methods

4.2.1 Materials

Poly(styrene-*b*-isoprene-*b*-styrene) (SIS) films were flow coated onto the silicon substrates as described in Chapter 3, and all of the films used in this chapter were ≈90 nm in thickness.

The elastomer pad was prepared from polydimethylsiloxane (PDMS, Dow Corning Sylgard 184) at 10:1 w/w ratio of base to curing agent. The mixture of base and curing agents were stirred vigorously for 5 min, followed by degassing in a desiccator for 30 min until no bubbles were formed. Then the mixture was spread into a plastic dish and cured in an oven at 80 °C for 2 h. The thickness of the PDMS pad was approximately 0.3 mm, controlled by the amount of PDMS and the diameter of the plastic dish. After curing, the PDMS was allowed to cool down to room temperature slowly before being peeled off from the plastic dish.

4.2.2 Raster Solvent Vapor Annealing and Soft Shear

A schematic of RSVA-SS is shown in Figure 4.1. In this case, N_2 gas (25 mL min^{-1}) was bubbled through liquid toluene to produce a solvent-rich vapor stream. An unpatterned elastomer pad (PDMS) was laminated onto the SIS film conformally. Then, toluene vapor was directed onto the film using a nozzle. As an example, the nozzle was constructed from a ground-flat 21-gauge hypodermic needle (0.8 mm in diameter) attached to a vertical micrometer stage set 0.2 mm above the PDMS surface. The width of the rastering area was ≈4 mm and could be tuned by changing solvent

flow rate, nozzle diameter, and needle height. The substrate-supported films were affixed to a programmable motorized stage to control the rastering speed and position. The rastering speed was 10 μm/s for the experiments performed in this chapter, unless specified otherwise. The scale-up flat nozzle was custom-built using aluminum and had two inlets for solvent vapor; the slit opening had a dimension of 5 cm × 1 mm.

4.2.3 Characterization techniques

The elastomeric capping layer was removed easily after RSVA-SS without damaging the BP film. Nanostructure formation and orientation was assessed by atomic force microscopy (AFM) on a Bruker Veeco Dimension 3100 operating in tapping mode. AFM images were taken in the center of the annealed area along the rastering direction, but the quality of alignment/orientation did not degrade until the very edge of the rastered area. Optical microscopy images were collected on a Nikon microscope equipped with a 5 MP CCD camera (Nikon Eclipse LV100).

4.3 Results and Discussion

4.3.1 Pattern versatility

The results of single RSVA-SS passes that were horizontal, vertical and diagonal to the rectangular PDMS pad are shown in Figure 4.1. A typical dimension of PDMS pad was 20 mm × 10 mm × 0.3 mm, rastering speed was 10 μm/s. The alignment of cylindrical domains in the SIS films was correlated strongly to the rastering direction instead of PDMS shape. This long range ordering of SIS cylinders persisted across the entire area that was rastered by toluene vapor as determined through multiple AFM measurements across the surface. Although only the surface morphology was assessed in this study, the through-thickness nanostructure of films

subjected to soft shear annealing has been investigated previously by grazing incidence small-angle X-ray scattering (GISAXS).[33] In that case, the soft shear process produced highly ordered cylindrical nanostructures over a range of film thickness (40 nm - 1 μm). Similar order through the thickness of the films is expected in this work, given that our film thickness is 90 nm and well within the range of the previous study.

The implementation of a solvent vapor delivery nozzle generated a localized (point) SVA zone in which both the PDMS and BP film were swollen by uptake of the solvent vapor, which plasticized the BP to enhance its mobility and enable domain ordering. Because the film was fixed to the substrate and moved with the motorized stage, an advancing swelling front and receding deswelling front were created. The swelling and deswelling of the PDMS pad produced a soft shear field to align the BP domains, similar in effect to CZA-SS in which shear force is obtained from the thermal expansion and contraction of PDMS. SIS cylinders were aligned with their long-axes parallel to the shear flow direction, suggesting this orientation is more energetic favorable. The polymer chains could "slide" to form long-range order domain structures and minimize the amount of chain mixing (see Appendix B). The rastering speed strongly impacted the solvent swelling and deswelling rates.[39] With the parameters employed in this work, highly oriented cylinders were produced with a rastering speed of 10 μm/s, and the SIS film retained its as cast morphology with a rastering speed of 100 μm/s (see Appendix B). The width of the rastered area was approximately 4 mm for this particular setup with high pattern fidelity except as one approached the edge of the rastered zone (see Appendix B). Because the alignment quality correlates with the swollen ratio of the PDMS pad,[37] the films lose alignment

at the end of the edge of the rastered region. At present, the lack of a step transition between highly aligned and unaligned structures at the edge of the rastered region is a potential shortcoming of RSVA-SS in comparison to graphoepitaxy or chemical prepatterning. The key process variables such as rastering speed, solvent flow rate, nozzle dimension, nozzle height, *etc*. are coupled in their influence on the solvent field, and ultimately, on the swelling ratio of the PDMS pad and the alignment quality of the SIS film. These parameters, together with the physical properties of the PDMS pad (*e.g.*, crosslink density, thickness, *etc*.), will be investigated in detail in future studies.

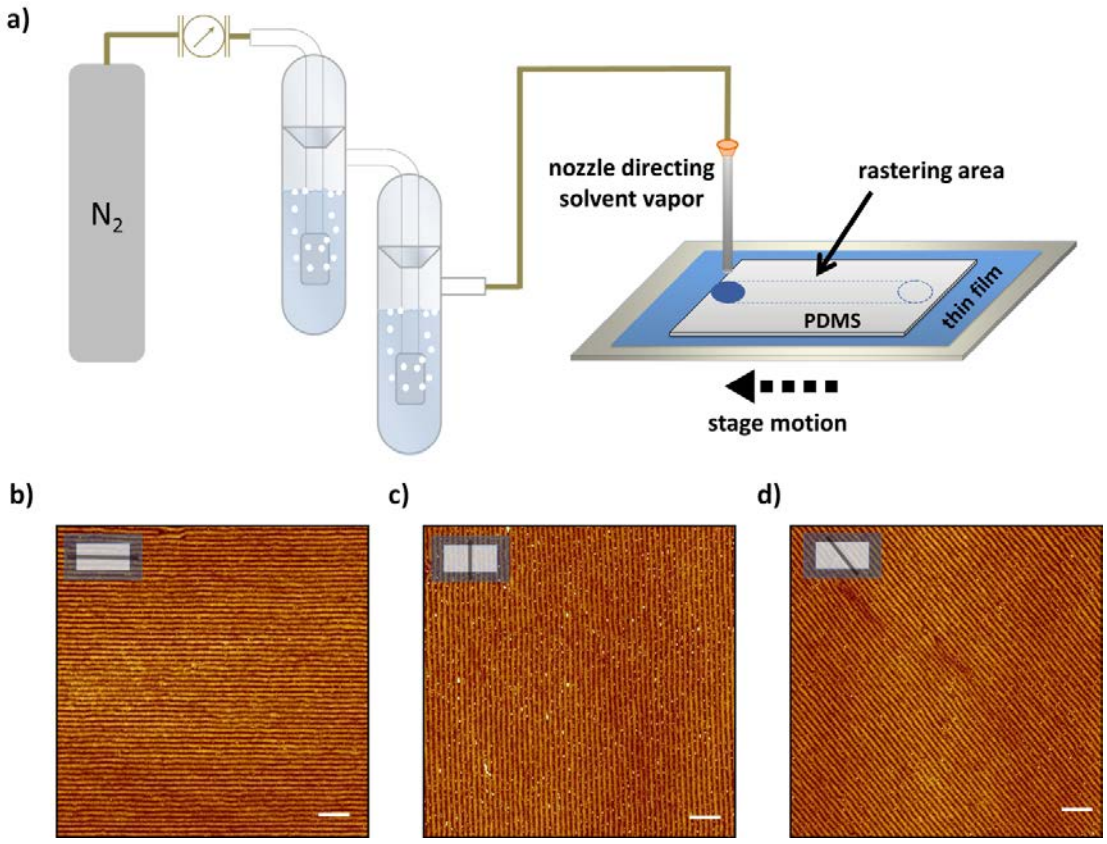

Figure 4.1: (a) Schematic of the RSVA-SS process. (b), (c), and (d) AFM phase images of the SIS thin films treated with RSVA-SS, demonstrating in-plane horizontal, vertical, and diagonal alignment of SIS cylinders. The orientation of the SIS cylinders was correlated strongly with the rastering path as indicated in the inset. Scale bars represent 200 nm. Reprinted with permission from Luo, M.; Scott, D. M.; Epps, T. H. *ACS Macro Letters* 2015, 4, (5), 516-520.

A key feature of the RSVA-SS technique is the ability to produce complex patterns such as dashes, crossed lines, and curved structures as demonstrated in Figure 4.2 and Figure 4.3. First, a dash pattern was achieved by applying alternating slow and fast rastering speeds (10 μm/s *versus* 100 μm/s). The SIS cylinders were strongly aligned in the 'slow' rastered region, as compared to in the 'fast' rastered region where

the cylinders remained disordered due to low solvent uptake. The low uptake of solvent in the 'fast' regions resulted in limited expansion and contraction of the PDMS pad and limited chain mobility in SIS (Figure 4.2a). The borders between the fast and slow raster regions (poor alignment *versus* high alignment) were not as sharp as typically demonstrated by graphoepitaxy or chemical prepatterning. This alignment edge width in RSVA-SS may not be ideal for all applications, and combining RSVA-SS with other available tools might help improve the accuracy of the patterns.[31, 35]

A crossed line pattern, was produced by rastering a line pattern, changing the raster direction, and rastering a second (orthogonal) line pattern. In this case, a new PDMS pad was used for each pass because the shape of the PDMS pad did not fully recover after deswelling. In Figure 4.2b, the alignment of the SIS cylinders was overridden by the second rastering pass in the coincident region, suggesting RSVA-SS can direct BP cylinders independent of any preexisting orientation, and a single BP thin film can be patterned multiple times. This facile, independent, and reusable patterning strategy is important for practical applications with BPs and, to our knowledge, is not achievable with other methods. Edge effects similar to those found in the dash pattern were present in the crossed line patterns as well; the use of other available tools may lead to the potential fabrication of well-defined structures such as T-junctions and nanosquare arrays.[31, 35]

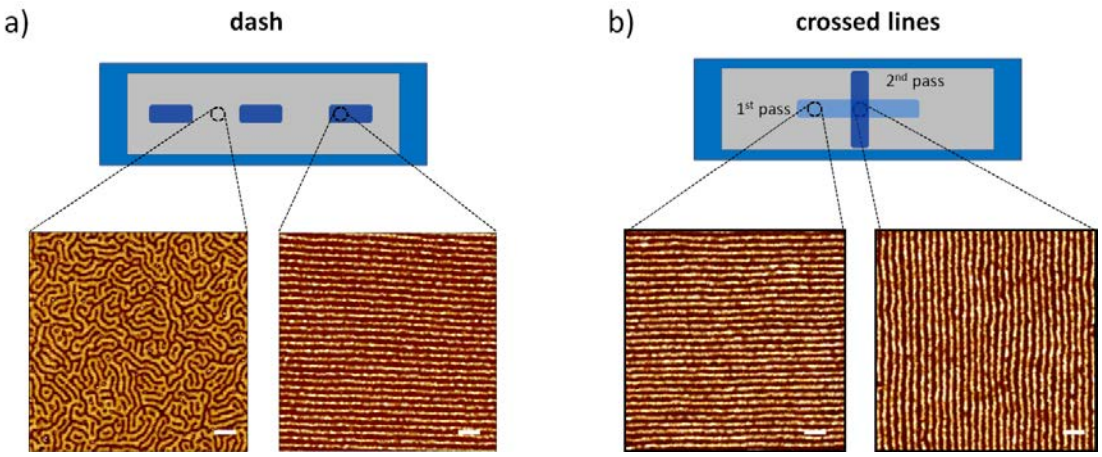

Figure 4.2: AFM phase images (a) dash pattern**.** The macroscopic dashes were spaced 5 mm apart, and the speeds for the 'fast' and 'slow' rastered regions were 100 μm/s and 10 μm/s, respectively. (b) Crossed line pattern. The SIS thin film was exposed to two orthogonal RSVA-SS linear pattern steps. Scale bars represent 100 nm for all AFM images. Reprinted with permission from Luo, M.; Scott, D. M.; Epps, T. H. *ACS Macro Letters* 2015, 4, (5), 516-520.

Versatile patterns could be achieved by using a two-dimensional motorized stage. A macroscopic "UD" pattern was demonstrated in Figure 4.3, which contained SIS cylinders that were microscopically aligned along the local shear direction. Again, this ability to "write" ordered BP nanostructures freely on pattern-free substrates based on the spatiotemporal swelling/deswelling of a PDMS pad offers unique advantages over conventionally patterning methods due to its simplicity and efficiency. The font size of the patterns could be tuned easily by the programmable stage and nozzle dimension, allowing controlled pattern formation in an on-demand fashion for practical use in various applications.

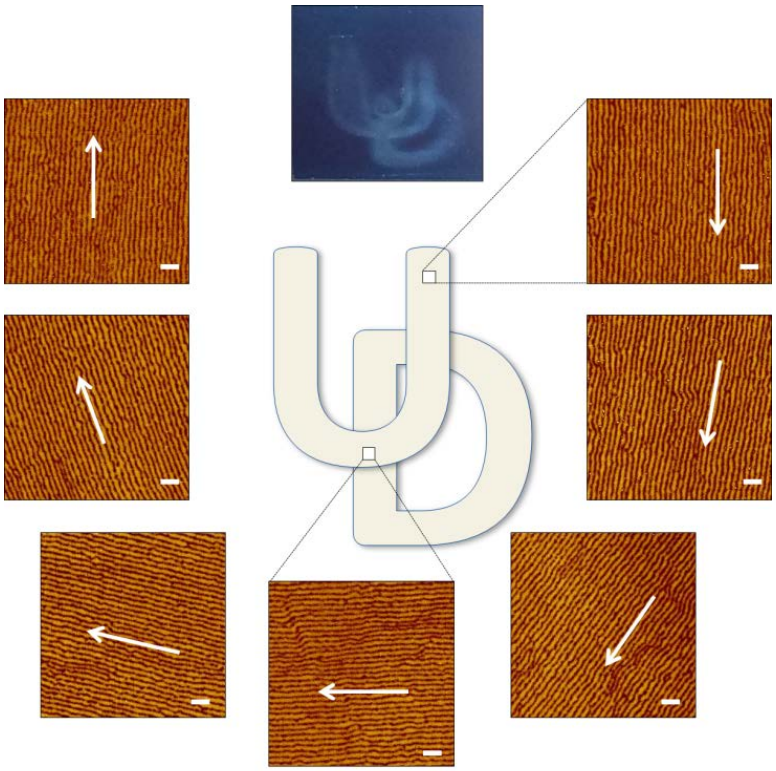

Figure 4.3: UD pattern. A UD pattern (top) was visible due to the shear effect (optical image with enhanced contrast). The SIS domains were aligned along the local shear direction as shown in the AFM phase images. Arrows indicate direction of raster. Font size was 10 mm. Scale bars represent 100 nm for all AFM images. Reprinted with permission from Luo, M.; Scott, D. M.; Epps, T. H. *ACS Macro Letters* 2015, 4, (5), 516-520.

4.3.2 Erase-rewrite capability

A second key feature of RSVA-SS is that the aligned BP pattern could be erased easily by a simple 'bell jar' SVA treatment (Figure 4.4). Upon solvent removal from a film swollen to ~160% of the original film thickness, the film morphology was poorly ordered, similar to the as-cast morphology, and allowed for repatterning. Additionally, the nanopatterns could be erased locally by taking advantage of the

RSVA process alone.[39] This erase and rewrite capability affords additional advantages over conventional patterning methods such as graphoepitaxy and chemical prepatterning.

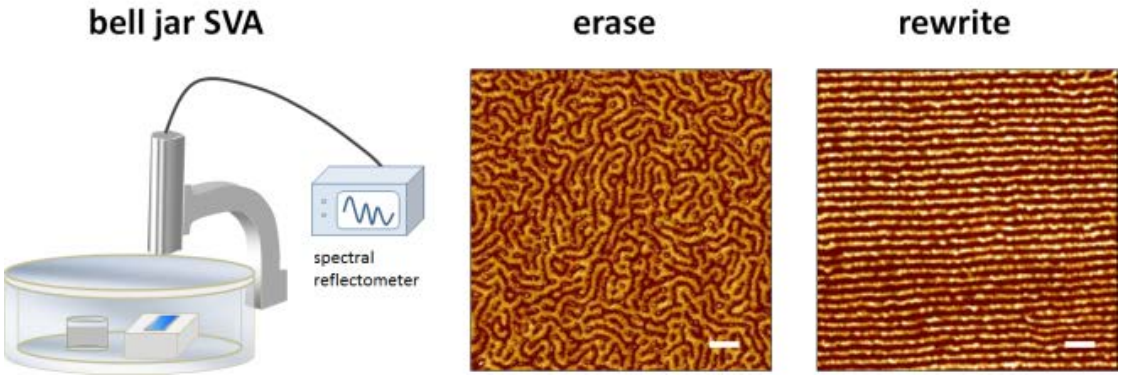

Figure 4.4: Erase-rewrite process. Aligned SIS domains became poorly ordered (middle AFM phase image) after a 'bell jar' SVA treatment and were re-aligned by RSVA-SS (right AFM phase image). Scale bars represent 100 nm for all AFM images. Reprinted with permission from Luo, M.; Scott, D. M.; Epps, T. H. *ACS Macro Letters* 2015, 4, (5), 516-520.

4.3.3 Scalability

Another exciting aspect of RSVA-SS is its scalability for industrial production. For example, a flat nozzle with a slit opening of dimension 5 cm × 1 mm (Figure 4.5) was fabricated. Two inlets for solvent vapor stream, along with a graded opening, allowed the solvent to distribute uniformly through the thin slit. After the RSVA-SS process, multiple locations were examined by AFM and indicated a high degree of orientational ordering in the direction of the RSVA-SS, and this ordering persisted across the entire area exposed to the process. The RSVA-SS approach provides a

feasible and scalable pathway to fabricate highly ordered BP cylinders at relatively high speed (mm/min) over unlimited dimensions.

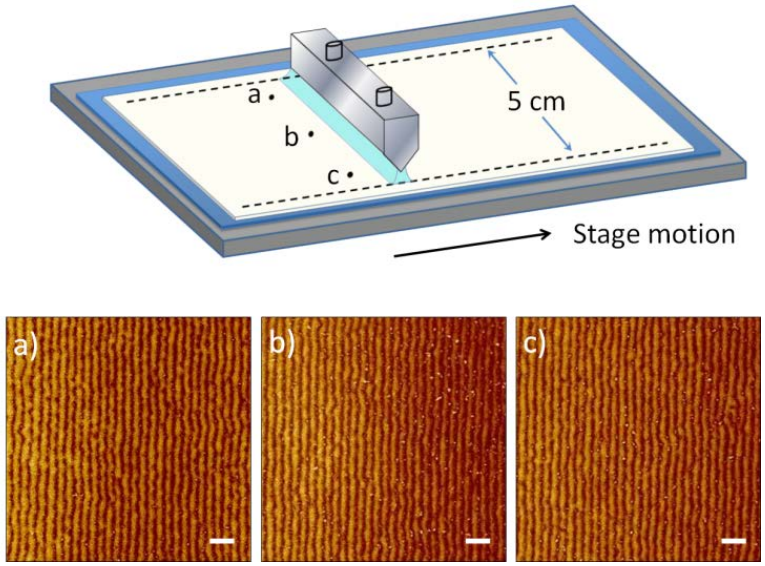

Figure 4.5: Large-scale production of highly ordered cylinders. High quality of alignment in the rastering direction are demonstrated in the AFM phase images of SIS thin film at different locations (a and c were 0.5 mm from the nozzle edge, b was in the center of the film). Scale bars correspond to 100 nm. Reprinted with permission from Luo, M.; Scott, D. M.; Epps, T. H. *ACS Macro Letters* 2015, 4, (5), 516-520.

4.4 Conclusion

In summary, a directed self-assembly method termed RSVA-SS was developed to fabricate oriented BP cylinders on pattern-free substrates. The simplicity of the apparatus and the versatility of patterns are demonstrated. The unique ability to directly write macroscopic patterns with microscopically aligned BP nanostructures will unlock new avenues of applied research in nanotechnology and pave the way toward practical industrial use of hierarchically-patterned BP nanostructures.

Additionally, the capability to erase and rewrite the patterns affords advantages over conventional patterning methods such as graphoepitaxy and chemical prepatterning. Furthermore, the ability to expand or shrink the "writing" size of the oriented regions from millimeters to centimeters (decoupled from the size of the PDMS pad) provides a unique handle for manipulating pattern formation in an on-demand fashion.

At present, the lack of resolution and pattern fidelity at the transition region between highly aligned and unaligned structures is a major shortcoming of RSVA-SS in comparison to graphoepitaxy or chemical prepatterning. To address this problem, photolithography was used to create high resolution patterns on the PDMS pad. These patterns define the area where the BP thin film nanostructures are controlled by the RSVA-SS process, and a sharp interface between aligned and unaligned regions is envisioned. The efforts of fabricating industrial-relevant structures such as T-junctions will be discussed in Chapter 7.

Finally, researchers have devoted significant efforts to the design of BPs with highly incompatible segments and low molar mass to reduce the features sizes at sub-10 nm scale. Additionally, more complex materials, such as liquid crystal BPs,[40] multi-block copolymers,[41-44] tapered BPs,[45-48] and cyclic copolymers,[49] that portend very interesting alignment behavior and nanoscale structures have attracted a great deal of interest. However, processing these BPs faces significant challenges and the methods to achieve macroscopic alignment of the nanostructures remain largely unexplored. The RSVA-SS approach may provide a feasible pathway for the continuous processing of these BP systems.

REFERENCES

1. Bates, C. M.; Maher, M. J.; Janes, D. W.; Ellison, C. J.; Willson, C. G. *Macromolecules* **2013,** 47, (1), 2-12.

2. Guarini, K. W.; Black, C. T.; Zhang, Y.; Kim, H.; Sikorski, E. M.; Babich, I. V. *J. Vac. Sci. Technol. B* **2002,** 20, (6), 2788-2792.

3. Park, M.; Chaikin, P. M.; Register, R. A.; Adamson, D. H. *Appl. Phys. Lett.* **2001,** 79, (2), 257-259.

4. Chai, J.; Buriak, J. M. *ACS Nano* **2008,** 2, (3), 489-501.

5. Black, C. T. *Appl. Phys. Lett.* **2005,** 87, (16), 163116.

6. Terris, B. D.; Thomson, T. *J. Phys. D: Appl. Phys.* **2005,** 38, (12), R199.

7. Park, S.; Lee, D. H.; Xu, J.; Kim, B.; Hong, S. W.; Jeong, U.; Xu, T.; Russell, T. P. *Science* **2009,** 323, (5917), 1030-1033.

8. Yang, S. Y.; Ryu, I.; Kim, H. Y.; Kim, J. K.; Jang, S. K.; Russell, T. P. *Adv. Mater.* **2006,** 18, (6), 709-712.

9. Bang, J.; Kim, S. H.; Drockenmuller, E.; Misner, M. J.; Russell, T. P.; Hawker, C. J. *J. Am. Chem. Soc.* **2006,** 128, (23), 7622-7629.

10. Zschech, D.; Kim, D. H.; Milenin, A. P.; Scholz, R.; Hillebrand, R.; Hawker, C. J.; Russell, T. P.; Steinhart, M.; Gösele, U. *Nano Lett.* **2007,** 7, (6), 1516-1520.

11. Ruiz, R.; Kang, H.; Detcheverry, F. A.; Dobisz, E.; Kercher, D. S.; Albrecht, T. R.; de Pablo, J. J.; Nealey, P. F. *Science* **2008,** 321, (5891), 936-939.

12. Young, W.-S.; Kuan, W.-F.; Epps, T. H., III. *J. Polym. Sci. Part B: Polym. Phys.* **2014,** 52, (1), 1-16.

13. Ruzette, A.-V. G.; Soo, P. P.; Sadoway, D. R.; Mayes, A. M. *J. Electrochem. Soc.* **2001,** 148, (6), A537-A543.

14. Luo, M.; Epps, T. H., III. *Macromolecules* **2013,** 46, (19), 7567-7579.

15. Mishra, V.; Fredrickson, G. H.; Kramer, E. J. *ACS Nano* **2012,** 6, (3), 2629-2641.

16. Albert, J. N. L.; Epps, T. H., III. *Materials Today* **2010,** 13, (6), 24-33.

17. Segalman, R. A.; Yokoyama, H.; Kramer, E. J. *Adv. Mater.* **2001,** 13, (15), 1152-1155.

18. Bang, J.; Jeong, U.; Ryu, D. Y.; Russell, T. P.; Hawker, C. J. *Adv. Mater.* **2009,** 21, (47), 4769-4792.

19. Kim, S. O.; Solak, H. H.; Stoykovich, M. P.; Ferrier, N. J.; de Pablo, J. J.; Nealey, P. F. *Nature* **2003,** 424, (6947), 411-414.

20. Stoykovich, M. P.; Kang, H.; Daoulas, K. C.; Liu, G.; Liu, C.-C.; de Pablo, J. J.; Müller, M.; Nealey, P. F. *ACS Nano* **2007,** 1, (3), 168-175.

21. Olszowka, V.; Tsarkova, L.; Boker, A. *Soft Matter* **2009,** 5, (4), 812-819.

22. Majewski, P. W.; Gopinadhan, M.; Osuji, C. O. *J. Polym. Sci. Part B: Polym. Phys.* **2012,** 50, (1), 2-8.

23. Yu, H.; Iyoda, T.; Ikeda, T. *J. Am. Chem. Soc.* **2006,** 128, (34), 11010-11011.

24. Winey, K. I.; Patel, S. S.; Larson, R. G.; Watanabe, H. *Macromolecules* **1993,** 26, (16), 4373-4375.

25. Young, W. S.; Epps, T. H., III. *Macromolecules* **2012,** 45, (11), 4689-4697.

26. Lee, W.-K.; Kim, H. D.; Kim, E. Y. *Current Applied Physics* **2006,** 6, (4), 718-722.

27. Scott, D. B.; Waddon, A. J.; Lin, Y. G.; Karasz, F. E.; Winter, H. H. *Macromolecules* **1992,** 25, (16), 4175-4181.

28. Dair, B. J.; Honeker, C. C.; Alward, D. B.; Avgeropoulos, A.; Hadjichristidis, N.; Fetters, L. J.; Capel, M.; Thomas, E. L. *Macromolecules* **1999,** 32, (24), 8145-8152.

29. Gupta, V. K.; Krishnamoorti, R.; Chen, Z. R.; Kornfield, J. A.; Smith, S. D.; Satkowski, M. M.; Grothaus, J. T. *Macromolecules* **1996,** 29, (3), 875-884.

30. Angelescu, D. E.; Waller, J. H.; Adamson, D. H.; Deshpande, P.; Chou, S. Y.; Register, R. A.; Chaikin, P. M. *Adv. Mater.* **2004,** 16, (19), 1736-1740.

31. Kim, S. Y.; Nunns, A.; Gwyther, J.; Davis, R. L.; Manners, I.; Chaikin, P. M.; Register, R. A. *Nano Lett.* **2014,** 14, (10), 5698-5705.

32. Singh, G.; Yager, K. G.; Berry, B.; Kim, H.-C.; Karim, A. *ACS Nano* **2012,** 6, (11), 10335-10342.

33. Qiang, Z.; Zhang, L.; Stein, G. E.; Cavicchi, K. A.; Vogt, B. D. *Macromolecules* **2014,** 47, (3), 1109-1116.

34. Berry, B. C.; Bosse, A. W.; Douglas, J. F.; Jones, R. L.; Karim, A. *Nano Lett.* **2007,** 7, (9), 2789-2794.

35. Jeong, J. W.; Hur, Y. H.; Kim, H.-j.; Kim, J. M.; Park, W. I.; Kim, M. J.; Kim, B. J.; Jung, Y. S. *ACS Nano* **2013,** 7, (8), 6747-6757.

36. Sinturel, C.; Vayer, M.; Morris, M.; Hillmyer, M. A. *Macromolecules* **2013,** 46, (14), 5399-5415.

37. Qiang, Z.; Zhang, Y.; Groff, J. A.; Cavicchi, K. A.; Vogt, B. D. *Soft Matter* **2014,** 10, (32), 6068-6076.

38. Qiang, Z.; Zhang, Y.; Wang, Y.; Bhaway, S. M.; Cavicchi, K. A.; Vogt, B. D. *Carbon* **2015,** 82, (0), 51-59.

39. Seppala, J. E.; Lewis, R. L., III; Epps, T. H., III. *ACS Nano* **2012,** 6, (11), 9855-9862.

40. Yu, H.; Li, J.; Ikeda, T.; Iyoda, T. *Adv. Mater.* **2006,** 18, (17), 2213-2215.

41. Ludwigs, S.; Boker, A.; Voronov, A.; Rehse, N.; Magerle, R.; Krausch, G. *Nat. Mater.* **2003,** 2, (11), 744-747.

42. Lee, D. H.; Park, S.; Gu, W.; Russell, T. P. *ACS Nano* **2011,** 5, (2), 1207-1214.

43. van Zoelen, W.; ten Brinke, G. *Soft Matter* **2009,** 5, (8), 1568-1582.

44. Bates, F. S.; Hillmyer, M. A.; Lodge, T. P.; Bates, C. M.; Delaney, K. T.; Fredrickson, G. H. *Science* **2012,** 336, (6080), 434-440.

45. Mastroianni, S. E.; Epps, T. H., III. *Langmuir* **2013,** 29, (12), 3864-3878.

46. Roy, R.; Park, J. K.; Young, W. S.; Mastroianni, S. E.; Tureau, M. S.; Epps, T. H. *Macromolecules* **2011,** 44, (10), 3910-3915.

47. Kuan, W. F.; Roy, R.; Rong, L. X.; Hsiao, B. S.; Epps, T. H. *ACS Macro Letters* **2012,** 1, (4), 519-523.

48. Zhang, W.; Allgaier, J.; Zorn, R.; Willbold, S. *Macromolecules* **2013,** 46, (10), 3931-3938.

49. Poelma, J. E.; Ono, K.; Miyajima, D.; Aida, T.; Satoh, K.; Hawker, C. J. *ACS Nano* **2012,** 6, (12), 10845-10854.

Chapter 5

DETERMINATION OF INTERFACIAL MIXING IN TAPERED BLOCK POLYMER THIN FILMS

Tapered block polymers (TBPs) represent an emerging class of macromolecules, and the interfacial manipulation of these polymers has led to unique and diverse self-assembly behavior and properties. In this chapter, I describe both the experimental and theoretical studies of the influence of non-tapered and tapered (normal tapered and inverse tapered) interfaces on interfacial mixing, BP thermodynamic properties (*i.e.*, glass transition temperatures, changes in heat capacity), and the free surface morphologies in thin films. The quantitative measurement of the interfacial mixing in these tapered materials allows us to connect macroscopic physical properties to macromolecular structure and sequence, and it furthers our understanding of interfacial modifications as a valuable tool for materials design. Text and figures are reproduced and adapted with permission from Luo, M., *et al. Macromolecules*, 2016, 49, (14), 5213-5222.

5.1 Introduction

TBPs offer a unique opportunity to tune the structure of a given BP system.[1-6] By introducing a tapered middle region with a gradient monomer composition profile between pure A and B blocks, the effective Flory-Huggins interaction parameter (χ) can be reduced, leading to lower order-disorder transition temperatures (T_{ODT}'s) relative to the corresponding non-tapered BPs.[2, 3, 7] Thus, tapering potentially allows access to higher molecular weight materials that reside in weak to intermediate

segregation strength regimes at accessible temperatures.[1, 8] A recent self-consistent field theory study found that normal tapering (A-AB-B) widens the bicontinuous gyroid region of the phase diagram,[7] and that result has been supported by several experimental precedents.[1, 2] The manipulation of BP morphologies and thermal transitions is especially relevant for transport and separation applications.[1, 2, 8] Thus, there is significant interest in using tapered interfaces to control the nanostructures and influence the macroscopic physical properties of BPs. In particular, our research group has been developing interfacially-modified (tapered) BP systems, with a specific focus on network-forming materials.[1, 8]

The impact of tapered interfaces on the structure and thermodynamic properties of BPs has been studied both theoretically and experimentally by varying the fraction of interfacial segments and altering the sequence of monomer addition (*e.g.*, normal taper *versus* inverse taper, see Figure 5.1).[3, 5, 7] The presence of a tapered interface generally promotes the mixing of unlike segments in the interfacial region. Hodrokoukes *et al.* found that increasing the amount of the tapered middle region in the inverse tapered polymer improved compatibility, but the key factor was the segment sequencing near the interface, with normal tapered polymer being less compatible than the inverse tapered polymer.[3] Additionally, the glass transition temperatures (T_g's) and aforementioned T_{ODT}'s are tunable by changing the taper composition without altering the morphology, which can facilitate melt processing. For example, Knoll and coworkers examined an asymmetric poly(styrene-*b*-butadiene-*b*-styrene) (SBS) with a tapered transition between the polybutadiene (PB) block and the longer polystyrene (PS) block.[4, 6] In their work, the short PS block mixed into the PB segment, which led to an increase in the T_g of the PB-containing phase as well as a

significant decrease of the relaxation time of the materials. Further studies by Jouenne *et al.* also on an asymmetric S-SB-S triblock polymer, indicated that the styrene/butadiene composition gradient could improve ductility in comparison to analogous non-tapered SBS triblock polymers.[9]

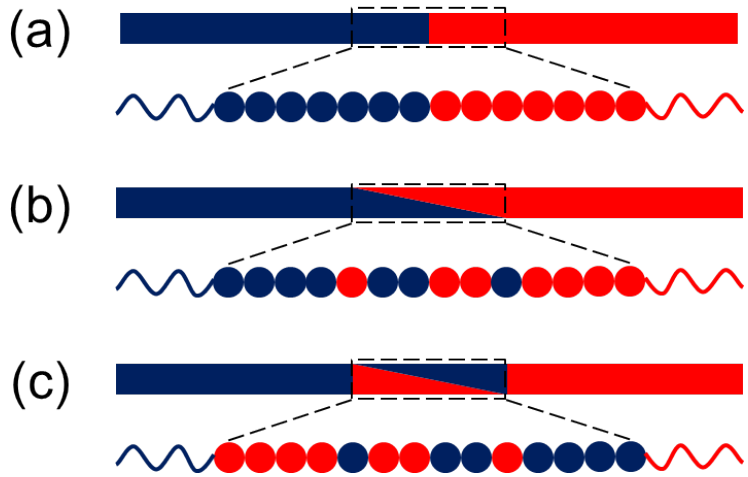

Figure 5.1: Illustration of (a) diblock polymer, (b) normal tapered BP, and (c) inverse tapered BP. Reprinted with permission from Luo, M., *et al.* *Macromolecules*, 2016, 49, (14), 5213-5222.

Several prior modeling studies have explored the effects of modifications in polymer sequence such as gradients and tapers.[7, 10] For example, Pakula *et al.* considered gradient copolymers for which composition smoothly varied over the entire polymer length as represented by either linear, quadratic, or cubic segment profiles. They found the T_{ODT}'s could be controlled by adjusting the steepness of the composition variation.[11] Hall and coworkers systematically investigated the effect of tapering on morphology and interfacial behavior using self-consistent field theory, fluids density functional theory (fDFT), and molecular dynamics simulations.[7, 10, 12]

These works provided phase diagrams and lamellar density profiles for normal and inverse (linear) tapered BPs with various taper volume fractions.

Although the tailored interface has led to unique properties in these tapered BPs, there have been only a few studies that qualitatively inferred the interfacial mixing characteristics. Analyses of small-angle X-ray scattering (SAXS) and rheology data have shown that the T_{ODT} of an inverse tapered isoprene/styrene BP decreased by about 100 K relative to a normal tapered BP of similar molecular weight and composition, possibly indicating a wider effective interfacial region in the former.[3] Sigle *et al*. employed phase contrast tapping-mode atomic force microscopy (AFM) to visualize the interfacial structures qualitatively and noted the phase contrast between microphase-separated domains was reduced in normal and inverse tapered isoprene/styrene BPs relative to the non-tapered analogue.[5] However, in their case, the linear phase contrast intensity of the normal tapered polymer was smoother in comparison to the inverse tapered polymer, which suggested a wider interfacial region in the normal-tapered BP. The difficulty in interpreting the above results necessitates a quantitative determination of the interfacial mixing in tapered BPs.

Thus, this chapter presents the first quantitative measurements of interfacial mixing in TBPs for normal tapered poly(isoprene-*b*-isoprene/styrene-*b*-styrene) (I-IS-S) and inverse tapered I-SI-S using X-ray reflectivity (XRR) and differential scanning calorimetry (DSC). The density profiles derived from XRR data were paired with theoretical efforts using fDFT and showed good agreement. Furthermore, the influence of the tapered interfaces on the BP thermodynamic properties (*i.e.*, glass transition temperatures, changes in heat capacity) and the free surface morphologies in

thin films were investigated, and the results indicated that the monomer sequence is an important determinant of macroscopic physical properties.

5.2 Materials and Methods

5.2.1 Materials

The I-S diblock polymers were synthesized by sequential living anionic polymerization of the PI block in cyclohexane at 40 °C, followed by the PS block, with *sec*-butyllithium (Acros, 1.3 M in hexanes) as the initiator under an argon atmosphere. Normal tapered I-IS-S and inverse tapered I-SI-S polymers were synthesized by sequential living anionic polymerization of the PI block in cyclohexane at 40 °C, followed by a region that tapered linearly from nearly pure PI to nearly pure PS (or nearly pure PS to nearly pure PI for the inverse tapered polymer) using automated syringe pumps, and finally a PS block. The detailed synthesis methods are described elsewhere.[1, 2]

5.2.2 Bulk Polymer Characterization

The number-average molecular weights and dispersity of the BPs were determined by size-exclusion chromatography. The volume fractions were calculated using ^{1}H nuclear magnetic resonance spectroscopy peak integrations and homopolymer densities ($\rho_{PI,140\,°C} = 0.83$ g cm^{-3}, $\rho_{PS,140\,°C} = 0.97$ g cm^{-3}).[13] All of the BPs studied had a nearly symmetric composition. The volume of the tapered segment was estimated by using a linear combination of the PI and PS homopolymer densities weighted by the mole fraction of PI and PS repeat units in the tapered region. All of the BPs formed lamellae as characterized by SAXS and transmission electron

microscopy, and the domain spacings (Table 5.1) were calculated from the primary peak location in 1-D azimuthally-integrated SAXS profiles (see Appendix C).

DSC measurements were performed on a Discovery DSC (TA Instruments) using a temperature range of -90 °C to 150 °C. Samples were treated through three heating/cooling cycles at 10 °C min^{-1} with a continuous N_2 purge (50 mL min^{-1}). The second and third heating/cooling cycles were nearly identical, and the T_g's were determined from the midpoint of the inflections in the second heating trace.

Dynamic mechanical analysis (DMA) experiments were conducted on an ARES-G2 strain-controlled rheometer with 8 mm diameter parallel plate geometry under a nitrogen atmosphere. Polymer discs (0.3 mm in thickness and 8 mm in diameter) were molded at elevated temperature (110 °C for I-S and I-IS-S, 90 °C for I-SI-S) and pressure (0.2 t per 50 mm^2 sample) for 15 min. Temperature-dependent data of storage (G') and loss (G'') moduli were obtained during dynamic shear at a constant frequency of 6.28 rad/s and strain amplitudes of 0.4–3%. The temperature ramp rate was 3 °C min^{-1}.

5.2.3 Thin Film Preparation and Characterization

The I-S, I-IS-S, and I-SI-S thin films were cast onto silicon substrates by flow coating as described in Chapter 2 Section 2.2. Films of uniform thickness were produced in constant velocity mode, and films of gradient thickness were fabricated in acceleration mode. Film thicknesses were measured using a reflectance spectrometer (Filmetrics F20-UV). The films were stored under vacuum overnight and subsequently annealed at elevated temperature under argon atmosphere. The optimal annealing condition was determined by monitoring the growth of island/hole structures with *in situ* optical microscopy. As the film equilibrated, the size and

surface coverage of the island/hole plateaued (see Appendix C). The I-S and I-IS-S films were annealed at 100 °C for 6 h, and the I-SI-S film was annealed at 90 °C for 6 h.

Optical microscopy images were collected on a Nikon microscope equipped with a 5 MP CCD camera (Nikon Eclipse LV100). *In situ* optical microscopy was conducted using a Linkam thermal stage as described in Chapter 2 Section 2.6.1. The free surface morphologies of polymer films were assessed by AFM (Veeco Dimension 3100) after the thin films were quenched to room temperature using a metal plate.

XRR was performed on an Ultima IV unit (Rigaku) at room temperature with a thin, parallel beam of Cu Kα radiation, $\lambda = 0.154$ nm, incident on the quenched samples. The beam was sized to capture the critical edge of the samples for best results and fit accuracy. XRR profiles were collected by scanning a small incident angle (θ) of X-rays from the source and a detection angle (2θ) of reflected X-rays ($0° < 2\theta < 4°$). To aid in the analysis, we used the density values at 140 °C as initial guesses for the XRR fitting ($\rho_{PI,140\,°C} = 0.83$ g cm^{-3}, $\rho_{PS,140\,°C} = 0.97$ g cm^{-3}).[13] Optimization and refinement to achieve final densities, film thickness, and roughness parameters then were performed using GlobalFit software.

5.2.4 Fluids Density Functional Theory Calculations

In collaboration with the Hall group in the Department of Chemical and Biomolecular Engineering of the Ohio State University, fDFT calculations were performed by Jonathan R. Brown for the polymer system studied here. The fDFT uses statistical mechanical principles to cast the free energy of a system of classical particles in terms of functionals of the density profile. Thus, the equilibrium density profile that minimizes the free energy can be found using a numerical optimization

procedure. The open source code Tramonto[14] was employed to perform the calculations with White Bear hard sphere functionals and iSAFT functionals to describe the polymer connectivity.[15, 16] The polymer model considered freely jointed chains of hard spheres with diameter σ equal to the bond length. Pairwise interactions were modeled with an attractive Lennard-Jones (LJ) potential cut off after 2.5σ, for which the hard core size σ is the LJ distance parameter, using a Weeks-Chandler-Anderson approach in which the potential is purely attractive (*i.e.*, the potential energy is constant at its minimum value at distances less than the minimum energy distance).[14, 17] The calculations were performed at a constant pressure of 0 (as is often chosen in molecular dynamics simulations that apply a similar model).[18] The monomer number density for the homopolymer system with this model was $\rho = 0.835\sigma^{-3}$. All details of the model, the sequence used to approximate the linear taper, and the implementation, other than the potential cutoff and value of the pressure noted above, were discussed in prior work.[10] Because monomer interactions were calculated using a strict mean field approximation, the mapping to χ was straightforward.[10]

5.3 Results and Discussion

5.3.1 Interfacial Mixing Characteristics

Illustrations of the macromolecular architectures of the I-S, I-IS-S, and I-SI-S polymers are depicted in Figure 5.1. The polymers had similar molecular weights and nearly symmetric compositions (Table 5.1). The diblock I-S polymer served as a control with nearly discrete block junctions, whereas the tapered I-IS-S polymer had a gradient region that varied from mostly PI to mostly PS between pure PI and PS blocks, and the inverse tapered I-SI-S had a gradient region that varied from mostly PS

to mostly PI between pure PI and PS blocks. The volume composition of both tapered regions was approximately 30%. All polymers formed lamellae in bulk and thin film studies, and the domain spacings are listed in Table 5.1.

Table 5.1: Molecular characteristics of the BPs

Polymer	Tapered (vol%)	M_n (g mol^{-1})	Dispersity	Volume fraction (f_{PI})	Domain spacing from SAXS (nm)
I-S	0	23,200	1.06	0.494	18.4
I-IS-S	28	25,100	1.08	0.494	20.1
I-SI-S	30	24,400	1.06	0.503	18.8

XRR was employed to probe the interfacial thickness in these tapered BPs. Thin films were cast onto silicon wafers from I-S, I-IS-S, and I-SI-S solutions in cyclohexane. After casting, the thin films were thermally annealed in an argon atmosphere to promote the formation of parallel-oriented lamellae, which were ideal for XRR characterization.[19] The PI layer segregates to both the free surface and substrate surface due to its low surface energy and affinity for the silicon oxide (*i.e.*, symmetric wetting). Thus, uniform free surfaces could be found at film thicknesses of nL_0 (n = 1, 2, 3,…; L_0 is the domain spacing of the BP).

XRR measurements were conducted on uniform I-S (126 nm), I-IS-S (118 nm), and I-SI-S (126 nm) thin films (Figure 5.2). After thermal annealing at approximately 90–100 °C for 6 h, the thin films were quenched to room temperature, kinetically trapping the film microstructures. Analysis using GlobalFit software provided the profiles and final density values that are reported in Figure 5.2. The I-S and I-SI-S films studied here were approximately 7 L_0, and the I-IS-S film was approximately 6 L_0 due to its slightly larger domain spacing. XRR data exhibited small-period

oscillations associated with the film thickness, and large-period oscillations were associated with the thicknesses of the lamellar layers. The I-S and I-IS-S films had two clear Kiessig fringes from the lamellar layers (marked by arrows in Figure 5.2). However, the intensity of these Kiessig fringes was damped in the I-SI-S film. It was postulated that the PI-rich and PS-rich layers in the I-SI-S film had less contrast (*i.e.*, smaller scattering length density differences due to increased mixing). Thus, the I-SI-S film more prominently exhibited small-period oscillations characteristic of the whole film thickness. Furthermore, the amplitude of the oscillation decreased more rapidly for the I-SI-S film than for the I-IS-S and I-S films. As the surface roughness was less than 1 nm for all films (measured by AFM, see Appendix C), the different decay rates in the X-ray reflectivity data likely originated from the differences in interfacial roughness. These results indicated the I-SI-S film likely had a larger interfacial roughness.

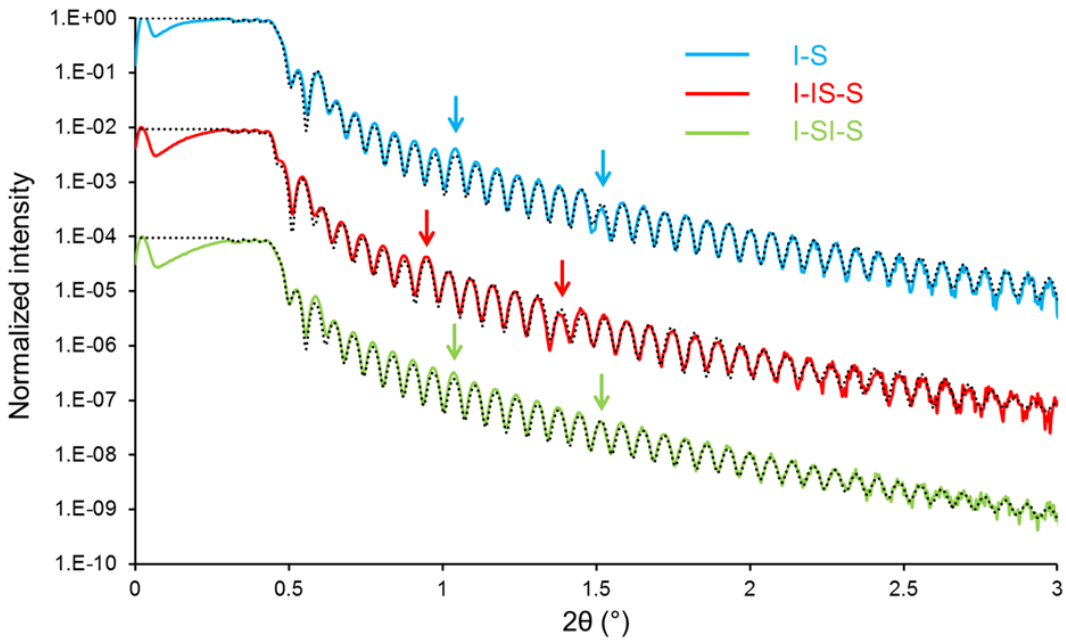

I-S film

Layers	Thickness (nm)	Density (g cm^{-3})	Roughness (nm)	
PI	3.8	0.82	0.6	
PS	8.0	1.00	1.7	
PI	8.6	0.82	1.8	×6
PS	9.8	1.06	2.0	
PI	4.1	0.82	1.9	
Si/O_2	1.6	2.55	0.4	

I-IS-S film

Layers	Thickness (nm)	Density (g cm^{-3})	Roughness (nm)	
PI	4.1	0.82	0.8	
PS	8.1	1.00	2.0	
PI	8.6	0.83	2.0	×5
PS	11.8	1.01	2.1	
PI	4.0	0.82	2.6	
Si/O_2	1.0	2.52	0.4	

I-SI-S film

Layers	Thickness (nm)	Density (g cm^{-3})	Roughness (nm)	
PI	3.6	0.83	0.9	
PS	7.7	1.01	4.0	
PI	8.3	0.83	4.0	×6
PS	10.1	1.01	4.4	
PI	3.7	0.82	5.0	
Si/O_2	1.5	2.60	0.4	

Figure 5.2: XRR profiles for I-S (blue), I-IS-S (red), and I-SI-S (green) films. The solid lines denote the measured profile, and dotted lines denote the fit profile. Arrows mark prominent Kiessig fringes. The tables list the fitting parameters for the model for which the "Roughness" corresponds to the likely interfacial mixing region between discrete layers. XRR curves are shifted vertically for clarity. Reprinted with permission from Luo, M., *et al. Macromolecules*, 2016, 49, (14), 5213-5222.

The calculated XRR profiles for the thin film samples also are shown in Figure 5.2. The model for the calculated profiles incorporates a capping layer of PI at the free surface, followed by a PS layer and 6 repeats of PI-PS lamellae (except for the I-IS-S BP for which the model consists of 5 repeats of PI-PS lamellae), and a wetting

layer of PI at the substrate. This model provided a very good fit for the data. The lamellar domain spacing could be determined by summing the PI and PS layer thicknesses. Importantly, the interfacial roughness (δ) could be resolved quantitatively. The interfacial profile typically is described by a Gaussian distribution, and the interfacial roughness represents the standard deviation of the Gaussian distribution. The average interfacial roughness for the I-S film was ~1.9 nm from our XRR fitting. There was a slight increase in the interfacial roughness in the I-IS-S film (~2.1 nm). The I-SI-S film showed a more significant increase of interfacial roughness to ~4.2 nm, which was expected as the I-SI-S possessed the largest miscibility. The effective interfacial thickness (t) can be computed using $t = (2\pi)^{1/2}\delta \approx 2.5\delta$ according to Anastasiadis *et al*.[20] In Anastasiadis *et al*.'s work, neutron reflectivity was used to quantify the interfacial thickness of a 30 000 g mol^{-1} PS-*b*-poly(methyl methacrylate) (PS–PMMA) polymer, which had a similar segregation strength to the I-S polymers studied herein. It was determined that the roughness parameter, δ, was 2.0 nm (close to our non-tapered diblock polymer result), and $t \approx 5.0$ nm.[20] Theoretical predictions of interfacial thickness for the PS–PMMA BPs by Semenov supported Anastasiadis et al.'s results when taking into account the corrections of chain-end effects and fluctuations of concentration profiles.[21]

Normalized lamellar density profiles derived from XRR models are shown in Figure 5.3. The normal tapered I-IS-S polymer had a similar density profile to the non-tapered diblock I-S, while the inverse tapered I-SI-S polymer demonstrated a wider interface and greater mixing within the defined PI and PS domains. It is highly plausible that the normal tapered interface has a relatively small effect for this system due to the modest BP molecular weight (low segregation strength regime), which leads

to a comparable domain interface profile between the I-S and I-IS-S for short to moderate tapers. Singh *et al.* examined normal tapered I-IS-S with 20 vol% tapered fraction and found that the T_{ODT} only decreased by ~2 °C in comparison to non-tapered I-S diblock polymer (T_{ODT} ~177 °C).[2] Increasing the tapered fraction to 35 vol% decreased the T_{ODT} by ~6 °C. However, the inverse tapered I-SI-S (20 vol% tapered fraction) exhibited a substantial decrease of ~29 °C, suggesting that an inverse tapered interface is more effective at increasing domain miscibility. Brown *et al*. determined the critical points (χN_{crit}) for the normal and inverse tapered systems as a function of taper size using random phase approximation and self-consistent field theory.[7] The χN_{crit} was ~10.5 for the diblock polymer system, while it increased ~13% for the 30% normal taper system (χN_{crit} = 11.9) and increased ~61% for the 30% inverse tapered system (χN_{crit} = 16.9). For the normal tapered system to show a similar effect to the inverse tapered polymer, the tapered fraction needed to be increased to ~65%. We have examined the T_{ODT} for the polymers studied here using DMA, and the results further corroborate our hypothesis (see Appendix C). The T_{ODT} was 160 °C for the non-tapered I-S polymer, 158 °C for the normal tapered I-IS-S polymer, and 94 °C for the inverse tapered I-SI-S polymer. The segregation strengths at the order–disorder transition temperature (χN_{ODT}) for our polymers were 11.6, 12.6, and 15.2 for the I-S, I-IS-S, and I-SI-S polymers, respectively, calculated using the χ–T relation ($\chi = -0.016 + 25.12/T$) determined by Mori et al.[22] and statistical segment length N_{stat}.[23] Considering the variability of the χ–T relation, these results were in reasonable agreement with the predictions from Brown *et al*.[7]

The lamellar density profiles were compared to those calculated from fDFT, also in Figure 5.3. In the fDFT calculations, a fixed sequence of monomers was used

to represent the tapered region.[10] The fDFT results at constant χN are not strongly dependent on N for reasonably large values of N; therefore, modeling a linear gradient with such a fixed sequence is valid. The same value of χ was used for all systems, and slightly different values of N were used to match the experimental differences in molecular weight. The polymers studied here were approximately 150 monomers long, corresponding to a mapping of one bead to 160 g/mol of polymer. Note that this value is between the Kuhn segment size of PI (120 g/mol) and PS (720 g/mol) given by Rubinstein and Colby;[24] this very simple freely jointed model with a single mapping to molecular weight does not consider the difference between the stiffness of PS and PI. Specifically, N = 146, 157, and 153 were used for the diblock, normal tapered, and inverse tapered systems, respectively, with 44 beads making up the normal taper and 46 beads for the inverse taper. The phase separation of the two blocks is driven by a smaller LJ attraction between unlike beads; like beads have ε_{ii} = 1, and unlike beads have $\varepsilon_{IS} < 1$. ε_{IS} was varied to obtain a best fit to the experimental data for the inversed tapered system to an accuracy of χN = 0. 5 (the mapping to χN was performed as in ref 10). This matching approach yielded the density profiles shown in Figure 5.3 with ε_{IS} = 0.9805. The corresponding χN values were 19.3, 20.7, and 20.2 for the diblock, normal tapered, and inverse tapered systems, which had lamellar spacings of 20.6, 21.4, and 18.2 (in units of the monomer diameter, σ), respectively. These lamellar density profiles showed very good agreement with those derived from XRR.

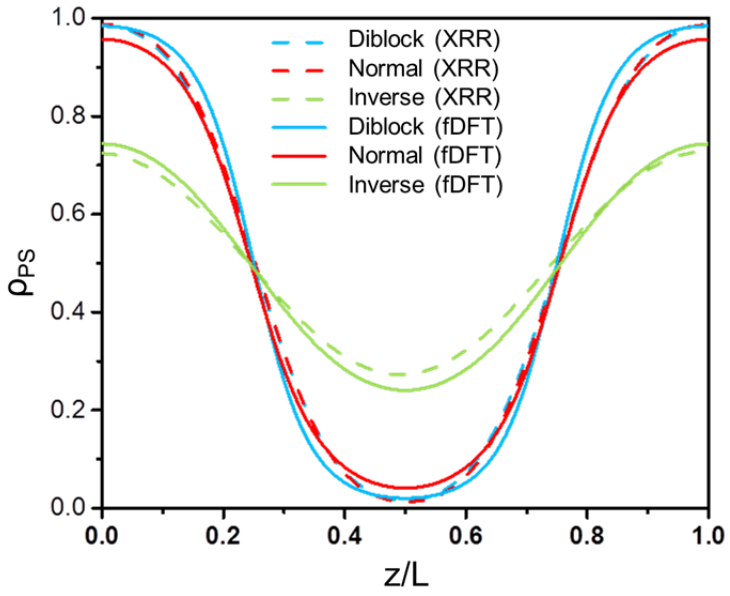

Figure 5.3: Normalized lamellar density profile of PS *versus* perpendicular distance across the lamellae of width L at $\chi N \approx 14$ for symmetric ($f_A = f_B = 0.5$) systems for diblock, normal and inverse tapered BPs. Dashed lines are the profiles derived from XRR modeling, while solid lines are the profiles from fDFT calculations. Reprinted with permission from Luo, M., *et al. Macromolecules*, 2016, 49, (14), 5213-5222.

5.3.2 Influence on Thermal Properties

DSC was used to characterize the thermal properties of I-S, I-IS-S and I-SI-S BPs. The data are summarized in Table 5.2. Two glass transition temperatures were apparent in each trace representing the PI-rich and PS-rich domains (see Figure 5.4). Important inferences about miscibility can be drawn by analyzing the shift in the T_g of the two domains. The glass transition temperature of the PI-rich phase ($T_{g\text{-}PI}$) for each BP was located at approximately -60 °C, which is close to the literature value for PI homopolymers.[25, 26] For the normal tapered and inverse tapered polymers, a very small but possible shift of $T_{g\text{-}PI}$ to higher temperatures could be discerned from the

data, and there was a broader T_g response in the inverse taper I-SI-S polymer possibly due to increased mixing with PS. The absence of a substantial endothermic peak near the $T_{g\text{-}PI}$ in the I-SI-S polymer also suggested that the motion of the PI chains was hindered by the glassy PS domains.[25]

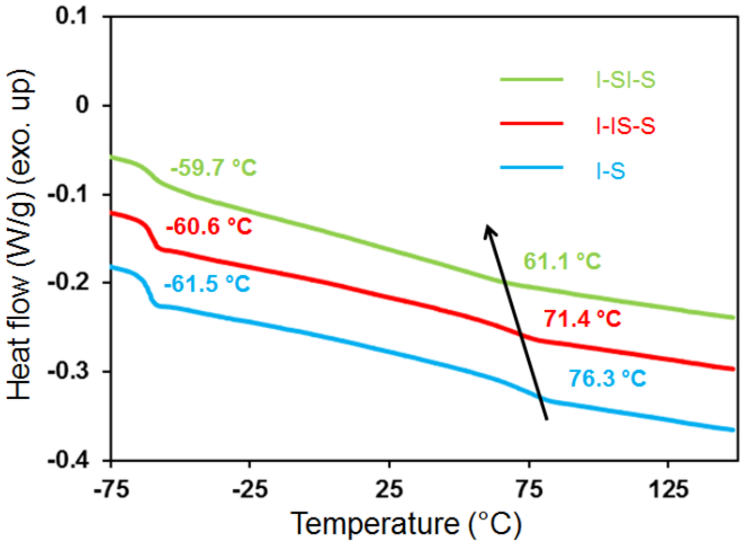

Figure 5.4: DSC trace on second heating (10 °C min^{-1}, N_2 flow) for I-S (blue), I-IS-S (red) and I-SI-S (green) BPs, normalized by the total mass. The arrow is to guide the eye to the shift in $T_{g\text{-}PS}$. DSC curves are shifted vertically for clarity. Reprinted with permission from Luo, M., *et al. Macromolecules*, 2016, 49, (14), 5213-5222.

For the PS-rich domain, the $T_{g\text{-}PS}$ of the I-S BP was 76.3 °C. Fox and Flory suggested an empirical equation to predict the molecular weight dependence of the T_g of PS homopolymer:[27]

$$T_g = 100\,°C - \frac{1.8\times10^5}{M_n} \qquad 5.1$$

Using the Fox-Flory equation, PS homopolymer with a molecular weight of 12,500 g mol^{-1} (corresponding to the molecular weight of PS block in the I-S polymer) would have a T_g of 85.6 °C. The endothermic response of PS was found weak and broad in comparison to that of PI. From these results, it was evident that increasing the temperature during the heating cycle promoted mixing between the PS phase and the PI phase and led to a broad response of $T_{g\text{-}PS}$. The $T_{g\text{-}PS}$ for the I-IS-S and I-SI-S polymers was 71.4 °C and 61.1 °C, respectively. These results were consistent with a previous study of Hodrokoukes *et al.*, which showed the $T_{g\text{-}PI}$ measurements were fairly close, but the $T_{g\text{-}PS}$ had a significant drop in I-IS-S and I-SI-S polymers.[3] Although Hodrokoukes *et al.* did not comment on the shape of their DSC traces, similar traces were reported by Prud'homme and coworkers in which they investigated the T_g for a series of I-S BPs with varying molecular weights.[25] Prud'homme also noted the $T_{g\text{-}PI}$ only increased slightly in comparison to the homopolymer PI, and the endothermic peak was weak, while the $T_{g\text{-}PS}$ shifted significantly toward lower temperatures with decreasing molecular weight. The shift in T_g also has been recognized as an indicator of block component miscibility in random, gradient, and tapered copolymer systems[3, 28, 29] Herein, the degree of mixing between PI and PS blocks increased from I-S (non-tapered) to I-IS-S (normal tapered) to I-SI-S (inverse tapered).

The increased mixing was more obvious when considering the change of the heat capacity at the glass transition. The ΔC_P for the PI-rich phase was evaluated by measuring the difference in height between the extrapolated base lines recorded above and below the $T_{g\text{-}PI}$ (Appendix C). The normalized values of $\Delta C_{P\text{-}PI}$ were 0.39 J g^{-1} K^{-1} for I-S, 0.39 J g^{-1} K^{-1} for I-IS-S, and 0.35 J g^{-1} K^{-1} for I-SI-S (the values of ΔC_P for

each phase were given per gram of the respective block in the particular sample, see Table 5.2). The value of ΔC_P for homopolymer PI is 0.39 J g^{-1} K^{-1} according to literature.[25] The I-SI-S data indicated a small, but significant, reduction in $\Delta C_{P\text{-}PI}$, suggesting there was enhanced mixing of the PS component in the PI phase in the inverse tapered lamellae.

The normalized values of $\Delta C_{P\text{-}PS}$ were 0.26 J g^{-1} K^{-1} for I-S, 0.24 J g^{-1} K^{-1} for I-IS-S, and 0.18 J g^{-1} K^{-1} for I-SI-S (Table 2). Insights regarding the thickness of the interfacial region could be drawn from a quantitative analysis of $\Delta C_{P\text{-}PS}$.[25, 30, 31] The glass transition of the PS chains located in the interfacial region was considered to distribute over a wide range of temperatures between the $T_{g\text{-}PI}$ and $T_{g\text{-}PS}$.[30, 31] Morese-Seguela *et al.* assumed that these interfacial PS chain segments had a minimal impact on the glass transition behavior at $T_{g\text{-}PS}$, and the weight fraction of these PS chains could be estimated by the quantity $(1 - \Delta C_P / \Delta C_{P,\,pure\,PS})$, in which $\Delta C_{P,\,pure\,PS}$ was the heat capacity change at the glass transition for homopolymer PS ($\Delta C_{P,\,pure\,PS}$ = 0.31 J g^{-1} K^{-1}).[25] The thickness of the interfacial region on either side of a PS lamella (t_S) then could be written as:

$$t_S = \frac{L_{PS}}{2}\left[1 - \frac{\Delta C_P}{\Delta C_{P,\,pure\,PS}}\right] \qquad 5.2$$

in which L_{PS} was the lamellar thickness of the PS layer.[25] For our I-S polymers, with styrene weight fractions of ~0.54, L_{PS} was close to 1.60 ± 0.15 times the unperturbed root-mean-square end-to-end distance, $(r_0^2)^{1/2}$, of a homopolystyrene chain of the same molecular weight as the PS block in the BP.[32] Because $(r_0^2)^{1/2} = 0.067 M_n^{1/2}$ for bulk homopolystyrene,[25] one could estimate the following empirical relationship between L_{PS} and the molecular weight of the PS block ($M_{n\text{-}PS}$):

$$L_{PS} = (0.107 \pm 0.010) M_{n-PS}^{1/2} \text{ (nm)} \quad 5.3$$

Using Eq. 5.3, the estimated thicknesses of PS lamellae were 12.0 ± 1.1 nm, 12.4 ± 1.2 nm, and 12.3 ± 1.1 nm for the diblock, normal tapered, and inverse tapered systems, respectively, and we note that the lower bounds of these values were close to the values computed from XRR model. t_S then was calculated as 1.0 ± 0.1 nm for I-S, 1.4 ± 0.1 nm for I-IS-S, and 2.6 ± 0.2 nm for I-SI-S by substituting the above values into Eq. (2). Thus, the total thickness of the interfacial region is $t_{DSC} = t_S + t_I \approx 2t_S$ when one accounts for the interfacial region on the PI side. We note the interfacial thicknesses of the I-S, I-IS-S, and I-SI-S polymers estimated from DSC had a similar trend to the XRR results; however, the values were somewhat smaller in comparison to *t* determined from XRR (Table 5.2). The discrepancy in the estimation of interfacial thickness may result from the fact that DSC explores the region where the molecular motion of the PS segments is different from the rest of phase by being in close proximity to the PI segments,[30, 31] while XRR detects differences in scattering length density, which directly relates to the degree of mixing of the two components and likely provides a more accurate compositional profile across the interface.[33]

Table 5.2: DSC data for the BPs studied herein

Polymer	$T_{g\text{-}PI}$ (°C)	$T_{g\text{-}PS}$ (°C)	$\Delta C_{P\text{-}PI}$ (J g^{-1} K^{-1})	$\Delta C_{P\text{-}PS}$ (J g^{-1} K^{-1})	t_{DSC} (nm)[a]	δ from XRR (nm)	t from XRR (nm)[b]
I-S	-61.5	76.3	0.39	0.26	1.9	1.9	4.8
I-IS-S	-60.6	71.4	0.39	0.24	2.8	2.1	5.2
I-SI-S	-59.7	61.1	0.35	0.18	5.2	4.2	10.5

a: estimated from Equation (2)
b: calculated from $t \approx 2.5\delta$

5.3.3 Free Surface Morphologies in Thin Films

The interfacial mixing phenomena described above also influenced the free surface morphology of the thin films. During thermal annealing, island/hole structures formed at the film surface when the thickness of the film was incommensurate with the BP domain spacing.[34] When examining the free surface morphologies of these three films, the island/hole structures of inverse tapered I-SI-S thin film appeared much larger in comparison to diblock I-S and normal tapered I-IS-S films (Figure 5.5). The equilibrium size distribution of the structures was analyzed using ImageJ. Because the surface pattern evolved with the surface coverage (large islands formed when the surface coverage was small), the size of the island structures was analyzed at similar surface coverage ~30%. A log-normal distribution accurately captured the size distribution as shown in Figure 5.6. Comparison of island sizes was made using the mode of the characterized log-normal distribution (global maximum of the probability density function). The modes of the island size distributions were $1.3 \pm 0.4\ \mu m^2$ for the I-S film, $1.4 \pm 0.4\ \mu m^2$ for the I-IS-S film, and $8.5 \pm 0.4\ \mu m^2$ for the I-SI-S film. Previous studies have demonstrated the size of these surface patterns depends on the molecular weight of the BPs,[35, 36] annealing temperature,[37] and surface energetics of the substrates.[38, 39] The influence of molecular weight and annealing temperature was interpreted to arise from variations in surface elasticity as defined by the bending elasticity of the outer block polymer layer.[35-37, 40] Decreasing the molecular weight (*i.e.*, outer block polymer layer) or increasing the annealing temperature causes the surface elasticity to decrease and results in the formation of larger surface patterns. In our case, the substrate surface was identical for all samples. The top surface was covered by PI due to its low surface energy. For the inverse tapered I-SI-S polymer, the PI-rich domain was smaller, and the annealing temperature (90 °C) was closer to

the polymer's T_{ODT} (94 °C) due to increased mixing. Thus, the surface elasticity was smaller in comparison to the non-tapered and normal tapered BPs, possibly leading to larger island/hole structures. The importance of surface elasticity in BP pattern formation could be demonstrated further by AFM line scans across the island structures (Figure 5.7). The slopes at the boundary of island structures were 51 nm μm^{-1}, 44 nm μm^{-1}, and 21 nm μm^{-1} for the I-S, I-IS-S, and I-SI-S films, respectively. The I-SI-S film showed a more gradual slope across the island boundaries, suggesting that the resistance to deformation (stretching/compression) is lower in the inverse tapered polymer, and the island boundary profile is closer to that of an unstructured liquid (which would have a zero slope, *e.g.*, a uniform film of PI). The lamellar domain spacing determined from the height of the island structures (Figure 5.7) was consistent with the SAXS measurements for the bulk polymers, suggesting that the surface relief structures were equilibrated. Thus, these results demonstrate tapered interfacial manipulation as a new approach to tune the surface patterns in thin films that could be useful for many technological applications.

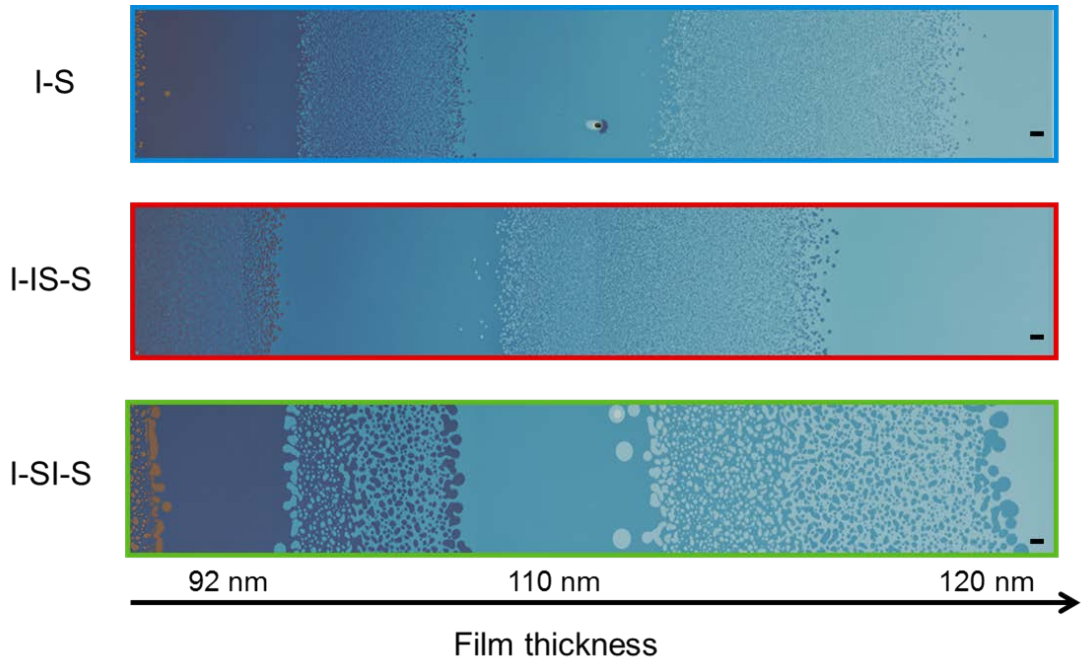

Figure 5.5: Optical images of gradient thickness I-S, I-IS-S and I-SI-S films showing cyclic changes of island/hole structures. The I-S and I-IS-S films were annealed at 100 °C for 6 h, and the I-SI-S film was annealed at 90 °C for 6 h. Close to the commensurability condition, films appeared featureless; with increasing film thickness, the morphology progressed from islands to bicontinuous island/hole structures to holes to featureless at the next commensurate thickness. Note the difference in island/hole sizes between the I-SI-S (inverse tapered) BP and the I-S (non-tapered) and I-IS-S (normal tapered) BPs. The scale bars represent 20 μm. Reprinted with permission from Luo, M., *et al. Macromolecules*, 2016, 49, (14), 5213-5222.

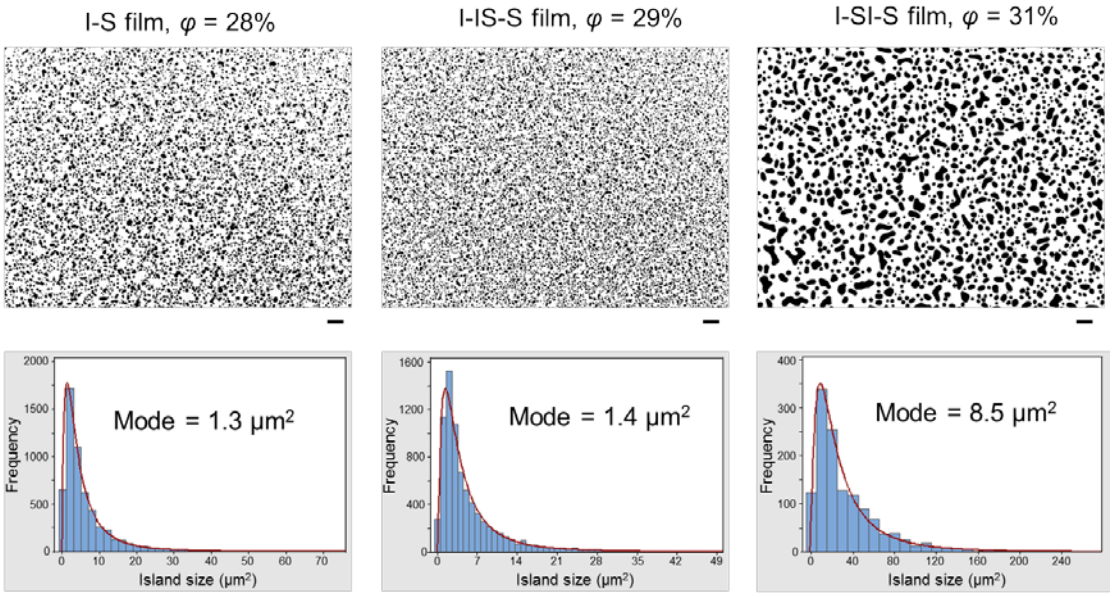

Figure 5.6: Top: optical images (converted to binary images by ImageJ) of I-S, I-IS-S and I-SI-S films showing island structures. Scale bars represent 20 μm. Bottom: histograms of sizes of island structures fit to log-normal distributions (red curve). Comparison of island size was on the basis of the mode of the characterized log-normal distribution (*i.e.*, global maximum of the probability density function). Reprinted with permission from Luo, M., *et al. Macromolecules*, 2016, 49, (14), 5213-5222.

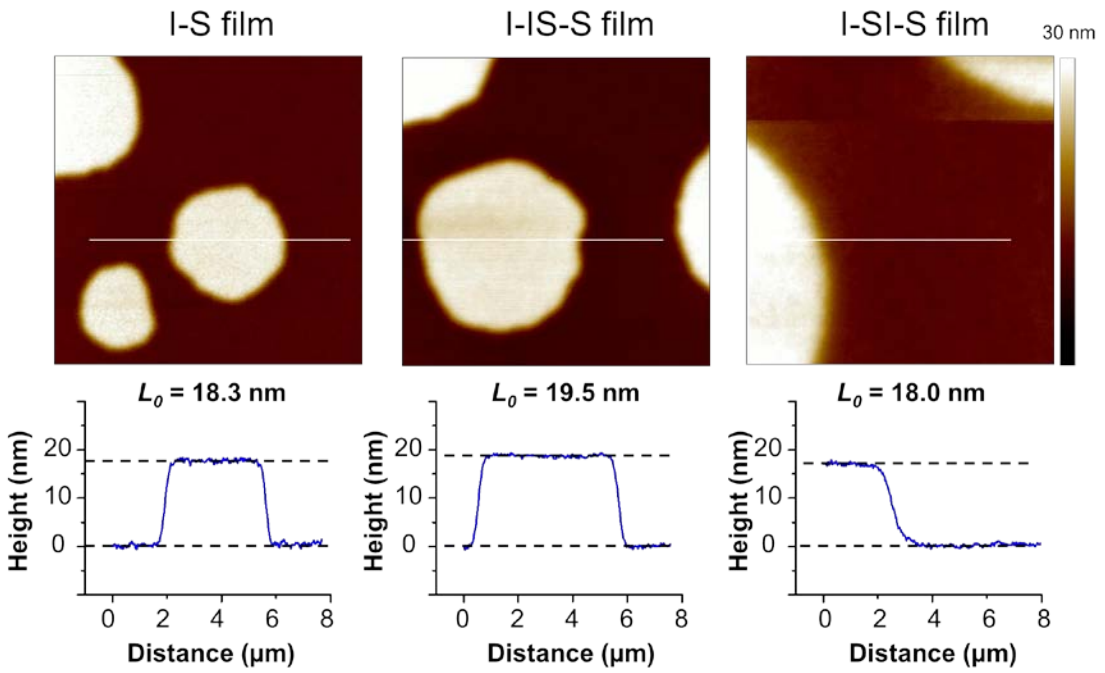

Figure 5.7: AFM height images and corresponding sectional analysis showed that the differences between the high and low regions are ~L_0. The I-SI-S film showed a more gradual slope across the island boundary. Reprinted with permission from Luo, M., *et al. Macromolecules*, 2016, 49, (14), 5213-5222.

5.4 Conclusion

Interfacial modification through tapering constitutes an additional design parameter that permits the manipulation of BP structure and properties. This chapter reports the first quantitative measurements of interfacial mixing characteristics in TBP thin films. The experimental and theoretical results indicated that the monomer sequence is important to macroscopic physical properties. Specifically, the inverse tapered interface greatly improved the compatibility between the block domains, widened the interfacial region, and increased the size of the surface relief structures (island/hole structures). The quantitative analysis of the interfacial mixing in these

tapered materials allows us to connect macroscopic physical properties to microscopic molecular structures and furthers our understanding of interfacial modifications as a valuable tool for materials design. More importantly, our research group demonstrated taper interfacial modification as a promising strategy for designing highly tunable, mechanically-stable, and easily-processable BP electrolytes for lithium battery applications. The work herein will provide useful insights in optimizing synthetic parameters to achieve desired properties.

REFERENCES

1. Roy, R.; Park, J. K.; Young, W.-S.; Mastroianni, S. E.; Tureau, M. S.; Epps, T. H., III. *Macromolecules* **2011,** 44, (10), 3910-3915.

2. Singh, N.; Tureau, M. S.; Epps, T. H., III. *Soft Matter* **2009,** 5, (23), 4757-4762.

3. Hodrokoukes, P.; Floudas, G.; Pispas, S.; Hadjichristidis, N. *Macromolecules* **2001,** 34, (3), 650-657.

4. Adhikari, R.; Michler, G. H.; Huy, T. A.; Ivan'kova, E.; Godehardt, R.; Lebek, W.; Knoll, K. *Macromol. Chem. Phys.* **2003,** 204, (3), 488-499.

5. Sigle, J. L.; Clough, A.; Zhou, J.; White, J. L. *Macromolecules* **2015,** 48, (16), 5714-5722.

6. Huy, T. A.; Hai, L. H.; Adhikari, R.; Weidisch, R.; Michler, G. H.; Knoll, K. *Polymer* **2003,** 44, (4), 1237-1245.

7. Brown, J. R.; Sides, S. W.; Hall, L. M. *ACS Macro Letters* **2013,** 2, (12), 1105-1109.

8. Kuan, W.-F.; Roy, R.; Rong, L.; Hsiao, B. S.; Epps, T. H., III. *ACS Macro Letters* **2012,** 1, (4), 519-523.

9. Jouenne, S.; González-León, J. A.; Ruzette, A.-V.; Lodefier, P.; Tencé-Girault, S.; Leibler, L. *Macromolecules* **2007,** 40, (7), 2432-2442.

10. Brown, J. R.; Seo, Y.; Maula, T. A. D.; Hall, L. M. *J. Chem. Phys.* **2016,** 144, (12), 124904.

11. Pakula, T.; Matyjaszewski, K. *Macromol. Theory Simul.* **1996,** 5, (5), 987-1006.

12. Seo, Y.; Brown, J. R.; Hall, L. M. *Macromolecules* **2015,** 48, (14), 4974-4982.

13. Fetters, L. J.; Lohse, D. J.; Richter, D.; Witten, T. A.; Zirkel, A. *Macromolecules* **1994,** 27, (17), 4639-4647.

14. *Tramonto Software* **2015,** https://software.sandia.gov/DFTfluids/index.html.

15. Oleksy, A.; Hansen, J.-P. *Mol. Phys.* **2006,** 104, (18), 2871-2883.

16. Jain, S.; Dominik, A.; Chapman, W. G. *J. Chem. Phys.* **2007,** 127, (24), 244904.

17. Weeks, J. D.; Chandler, D.; Andersen, H. C. *J. Chem. Phys.* **1971,** 54, (12), 5237-5247.

18. Jain, T. S.; de Pablo, J. J. *Phys. Rev. Lett.* **2004,** 92, (15), 155505.

19. Gilbert, J. B.; Luo, M.; Shelton, C. K.; Rubner, M. F.; Cohen, R. E.; Epps, T. H., III. *ACS Nano* **2015,** 9, (1), 512-520.

20. Anastasiadis, S. H.; Russell, T. P.; Satija, S. K.; Majkrzak, C. F. *J. Chem. Phys.* **1990,** 92, (9), 5677-5691.

21. Semenov, A. N. *Macromolecules* **1993,** 26, (24), 6617-6621.

22. Mori, K.; Okawara, A.; Hashimoto, T. *J. Chem. Phys.* **1996,** 104, (19), 7765-7777.

23. Han, C. D.; Baek, D. M.; Kim, J. K.; Ogawa, T.; Sakamoto, N.; Hashimoto, T. *Macromolecules* **1995,** 28, (14), 5043-5062.

24. Rubinstein, M.; Colby, R. H., *Polymer Physics*. Oxford University Press: New York, 2003.

25. Morèse-Séguéla, B.; St-Jacques, M.; Renaud, J. M.; Prud'homme, J. *Macromolecules* **1980,** 13, (1), 100-106.

26. Widmaier, J. M.; Meyer, G. C. *Macromolecules* **1981,** 14, (2), 450-452.

27. Fox, T. G.; Flory, P. J. *J. Appl. Phys.* **1950,** 21, (6), 581-591.

28. Kim, J.; Mok, M. M.; Sandoval, R. W.; Woo, D. J.; Torkelson, J. M. *Macromolecules* **2006,** 39, (18), 6152-6160.

29. Zhou, Y. N.; Li, J. J.; Luo, Z. H. *J. Polym. Sci. A Polym. Chem.* **2012,** 50, (15), 3052-3066.

30. Miwa, Y.; Tanida, K.; Yamamoto, K.; Okamoto, S.; Sakaguchi, M.; Sakai, M.; Makita, S.; Sakurai, S.; Shimada, S. *Macromolecules* **2004,** 37, (10), 3707-3716.

31. Miwa, Y.; Yamamoto, K.; Sakaguchi, M.; Sakai, M.; Tanida, K.; Hara, S.; Okamoto, S.; Shimada, S. *Macromolecules* **2004,** 37, (3), 831-839.

32. Séguéla, R.; Prud'homme, J. *Macromolecules* **1978,** 11, (5), 1007-1016.

33. Tanaka, H.; Nishi, T. *J. Chem. Phys.* **1985,** 82, (9), 4326-4331.

34. Albert, J. N. L.; Epps, T. H., III. *Materials Today* **2010,** 13, (6), 24-33.

35. Smith, A. P.; Douglas, J. F.; Meredith, J. C.; Amis, E. J.; Karim, A. *Phys. Rev. Lett.* **2001,** 87, (1), 015503.

36. Smith, A. P.; Douglas, J. F.; Meredith, J. C.; Amis, E. J.; Karim, A. *J. Polym. Sci. Part B: Polym. Phys.* **2001,** 39, (18), 2141-2158.

37. Smith, A. P.; Douglas, J. F.; Amis, E. J.; Karim, A. *Langmuir* **2007,** 23, (24), 12380-12387.

38. Peters, R. D.; Yang, X. M.; Kim, T. K.; Nealey, P. F. *Langmuir* **2000,** 16, (24), 9620-9626.

39. Shelton, C. K.; Epps, T. H., III. *Macromolecules* **2015,** 48, (13), 4572-4580.

40. Wang, Z. G.; Safran, S. A. *J. Chem. Phys.* **1991,** 94, (1), 679-687.

Chapter 6

DEPTH PROFILING IN NANOSTRUCTURED BLOCK POLYMER ELECTROLYTE THIN FILMS

In this chapter, the unique capabilities of high resolution C_{60}^{+} depth profiling X-ray photoelectron spectroscopy (XPS) was demonstrate as a method to resolve the ion distribution in a lamellar forming block polymer (BP) electrolyte thin film, which is previously considered challenging by conventional scattering or electron microscopy technique. This novel experimental technique is potentially applicable to investigations of nanoscale distributions of additives in a myriad of nanostructured polymer thin film systems. Text and figures are reproduced and adapted with permission from Gilbert, J. B.; Luo, M.; Shelton, C. K.; Rubner, M. F.; Cohen, R. E.; Epps III, T. H. *ACS Nano* **2014,** 9, (1), 512-520.

6.1 Introduction

In recent years, BPs with an ion-solvating block, typically poly(ethylene oxide) (PEO), and a non-conducing block such as polystyrene (PS), have received considerable attention as viable rechargeable battery membrane materials because of their high thermal, mechanical and electrochemical stabilities compared to the traditional liquid or gel-like electrolyte systems.[1] The liquid-like PEO block (usually complexed with a metal salt such as a lithium salt) forms ion-conducting pathways, while the rigid PS block provides mechanical strength to resist lithium dendrite formation and confer thermal and mechanical stability. Because the conductivity and

mechanical strength are decoupled, it becomes possible to design battery systems that simultaneously address improvements in ion conductivity and mechanical properties.[2, 3]

Extensive studies have focused on elucidating the relationship between mechanical properties, ionic conductivity, and BP morphologies.[1, 4-8] While the morphology effects on mechanical properties of BP electrolytes have been well-studied and understood,[7, 8] the morphology effects (domain structure, domain size *etc.*) on the ionic conductivities are much more complicated. In the simplest symmetric PS-PEO lamellar systems doped with lithium salt, Panday *et al.* demonstrated that the ion conductivity increased with increasing molecular weight of the PEO block (M_{PEO}, 7 to 98 kg/mol),[3] while Yuan *et al.* investigated the low molecular regime (M_{PEO}, 1.5 to 7 kg/mol) and found the ion conductivity decreased with increasing M_{PEO}.[9] This non-monotonic change in the conductivity of the BP systems with changing molecular weight (changing lamellar domain size), prompted efforts to understand the influence of local ion distribution in lamellar domains on conductivity. Gomez *et al.* presented the first direct imaging of lithium ions in PS-PEO bulk system using energy-filtered transmission electron microscopy (EFTEM).[10] They showed that the lithium salt was progressively more localized to the middle of the PEO lamellae with increasing M_{PEO} (16 to 98 kg/mol), and the increase of ion conductivity at higher molecular weights was strongly correlated to the localization of the lithium cation. The authors attributed the localization effect to inhomogeneous local stress field in BP microdomains, as calculated from self-consistent field theory for the salt-free system. However, the quantitative determination of salt distribution profiles was difficult by EFTEM. Additionally, in contrast to that report, a uniform distribution of lithium ions was

posited by Nakamura and Wang when considering the Li+ ions bonded to the EO groups can freely redistribute on the backbone, suggesting factors such as electrostatic potential and local solvation energy be equally important in affecting the ion distribution.[11]

To address this unresolved and important topic, XPS depth profiling with C_{60}^{+} sputtering was employed herein to determine the ion distribution in lithium salt-doped BP thin films. The electrolytes of interest are mixtures of lithium triflate (lithium trifluoromethanesulfonate) and lamellar-forming PS-poly(oligo(oxyethylene) methacrylate) (PS-POEM) copolymer. The room temperature conductivity of this PEO-grafted BP is of great interest given the substantial improvement over PEO-linear BP.[12, 13] Through XPS depth profiling analysis, the presence of the lithium salt in the POEM region was confirmed and the lithium distribution was directly correlated to the POEM concentration. Furthermore, chemical state and atomic composition of the film were analyzed through the deconvolution of the C1s signal, indicating the lithium ions appear to be distributed uniformly in the POEM domains. These results have important implications for understanding local environment of ions in nanostructured polymer systems and provide crucial insights for the future design and optimization of BP structures for high efficiency energy storage devices.

6.2 Materials and Methods

6.2.1 Materials and Thin Film Preparation

The PS-POEM used in this study had an overall molecular weight of 36 kg/mol (PS_{20k}-$POEM_{16k}$) and formed lamellae in the bulk with domain spacing (L_0) of 26.1 nm (determined from small angle X-ray scattering [SAXS], see Appendix D).

The calculated weight fraction of the PS block was 0.56. The volume fraction for the PS block was ~0.60 calculated using polymer densities $\rho_{POEM,\ 25\ °C}$ = 1.197 g cm^{-3} (measured from densitometer) and $\rho_{PS,\ 25\ °C}$ = 1.05 g cm^{-3} (from literature[14]); therefore the PS domain thickness was approximately ~15.6 nm.

Blends of PS-POEM and $LiCF_3SO_3$ were generated in tetrahydrofuran (THF) solution in an argon glovebox, and methanol was added to the mixture to help dissolve the polymer-salt complex. The salt concentration (ether oxygen to lithium cation ratio, [EO]:[Li]) was either 12:1 or 6:1. Thin films of PS-POEM doped with lithium triflate were fabricated by flow coating from a blend solution onto the silicon wafers as illustrated in Figure 6.1. Film thicknesses were measured using a reflectance spectrometer (Filmetrics F20-UV). After casting, the thin films were annealed at 135 °C under vacuum for 6 h to promote the formation of parallel-oriented lamellar nanostructures in the films, which was ideal for the intradomain characterization of the thin films by XPS.

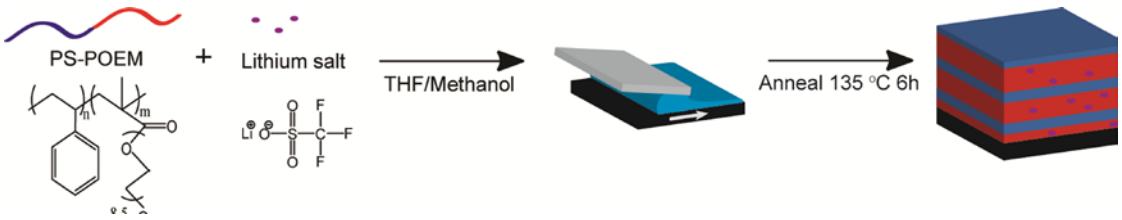

Figure 6.1: Fabrication schematic of lamellar PS-POEM lithium-doped thin films. Reprinted with permission from Gilbert, J. B.; Luo, M.; Shelton, C. K.; Rubner, M. F.; Cohen, R. E.; Epps III, T. H. *ACS Nano* 2014, 9, (1), 512-520.

6.2.2 Thin Film Characterization

Optical microscopy images of the thin films were collected on a Nikon microscope equipped with a 5 MP CCD camera (Nikon Eclipse LV100). The topologies of the polymer films were assessed by tapping mode AFM (Veeco Dimension 3100). X-ray Reflectivity measurements were conducted X-ray reflectivity measurements were performed for the polymer thin films on the lithium salt doped thin films using an Ultima IV unit (Rigaku) as described in Chapter 2 Section 2.7.2. A thin, parallel beam of Cu Kα radiation, $\lambda = 0.154$ nm, was incident on the samples. The beam was sized to capture the critical edge of the samples for best results and fit accuracy. XRR profiles were collected by scanning a small incident angle (θ) of X-rays from the source and a detection angle (2θ) of reflected X-rays ($0° < 2\theta < 3°$). The fit profiles across the film thicknesses were calculated using the GlobalFit software.

In collaboration with the Cohen group in the Department of Chemical Engineering and the Rubner group in the Department of Materials Science and Engineering at MIT, XPS depth profiling was performed by Jonathan B. Gilbert for the polymer samples studied here (More details about XPS depth profiling are available in Chapter 2 Section 2.8). C1s, O1s, F1s, Li1s and Si2p signals were collected after each etching step. The detailed XPS acquisition parameters are in Appendix D. Spectra peaks were fit in CasaXPS, and data were plotted and analyzed using Matlab.

6.3 Results and Discussion

6.3.1 Nanostructured Block Polymer Electrolyte Films

The domain structure of the thin film samples were characterized by optical microscopy and AFM. The optical images revealed that the gradient thickness films exhibited cyclic changes between island/hole structures and uniform surface regions (Figure 6.2a), which was expected for parallel orientations of lamellar nanostructures in thin film geometries.[15] The lamellar domain spacing was determined from the height of the island/hole structures through AFM (Figure 6.2b). Upon salt loading, the lamellar domain spacing (L_0) increased from 26.8 nm (neat) to 36.0 nm (12:1 [EO]:[Li]) to 41.3 nm (6:1 [EO]:[Li]) (Figure 6.2b), as the salt preferentially swelled the POEM domain.[10] This increase in domain spacing was consistent with SAXS measurements of the comparable bulk materials (Figure 6.2c). The substantial change in domain spacing (over 50%) without a phase transition has been reported in other salt-doped BP systems.[16] From commensurability calculations, the PS-POEM films showed prominent island/hole structures at film thicknesses of nL_0, and uniform surfaces at (n+0.5) L_0, which indicated an asymmetric wetting conditions.[15] Due to the affinity of the polar methacrylate-based backbone and PEO side chain for the hydrophilic silicon oxide surface, the POEM block tended to segregate to the substrate. The PS block resided at the free surface supporting an asymmetric wetting assignment (the presence of POEM at the substrate and PS at the top surface was confirmed by XPS as discussed in a later section).

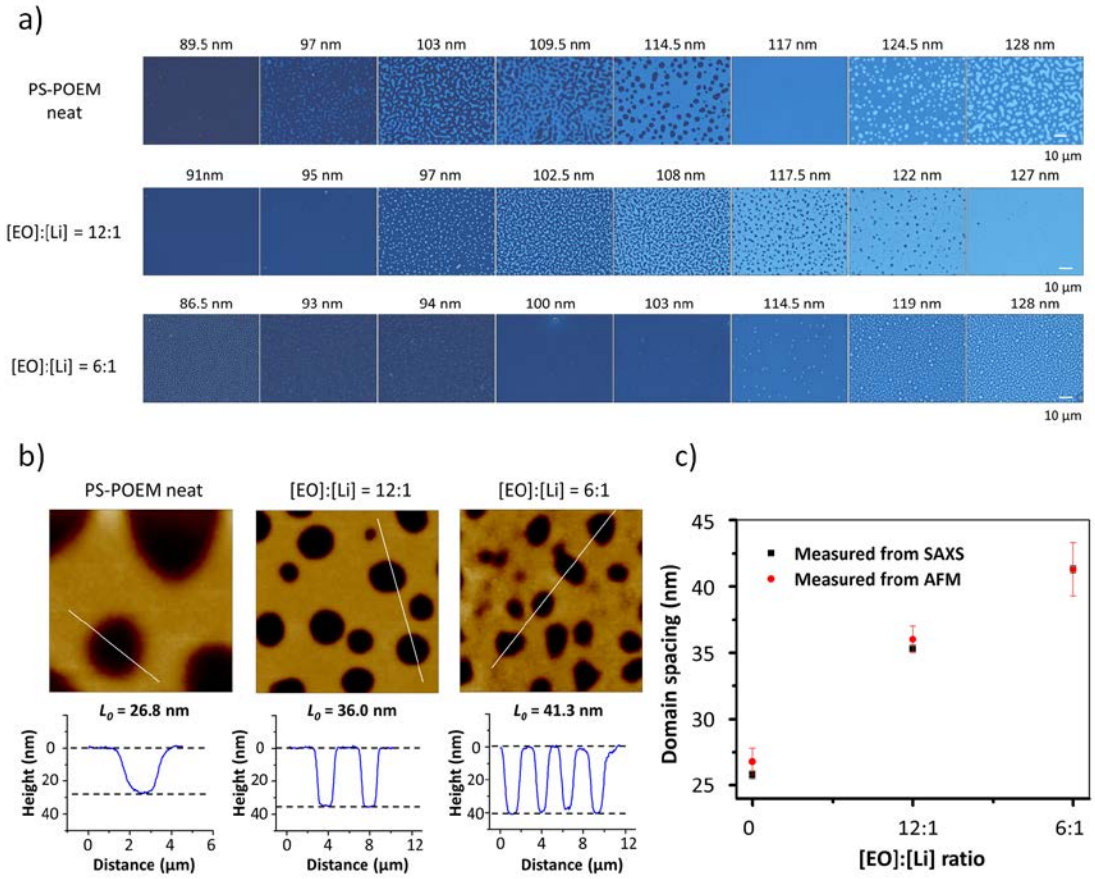

Figure 6.2: (a) Optical images of gradient thickness PS-POEM films (neat, [EO]:[Li] = 12:1 and 6:1) annealed at 135 °C for 6 h; (b) AFM height images and corresponding sections showed that the difference between the high and low regions are L_0; (c) Comparison of the measured domain thickness between AFM and SAXS. Reprinted with permission from Gilbert, J. B.; Luo, M.; Shelton, C. K.; Rubner, M. F.; Cohen, R. E.; Epps III, T. H. *ACS Nano* 2014, 9, (1), 512-520.

XRR experiments were performed on the thin film samples ([EO]:[Li] = 12:1 and 6:1) to confirm the layered structures. The film thicknesses were ~90 nm for [EO]:[Li] = 12:1 sample, and ~102 nm for [EO]:[Li] = 6:1 sample, thus, both of the films were at commensurate film thickness (2.5 L_0). The measured and model

calculated XRR profiles for these two samples were shown in Figure 6.3. The thin film model for the calculated profile incorporates a capping layer of PS at the air surface, a wetting layer of POEM at the substrate, and two repeats of POEM and PS layers in the bulk of the film. Because it is well known that salt solutions do not obey the ideal mixing rule,[17] the density of the salt-doped POEM layer was estimated from separate measurements on a salt-doped POEM homopolymer film ([EO]:[Li] = 6:1) using XRR; the density of the PS layer was based on values from the literature.[14] From the XRR fitting, the lamellar repeats (consisting of a POEM layer and a PS layer) were ~36 nm for [EO]:[Li] = 12:1 sample and ~40 nm for [EO]:[Li] = 6:1 sample, respectively. These values were in good agreement with the domain spacings measured from AFM and SAXS. Additionally, the fitted PS layer thickness was approximately 16 nm, which was similar to the values in the neat PS-POEM.

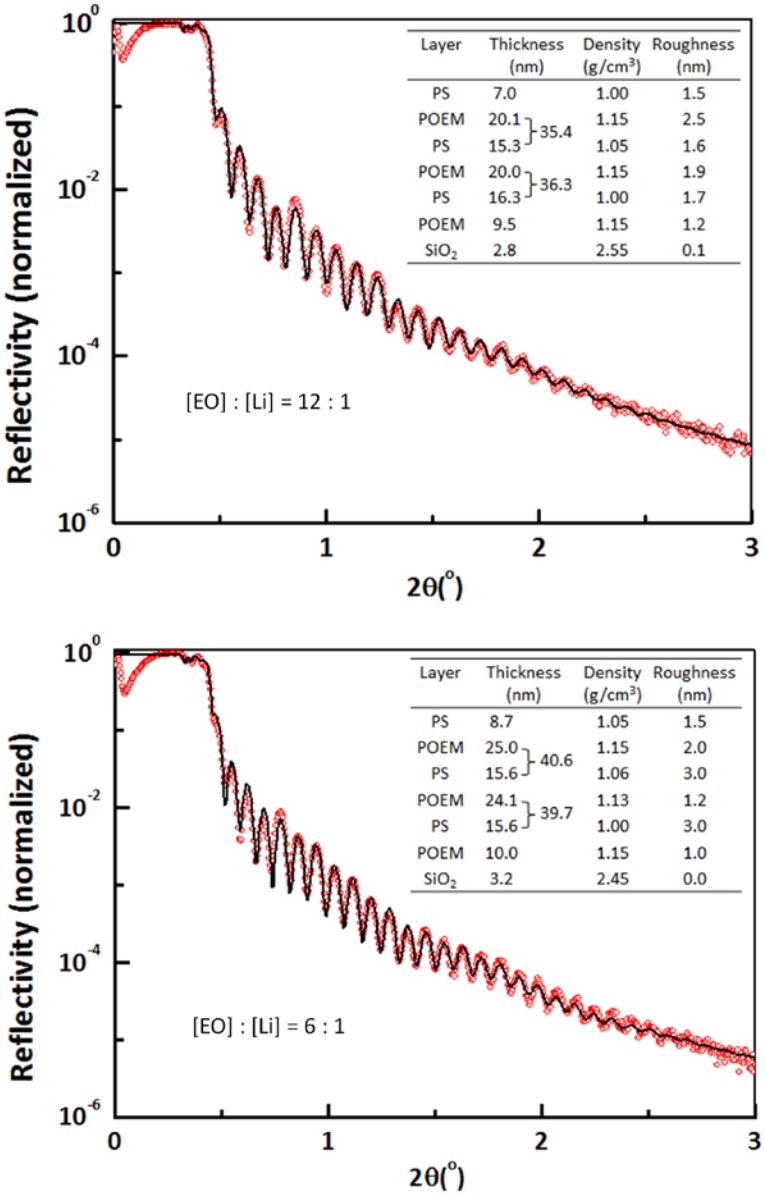

Figure 6.3: XRR profiles for the lithium-doped PS-POEM films with [EO]:[Li] of 12:1 (top) or 6:1 (bottom). The red "o" symbols denote the measured profile, and the solid line denotes the fit profile. The inset tables list the fitting parameters for the model. Reprinted with permission from Gilbert, J. B.; Luo, M.; Shelton, C. K.; Rubner, M. F.; Cohen, R. E.; Epps III, T. H. *ACS Nano* 2014, 9, (1), 512-520.

6.3.2 XPS Depth Profiling with C_{60}^+ Cluster-Ion Sputtering

XPS depth profiling with C_{60}^+ cluster-ion sputtering was used to resolve the material distribution profile normal to the substrate in the lithium-doped PS-POEM films. The alternative EFTEM technique is less quantitative for thin film analysis of dopants, such as lithium due to their small concentrations across the domains, and sample preparation and image analysis can be tedious depending on the nanostructure orientation. Note: the choice of EFTEM vs. cluster ion XPS can be system (or nanostructure) dependent,[18, 19] as each technique has potential limitations. XPS depth profiling is suitable for lamellar-forming BPs and also may be useful for probing domain profiles in other self-assembled nanostructures.[20, 21]

Using iterative etching and XPS data collection (Figure 6.4a), the discrete nanostructured lamellar regions noted in the XRR results could be reproduced. To minimize the X-ray damage, a large sample area (~0.1 mm^2) was analyzed. Furthermore, film thicknesses were chosen such that the film was free of island/hole structures. The thickness for the neat PS-POEM film was ~117 nm, corresponding to 4.5 L_0 ; the thickness for the lithium salt-doped PS-POEM film ([EO]:[Li] = 6:1) was ~102 nm, corresponding to 2.5 L_0. The alternating C1s and O1s signals of the neat lamellar thin film were shown Figure 6.4b. Near the silicon substrate, significant signal from the Si2p peak was identified as well as an increase in the O1s signal due to SiO_2. The alternating intensity of the O1s spectra was displayed in Figure 6.4c, for which the red spectra represents to the POEM layers (high oxygen content in EO side-chains), and the blue spectra corresponds to the PS layers (very low, but non-zero oxygen content owing to etching roughness effects[22]). The C1s signal in Figure 6.4d depicts a similar alternating structure, and two C1s peaks (285.0 eV and 286.5 eV) could be detected. For the blue spectra representing the PS layers, the C1s peak at

285.0 eV corresponds to carbon-carbon bonds and is the dominant feature. For the red spectra representing the POEM layers, the C1s peak at 286.5 eV primarily results from the ether bonds in the PEO side chain. There was also a carbon-carbon bonding peak in the red spectra at 285.0 eV due to the carbon-carbon backbone with a minor contribution from the underlying PS layer. The atomic profile in Figures 6.4c and 6.4d also supports the notion that the film demonstrates asymmetric wetting, with PS at the air interface and POEM in contact with the substrate.

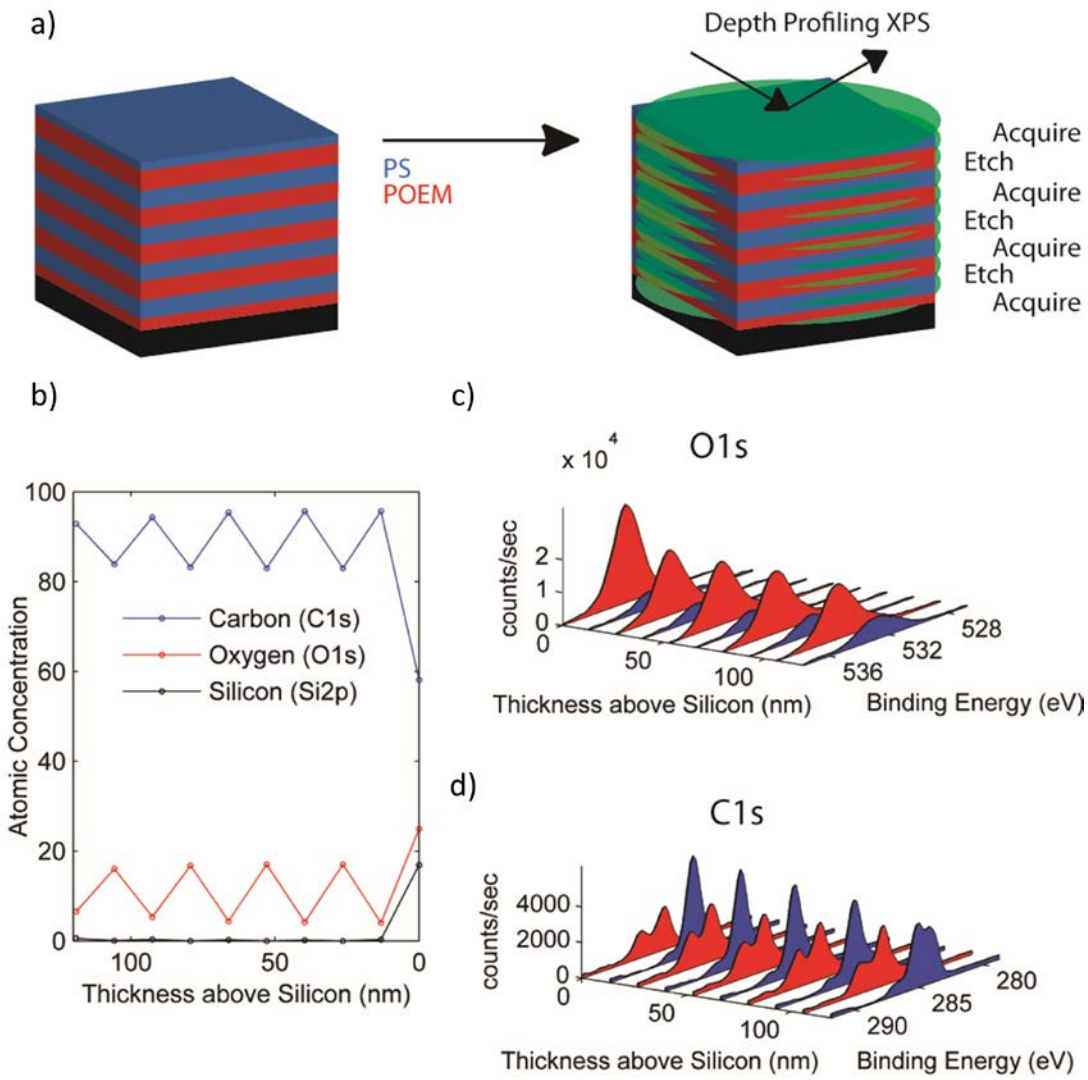

Figure 6.4: XPS depth profiling of the neat PS-POEM film. (a) Schematic of depth profiling XPS analysis. (b) Atomic concentration *versus* thickness above the silicon substrate. (c) and (d) O1s and C1s photoelectron spectra, respectively, showing the alternating intensity of a lamellar BP film. The red and blue spectra are primarily representative of the POEM and PS lamellae, respectively. Reprinted with permission from Gilbert, J. B.; Luo, M.; Shelton, C. K.; Rubner, M. F.; Cohen, R. E.; Epps III, T. H. *ACS Nano* 2014, 9, (1), 512-520.

6.3.3 Determination of Lithium Ion Distribution

To analyze the distribution of lithium ions within BP electrolyte films, the effective C_{60}^+ etch rate was decreased to allow for higher resolution in the axial distribution. Also lithium salt was added at a [EO]:[Li] = 6:1 ratio to maximize the lithium signal. The alternating C1s, Li1s, F1s and O1s signals were shown in Figure 6.5d-g, and the resulting depth profile (Figure 6.5a) captured the repeating structure of a lamellar PS-POEM film doped with lithium salt. The domain spacing as measured by the distance between the peaks of Figure 6.5a (~ 40 nm), also matched the spacing measured *via* XRR (Figure 6.3). Furthermore in the O1s rich region there was significant Li1s and F1s signal, supporting the segregation of the lithium-ion and fluorine-containing triflate counter-ion ($CF_3SO_3^-$) in the oxygen rich POEM layers. This capability to measure accurate domain structure and atomic composition as a function of depth in organic nanostructured films is a strength of cluster-ion depth profiling XPS.

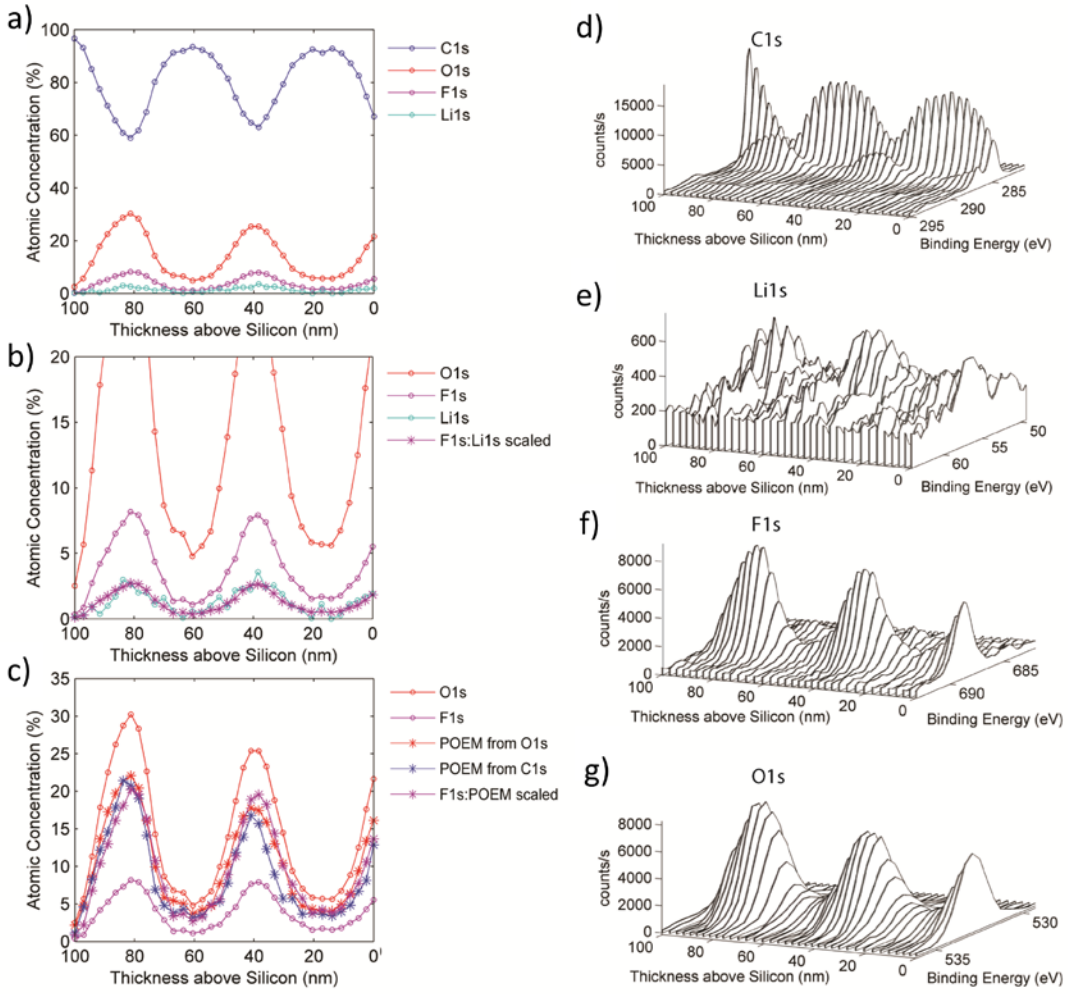

Figure 6.5: XPS depth profiling of PS-POEM doped with Li salt ([EO]:[Li] = 6:1). (a) Atomic concentration profile with depth. (b) Rescaled atomic concentration profile with depth to focus on lower concentration species, includes overlay of F1s scaled to Li1s signal. (c) Distribution of POEM block within the film analyzed via O1s signal or fitting the C1s peaks. To compare the salt distribution to the POEM distribution the F1s is scaled to POEM. (d), (e), (f) and (g) 3D spectra of the C1s, Li1s, F1s and O1s regions respectively. The differing etch rates of PS vs. POEM (see Appendix D) were taken into account in plotting the data. Reprinted with permission from Gilbert, J. B.; Luo, M.; Shelton, C. K.; Rubner, M. F.; Cohen, R. E.; Epps III, T. H. *ACS Nano* 2014, 9, (1), 512-520.

The sinusoidal nature of the atomic concentration profile in Figure 6.5a has been seen previously in nanostructured inorganic multilayer systems analyzed with secondary ion mass spectrometry (SIMS) and depth profiling XPS.[22, 23] The broadened interface can be attributed to experimental effects such as etching induced roughness (σ), atomic mixing (w) and the inelastic mean free path (IMFP) (λ) of the photoelectron measured. To enable the analysis of the underlying structure, Hofmann *et al.* has developed an analytical technique called the mixing-roughness-information depth (MRI) model to account these effects.[24] The MRI model showed excellent agreement with the depth profiling XPS data when σ = 5 nm was used (Figure 6.6). Because roughness likely is a dominant factor altering the profile, studies should consider employing the lowest beam energy possible, along with sample rotation and a large incidence angle to achieve the best resolution.

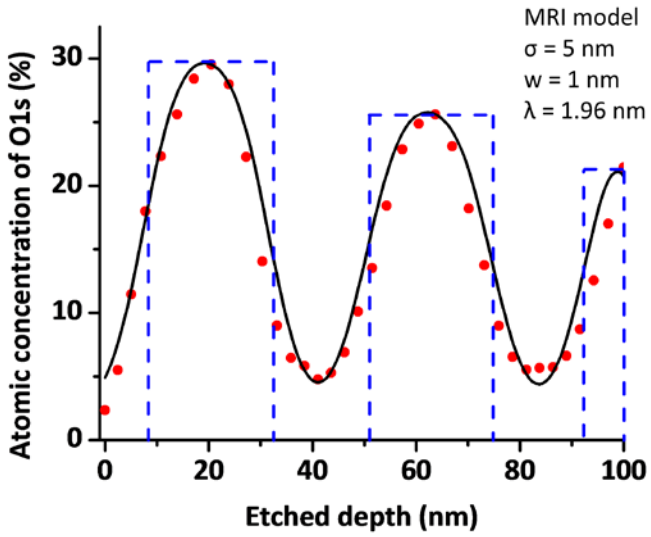

Figure 6.6: MRI model fit for the measured O1s depth profile. The dot symbols denote the measured profile, and the solid line denotes the fit profile from MRI model. The dash lines represent the position of the POEM block according to XRR results. Etching roughness (σ) and atomic mixing (w) were determined from the best fit to the depth profile. The information depth (λ) was estimated using the inelastic mean free path (IMFP) of O1s. Decreasing POEM intensity is noted due to X-ray damage and etching roughness. Reprinted with permission from Gilbert, J. B.; Luo, M.; Shelton, C. K.; Rubner, M. F.; Cohen, R. E.; Epps III, T. H. *ACS Nano* 2014, 9, (1), 512-520.

To determine the pairing or dissociation state of the lithium-ion and the fluorine containing counter-ion, the F1s signal was multiplied by the molar ratio of lithium to fluorine in the lithium salt (1:3), see Figure 6.5b. The resulting profile, 'F1s:Li1s scaled', allows for direct comparison of atomic concentrations. As 'F1s:Li1s scaled' overlays very closely with the Li1s signal, it indicates that the lithium-ion and the fluorine-containing triflate anion have a similar distribution in the POEM domains.[10]

The local distribution of lithium-ion within the POEM lamellae could be determined by analyzing the atomic and chemical composition of the film as demonstrated in Figure 6.5c. In the salt-doped PS-POEM system there are only two sources of oxygen (POEM and the lithium salt); by subtracting the contribution of the triflate counter-ion from the total oxygen signal, the axial distribution of the POEM within the film could be determined. Because the counter-ion ($CF_3SO_3^-$) has an equal molar ratio of fluorine and oxygen, the F1s signal represents the distribution of the triflate counter-ion. Therefore, the POEM concentration ('POEM from O1s') was determined by subtracting the F1s concentration from the O1s concentration. A complementary method for analyzing the POEM distribution is through component analysis of the C1s region. As shown in Figure 6.5d, the C1s region contained a variety of peaks, each corresponding to different chemical bonding states present within the BP. For example, the alternating photoelectron peaks found at 285.0 eV and 286.5 eV related to carbon-carbon bonds in the PS region and ether bonds in the POEM region, respectively. Using the known binding energy of the polymer components, the C1s peaks could be deconvoluted and directly assigned to lithium salt (*i.e.*, CF_3 group), PS, or POEM. An example of fitting the spectra with these peaks in both a PS rich region and a POEM rich region is provided in Appendix D. The corresponding POEM distribution from the C1s component analysis is plotted in Figure 6.5c ('POEM from C1s'), and the results of the two methods ('POEM from O1s' and 'POEM from C1s') were qualitatively similar. It is important to note that the capability to analyze the chemical composition as well as the atomic concentration is not easily possible using other analysis techniques such as SIMS or EFTEM.

A final step in the analysis was to determine the distribution of the lithium salt within the POEM layers. To enable a direct comparison between the lithium salt and the POEM on the same scale, the F1s concentration was multiplied by its molar ratio within the POEM region. F1s was used in place of the Li1s signal because the F1s signal had a higher signal-to-noise ratio, and earlier analysis showed that the F1s and Li1s concentration are tightly correlated (Figure 6.5b). The scaling of the lithium salt distribution was accomplished by multiplying the F1s concentration by the molar ratio of oxygen in the BP to fluorine in the salt (10.5:4.25, in [EO]:[Li] = 6:1 salt films, see Table D1 in Appendix D). The similarity of the 'F1s:POEM scaled' profile to the POEM profile suggests that the lithium salt concentration directly correlates with the POEM concentration. If the lithium concentration was non-uniformly distributed, one would not expect to see the coupling of the POEM and 'F1s:POEM scaled' distributions as shown in Figure 6.5c.

Overall, the XPS depth profiling results clearly showed that the concentrations of the lithium-ions and the fluorine-containing triflate anions were correlated tightly, and the lithium ions appear to be uniformly distributed in the POEM (side chain oligo ethylene oxide) domains. This finding supports the theoretical work by Nakamura *et al.* predicting uniform lithium ion distributions in which the lithium ions are assumed to freely distribute among the binding sites of the different PEO chains.[11] The experimental results herein differ from the previous investigation of ion distributions in PS-PEO BPs (main chain ethylene oxide) gleaned from electron microscopy.[10] However, the apparently discrepancies could be explained by the intricacies of the copolymer architectures, with differences in energetics resulting from the coordination of metal ions to side chain *versus* main chain solubilizing segments.[25] It is posited that

the solvating groups in the side chains of POEM have higher chain mobility and increase the freedom to coordinate lithium ions,[25] leading to a more uniform distribution of lithium ions across POEM domains.

6.4 Conclusion

In summary, this chapter presents the first experimental, quantitative determination of lithium salt distributions in nanostructured BP electrolyte thin films through XPS depth profiling with C_{60}^{+} cluster ion sputtering. The findings reported herein have important implications for understanding local environment of ions in nanostructured polymer systems and provide crucial insights for the future design and optimization of BP structures for high efficiency energy storage devices. Additionally, the unique capabilities of C_{60}^{+} depth profiling XPS as demonstrated herein are potentially applicable to investigations of nanoscale distributions of additives in a myriad of polymer thin film systems.

In particular, our research group has been developing interfacially-modified (tapered) BP systems, with a specific focus on network-forming materials. More importantly, our research group demonstrated taper interfacial modification as a promising strategy for designing highly tunable, mechanically-stable, and easily-processable BP electrolytes for lithium battery applications.

REFERENCES

1. Young, W.-S.; Kuan, W.-F.; Epps, T. H., III. *J. Polym. Sci. Part B: Polym. Phys.* **2014,** 52, (1), 1-16.

2. Singh, M.; Odusanya, O.; Wilmes, G. M.; Eitouni, H. B.; Gomez, E. D.; Patel, A. J.; Chen, V. L.; Park, M. J.; Fragouli, P.; Iatrou, H.; Hadjichristidis, N.; Cookson, D.; Balsara, N. P. *Macromolecules* **2007,** 40, (13), 4578-4585.

3. Panday, A.; Mullin, S.; Gomez, E. D.; Wanakule, N.; Chen, V. L.; Hexemer, A.; Pople, J.; Balsara, N. P. *Macromolecules* **2009,** 42, (13), 4632-4637.

4. Majewski, P. W.; Gopinadhan, M.; Osuji, C. O. *Soft Matter* **2013,** 9, (29), 7106-7116.

5. Weber, R. L.; Ye, Y.; Schmitt, A. L.; Banik, S. M.; Elabd, Y. A.; Mahanthappa, M. K. *Macromolecules* **2011,** 44, (14), 5727-5735.

6. Wanakule, N. S.; Panday, A.; Mullin, S. A.; Gann, E.; Hexemer, A.; Balsara, N. P. *Macromolecules* **2009,** 42, (15), 5642-5651.

7. Khandpur, A. K.; Foerster, S.; Bates, F. S.; Hamley, I. W.; Ryan, A. J.; Bras, W.; Almdal, K.; Mortensen, K. *Macromolecules* **1995,** 28, (26), 8796-8806.

8. Dair, B. J.; Honeker, C. C.; Alward, D. B.; Avgeropoulos, A.; Hadjichristidis, N.; Fetters, L. J.; Capel, M.; Thomas, E. L. *Macromolecules* **1999,** 32, (24), 8145-8152.

9. Yuan, R.; Teran, A. A.; Gurevitch, I.; Mullin, S. A.; Wanakule, N. S.; Balsara, N. P. *Macromolecules* **2013,** 46, (3), 914-921.

10. Gomez, E. D.; Panday, A.; Feng, E. H.; Chen, V.; Stone, G. M.; Minor, A. M.; Kisielowski, C.; Downing, K. H.; Borodin, O.; Smith, G. D.; Balsara, N. P. *Nano Lett.* **2009,** 9, (3), 1212-1216.

11. Nakamura, I.; Wang, Z.-G. *Soft Matter* **2012,** 8, (36), 9356-9367.

12. Niitani, T.; Shimada, M.; Kawamura, K.; Dokko, K.; Rho, Y. H.; Kanamura, K. *Electrochemical and Solid State Letters* **2005,** 8, (8), A385-A388.

13. Ruzette, A. V. G.; Soo, P. P.; Sadoway, D. R.; Mayes, A. M. *J. Electrochem. Soc.* **2001,** 148, (6), A537-A543.

14. Momose, A.; Fujii, A.; Kadowaki, H.; Jinnai, H. *Macromolecules* **2005,** 38, (16), 7197-7200.

15. Albert, J. N. L.; Epps, T. H., III. *Materials Today* **2010,** 13, (6), 24-33.

16. Young, W. S.; Albert, J. N. L.; Schantz, A. B.; Epps, T. H., III. *Macromolecules* **2011,** 44, (20), 8116-8123.

17. Teran, A. A.; Balsara, N. P. *The Journal of Physical Chemistry B* **2013,** 118, (1), 4-17.

18. Kesava, S. V.; Fei, Z.; Rimshaw, A. D.; Wang, C.; Hexemer, A.; Asbury, J. B.; Heeney, M.; Gomez, E. D. *Advanced Energy Materials* **2014,** 4, (11), 1400116.

19. Vajjala Kesava, S.; Dhanker, R.; Kozub, D. R.; Vakhshouri, K.; Choi, U. H.; Colby, R. H.; Wang, C.; Hexemer, A.; Giebink, N. C.; Gomez, E. D. *Chem. Mater.* **2013,** 25, (14), 2812-2818.

20. Zhao, L. Y.; Eldridge, K. R.; Sukhija, K.; Jalili, H.; Heinig, N. F.; Leung, K. T. *Appl. Phys. Lett.* **2006,** 88, (3), 033111.

21. Sharma, H.; Sharma, S. N.; Singh, S.; Kishore, R.; Singh, G.; Shivaprasad, S. M. *Appl. Surf. Sci.* **2007,** 253, (12), 5325-5333.

22. Wang, J. Y.; Starke, U.; Mittemeijer, E. J. *Thin Solid Films* **2009,** 517, (11), 3402-3407.

23. Hofmann, S. *Appl. Surf. Sci.* **2005,** 241, (1–2), 113-121.

24. Hofmann, S. *Thin Solid Films* **2001,** 398–399, (0), 336-342.

25. Tarascon, J. M.; Armand, M. *Nature* **2001,** 414, (6861), 359-367.

Chapter 7

SUMMARY AND OUTLOOK

7.1 Dissertation Summary

Over the past few decades, the self-assembly of block polymer (BP) in thin films has received enormous research interest for its potential utility in emerging nanotechnologies such as nanolithography,[1, 2] nanotemplating,[3, 4] nanoporous membranes,[5, 6] and ultra-high-density storage media.[7-9] The functionality, shape, and size of the self-assembled BP nanostructures are readily tunable by changing their components, compositions, molecular weights, and molecular architecture, all of which make BPs ideal for cost-effective nanoscale fabrication technologies.[10] Control of the BP thin film nanostructures, domain orientation, and domain ordering are crucial for the widespread adoption of BP thin films for the aforementioned applications, and thorough understanding of the structure-property relationship is imperative for materials design. In this dissertation, I describe significant efforts to manipulate the BP thin film structures (Chapter 3), direct the nanostructure ordering (Chapter 4), and understand the influence of the macromolecular structure and sequence on the BP properties (Chapter 5 and 6).

7.1.1 Controlling Self-Assembly and Order of Nanostructure

BP thin film self-assembly is influenced strongly by the commensurability considerations (*i.e.* film thickness) and surface interactions.[11-14] Chapter 3 details the utilization of high-throughput gradient methods to screen the effects of film thickness

and substrate surface interaction on the nanostructure of BP thin films. The unique attributes from this chapter include (1) the use of a cylinder-forming poly(styrene-*b*-isoprene-*b*-styrene) (SIS) triblock copolymer with moderate difference in surface energy ($\Delta\gamma \sim 8$ mJ/m^2) between the individual blocks, whereas previous studies primarily focused on poly(styrene-*b*-methyl methacrylate) (PS-PMMA) diblock copolymer which has very similar surface energies ($\Delta\gamma < 1$ mJ/m^2) between the blocks;[15] (2) the generation of highly tunable surface energy gradients using chlorosilane monolayers that easily can be extended to other polymer systems of interest; (3) the identification of a morphology transformation from cylinders to hexagonally perforated lamellae (HPL) as a result of the preferential interactions between polymer blocks and chlorosilane monolayers, which has not been reported previously in the literature. Thus, Chapter 3 highlights a significant expansion of designer surface modification methods for the possible universal manipulation of thin film nanostructures. Additionally, the focused ion beam milling and lift-out method demonstrated in Chapter 3 permits facile cross-sectional analysis of BP thin films, and it is anticipated to be useful in future studies.

We note that the reorientation of SIS cylinders from parallel to perpendicular was not found on the benzyl-silane/*n*-butyl silane gradient substrate likely due to the disparate surface energies between the PI block and PS block. As it is well-known in the literature, the PS-PMMA can be readily oriented perpendicular on a neutral substrate because the interfacial energies of the two blocks at the free surface are balanced naturally at high temperature.[16] However, in the SIS system, the driving force for the PI block (low surface energy) to segregate to the free surface dominates the substrate effect, leading to parallel-oriented microdomains. To prompt the

substrate surface field more prominently, an ultra-thin lamellar forming PI-PS film on a benzyl-silane/*n*-butyl silane gradient substrate was examined. The film was approximately 27 nm as measured by spectral reflectance, corresponding to 1.5 L_0 (L_0 is the domain spacing). The PI-PS film exhibited different wetting behavior on each end of the substrate, *i.e.*, asymmetric wetting at the benzyl-silane end and symmetric wetting at the *n*-butyl end. The results indicated the PS block segregated to the benzyl-silane surface and the PI block segregated to the *n*-butyl silane surface, and a possible neutral surface window was revealed in the middle of the substrate. Therefore, the substrate surface effect became more apparent by reducing the film thickness. Generally, the propagation distance of the substrate field depends on the relative strength of the polymer-substrate interactions and the competing polymer-free surface interactions. For BPs that have very different surface energies in the constituent blocks, solvent vapor annealing (SVA) or top coats have been applied widely to establish neutral free surfaces (see more details in Chapter 1 Section 1.3.3). Some preliminary results of using SVA to manipulate the PI-PS nanostructures will be discussed in Section 7.2.1, and suggestions for stabilizing network structures also are provided.

Chapter 4 demonstrates an incredibly simple, yet highly effective method to achieve macroscopic alignment of nanostructures in BP thin films. Current approaches to direct the self-assembled BP nanostructures including graphoepitaxy, chemical prepatterning, and external fields (*e.g.*, magnetic fields, electric fields, *etc.*) are afflicted with major disadvantages. For example, graphoepitaxy only can pattern a limited area (on the order of μm^2) and sacrifices valuable substrate area; chemical prepatterning involves multiple steps of substrate modification at the nanometer scale,

making this process prohibitively slow and high cost; electric fields and magnetic fields are applicable only to select polymer systems. Hence, new, simple, and adaptable approaches such as the one reported in Chapter 4 are vital. This raster solvent vapor annealing-soft shear (RSVA-SS) method substantially improves on previous alignment approaches by using simple SVA instrumentation to unlock an array of alignment patterns and provides feasibility and flexibility for practical industrial production. As illustrated in Chapter 4, complex patterns such as dashes, crossed lines, and curves can be imparted easily to thin films on featureless and untreated substrates through the implementation of a solvent vapor delivery nozzle, poly(dimethylsiloxane) (PDMS) shearing pad, and motorized stage. The capability to write, erase, and rewrite the patterns affords advantages over conventional patterning methods such as graphoepitaxy and chemical prepatterning. Additionally, the ability to expand or shrink the "writing" size of the oriented regions from millimeters to centimeters (decoupled from the size of the PDMS pad) provides a unique handle for controlling pattern formation in an on-demand fashion.

At present, the lack of resolution and pattern fidelity at the transition region between highly aligned and unaligned structures is a major shortcoming of RSVA-SS in comparison to graphoepitaxy or chemical prepatterning. This problem is addressed in Section 7.2.2, and efforts of fabricating industrial-relevant structures such as T-junctions that have sharp transition will be demonstrated.

Finally, the RSVA-SS approach provides a feasible pathway for the continuous processing of various copolymer systems, especially those containing complex molecular structures such as tapered, branded, cyclic, and star BPs. The unique self-assembly behavior of cyclic and star BPs will be discussed in Section 7.2.3.

7.1.2 Connecting Macromolecular Structure to Block Polymer Properties

Tapered block polymers (TBPs) offer a unique opportunity to tune the structure, thermodynamics, and mechanical properties of a given BP system.[17-22] Incorporating a tapered interface in BPs has been shown to reduce the effective Flory-Huggins interaction parameter (χ), increase the block compatibility, and lead to lower order-to-disorder transition temperatures (T_{ODT}'s) relative to the corresponding non-tapered BPs.[18, 19, 23] Thus, there is significant interest to manipulate the volume fraction and monomer sequence of the tapered region to control the nanostructures and influence the macroscopic physical properties of TBPs.

Chapter 5 provides the first quantitative measurements of interfacial mixing in TBPs for normal tapered poly(isoprene-b-isoprene/styrene-b-styrene) (I-IS-S) and inverse tapered I-SI-S using X-ray reflectivity (XRR) and differential scanning calorimetry (DSC). The normal tapered I-IS-S polymer (30 vol% tapering) was found to have similar interfacial mixing to the respective diblock polymer, while the inverse tapered I-SI-S polymer (30 vol% tapering) had significantly wider interfaces (double the interfacial width) and less pure domains. Furthermore, the density profiles derived from XRR data were paired with theoretical efforts using fluids density functional theory (fDFT) and showed good agreement. Additionally, the influence of the tapered interfaces with regard to the BP thermodynamic properties (*i.e.*, glass transition temperatures, changes in heat capacity) and the free surface morphologies in thin films were explored in Chapter 5, and the results indicate that the monomer sequence is an important determinant of macroscopic physical properties. Specifically, the inverse tapered interface greatly improved the compatibility between block domains, leading to the formation of larger island/hole structures in I-SI-S thin films due to decreased surface elasticity from greater mixing between domains. Thus, the quantitative

measurement of the interfacial mixing in these tapered materials allows us to connect macroscopic physical properties to macromolecular structure and sequence, and it furthers our understanding of interfacial modifications as a valuable tool for materials design.

Recently, our research group demonstrated taper interfacial modification as a promising strategy for designing highly tunable, mechanically-stable, and easily-processable BP electrolytes for lithium battery applications. It is important to understand the local environment of ions in these TBPs, especially at the BP interfaces. The methodology developed in Chapter 5 will be suitable to study the change of interfacial mixing upon lithium salt doping and will provide insights in optimizing synthetic parameters (*e.g.,* tapered volume fraction, monomer sequence) to achieve desired properties.

Chapter 6 describes the unique capabilities of high resolution C_{60}^{+} depth profiling X-ray photoelectron spectroscopy (XPS) to resolve the ion distribution in a lamellar forming BP electrolyte thin film, which was previously considered challenging by conventional electron microscopy technique. The studied PS-poly(oligo(oxyethylene) methacrylate) (PS-POEM) copolymer has branched oligo ethylene oxide side chain and provides high ion conductivity at room temperature in comparison to PS-PEO (main chain ethylene oxide) BP due to the suppression of PEO crystallization by short side chains. The XPS depth-profiling results clearly showed that the concentrations of the doped lithium-ions and the fluorine-containing triflate anions were correlated tightly, and the lithium ions appeared to be uniformly distributed in the POEM domains. This finding differs from a previous report in which lithium ions were localized in the center of the PEO domain as gleaned from

energy-filtered transmission electron microscopy (EFTEM).[24] The apparently discrepancies were explained by the intricacies of the copolymer architectures, with differences in energetics resulting from the coordination of metal ions to side chain *versus* main chain solubilizing segments.[25] It is posited that the solvating groups in the side chains of POEM have higher chain mobility and increase the freedom to coordinate lithium ions,[25] leading to a more uniform distribution of lithium ions across POEM domains. Thus, these results provide useful insights for the future design and optimization of BP structures (*e.g.*, molecular weight, side chain length, composition, *etc*.) for high efficiency energy storage devices. Furthermore, the XPS with C_{60}^{+} depth profiling technique as demonstrated herein are applicable to investigations of nanoscale distributions of molecules (*e.g.*, additives) in a myriad of polymer thin film systems.

7.1.3 Concluding Remarks

Overall, this dissertation describes significant efforts to manipulate the block polymer thin film structures, direct the nanostructure ordering, and understand the connection between the macromolecular molecular structures and the BP properties. The high-throughput gradient methods demonstrated in Chapter 3 are highly adaptable for the possible universal manipulation of BP thin film nanostructures. The RSVA-SS method developed in Chapter 4 substantially improves on previous approaches by using simple instrumentation to unlock an array of alignment patterns with a variety of self-assembling polymers and provides feasibility and flexibility for practical industrial production. Chapter 5 and Chapter 6 present the first quantitative determination of the interfacial mixing characteristics in TBPs and lithium ion distribution in BP electrolyte thin films, respectively. These studies help us to build

connections between the macromolecular molecular structures and the BP properties, and further our understanding of BP thin film self-assembly. The methodologies developed in these chapters will be useful for the future design and optimization of interfacially modified BP electrolyte systems for high efficiency energy storage devices.

7.2 Recommendation for Future Directions

7.2.1 Using Solvent to Manipulate Block Polymer Structures

SVA has widespread use and proven capability to produce controlled morphologies with long-range ordering in BP thin films.[10, 26] During solvent vapor annealing, the solvent vapor molecules swell the BP film and dilute the polymer. This dilution effectively lowers the glass transition temperatures of the polymer blocks, reduces the viscosity, and increases the chain mobility.[27] If a selective solvent is used, the relative composition of the blocks can be altered due to the preferentially swelling of specific blocks, leading to changes in BP morphologies. [28, 29] For example, Jeong *et al.* found that different morphologies such as spheres, cylinders, hexagonally perforated lamellae, and lamellae could be generated from a single lamellar-forming poly(2-vinylpyridine)-*b*-PDMS (P2VP-PDMS) copolymer by tuning the solvent selectivity towards the P2VP block. These results were summarized in a phase diagram, displaying different morphologies as functions of swelling ratios (swollen film thickness/dry film thickness) and solvent solubility parameter. Though the phase behavior of BP subjected to SVA is well-studied experimentally and theoretically,[26, 30, 31] new macromolecular designs that incorporate multiblocks, tapered segment profile, and cyclic architecture significantly complicate the understanding of self-assembly,

yet potentially offer exciting opportunities for diverse structures with enhanced functionality and properties. For example, the non-tapered I-S, normal tapered I-IS-S, and inverse tapered I-SI-S films were annealed in *n*-hexane (selective to the PI block) for 6 h. The preferential swelling of *n*-hexane to the PI block increases the relative composition of the PI block, thus lead to morphological changes. However, the three films exhibited different surface morphologies (Figure 7.1) at the same swollen ratio (~1.55) despite the same block composition in the dry film. The I-S and I-IS-S films showed a morphology transition from parallel lamellae to parallel cylinders, while the I-SI-S films displayed a hexagonally packed dot structures, indicating a perpendicular cylindrical structure or spherical structure. Follow-up experiments should consider changing the swollen ratio and/or annealing time to further investigate the morphology transformation. Although several theoretical studies have demonstrated how taper length (volume) and monomer sequence affect the phase diagram,[23, 32] the understanding of TBP under SVA is lacking, suggesting a future collaboration opportunity with the Hall group at OSU and Jayaraman group at UD.

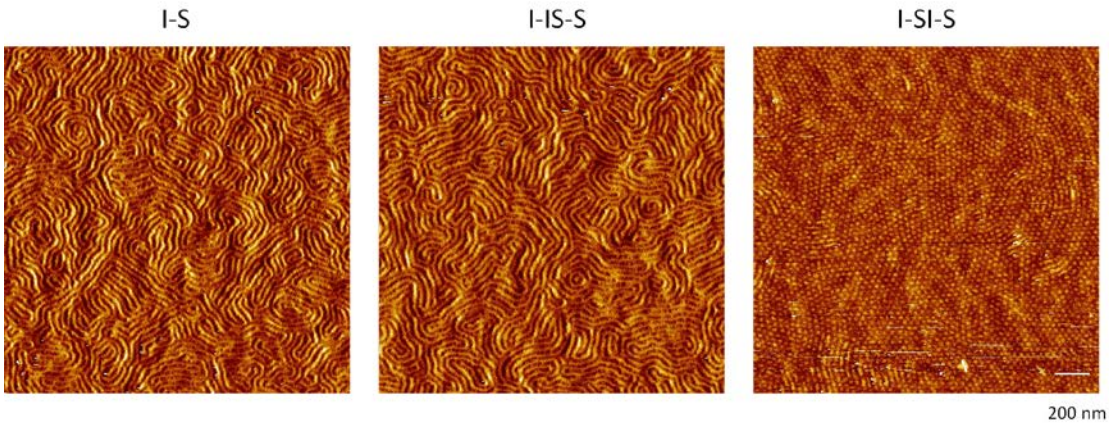

Figure 7.1: Preliminary results of I-S, I-IS-S, and I-SI-S films under *n*-hexane SVA for 6 h. The dry film thicknesses were ~70 nm, and the swollen ratio was approximately 1.55 for all of the films. The atomic force microscopy (AFM) phase images of the I-S and I-IS-S films showed parallel cylindrical structures, while the I-SI-S film showed hexagonally packed dot structures. The scale bar represents 200 nm and applies to all images.

The solvent vapor in the film also can mitigate the polymer-substrate interaction and establish new polymer-free surface interaction.[33, 34] The gyroid network structure is of great interest for solar cell, conducting membrane, and porous filtration membrane applications due to its 3D Interconnecting structures. However, it is difficult to achieve this structure in thin films. BP that forms a network structure in the bulk often transits to lamellae or cylinders in thin film geometries due to the strong surface interactions.[14] Recently, the gyroid network structures have been stabilized in thin films by SVA with neutral solvents and neutral substrate modification.[33] Ho and coworkers employed 1,2-dichloroethane as a neutral solvent for the gyroid-forming poly(styrene-*b*-L-lactide) (PS−PLLA) BP, and used hydroxyl-terminated PS (PS-OH) and hydroxyl-terminated PLLA (PLLA-OH) brushes to create a neutral silicon substrate.[33] They found the (211) plane of the gyroid phase oriented parallel to the

free surface. It is important to note that the swollen film thickness should be commensurate with the domain spacing of the (211) plane to promote the gyroid morphology.

Furthermore, the swelling and deswelling (solvent evaporation) processes can affect the commensurability between the polymer domain spacing and the film thickness, and induce changes in the orientation of the BP nanostructures.[35, 36] In a follow-up study, Ho and coworkers systematically examined the morphological evolution of the gyroid-forming PS-PLLA with varying solvent evaporation rates.[34] Using a partially PS-selective solvent chloroform, interesting phase transitions from disorder to perpendicular cylinder and then gyroid were identified during solvent evaporation. Additionally, the composition of the brush coated silicon substrate was tuned by increasing the composition of the grafted PLLA−OH to balance the selectivity of the substrate because the PS brush on the functionalized substrate would be stretched by chloroform during the solvent while the PLLA chains would recoil.

Therefore, stabilizing the gyroid network structures in thin films requires consideration of substrate and free surface interactions as well as film thickness constraints all together. The substrate gradient and film thickness methods developed in Chapter 3 can be applied in future studies to screen the film thickness and substrate surface conditions for the BP system of interest.

7.2.2 Fabricating T-Junction Structures

The ability to fabricate nanostructures with high precision and well-defined orientations in BP thin films is of crucial importance to the advancement of nanotechnology. The RSVA-SS approach provides a simple but effective method to achieve directed alignment of nanostructures at macroscopic scale. However, the lack

of resolution and pattern fidelity at the transition region between highly aligned and unaligned structures is a major shortcoming of this process in comparison to graphoepitaxy or chemical prepatterning. To address this problem, this thesis presents an approach that combines the RSVA-SS process with soft lithography, in which the PDMS elastomer pad is patterned by photolithography.

Soft lithography is a set of techniques for fabricating or replicating structures using elastomeric stamps, molds, and conformable photomasks.[37] In soft lithography, an elastomeric stamp is patterned by photolithography with feature sizes ranging from 30 nm to 100 μm, and the patterns can be transferred to the targeting substrate or film. It provides a convenient, effective, and low-cost method for the formation and manufacturing of micro- and nanostructures. It has been used widely in the fabrication of arrays of biosensors, microfluidics, lab-on-a-chip, and flexible electronics or photonics.[38-40]

The workflow for soft lithography is shown in Figure 7.2 and described as follows. Epoxy negative photoresist SU-8 2035 (MicroChem Corp.) was used to create protruding features on a silicon substrate (serve as a master pattern for the PDMS stamp). An SU-8 film of thickness ~100 μm was spin coated onto the silicon wafer. A process of "soft bake – UV exposure with photomask – post exposure bake" was employed to generate permanent structures on the photoresist films. In our case, the patterned features on the photoresist film consisted of linear gratings where each grating was 100 μm wide and extended over a width of 30 mm. After post exposure bake, the SU-8 film was submerged into a bath of SU-8 developer (MicroChem Corp.), and the unexposed photoresist film was washed off, leaving stiff SU-8 patterns on the silicon wafer. This master template then was used to fabricate the PDMS stamp

as described previously in Chapter 4. The resulting PDMS stamp could be laminated onto the SIS film, and RSVA-SS was performed across the PDMS stamp (see Figure 7.3). The RSVA-SS with patterned PDMS stamp created a sharp interface between the sheared region (where PDMS touches the BP film) and unsheared region (where an air gap insulates the BP polymer) as demonstrated in Figure 7.3. Thus, this RSVA-SS-soft lithography approach enables high-throughput patterning of polymer nanostructures at great precision and at low costs.

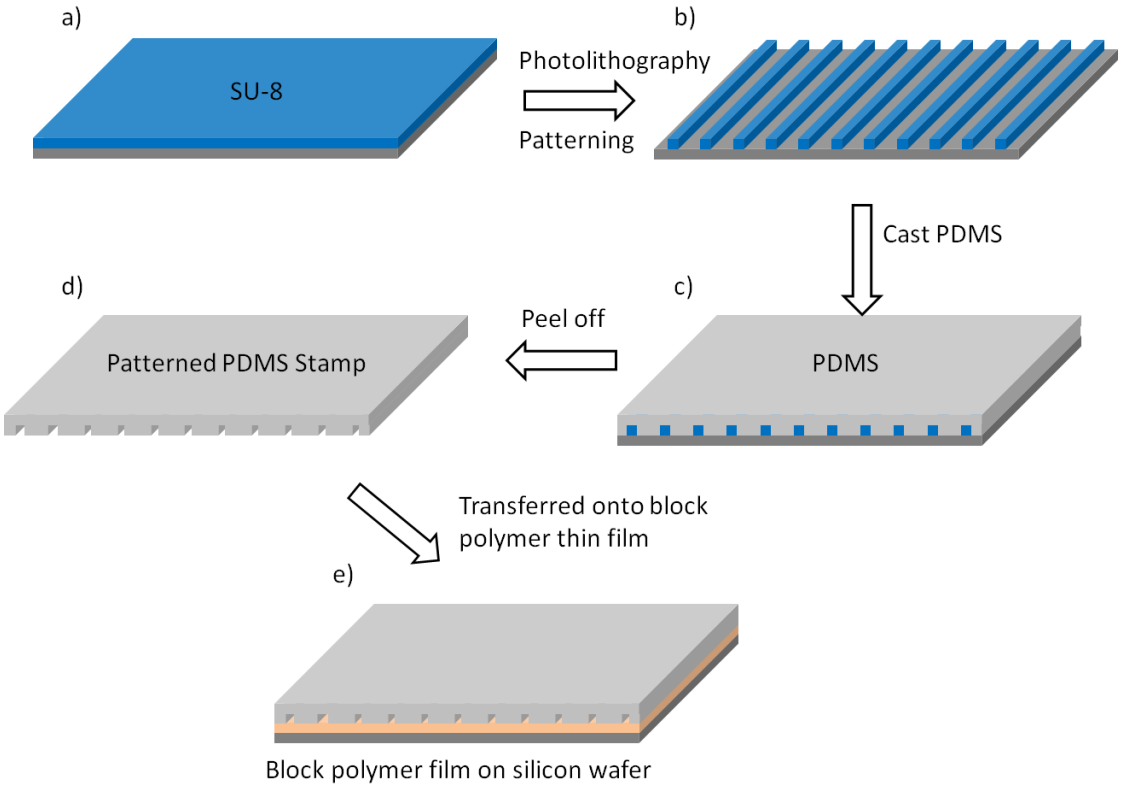

Figure 7.2: Process flow for the fabrication of PDMS stamp. a) SU-8 film cast on a silicon substrate. b) Photolithographic fabrication of SU-8 template. c) PDMS cast onto the SU-8 master. d) PDMS peeled off. e) PDMS transferred onto a BP thin film.

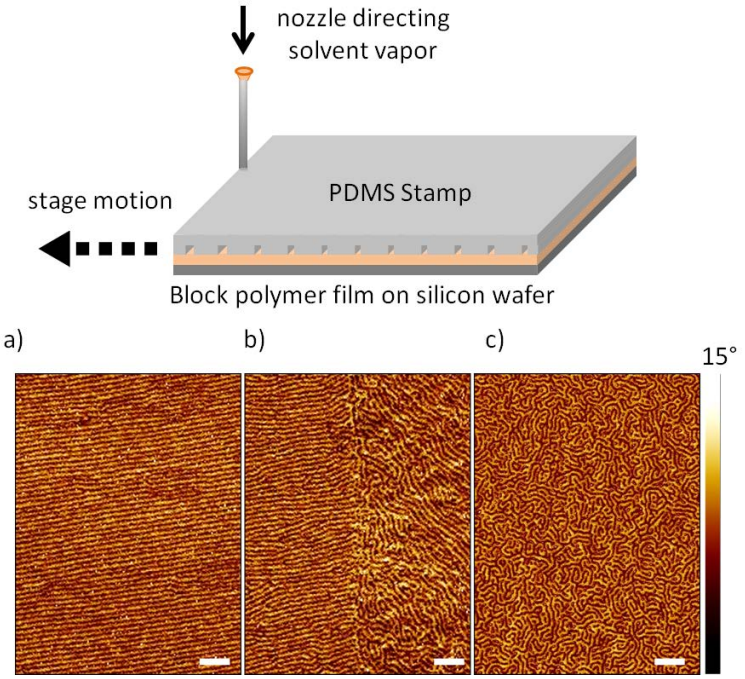

Figure 7.3: Schematic of RSVA-SS process with patterned PDMS stamp (top). AFM phase images demonstrating SIS cylinder alignment across the interface (bottom), a) sheared region, b) interface, c) unsheared region. Scale bars represent 200 nm.

This combinatorial approach offers a potential opportunity to fabricate more industrial relevant structures such as bends, jogs, T-junctions. A proof-of-principle trial of T-junction is shown in Figure 7.4, in which two RSVA-SS paths are applied orthogonally. In the first step, a non-patterned PDMS was used, and the whole SIS film was aligned unidirectionally. In the second step, the SIS film was rotated by 90 °C, and a patterned PDMS pad was employ, thus only select area was shear aligned. The second raster path overwrote the patterns formed in the prior step where the patterned PDMS pad touched the SIS film. While the SIS cylinders remained intact under the air gap regions. Examination of the SIS structures at the intersection

revealed well-aligned SIS cylinders following the corresponding raster direction. However, a defective region approximately 0.8 - 1 μm in width was apparent at the intersection. Further AFM height profile measurement indicated this region was ~100 nm higher than the sides. It is posited that the shear field in the second raster step was in excess, and thus the edge of the channel "shoveled up" a portion of the polymer film. In a follow-up experiment, the shear force was reduced by decreasing the solvent flow rate (*i.e.*, decreasing the degree of PDMS swelling), and the "ridge" defect was alleviated significantly (Figure 7.5). However, the alignment quality was degraded, suggesting the shear field was deficient. Therefore, a detailed study of controlled shearing field is highly recommended in the future.

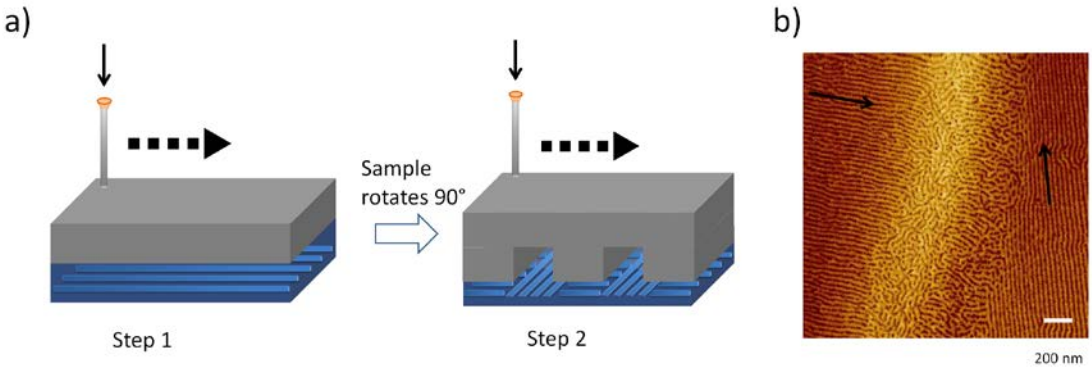

Figure 7.4: a) Schematic of RSVA-SS process to fabricate T-junction structures. b) AFM phase images illustrate the SIS cylinder alignment at the intersection. A "ridge" defect approximately 0.8 - 1 μm in width was apparent. The two raster paths were not perfectly orthogonal because the patterned PDMS was not highly aligned to the first raster direction.

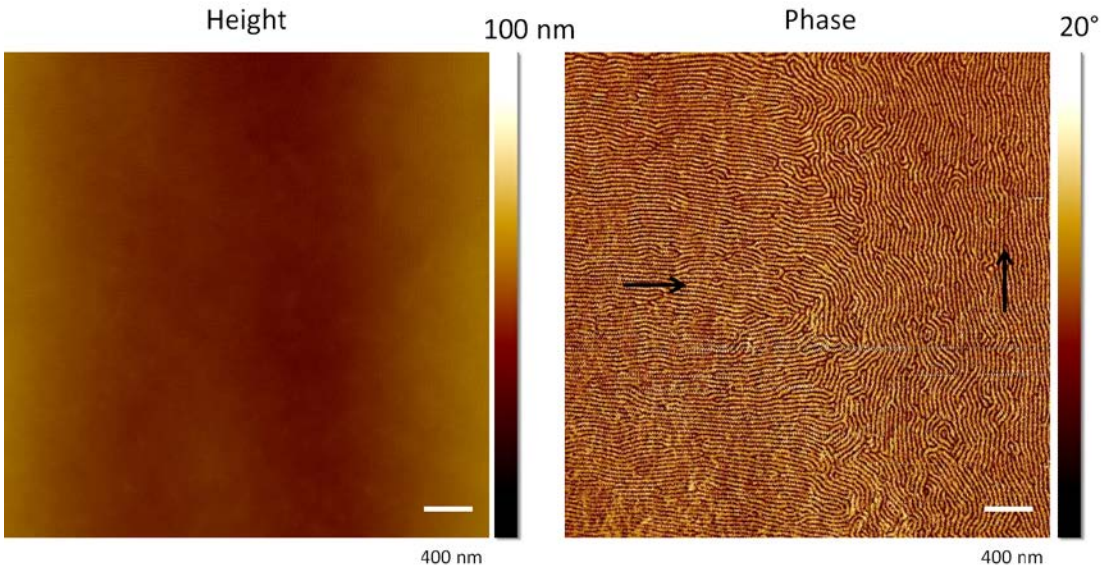

Figure 7.5: AFM height and phase images of T-junction structures fabricated when the solvent flow rate was reduced. The "ridge" defect was alleviated but the alignment of the SIS cylinders was degraded.

7.2.3 Cyclic and Star Block Polymers

Directed self-assembly of BPs is gaining momentum as a viable means for extending optical lithography beyond its current limits. Sub-10 nm BP domains are targeted to meet the demands for ever-reducing feature sizes in integrated circuits (IC) and data storage media (*e.g.*, 8 nm resolution for dynamic random access memory [DRAM] ½ pitch in 2024),[41] but there are relatively few self-assembled BPs that can achieve these dimensions and maintain their desired application-oriented properties.[42, 43] In general, self-assembly of small structures requires a low degree of polymerization (N) and a high Flory-Huggins interaction parameter (χ).[44, 45] However, for a select BP system, there is a minimum value of N necessary for self-assembly. Self-consistent mean field theory predicts that the χN needs to exceed 10.5 for symmetric AB diblock copolymers to form ordered structures.[46] Therefore, significant

research efforts have been devoted to synthesizing high χ – low N BPs. As mentioned early, control of domain orientation and alignment in these high χ BPs is challenging due to the strong surface preference effects.

Block architecture likely will play an increasingly important role in BPs. For example, cyclic and star BPs portend very interesting nanoscale structures and alignment behavior. Cyclic BPs are comprised of two or more polymer blocks that are covalently linked together such that there are no chain ends. Due to this intriguing architecture, cyclic BPs exhibit smaller hydrodynamic volumes and self-assemble into domains with smaller feature sizes than the linear BPs.[47-49] The continuous nature of cyclic BPs limits potential chain entanglement and alters chain conformation and mobility. The cyclic BPs exhibit different properties in comparison to linear counterparts of similar molecular weight, including higher density, lower intrinsic viscosity, lower translational friction coefficients, higher glass transition temperatures, higher critical solution temperature, increased rate of crystallization, and higher refractive index.[50-54] Additionally, the morphological transitions of cyclic BPs can differ from the linear BPs due to the increased interfacial curvature in cyclic BPs. To the author's knowledge, there is to date only one thin film study of cyclic BPs. Poelma *et al.* showed cyclic PS-PEO formed perpendicular cylindrical structures in thin films, where the domain size of the cyclic PS-PEO was ~33% smaller than the linear analogue.[49] The surface interactions between the cyclic BPs and substrate/free surfaces remain largely unexplored. It will be interesting to investigate the substrate surface effects on self-assembly of cyclic BPs in thin films in the future using the gradient methods described in this thesis.

Star BPs represent an emerging class of macromolecules with a general structure consisting of several (more than three) linear chains connected to a central core. The core of the star BPs can be an atom, molecule, or macromolecule. Star BPs with arms equivalent in length and structure are considered homogeneous, and ones with variable lengths and structures are considered heterogeneous. The unique star-shaped architecture allows for increase of the overall molecular weight while the *N* of the individual arm remains the same.[55, 56] Recent work have shown that star BPs exhibit larger interaction parameter χ than the linear analogues due to entropic contributions χ_S.[57-61] Thus, star BPs effectively increase the segregation strength without altering the phase separation size scale.[59, 62, 63] These benefits can be exploited to self-assemble nanostructures with < 10 nm feature sizes. The star-shape architecture also has the ability to produce unique morphologies in bulk,[63-65] including networks.[65-68] Recently, it has been shown that neutralization of substrate and free surface interactions was facilitated by star BP architectures.[69] Although studies of phase behavior of cyclic and star BPs are emerging,[70-72] fundamental insights into the relationship macromolecular architecture and self-assembly properties are needed.

7.2.4 Tapered Block Polymer Electrolyte

BP electrolytes have become increasingly attractive for lithium battery applications due to their high thermal, mechanical, and electrochemical stability in comparison to traditional liquid-form electrolytes. However, BP electrolytes often suffer from poor ionic conductivity due to the limited chain mobility at low temperature. In the simplest symmetric PS-PEO lamellar system doped with lithium salt, Panday *et al.* demonstrated that increasing the molecular weight of BPs increases the ionic conductivity and mechanical properties.[73] However, high molecular weight materials are difficult to

process because of their high glass transition temperature, order-disorder transition temperature, and viscosity. Recently, our research group have demonstrated taper interfacial modification as a promising strategy for designing highly tunable, mechanically-stable, and easily-processable BP electrolytes.[74] The tapered interfaces provide a unique handle for manipulating the glass transition temperature of BP electrolytes through adjustments in the taper sequence and taper fraction (the effect of tapered interfaces on the glass transition temperature was discussed in great detail in Chapter 5). Additionally, a double-gyroid network phase window was found in ion-doped normal tapered BP system, while no network morphologies were detected in the non-tapered and inverse-tapered materials. Theoretical work by Brown *et al.* suggested that the normal tapered interface could relieve the packing frustration inherent to the gyroid morphology and widen the network phase window. Therefore, it is important to understand the change of interfacial characteristics upon salt doping and local ion distribution in these TBPs. The methodology developed in Chapter 5 and Chapter 6 will be useful to elucidate these questions and provide insights in optimizing synthetic parameters (*e.g.*, tapered volume fraction, monomer sequence) to achieve desired properties.

REFERENCES

1. Zschech, D.; Kim, D. H.; Milenin, A. P.; Scholz, R.; Hillebrand, R.; Hawker, C. J.; Russell, T. P.; Steinhart, M.; Gösele, U. *Nano Lett.* **2007,** 7, (6), 1516-1520.

2. Ruiz, R.; Kang, H.; Detcheverry, F. A.; Dobisz, E.; Kercher, D. S.; Albrecht, T. R.; de Pablo, J. J.; Nealey, P. F. *Science* **2008,** 321, (5891), 936-939.

3. Chai, J.; Buriak, J. M. *ACS Nano* **2008,** 2, (3), 489-501.

4. Jung, Y. S.; Jung, W.; Tuller, H. L.; Ross, C. A. *Nano Lett.* **2008,** 8, (11), 3776-3780.

5. Bang, J.; Kim, S. H.; Drockenmuller, E.; Misner, M. J.; Russell, T. P.; Hawker, C. J. *J. Am. Chem. Soc.* **2006,** 128, (23), 7622-7629.

6. Yang, S. Y.; Ryu, I.; Kim, H. Y.; Kim, J. K.; Jang, S. K.; Russell, T. P. *Adv. Mater.* **2006,** 18, (6), 709-712.

7. Park, S.; Lee, D. H.; Xu, J.; Kim, B.; Hong, S. W.; Jeong, U.; Xu, T.; Russell, T. P. *Science* **2009,** 323, (5917), 1030-1033.

8. Xiao, S.; Yang, X.; Park, S.; Weller, D.; Russell, T. P. *Adv. Mater.* **2009,** 21, (24), 2516-2519.

9. Naito, K.; Hieda, H.; Sakurai, M.; Kamata, Y.; Asakawa, K. *IEEE Trans. Magn.* **2002,** 38, (5), 1949-1951.

10. Luo, M.; Epps, T. H., III. *Macromolecules* **2013,** 46, (19), 7567-7579.

11. Albert, J. N. L.; Epps, T. H., III. *Materials Today* **2010,** 13, (6), 24-33.

12. Segalman, R. A. *Materials Science and Engineering: R: Reports* **2005,** 48, (6), 191-226.

13. Fasolka, M. J.; Mayes, A. M. *Annu. Rev. Mater. Res.* **2001,** 31, (1), 323-355.

14. Epps, T. H., III; DeLongchamp, D. M.; Fasolka, M. J.; Fischer, D. A.; Jablonski, E. L. *Langmuir* **2007,** 23, (6), 3355-3362.

15. Vu, T.; Mahadevapuram, N.; Perera, G. M.; Stein, G. E. *Macromolecules* **2011,** 44, (15), 6121-6127.

16. Mansky, P.; Liu, Y.; Huang, E.; Russell, T.; Hawker, C. *Science* **1997,** 275, (5305), 1458-1460.

17. Roy, R.; Park, J. K.; Young, W.-S.; Mastroianni, S. E.; Tureau, M. S.; Epps, T. H., III. *Macromolecules* **2011,** 44, (10), 3910-3915.

18. Singh, N.; Tureau, M. S.; Epps, T. H., III. *Soft Matter* **2009,** 5, (23), 4757-4762.

19. Hodrokoukes, P.; Floudas, G.; Pispas, S.; Hadjichristidis, N. *Macromolecules* **2001,** 34, (3), 650-657.

20. Adhikari, R.; Michler, G. H.; Huy, T. A.; Ivan'kova, E.; Godehardt, R.; Lebek, W.; Knoll, K. *Macromol. Chem. Phys.* **2003,** 204, (3), 488-499.

21. Sigle, J. L.; Clough, A.; Zhou, J.; White, J. L. *Macromolecules* **2015,** 48, (16), 5714-5722.

22. Huy, T. A.; Hai, L. H.; Adhikari, R.; Weidisch, R.; Michler, G. H.; Knoll, K. *Polymer* **2003,** 44, (4), 1237-1245.

23. Brown, J. R.; Sides, S. W.; Hall, L. M. *ACS Macro Letters* **2013,** 2, (12), 1105-1109.

24. Gomez, E. D.; Panday, A.; Feng, E. H.; Chen, V.; Stone, G. M.; Minor, A. M.; Kisielowski, C.; Downing, K. H.; Borodin, O.; Smith, G. D.; Balsara, N. P. *Nano Lett.* **2009,** 9, (3), 1212-1216.

25. Tarascon, J. M.; Armand, M. *Nature* **2001,** 414, (6861), 359-367.

26. Sinturel, C.; Vayer, M.; Morris, M.; Hillmyer, M. A. *Macromolecules* **2013,** 46, (14), 5399-5415.

27. Kim, E.; Ahn, H.; Park, S.; Lee, H.; Lee, M.; Lee, S.; Kim, T.; Kwak, E.-A.; Lee, J. H.; Lei, X.; Huh, J.; Bang, J.; Lee, B.; Ryu, D. Y. *ACS Nano* **2013**, 1952-1960.

28. Hsieh, I. F.; Sun, H.-J.; Fu, Q.; Lotz, B.; Cavicchi, K. A.; Cheng, S. Z. D. *Soft Matter* **2012,** 8, (30), 7937-7944.

29. Paik, M. Y.; Bosworth, J. K.; Smilges, D.-M.; Schwartz, E. L.; Andre, X.; Ober, C. K. *Macromolecules* **2010,** 43, (9), 4253-4260.

30. Knoll, A.; Horvat, A.; Lyakhova, K. S.; Krausch, G.; Sevink, G. J. A.; Zvelindovsky, A. V.; Magerle, R. *Phys. Rev. Lett.* **2002,** 89, (3), 035501.

31. Knoll, A.; Magerle, R.; Krausch, G. *J. Chem. Phys.* **2004,** 120, (2), 1105-1116.

32. Seo, Y.; Brown, J. R.; Hall, L. M. *Macromolecules* **2015,** 48, (14), 4974-4982.

33. She, M.-S.; Lo, T.-Y.; Ho, R.-M. *Macromolecules* **2013,** 47, (1), 175-182.

34. Wu, Y.-H.; Lo, T.-Y.; She, M.-S.; Ho, R.-M. *ACS Appl. Mater. Interfaces* **2015,** 7, (30), 16536-16547.

35. Kim, G.; Libera, M. *Macromolecules* **1998,** 31, (8), 2569-2577.

36. Albert, J. N. L.; Young, W.-S.; Lewis, R. L., III; Bogart, T. D.; Smith, J. R.; Epps, T. H., III. *ACS Nano* **2012,** 6, (1), 459-466.

37. Xia, Y.; Whitesides, G. M. *Annual Review of Materials Science* **1998,** 28, (1), 153-184.

38. Whitesides, G. M.; Ostuni, E.; Takayama, S.; Jiang, X.; Ingber, D. E. *Annu. Rev. Biomed. Eng.* **2001,** 3, (1), 335-373.

39. Qin, D.; Xia, Y.; Whitesides, G. M. *Nat. Protoc.* **2010,** 5, (3), 491-502.

40. Rogers, J. A.; Nuzzo, R. G. *Materials today* **2005,** 8, (2), 50-56.

41. International Technology Roadmap for Semiconductors, 2012. http://www.itrs.net

42. Park, S.-M.; Liang, X.; Harteneck, B. D.; Pick, T. E.; Hiroshiba, N.; Wu, Y.; Helms, B. A.; Olynick, D. L. *ACS Nano* **2011,** 5, (11), 8523-8531.

43. Son, J. G.; Chang, J.-B.; Berggren, K. K.; Ross, C. A. *Nano Lett.* **2011,** 11, (11), 5079-5084.

44. Cushen, J. D.; Bates, C. M.; Rausch, E. L.; Dean, L. M.; Zhou, S. X.; Willson, C. G.; Ellison, C. J. *Macromolecules* **2012,** 45, (21), 8722-8728.

45. Jeong, J. W.; Park, W. I.; Kim, M.-J.; Ross, C. A.; Jung, Y. S. *Nano Lett.* **2011,** 11, (10), 4095-4101.

46. Cochran, E. W.; Garcia-Cervera, C. J.; Fredrickson, G. H. *Macromolecules* **2006,** 39, (7), 2449-2451.

47. Matsushita, Y.; Iwata, H.; Asari, T.; Uchida, T.; ten Brinke, G.; Takano, A. *J. Chem. Phys.* **2004,** 121, (2), 1129-1132.

48. Zhu, Y.; Gido, S. P.; Iatrou, H.; Hadjichristidis, N.; Mays, J. W. *Macromolecules* **2003,** 36, (1), 148-152.

49. Poelma, J. E.; Ono, K.; Miyajima, D.; Aida, T.; Satoh, K.; Hawker, C. J. *ACS Nano* **2012,** 6, (12), 10845-10854.

50. Bannister, D. J.; Semlyen, J. A. *Polymer* **1981,** 22, (3), 377-381.

51. Shin, E. J.; Jeong, W.; Brown, H. A.; Koo, B. J.; Hedrick, J. L.; Waymouth, R. M. *Macromolecules* **2011,** 44, (8), 2773-2779.

52. Qiu, X.-P.; Tanaka, F.; Winnik, F. M. *Macromolecules* **2007,** 40, (20), 7069-7071.

53. Orrah, D. J.; Semlyen, J. A.; Ross-Murphy, S. B. *Polymer* **1988,** 29, (8), 1455-1458.

54. Clarson, S. J.; Semlyen, J. A. *Polymer* **1986,** 27, (10), 1633-1636.

55. Chen, Q. *Rheol. Acta* **2012,** 51, (4), 343-355.

56. Laurent, B. A.; Grayson, S. M. *J. Am. Chem. Soc.* **2006,** 128, (13), 4238-4239.

57. Martter, T.; Foster, M.; Yoo, T.; Xu, S.; Lizzaraga, G.; Quirk, R.; Butler, P. *Macromolecules* **2002,** 35, (26), 9763-9772.

58. Martter, T. D.; Foster, M. D.; Yoo, T.; Xu, S.; Lizzaraga, G.; Quirk, R. P.; Butler, P. D. *Macromolecules* **2002,** 35, (26), 9763-9772.

59. Matsen, M. W. *Macromolecules* **2012,** 45, (4), 2161-2165.

60. Ijichi, Y.; Hashimoto, T.; Fetters, L. J. *Macromolecules* **1989,** 22, (6), 2817-2824.

61. Hashimoto, T.; Ijichi, Y.; Fetters, L. J. *The Journal of Chemical Physics* **1988,** 89, (4), 2463-2472.

62. Alward, D. B.; Kinning, D. J.; Thomas, E. L.; Fetters, L. J. *Macromolecules* **1986,** 19, (1), 215-224.

63. Matsen, M. W.; Schick, M. *Macromolecules* **1994,** 27, (23), 6761-6767.

64. Han, W.; Tang, P.; Li, X.; Qiu, F.; Zhang, H.; Yang, Y. *The Journal of Physical Chemistry B* **2008,** 112, (44), 13738-13748.

65. Thomas, E. L.; Alward, D. B.; Kinning, D. J.; Martin, D. C.; Handlin, D. L.; Fetters, L. J. *Macromolecules* **1986,** 19, (8), 2197-2202.

66. Aggarwal, S. L. *Polymer* **1976,** 17, (11), 938-956.

67. Kinning, D. J.; Thomas, E. L.; Alward, D. B.; Fetters, L. J.; Handlin, D. L. *Macromolecules* **1986,** 19, (4), 1288-1290.

68. Herman, D. S.; Kinning, D. J.; Thomas, E. L.; Fetters, L. J. *Macromolecules* **1987,** 20, (11), 2940-2942.

69. Kim, S.; Yoo, M.; Baettig, J.; Kang, E. H.; Koo, J.; Choe, Y.; Choi, T. L.; Khan, A.; Son, J. G.; Bang, J. *Acs Macro Letters* **2015,** 4, (1), 133-137.

70. Fan, X.; Huang, B.; Wang, G.; Huang, J. *Macromolecules* **2012,** 45, (9), 3779-3786.

71. Kalogirou, A.; Moultos, O. A.; Gergidis, L. N.; Vlahos, C. *Macromolecules* **2014,** 47, (16), 5851-5859.

72. Wang, X.; Li, L.; Ye, X.; Wu, C. *Macromolecules* **2014,** 47, (7), 2487-2495.

73. Panday, A.; Mullin, S.; Gomez, E. D.; Wanakule, N.; Chen, V. L.; Hexemer, A.; Pople, J.; Balsara, N. P. *Macromolecules* **2009,** 42, (13), 4632-4637.

74. Kuan, W.-F.; Remy, R.; Mackay, M. E.; Epps III, T. H. *RSC Advances* **2015,** 5, (17), 12597-12604.

Appendix A

SUPPORTING INFORMATION FOR CHAPTER 3

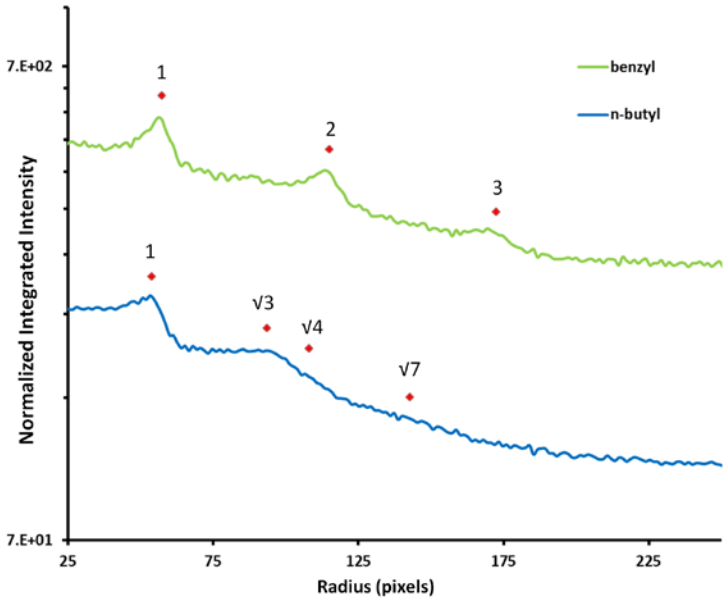

Figure A.1: 1D profiles for azimuthally integrated FFTs of the AFM phase images shown in Figure 3.2. The film thickness was 89 nm. FFTs were prepared by opening an 8-bit greyscale image in ImageJ, despeckling, enhancing contrast (default), and then calculating the 2D FFT. The 1D profiles display only a moderate degree of hexagonal ordering on the *n*-butyl surface. Reprinted with permission from Luo M., *et al.* *Macromolecules* 2013, 46, (5), 1803-1811.

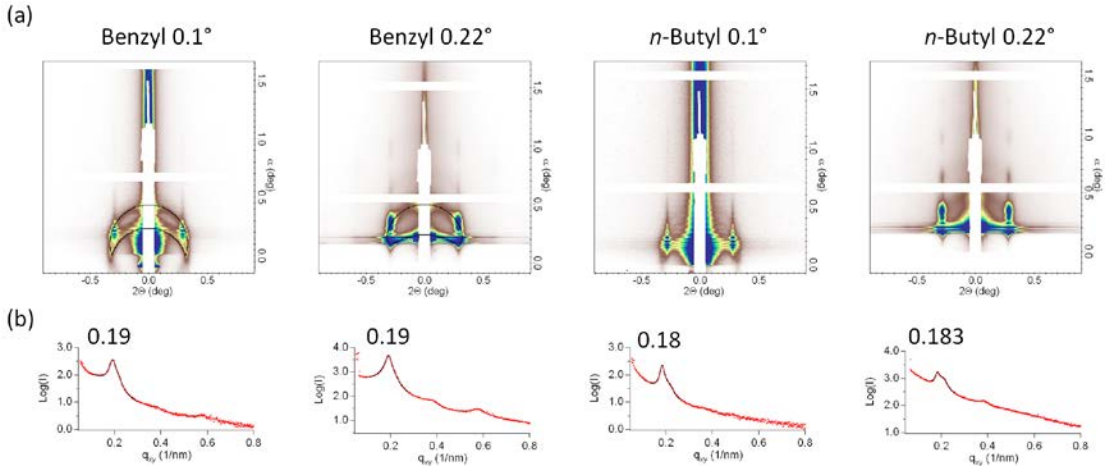

Figure A.2: (a) GISAXS data of benzyl and *n*-butyl samples acquired with an incident angle of 0.1° and 0.22°. Films were annealed at 135 °C for 12 h. The film thickness was ≈90 nm. Black contours mark the Debye-Scherrer ring. We note that the out-of-plane order was improved on *n*-butyl sample (little or no powder ring), while the benzyl sample contained randomly oriented domains. (b) 1D profiles of the in-plane line cuts for all samples with the first order peak position noted above the profile. Line cuts were taken from the region near the critical angle. The first order peak decreased on the *n*-butyl sample, indicating an increasing *d*-spacing of 4% for the HPL structure. A shoulder on the first peak near the critical angle existed for all the samples. This peak relates to misorientation of the layers along the out-of-plane axis, or coexistence between two phases. All samples on *n*-butyl surfaces likely have some signal from parallel cylinders, as discussed in the manuscript. Reprinted with permission from Luo M., *et al. Macromolecules* 2013, 46, (5), 1803-1811.

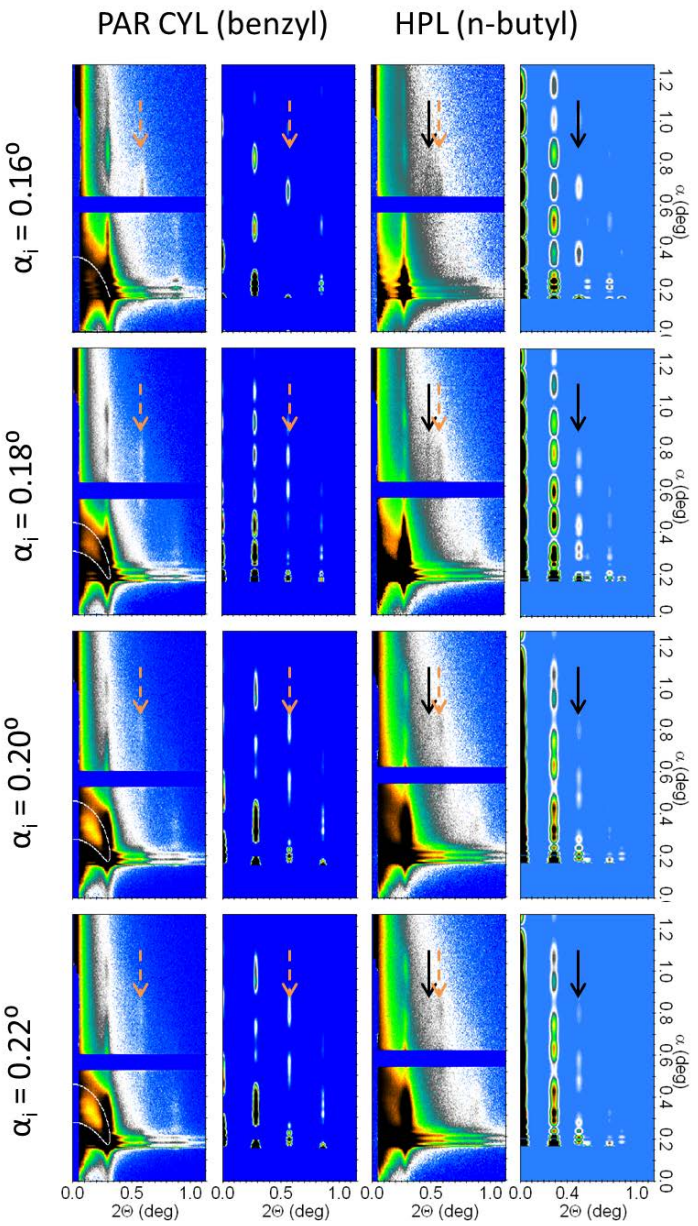

Figure A.3: Comparison between experiment and DWBA simulations for parallel cylinders and hexagonal perforations, both with ABA stacking. The dashed orange arrow denotes the second-order peak for parallel cylinders, while the solid black arrow denotes the √3 peak for in-plane hexagonal symmetry. White contours denote the trajectory for Debye-Scherrer rings. The data for the films on *n*-butyl surfaces are consistent with a mixture of ABA hexagonally-perforated lamellae and ABA cylinders. Reprinted with permission from Luo M., *et al. Macromolecules* 2013, 46, (5), 1803-1811.

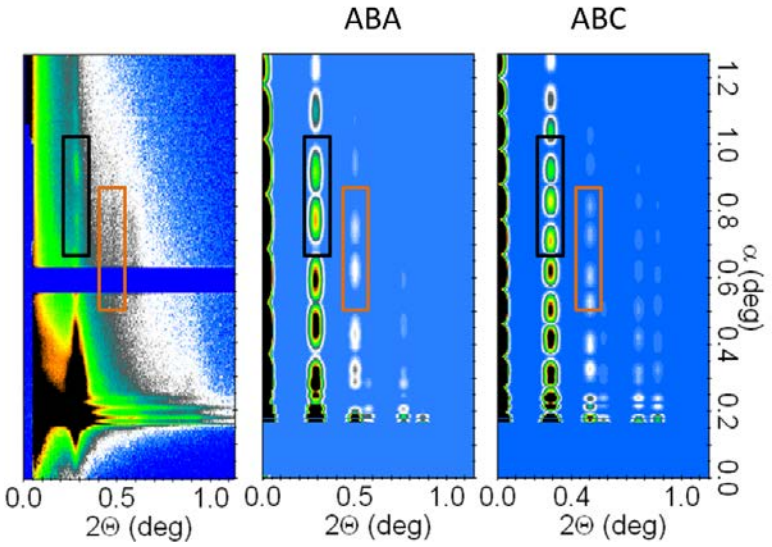

Figure A.4: Comparison between experiment and DWBA simulations for hexagonal perforations at an incident angle of 0.18°. Both ABA and ABC stacking sequences are considered. The simulated ABA stacking compares well with experimental data; the simulated ABC stacking does not compare well with experimental data. Reprinted with permission from Luo M., *et al. Macromolecules* 2013, 46, (5), 1803-1811.

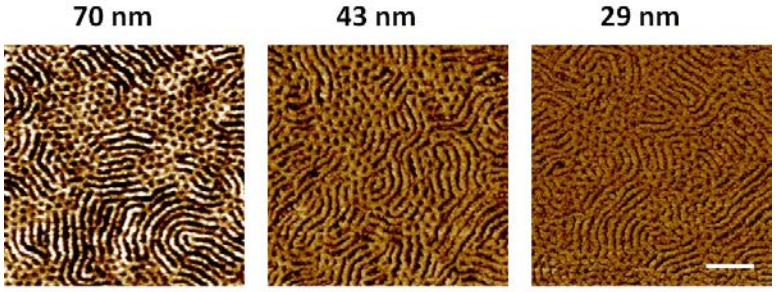

Figure A.5: UVO etching followed by AFM imaging of an 87 nm thick SIS film on *n*-butyl silane substrate. The images show that the parallel cylinders persist through the depth of the film. The possibility of parallel cylinders at the film surface on top of an underlying HPL structure is not supported by this analysis. Scale bar is 200 nm and applies to all images. Reprinted with permission from Luo M., *et al. Macromolecules* 2013, 46, (5), 1803-1811.

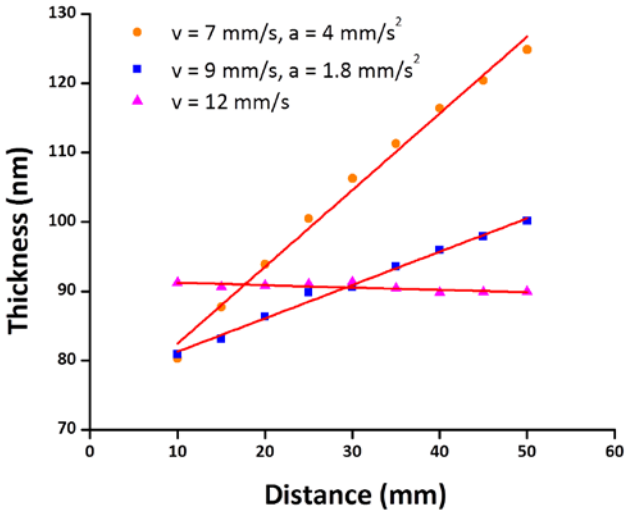

Figure A.6: Thickness profiles for the gradient thickness films and constant thickness films. Coating speed: v = 7 mm/s, acceleration: a = 4 mm/s^2, was used to fabricate a useable thickness gradient from 80 nm - 125 nm. The analyzed gradient spanned 40 mm in length (1" in width), and the resulting slope was approximately 1.1 nm/mm. Coating speed: v = 9 mm/s, acceleration: a = 1.8 mm/s^2, was used to produce a thickness gradient from 80 nm to 100 nm to investigate the film thickness effect close to 90 nm. The gradient was approximately 0.5 nm/mm. The constant thickness film was cast using constant speed, v = 12 mm/s. Reprinted with permission from Luo M., *et al. Macromolecules* 2013, 46, (5), 1803-1811.

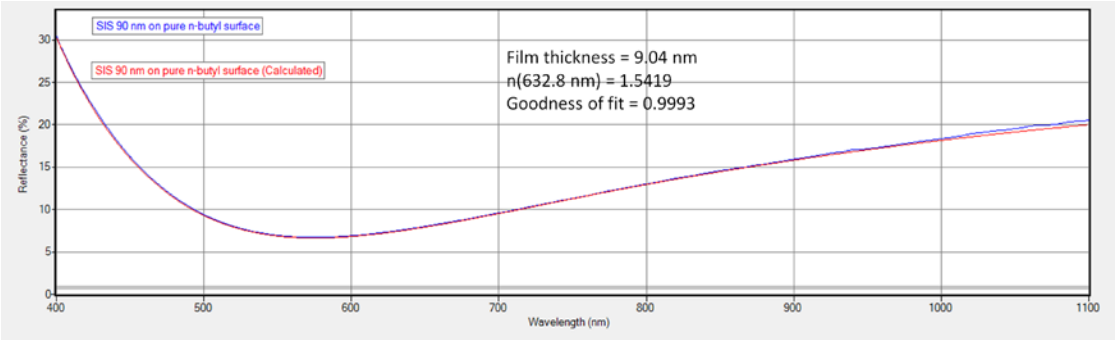

Figure A.7: Spectral reflectance measurement on the 90 nm thick SIS film. The reflectance spectrum was modeled using $R \approx A + B\cos(4\pi nt/\lambda)$, where A and B are constants, and *n* is the refractive index, and *t* is the film thickness. The initial value *n* for the BP film was estimated by adding the refractive indexes of the homopolymers weighted by the volume fraction of the constituent blocks. The software then was allowed to fit the *t* and *n*, and the goodness of fit was usually > 0.99 for polymer films. For the SIS films studied here, the refractive index was $n = 1.54$, and the goodness of fit was 0.9993. The accuracy of the film thickness was within 1 nm, which facilitates the location of the desired film thickness region. Reprinted with permission from Luo M., *et al. Macromolecules* 2013, 46, (5), 1803-1811.

Quantitative Morphological Analysis from AFM Images

To determine the ratio of HPL structures to parallel cylinders in the SIS film across the gradient substrate, the AFM phase images were analyzed through an in-house JAVA program developed by Ronald Lewis.[70] More specifically, a code was developed in Java to quantify the fraction of dots (represent to HPL structure) *versus* lines (represent to parallel cylinders) in the AFM images. The image analysis process is described as follows: i) The AFM phase image is converted to binary image through ImageJ (Figure A.8) with white pixels representing structure and black pixels representing matrix, respectively. ii) The binary image then is loaded into the java program, which analyzes the color of each pixel, either black or white. The white

pixels are grouped by a nearest neighbor analysis. The number of pixels in each grouping is counted, and the size distribution is plotted as the frequency *versus* size of group (pixels) shown in Figure A.8. iii) The peak in the distribution profile can be considered to represent the dot structures because the dot structures are much smaller and more uniform in size, while the parallel cylindrical structures tend to be much larger and more polydispersed in size. A threshold that is twice of the peak location is applied to the groupings, which means that groups that are smaller than the threshold is assigned to dot structures and groups that are bigger than the threshold is assigned to parallel cylinders. iv) A re-coloring process is applied to the pixels according the assignment. The re-colored image showed good agreement with the original image (Figure A.8). Therefore, this process allows quantitative morphological analysis from AFM Images. The codes are available elsewhere.[70]

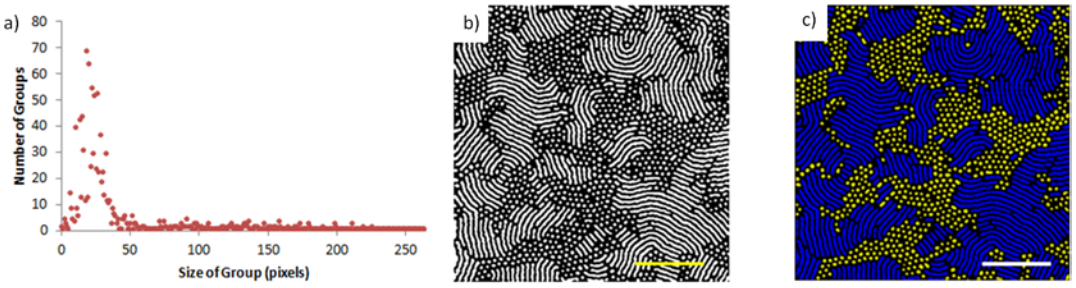

Figure A.8: a) Size distribution of the white groups in the sample AFM image shown in (b). c) Re-colored image after analysis to show regions of dot structures and parallel cylinders. The scale bars represent 500 nm. Adapted with permission from Lewis, R., senior thesis, University of Delaware, 2013.

Appendix B

SUPPORTING INFORMATION FOR CHAPTER 4

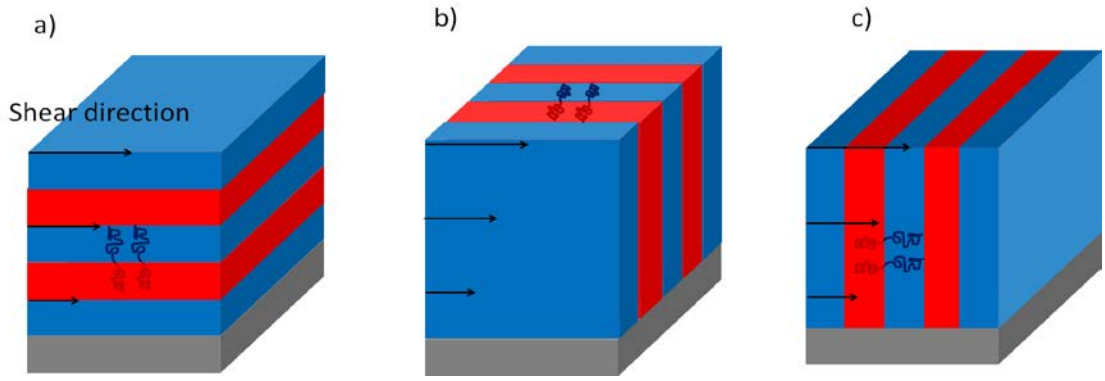

Figure B.1: Schematic representation of lamellar BP thin films under shear: (a) parallel, (b) perpendicular, and (c) transverse orientation. The arrows indicate the direction of an imposed shear field.

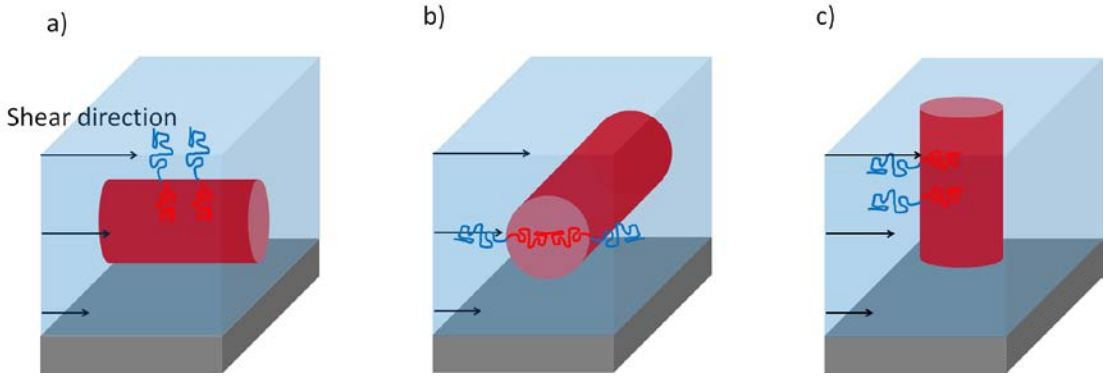

Figure B.2: Schematic representation of cylindrical BP thin films under shear: (a) parallel, (b) "log-rolling", and (c) perpendicular orientation. The arrows indicate the direction of an imposed shear field.

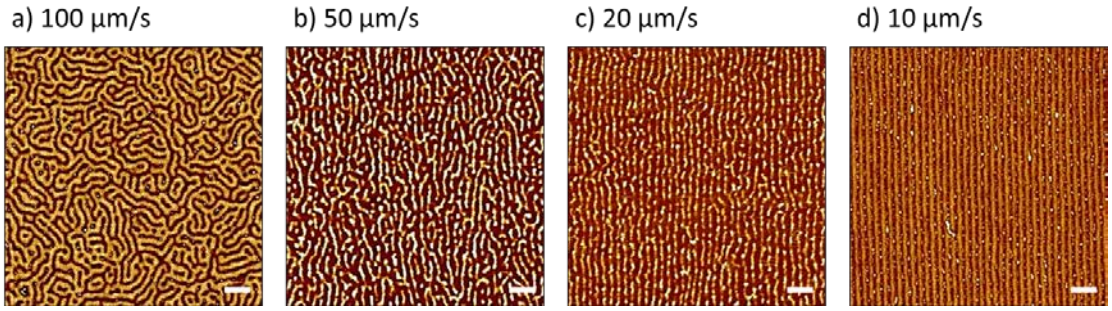

Figure B.3: Atomic force microscopy (AFM) phase images of the poly(styrene-*b*-isoprene-*b*-styrene) [SIS] thin films processed at different rastering speeds (a) 100 µm/s; (b) 50 µm/s; (c) 20 µm/s; (d) 10 µm/s. Scale bars represent 200 nm. Reprinted with permission from Luo, M.; Scott, D. M.; Epps, T. H. *ACS Macro Letters* 2015, 4, (5), 516-520.

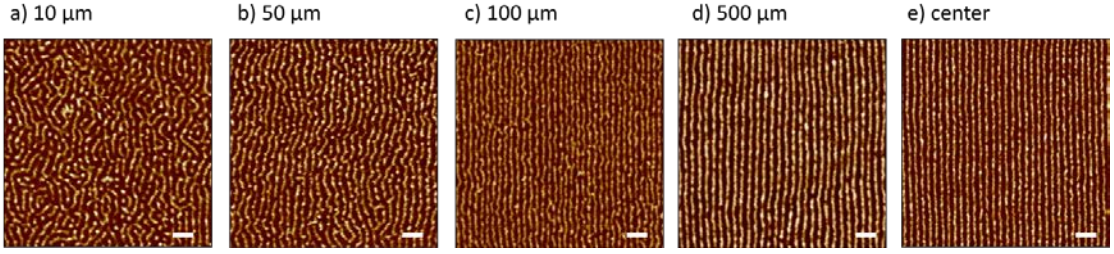

Figure B.4: AFM phase images of the SIS thin films near the edge of the rastered region *vs.* center of the rastered area. The total rastered area was 4000 µm (4 mm) wide. Distances from the edges are noted above the corresponding AFM phase images. Note: Approximately 95% of the rastered area shows high-quality cylinder alignment. Scale bars represent 200 nm. Reprinted with permission from Luo, M.; Scott, D. M.; Epps, T. H. *ACS Macro Letters* 2015, 4, (5), 516-520.

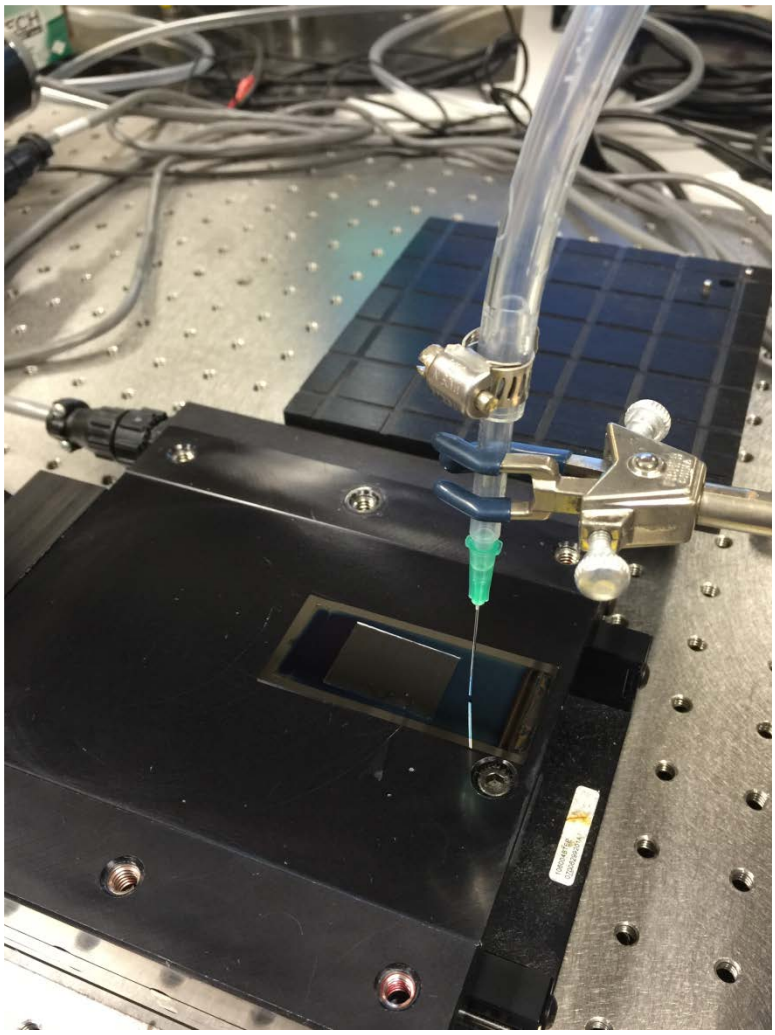

Figure B.5: Photography of RSVA-SS setup. The needle was mounted on a vertical micrometer stage set 0.2 mm above the PDMS surface. The substrate-supported films were affixed to a programmable motorized stage to control the rastering speed and position.

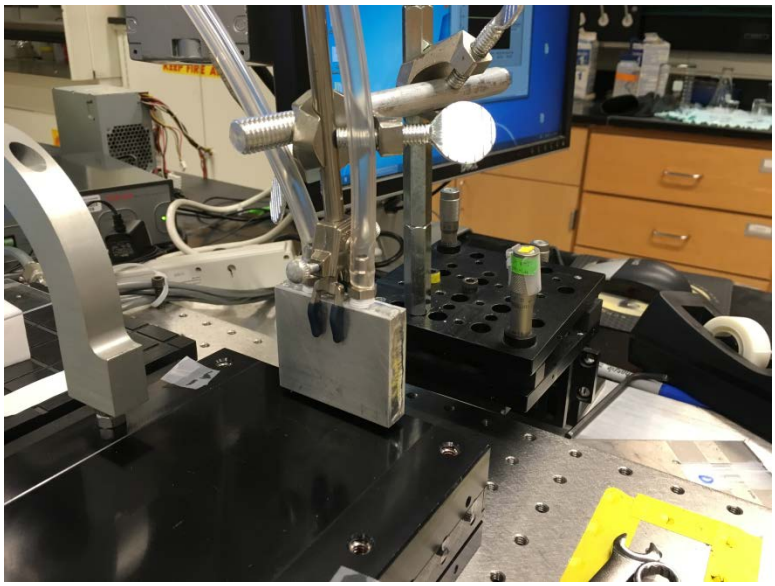

Figure B.6: Photography of the slit nozzle mounted on a vertical micrometer stage. Image courtesy of Douglas M. Scott.

Appendix C

SUPPORTING INFORMATION FOR CHAPTER 5

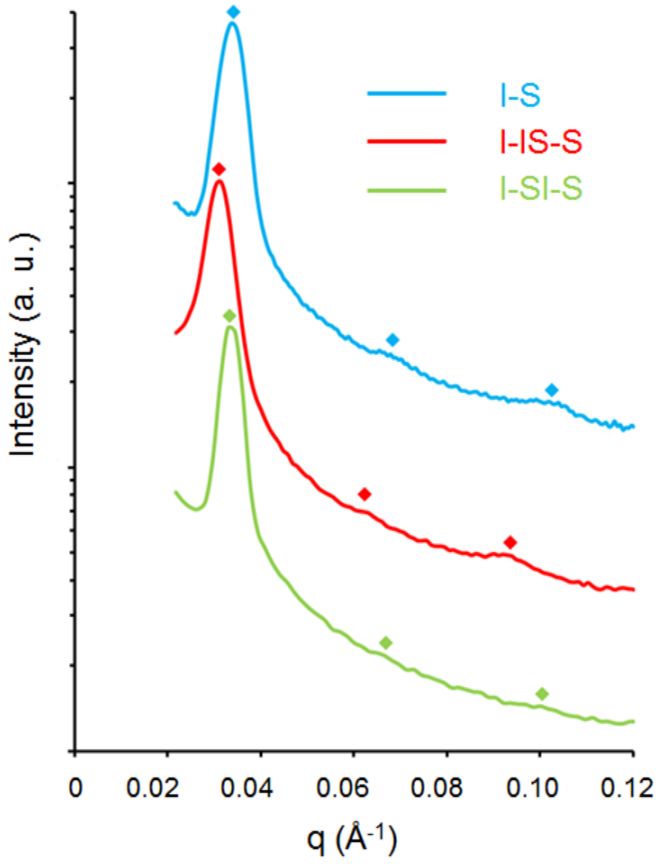

Figure C.1: Lab source small-angle X-ray scattering (SAXS) data for non-tapered poly(isoprene-*b*-styrene) (I-S), normal tapered I-IS-S, and inverse tapered I-SI-S block polymers at 25 °C. The diffraction peak locations for a lamellar morphology are marked by colored diamonds. The domain spacings, calculated from the primary peak location, are 18.4 nm for I-S, 20.1 nm for I-IS-S, and 18.8 nm for I-SI-S. SAXS curves are shifted vertically for clarity. Reprinted with permission from Luo, M., *et al.* *Macromolecules*, 2016, 49, (14), 5213-5222.

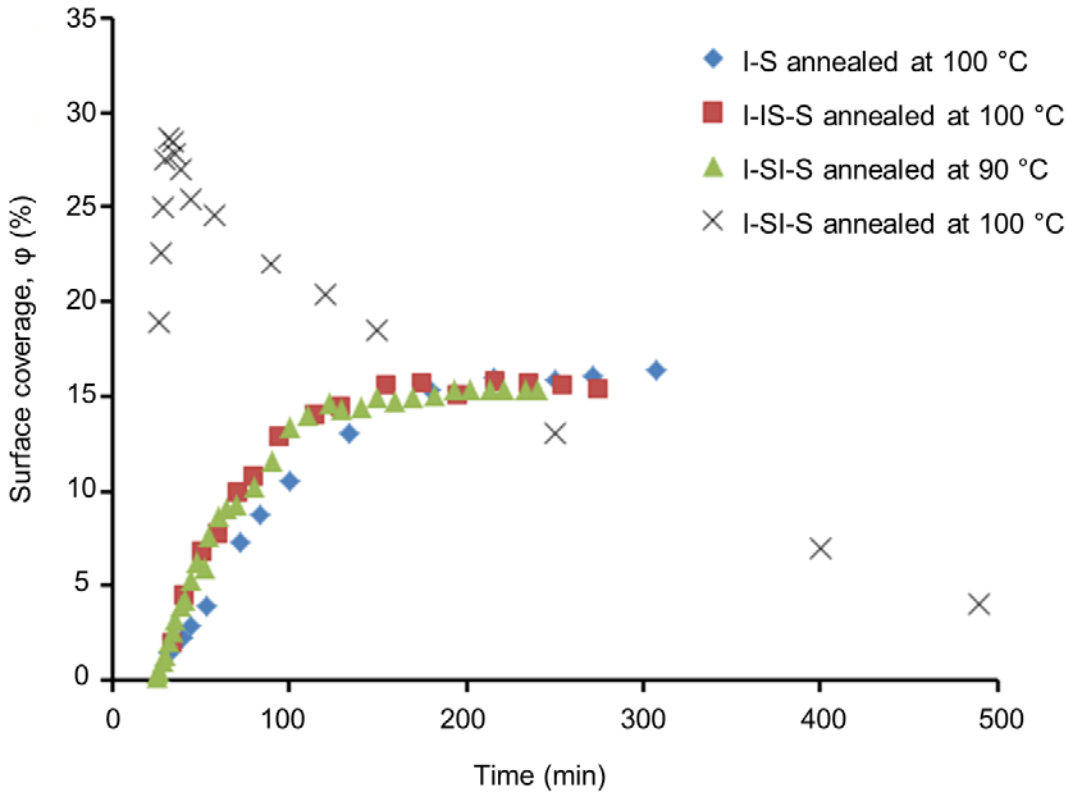

Figure C.2: Surface coverage of islands (φ) as a function of the annealing time for I-S, I-IS-S, and I-SI-S thin films at select annealing temperatures. For the I-S and I-IS-S films annealed at 100 °C and the I-SI-S film annealed at 90 °C, the surface coverage increases with time before reaching a plateau, giving an 'equilibrium' surface coverage. For the I-SI-S film annealed at a higher temperature (100 °C), the surface coverage exhibits an initial spike and then decreases toward zero. This behavior likely is caused by the lower order-disorder transition temperature of the I-SI-S film. Reprinted with permission from Luo, M., *et al. Macromolecules*, 2016, 49, (14), 5213-5222.

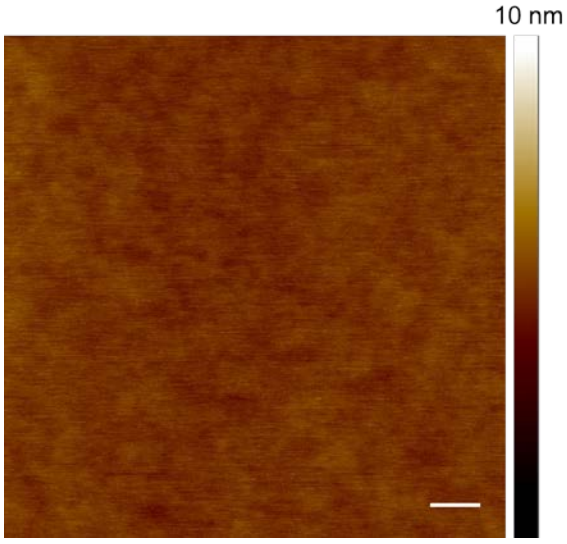

Figure C.3: Representative atomic force microscopy (AFM) height image of a uniform (smooth) I-S film after annealing at 100 °C for 6 h. The root mean square roughness is ~0.2 nm. Scale bar is 200 nm. Reprinted with permission from Luo, M., *et al. Macromolecules*, 2016, 49, (14), 5213-5222.

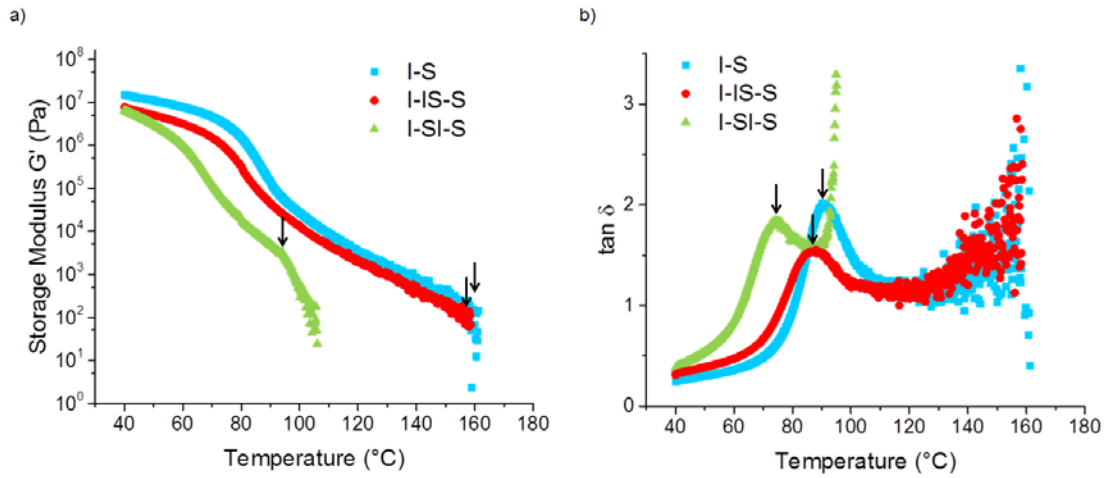

Figure C.4: Dynamic mechanical analysis for the bulk polymer samples. A strain amplitude of 0.4 – 3%, a frequency of 6.28 rad/s, and a heating rate of 3 °C/min were used for all samples. a) Storage modulus (*G'*) *versus* temperature for I-S (blue), I-IS-S (red), and I-SI-S (green) block polymers. The probable order-disorder transitions (ODTs) are indicated by arrows. The T_{ODT} was 160 °C for the non-tapered I-S polymer, 158 °C for the normal tapered I-IS-S polymer, and 94 °C for the inverse tapered I-SI-S polymer. b) tan δ *versus* temperature for I-S (blue), I-IS-S (red), and I-SI-S (green) block polymers. tan δ is defined by the ratio of the storage modulus (*G'*) to the loss modulus (*G''*). The rheological glass transition temperatures (T_gs) are indicated by arrows. The results follow the same trend noted in the differential scanning calorimetry (DSC) data, see main text for further details. The difference between the numerical values of the rheological T_g and calorimetric T_g for a given sample is expected as discussed in the literature. Reprinted with permission from Luo, M., *et al. Macromolecules*, 2016, 49, (14), 5213-5222.

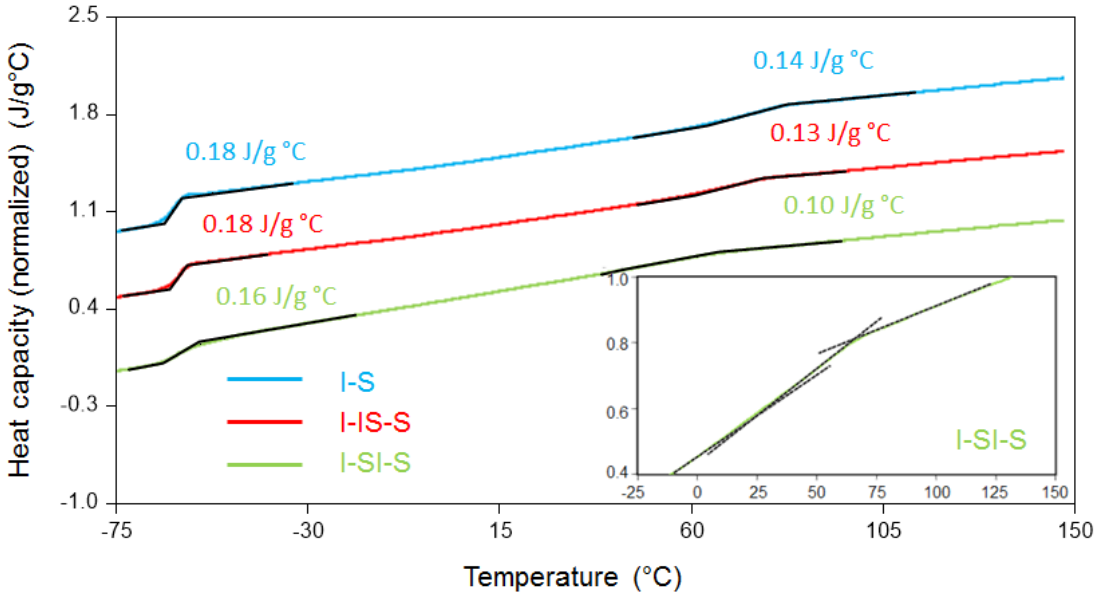

Figure C.5: DSC traces on second heating (10 °C min^{-1}, N_2 flow) for diblock I-S, normal tapered I-IS-S, and inverse tapered I-SI-S block polymers, normalized by the total mass of the sample. The heat capacity change (ΔC_P) for each phase is evaluated by measuring the difference in height between the extrapolated base lines above and below the glass transition. The inset zoomed-in figure highlights the two baselines (dash lines) for the I-SI-S sample. The values of ΔC_P for each phase are per gram of the respective monomer segment in the sample. The calculated values of $\Delta C_{P\text{-}PI}$ are 0.39 J g^{-1} K^{-1} for I-S, 0.39 J g^{-1} K^{-1} for I-IS-S, and 0.35 J g^{-1} K^{-1} for I-SI-S. The calculated values of $\Delta C_{P\text{-}PS}$ are 0.26 J g^{-1} K^{-1} for I-S, 0.24 J g^{-1} K^{-1} for I-IS-S, and 0.18 J g^{-1} K^{-1} for I-SI-S. Curves are shifted vertically for clarity. Reprinted with permission from Luo, M., *et al.* *Macromolecules*, 2016, 49, (14), 5213-5222.

Appendix D

SUPPORTING INFORMATION FOR CHAPTER 6

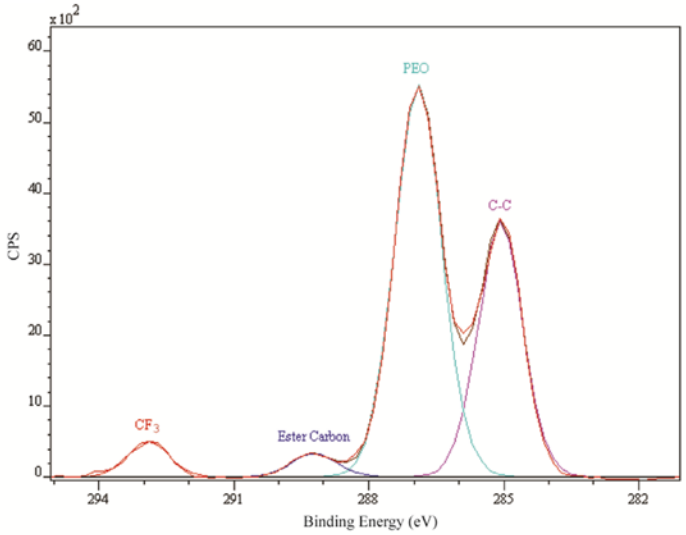

Figure D.1: Peak fitting of the C1s spectra in the POEM domain displaying peaks from the C-C (from POEM backbone, marked as C-C), C-O (from short ethylene oxide side chains, marked as PEO), C=O (from ester linkage, marked as Ester Carbon), and C-F (from lithium salt counterion, marked as CF_3). Adapted with permission from Gilbert, J. B.; Luo, M.; Shelton, C. K.; Rubner, M. F.; Cohen, R. E.; Epps III, T. H. *ACS Nano* 2014, 9, (1), 512-520.

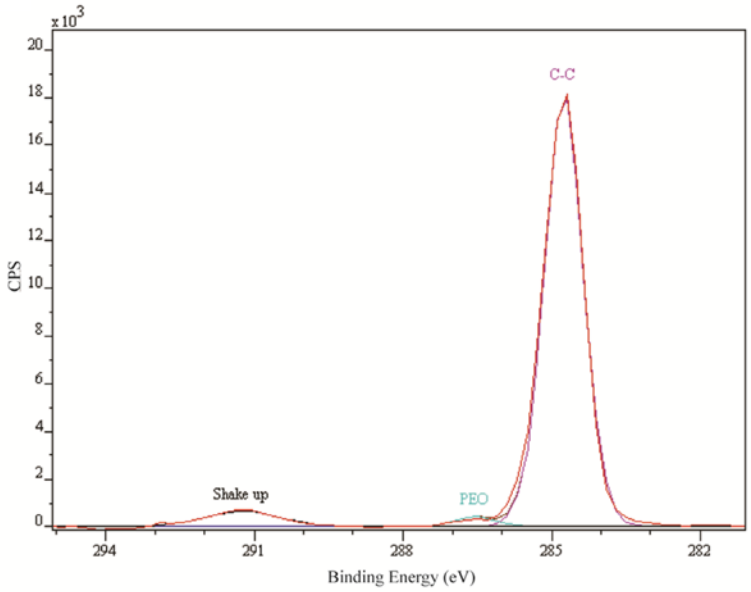

Figure D.2: Peak fitting of the C1s spectra in the PS domain displaying peaks from the carbon bonds (marked as C-C), a very minor peak from ethylene oxide side chain (marked as PEO), and C-C bond shake up peak due to π-> π^* stacking (marked as Shake up). Adapted with permission from Gilbert, J. B.; Luo, M.; Shelton, C. K.; Rubner, M. F.; Cohen, R. E.; Epps III, T. H. *ACS Nano* 2014, 9, (1), 512-520.

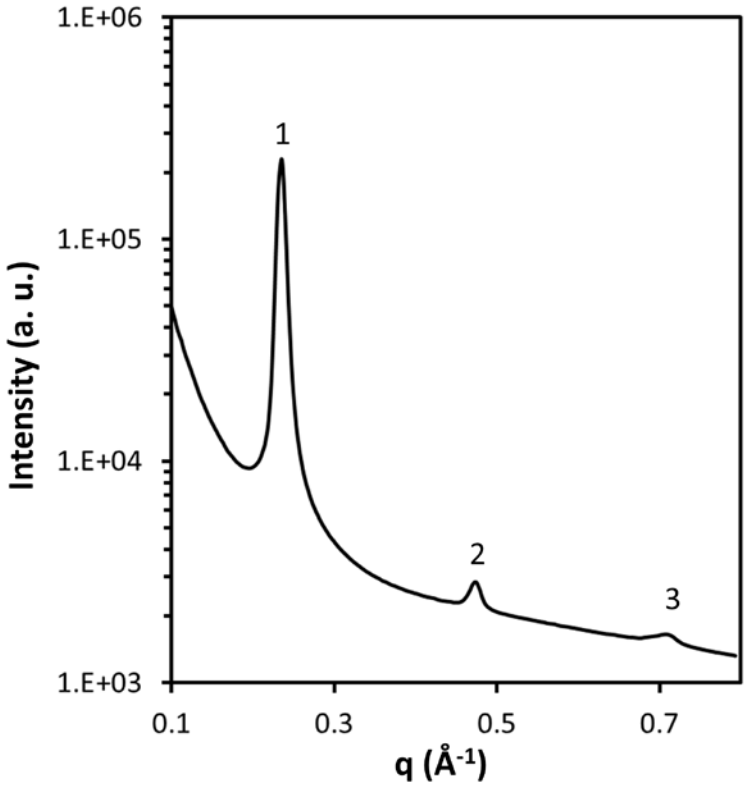

Figure D.3: Synchrotron SAXS data of the neat PS-POEM bulk sample from the DND-CAT beamline at the Advanced Photon Source of the Argonne National Laboratory (data acquired by Wei-Fan Kuan). The neat PS-POEM polymer exhibits a lamellar structure with diffraction peak ratios of 1, 2, and 3. The domain spacing *d* of the BP was 26.1 nm calculated from $d = 2\pi / q^*$. Reprinted with permission from Gilbert, J. B.; Luo, M.; Shelton, C. K.; Rubner, M. F.; Cohen, R. E.; Epps III, T. H. *ACS Nano* 2014, 9, (1), 512-520.

Table D.1: Idealized atomic composition ratios of the PS and POEM lamellae with [EO]:[Li] = 6:1.

	Component	**C**	**F**	**Li**	**O**
PS domain	PS	8	0	0	0
	Ideal atomic composition (%)	100%	0%	0%	0%
POEM domain	Lithium salt $LiCF_3SO_3$ ([EO]:[Li] = 6:1)	8.5/6 (1 $LiCF_3SO_3$ per 6 EO repeats)	8.5/6*3	8.5/6	8.5/6*3
	POEM	5 (backbone and ester) +2 (ether carbons) *8.5 repeats	0	0	2 (ester) +8.5 (ether)
	Ideal atomic composition (%) (total moles of atoms = 43.83)	23.42/43.83 =53.4%	4.25/43.83 = 9.7%	1.42/43.83 =3.2%	14.75/43.83 =33.6%

Note: the PS and POEM structures are shown in Figure 6.1. The average number of ethylene oxide repeat units per POEM side-chain was 8.5 as determined from proton nuclear magnetic resonance (^{1}H NMR) spectroscopy of the OEM monomer.

Table D.2: Etch rate of pure PS homopolymer (z_{PS}) and Li-doped POEM homopolymer films (z_{POEM}).

Homopolymer	Initial thickness (nm)	Time to completely etch through the film (trial 1) (min)	Time to completely etch through the film (trial 2) (min)	Rate (nm/min)
PS	72	14.79	15.07	4.82
POEM with [EO]:[Li] = 6:1	83	11.23	12.13	7.11

Note: The sputtering rate ratio is defined as $r = z_{PS} / z_{POEM}$. When adjusting etch rate for the PS-POEM BP thin film, a first-order approximation is to assume a linear relation between the instantaneous composition (of the altered layer) and the sputtering rates of the pure components. Therefore, the instantaneous etch rate is $\dot{z} = \dot{z}_{PS} x_{PS} + \dot{z}_{POEM} x_{POEM} = r\dot{z}_{POEM}(1 - x_{POEM}) + \dot{z}_{POEM} x_{POEM}$. In order to compute the instantaneous composition x_{POEM}, the O1s data was normalized by the ideal composition.

Appendix E

TEXT AND FIGURE REPRINT PERMISSIONS

Title: Stability of the Gyroid Phase in Diblock Copolymers at Strong Segregation

Author: Eric W. Cochran, Carlos J. Garcia-Cervera, Glenn H. Fredrickson

Publication: Macromolecules

Publisher: American Chemical Society

Date: Apr 1, 2006

PERMISSION/LICENSE IS GRANTED FOR YOUR ORDER AT NO CHARGE

This type of permission/license, instead of the standard Terms & Conditions, is sent to you because no fee is being charged for your order. Please note the following:

- Permission is granted for your request in both print and electronic formats, and translations.
- If figures and/or tables were requested, they may be adapted or used in part.
- Please print this page for your records and send a copy of it to your publisher/graduate school.
- Appropriate credit for the requested material should be given as follows: "Reprinted (adapted) with permission from (COMPLETE REFERENCE CITATION). Copyright (YEAR) American Chemical Society." Insert appropriate information in place of the capitalized words.
- One-time permission is granted only for the use specified in your request. No additional uses are granted (such as derivative works or other editions). For any other uses, please submit a new request.

If credit is given to another source for the material you requested, permission must be obtained from that source.

BACK CLOSE WINDOW

Title: Density Multiplication and Improved Lithography by Directed Block Copolymer Assembly

Author: Ricardo Ruiz,Huiman Kang,François A. Detcheverry,Elizabeth Dobisz,Dan S. Kercher,Thomas R. Albrecht,Juan J. de Pablo,Paul F. Nealey

Publication: Science

Publisher: The American Association for the Advancement of Science

Date: Aug 15, 2008

Order Completed

Thank you very much for your order.

This is a License Agreement between Ming Luo ("You") and The American Association for the Advancement of Science ("The American Association for the Advancement of Science"). The license consists of your order details, the terms and conditions provided by The American Association for the Advancement of Science, and the payment terms and conditions.

Get the printable license.

License Number	3871391308456
License date	May 17, 2016
Licensed content publisher	The American Association for the Advancement of Science
Licensed content publication	Science
Licensed content title	Density Multiplication and Improved Lithography by Directed Block Copolymer Assembly
Licensed content author	Ricardo Ruiz,Huiman Kang,François A. Detcheverry,Elizabeth Dobisz,Dan S. Kercher,Thomas R. Albrecht,Juan J. de Pablo,Paul F. Nealey
Licensed content date	Aug 15, 2008
Volume number	321
Issue number	5891
Type of Use	Thesis / Dissertation
Requestor type	Scientist/individual at a research institution
Format	Print and electronic
Portion	Figure
Number of figures/tables	1
Order reference number	None
Title of your thesis / dissertation	CONTROL SELF-ASSEMBLING AND ORDERING OF BLOCK POLYMER NANOSTRUCTURES IN THIN FILMS
Expected completion date	Jun 2016
Estimated size(pages)	200
Total	0.00 USD

ORDER MORE... CLOSE WINDOW

Title:	Ultrahigh-Density Nanowire Arrays Grown in Self-Assembled Diblock Copolymer Templates
Author:	T. Thurn-Albrecht,J. Schotter,G. A. Kästle,N. Emley,T. Shibauchi,L. Krusin-Elbaum,K. Guarini,C. T. Black,M. T. Tuominen,T. P. Russell
Publication:	Science
Publisher:	The American Association for the Advancement of Science
Date:	Dec 15, 2000

Order Completed

Thank you very much for your order.

This is a License Agreement between Ming Luo ("You") and The American Association for the Advancement of Science ("The American Association for the Advancement of Science"). The license consists of your order details, the terms and conditions provided by The American Association for the Advancement of Science, and the payment terms and conditions.

Get the printable license.

License Number	3871400104244
License date	May 17, 2016
Licensed content publisher	The American Association for the Advancement of Science
Licensed content publication	Science
Licensed content title	Ultrahigh-Density Nanowire Arrays Grown in Self-Assembled Diblock Copolymer Templates
Licensed content author	T. Thurn-Albrecht,J. Schotter,G. A. Kästle,N. Emley,T. Shibauchi,L. Krusin-Elbaum,K. Guarini,C. T. Black,M. T. Tuominen,T. P. Russell
Licensed content date	Dec 15, 2000
Volume number	290
Issue number	5499
Type of Use	Thesis / Dissertation
Requestor type	Scientist/individual at a research institution
Format	Print and electronic
Portion	Figure
Number of figures/tables	1
Order reference number	None
Title of your thesis / dissertation	CONTROL SELF-ASSEMBLING AND ORDERING OF BLOCK POLYMER NANOSTRUCTURES IN THIN FILMS
Expected completion date	Jun 2016
Estimated size(pages)	200
Total	0.00 USD

ORDER MORE... CLOSE WINDOW

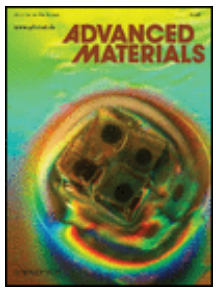

Title: Nanoporous Membranes with Ultrahigh Selectivity and Flux for the Filtration of Viruses

Author: S. Y. Yang,I. Ryu,H. Y. Kim,J. K. Kim,S. K. Jang,T. P. Russell

Publication: Advanced Materials

Publisher: John Wiley and Sons

Date: Feb 16, 2006

Order Completed

Thank you for your order.

This Agreement between Ming Luo ("You") and John Wiley and Sons ("John Wiley and Sons") consists of your license details and the terms and conditions provided by John Wiley and Sons and Copyright Clearance Center.

Your confirmation email will contain your order number for future reference.

Get the printable license.

License Number	3871400378994
License date	May 17, 2016
Licensed Content Publisher	John Wiley and Sons
Licensed Content Publication	Advanced Materials
Licensed Content Title	Nanoporous Membranes with Ultrahigh Selectivity and Flux for the Filtration of Viruses
Licensed Content Author	S. Y. Yang,I. Ryu,H. Y. Kim,J. K. Kim,S. K. Jang,T. P. Russell
Licensed Content Date	Feb 16, 2006
Licensed Content Pages	4
Type of use	Dissertation/Thesis
Requestor type	University/Academic
Format	Print and electronic
Portion	Figure/table
Number of figures/tables	1
Original Wiley figure/table number(s)	Figure 1
Will you be translating?	No
Title of your thesis / dissertation	CONTROL SELF-ASSEMBLING AND ORDERING OF BLOCK POLYMER NANOSTRUCTURES IN THIN FILMS
Expected completion date	Jun 2016
Expected size (number of pages)	200
Requestor Location	Ming Luo 150 Academy Street Newark, DE 19716 United States Attn: Ming Luo
Billing Type	Invoice

Title: Precisely Tunable Photonic Crystals From Rapidly Self-Assembling Brush Block Copolymer Blends

Author: Garret M. Miyake,Victoria A. Piunova,Raymond A. Weitekamp,Robert H. Grubbs

Publication: Angewandte Chemie International Edition

Publisher: John Wiley and Sons

Date: Sep 13, 2012

Order Completed

Thank you for your order.

This Agreement between Ming Luo ("You") and John Wiley and Sons ("John Wiley and Sons") consists of your license details and the terms and conditions provided by John Wiley and Sons and Copyright Clearance Center.

Your confirmation email will contain your order number for future reference.

Get the printable license.

License Number	3871400489581
License date	May 17, 2016
Licensed Content Publisher	John Wiley and Sons
Licensed Content Publication	Angewandte Chemie International Edition
Licensed Content Title	Precisely Tunable Photonic Crystals From Rapidly Self-Assembling Brush Block Copolymer Blends
Licensed Content Author	Garret M. Miyake,Victoria A. Piunova,Raymond A. Weitekamp,Robert H. Grubbs
Licensed Content Date	Sep 13, 2012
Licensed Content Pages	3
Type of use	Dissertation/Thesis
Requestor type	University/Academic
Format	Print and electronic
Portion	Figure/table
Number of figures/tables	1
Original Wiley figure/table number(s)	Figure 2
Will you be translating?	No
Title of your thesis / dissertation	CONTROL SELF-ASSEMBLING AND ORDERING OF BLOCK POLYMER NANOSTRUCTURES IN THIN FILMS
Expected completion date	Jun 2016
Expected size (number of pages)	200
Requestor Location	Ming Luo 150 Academy Street

	Newark, DE 19716 United States Attn: Ming Luo
Billing Type	Invoice
Billing address	Ming Luo 150 Academy Street Newark, DE 19716 United States Attn: Ming Luo
Total	0.00 USD

Would you like to purchase the full text of this article? If so, please continue on to the content ordering system located here: Purchase PDF

If you click on the buttons below or close this window, you will not be able to return to the content ordering system.

CLOSE WINDOW

Title: Effect of Composition of Substrate-Modifying Random Copolymers on the Orientation of Symmetric and Asymmetric Diblock Copolymer Domains

Author: Eungnak Han, Karl O. Stuen, Young-Hye La, et al

Publication: Macromolecules

Publisher: American Chemical Society

Date: Dec 1, 2008

PERMISSION/LICENSE IS GRANTED FOR YOUR ORDER AT NO CHARGE

This type of permission/license, instead of the standard Terms & Conditions, is sent to you because no fee is being charged for your order. Please note the following:

- Permission is granted for your request in both print and electronic formats, and translations.
- If figures and/or tables were requested, they may be adapted or used in part.
- Please print this page for your records and send a copy of it to your publisher/graduate school.
- Appropriate credit for the requested material should be given as follows: "Reprinted (adapted) with permission from (COMPLETE REFERENCE CITATION). Copyright (YEAR) American Chemical Society." Insert appropriate information in place of the capitalized words.
- One-time permission is granted only for the use specified in your request. No additional uses are granted (such as derivative works or other editions). For any other uses, please submit a new request.

If credit is given to another source for the material you requested, permission must be obtained from that source.

BACK CLOSE WINDOW

Title: Gradient Solvent Vapor Annealing of Block Copolymer Thin Films Using a Microfluidic Mixing Device

Author: Julie N. L. Albert, Timothy D. Bogart, Ronald L. Lewis, et al

Publication: Nano Letters

Publisher: American Chemical Society

Date: Mar 1, 2011

PERMISSION/LICENSE IS GRANTED FOR YOUR ORDER AT NO CHARGE

This type of permission/license, instead of the standard Terms & Conditions, is sent to you because no fee is being charged for your order. Please note the following:

- Permission is granted for your request in both print and electronic formats, and translations.
- If figures and/or tables were requested, they may be adapted or used in part.
- Please print this page for your records and send a copy of it to your publisher/graduate school.
- Appropriate credit for the requested material should be given as follows: "Reprinted (adapted) with permission from (COMPLETE REFERENCE CITATION). Copyright (YEAR) American Chemical Society." Insert appropriate information in place of the capitalized words.
- One-time permission is granted only for the use specified in your request. No additional uses are granted (such as derivative works or other editions). For any other uses, please submit a new request.

If credit is given to another source for the material you requested, permission must be obtained from that source.

BACK CLOSE WINDOW

Title: Polarity-Switching Top Coats Enable Orientation of Sub–10-nm Block Copolymer Domains

Author: Christopher M. Bates,Takehiro Seshimo,Michael J. Maher,William J. Durand,Julia D. Cushen,Leon M. Dean,Gregory Blachut,Christopher J. Ellison,C. Grant Willson

Publication: Science

Publisher: The American Association for the Advancement of Science

Date: Nov 9, 2012

Order Completed

Thank you very much for your order.

This is a License Agreement between Ming Luo ("You") and The American Association for the Advancement of Science ("The American Association for the Advancement of Science"). The license consists of your order details, the terms and conditions provided by The American Association for the Advancement of Science, and the payment terms and conditions.

Get the printable license.

License Number	3871461289304
License date	May 17, 2016
Licensed content publisher	The American Association for the Advancement of Science
Licensed content publication	Science
Licensed content title	Polarity-Switching Top Coats Enable Orientation of Sub–10-nm Block Copolymer Domains
Licensed content author	Christopher M. Bates,Takehiro Seshimo,Michael J. Maher,William J. Durand,Julia D. Cushen,Leon M. Dean,Gregory Blachut,Christopher J. Ellison,C. Grant Willson
Licensed content date	Nov 9, 2012
Volume number	338
Issue number	6108
Type of Use	Thesis / Dissertation
Requestor type	Scientist/individual at a research institution
Format	Print and electronic
Portion	Figure
Number of figures/tables	1
Order reference number	None
Title of your thesis / dissertation	CONTROL SELF-ASSEMBLING AND ORDERING OF BLOCK POLYMER NANOSTRUCTURES IN THIN FILMS
Expected completion date	Jun 2016
Estimated size(pages)	200
Total	0.00 USD

ORDER MORE... CLOSE WINDOW

Title: Block Copolymer Lithography
Author: Christopher M. Bates, Michael J. Maher, Dustin W. Janes, et al
Publication: Macromolecules
Publisher: American Chemical Society
Date: Jan 1, 2014

PERMISSION/LICENSE IS GRANTED FOR YOUR ORDER AT NO CHARGE

This type of permission/license, instead of the standard Terms & Conditions, is sent to you because no fee is being charged for your order. Please note the following:

- Permission is granted for your request in both print and electronic formats, and translations.
- If figures and/or tables were requested, they may be adapted or used in part.
- Please print this page for your records and send a copy of it to your publisher/graduate school.
- Appropriate credit for the requested material should be given as follows: "Reprinted (adapted) with permission from (COMPLETE REFERENCE CITATION). Copyright (YEAR) American Chemical Society." Insert appropriate information in place of the capitalized words.
- One-time permission is granted only for the use specified in your request. No additional uses are granted (such as derivative works or other editions). For any other uses, please submit a new request.

If credit is given to another source for the material you requested, permission must be obtained from that source.

nature publishing group

Title:	Block copolymers: With a little help from above
Author:	Justin E. Poelma and Craig J. Hawker
Publication:	Nature Nanotechnology
Publisher:	Nature Publishing Group
Date:	Dec 31, 1969

Order Completed

Thank you very much for your order.

This is a License Agreement between Ming Luo ("You") and Nature Publishing Group ("Nature Publishing Group"). The license consists of your order details, the terms and conditions provided by Nature Publishing Group, and the payment terms and conditions.

Get the printable license.

License Number	3871470230666
License date	May 17, 2016
Licensed content publisher	Nature Publishing Group
Licensed content publication	Nature Nanotechnology
Licensed content title	Block copolymers: With a little help from above
Licensed content author	Justin E. Poelma and Craig J. Hawker
Licensed content date	Dec 31, 1969
Type of Use	reuse in a dissertation / thesis
Volume number	5
Issue number	4
Requestor type	academic/educational
Format	print and electronic
Portion	figures/tables/illustrations
Number of figures/tables/illustrations	1
Figures	Figure 1
Author of this NPG article	no
Your reference number	None
Title of your thesis / dissertation	CONTROL SELF-ASSEMBLING AND ORDERING OF BLOCK POLYMER NANOSTRUCTURES IN THIN FILMS
Expected completion date	Jun 2016
Estimated size (number of pages)	200
Total	0.00 USD

ORDER MORE... CLOSE WINDOW

Title: Using Cylindrical Domains of Block Copolymers To Self-Assemble and Align Metallic Nanowires

Author: Jinan Chai, Jillian M. Buriak

Publication: ACS Nano

Publisher: American Chemical Society

Date: Mar 1, 2008

PERMISSION/LICENSE IS GRANTED FOR YOUR ORDER AT NO CHARGE

This type of permission/license, instead of the standard Terms & Conditions, is sent to you because no fee is being charged for your order. Please note the following:

- Permission is granted for your request in both print and electronic formats, and translations.
- If figures and/or tables were requested, they may be adapted or used in part.
- Please print this page for your records and send a copy of it to your publisher/graduate school.
- Appropriate credit for the requested material should be given as follows: "Reprinted (adapted) with permission from (COMPLETE REFERENCE CITATION). Copyright (YEAR) American Chemical Society." Insert appropriate information in place of the capitalized words.
- One-time permission is granted only for the use specified in your request. No additional uses are granted (such as derivative works or other editions). For any other uses, please submit a new request.

If credit is given to another source for the material you requested, permission must be obtained from that source.

Title: Directed Assembly of Block Copolymer Blends into Nonregular Device-Oriented Structures

Author: Mark P. Stoykovich,Marcus Müller,Sang Ouk Kim,Harun H. Solak,Erik W. Edwards,Juan J. de Pablo,Paul F. Nealey

Publication: Science

Publisher: The American Association for the Advancement of Science

Date: Jun 3, 2005

Order Completed

Thank you very much for your order.

This is a License Agreement between Ming Luo ("You") and The American Association for the Advancement of Science ("The American Association for the Advancement of Science"). The license consists of your order details, the terms and conditions provided by The American Association for the Advancement of Science, and the payment terms and conditions.

Get the printable license.

License Number	3871470140316
License date	May 17, 2016
Licensed content publisher	The American Association for the Advancement of Science
Licensed content publication	Science
Licensed content title	Directed Assembly of Block Copolymer Blends into Nonregular Device-Oriented Structures
Licensed content author	Mark P. Stoykovich,Marcus Müller,Sang Ouk Kim,Harun H. Solak,Erik W. Edwards,Juan J. de Pablo,Paul F. Nealey
Licensed content date	Jun 3, 2005
Volume number	308
Issue number	5727
Type of Use	Thesis / Dissertation
Requestor type	Scientist/individual at a research institution
Format	Print and electronic
Portion	Figure
Number of figures/tables	1
Order reference number	None
Title of your thesis / dissertation	CONTROL SELF-ASSEMBLING AND ORDERING OF BLOCK POLYMER NANOSTRUCTURES IN THIN FILMS
Expected completion date	Jun 2016
Estimated size(pages)	200
Total	0.00 USD

ORDER MORE... CLOSE WINDOW

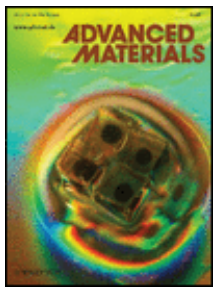

Title:	Macroscopic Orientation of Block Copolymer Cylinders in Single-Layer Films by Shearing
Author:	D. E. Angelescu,J. H. Waller,D. H. Adamson,P. Deshpande,S. Y. Chou,R. A. Register,P. M. Chaikin
Publication:	Advanced Materials
Publisher:	John Wiley and Sons
Date:	Sep 16, 2004

Order Completed

Thank you for your order.

This Agreement between Ming Luo ("You") and John Wiley and Sons ("John Wiley and Sons") consists of your license details and the terms and conditions provided by John Wiley and Sons and Copyright Clearance Center.

Your confirmation email will contain your order number for future reference.

Get the printable license.

License Number	3871471116459
License date	May 17, 2016
Licensed Content Publisher	John Wiley and Sons
Licensed Content Publication	Advanced Materials
Licensed Content Title	Macroscopic Orientation of Block Copolymer Cylinders in Single-Layer Films by Shearing
Licensed Content Author	D. E. Angelescu,J. H. Waller,D. H. Adamson,P. Deshpande,S. Y. Chou,R. A. Register,P. M. Chaikin
Licensed Content Date	Sep 16, 2004
Licensed Content Pages	5
Type of use	Dissertation/Thesis
Requestor type	University/Academic
Format	Print and electronic
Portion	Figure/table
Number of figures/tables	1
Original Wiley figure/table number(s)	Figure 2
Will you be translating?	No
Title of your thesis / dissertation	CONTROL SELF-ASSEMBLING AND ORDERING OF BLOCK POLYMER NANOSTRUCTURES IN THIN FILMS
Expected completion date	Jun 2016
Expected size (number of pages)	200
Requestor Location	Ming Luo 150 Academy Street Newark, DE 19716 United States Attn: Ming Luo

Billing Type	Invoice
Billing address	Ming Luo 150 Academy Street Newark, DE 19716 United States Attn: Ming Luo
Total	0.00 USD

Would you like to purchase the full text of this article? If so, please continue on to the content ordering system located here: Purchase PDF

If you click on the buttons below or close this window, you will not be able to return to the content ordering system.

CLOSE WINDOW

Title: Dynamic Thermal Field-Induced Gradient Soft-Shear for Highly Oriented Block Copolymer Thin Films

Author: Gurpreet Singh, Kevin G. Yager, Brian Berry, et al

Publication: ACS Nano

Publisher: American Chemical Society

Date: Nov 1, 2012

PERMISSION/LICENSE IS GRANTED FOR YOUR ORDER AT NO CHARGE

This type of permission/license, instead of the standard Terms & Conditions, is sent to you because no fee is being charged for your order. Please note the following:

- Permission is granted for your request in both print and electronic formats, and translations.
- If figures and/or tables were requested, they may be adapted or used in part.
- Please print this page for your records and send a copy of it to your publisher/graduate school.
- Appropriate credit for the requested material should be given as follows: "Reprinted (adapted) with permission from (COMPLETE REFERENCE CITATION). Copyright (YEAR) American Chemical Society." Insert appropriate information in place of the capitalized words.
- One-time permission is granted only for the use specified in your request. No additional uses are granted (such as derivative works or other editions). For any other uses, please submit a new request.

If credit is given to another source for the material you requested, permission must be obtained from that source.

BACK CLOSE WINDOW

Title:	Patterning surfaces with functional polymers
Author:	Zhihong NieandEugenia Kumacheva
Publication:	Nature Materials
Publisher:	Nature Publishing Group
Date:	Apr 1, 2008

Order Completed

Thank you very much for your order.

This is a License Agreement between Ming Luo ("You") and Nature Publishing Group ("Nature Publishing Group"). The license consists of your order details, the terms and conditions provided by Nature Publishing Group, and the payment terms and conditions.

Get the printable license.

License Number	3871480784005
License date	May 17, 2016
Licensed content publisher	Nature Publishing Group
Licensed content publication	Nature Materials
Licensed content title	Patterning surfaces with functional polymers
Licensed content author	Zhihong NieandEugenia Kumacheva
Licensed content date	Apr 1, 2008
Type of Use	reuse in a dissertation / thesis
Volume number	7
Issue number	4
Requestor type	academic/educational
Format	print and electronic
Portion	figures/tables/illustrations
Number of figures/tables/illustrations	1
High-res required	no
Figures	Figure 2
Author of this NPG article	no
Your reference number	None
Title of your thesis / dissertation	CONTROL SELF-ASSEMBLING AND ORDERING OF BLOCK POLYMER NANOSTRUCTURES IN THIN FILMS
Expected completion date	Jun 2016
Estimated size (number of pages)	200
Total	0.00 USD

Title: Molecular Transfer Printing Using Block Copolymers

Author: Shengxiang Ji, Chi-Chun Liu, Guoliang Liu, et al

Publication: ACS Nano

Publisher: American Chemical Society

Date: Feb 1, 2010

PERMISSION/LICENSE IS GRANTED FOR YOUR ORDER AT NO CHARGE

This type of permission/license, instead of the standard Terms & Conditions, is sent to you because no fee is being charged for your order. Please note the following:

- Permission is granted for your request in both print and electronic formats, and translations.
- If figures and/or tables were requested, they may be adapted or used in part.
- Please print this page for your records and send a copy of it to your publisher/graduate school.
- Appropriate credit for the requested material should be given as follows: "Reprinted (adapted) with permission from (COMPLETE REFERENCE CITATION). Copyright (YEAR) American Chemical Society." Insert appropriate information in place of the capitalized words.
- One-time permission is granted only for the use specified in your request. No additional uses are granted (such as derivative works or other editions). For any other uses, please submit a new request.

If credit is given to another source for the material you requested, permission must be obtained from that source.

BACK CLOSE WINDOW

Title: Generation of Monolayer Gradients in Surface Energy and Surface Chemistry for Block Copolymer Thin Film Studies

Author: Julie N. L. Albert, Michael J. Baney, Christopher M. Stafford, et al

Publication: ACS Nano

Publisher: American Chemical Society

Date: Dec 1, 2009

PERMISSION/LICENSE IS GRANTED FOR YOUR ORDER AT NO CHARGE

This type of permission/license, instead of the standard Terms & Conditions, is sent to you because no fee is being charged for your order. Please note the following:

- Permission is granted for your request in both print and electronic formats, and translations.
- If figures and/or tables were requested, they may be adapted or used in part.
- Please print this page for your records and send a copy of it to your publisher/graduate school.
- Appropriate credit for the requested material should be given as follows: "Reprinted (adapted) with permission from (COMPLETE REFERENCE CITATION). Copyright (YEAR) American Chemical Society." Insert appropriate information in place of the capitalized words.
- One-time permission is granted only for the use specified in your request. No additional uses are granted (such as derivative works or other editions). For any other uses, please submit a new request.

If credit is given to another source for the material you requested, permission must be obtained from that source.

Title:	Controlled vapor deposition approach to generating substrate surface energy/chemistry gradients
Author:	Julie N. L. Albert,Joey D. Kim,Christopher M. Stafford, et al.
Publication:	Review of Scientific Instruments
Volume/Issue	82/6
Publisher:	AIP Publishing LLC
Date:	Jun 9, 2011
Page Count:	7

Order Completed

Thank you for your order.

This Agreement between Ming Luo ("You") and AIP Publishing LLC ("AIP Publishing LLC") consists of your license details and the terms and conditions provided by AIP Publishing LLC and Copyright Clearance Center.

Your confirmation email will contain your order number for future reference.

Get the printable license.

License Number	3871510528906
License date	May 17, 2016
Licensed Content Publisher	AIP Publishing LLC
Licensed Content Publication	Review of Scientific Instruments
Licensed Content Title	Controlled vapor deposition approach to generating substrate surface energy/chemistry gradients
Licensed Content Author	Julie N. L. Albert,Joey D. Kim,Christopher M. Stafford, et al.
Licensed Content Date	Jun 9, 2011
Licensed Content Volume	82
Licensed Content Issue	6
Requestor type	Student
Format	Print and electronic
Portion	Figure/Table
Number of figures/tables	1
Requestor Location	Ming Luo 150 Academy Street Newark, DE 19716 United States Attn: Ming Luo
Billing Type	Invoice
Billing address	Ming Luo 150 Academy Street Newark, DE 19716

Title:	Generating thickness gradients of thin polymer films via flow coating
Author:	Christopher M. Stafford,Kristen E. Roskov,Thomas H. Epps III, et al.
Publication:	Review of Scientific Instruments
Volume/Issue	77/2
Publisher:	AIP Publishing LLC
Date:	Feb 24, 2006
Page Count:	7

Order Completed

Thank you for your order.

This Agreement between Ming Luo ("You") and AIP Publishing LLC ("AIP Publishing LLC") consists of your license details and the terms and conditions provided by AIP Publishing LLC and Copyright Clearance Center.

Your confirmation email will contain your order number for future reference.

Get the printable license.

License Number	3871960996536
License date	May 18, 2016
Licensed Content Publisher	AIP Publishing LLC
Licensed Content Publication	Review of Scientific Instruments
Licensed Content Title	Generating thickness gradients of thin polymer films via flow coating
Licensed Content Author	Christopher M. Stafford,Kristen E. Roskov,Thomas H. Epps III, et al.
Licensed Content Date	Feb 24, 2006
Licensed Content Volume	77
Licensed Content Issue	2
Requestor type	Student
Format	Print and electronic
Portion	Figure/Table
Number of figures/tables	1
Requestor Location	Ming Luo 150 Academy Street Newark, DE 19716 United States Attn: Ming Luo
Billing Type	Invoice
Billing address	Ming Luo 150 Academy Street Newark, DE 19716

Title: Writing Highly Ordered Macroscopic Patterns in Cylindrical Block Polymer Thin Films via Raster Solvent Vapor Annealing and Soft Shear

Author: Ming Luo, Douglas M. Scott, Thomas H. Epps

Publication: ACS Macro Letters

Publisher: American Chemical Society

Date: May 1, 2015

PERMISSION/LICENSE IS GRANTED FOR YOUR ORDER AT NO CHARGE

This type of permission/license, instead of the standard Terms & Conditions, is sent to you because no fee is being charged for your order. Please note the following:

- Permission is granted for your request in both print and electronic formats, and translations.
- If figures and/or tables were requested, they may be adapted or used in part.
- Please print this page for your records and send a copy of it to your publisher/graduate school.
- Appropriate credit for the requested material should be given as follows: "Reprinted (adapted) with permission from (COMPLETE REFERENCE CITATION). Copyright (YEAR) American Chemical Society." Insert appropriate information in place of the capitalized words.
- One-time permission is granted only for the use specified in your request. No additional uses are granted (such as derivative works or other editions). For any other uses, please submit a new request.

BACK CLOSE WINDOW

Title: Manipulating Nanoscale Morphologies in Cylinder-Forming Poly(styrene-b-isoprene-b-styrene) Thin Films Using Film Thickness and Substrate Surface Chemistry Gradients

Author: Ming Luo, Jonathan E. Seppala, Julie N. L. Albert, et al

Publication: Macromolecules

Publisher: American Chemical Society

Date: Mar 1, 2013

PERMISSION/LICENSE IS GRANTED FOR YOUR ORDER AT NO CHARGE

This type of permission/license, instead of the standard Terms & Conditions, is sent to you because no fee is being charged for your order. Please note the following:

- Permission is granted for your request in both print and electronic formats, and translations.
- If figures and/or tables were requested, they may be adapted or used in part.
- Please print this page for your records and send a copy of it to your publisher/graduate school.
- Appropriate credit for the requested material should be given as follows: "Reprinted (adapted) with permission from (COMPLETE REFERENCE CITATION). Copyright (YEAR) American Chemical Society." Insert appropriate information in place of the capitalized words.
- One-time permission is granted only for the use specified in your request. No additional uses are granted (such as derivative works or other editions). For any other uses, please submit a new request.

BACK CLOSE WINDOW

Title: Directed Block Copolymer Thin Film Self-Assembly: Emerging Trends in Nanopattern Fabrication

Author: Ming Luo, Thomas H. Epps

Publication: Macromolecules

Publisher: American Chemical Society

Date: Oct 1, 2013

PERMISSION/LICENSE IS GRANTED FOR YOUR ORDER AT NO CHARGE

This type of permission/license, instead of the standard Terms & Conditions, is sent to you because no fee is being charged for your order. Please note the following:

- Permission is granted for your request in both print and electronic formats, and translations.
- If figures and/or tables were requested, they may be adapted or used in part.
- Please print this page for your records and send a copy of it to your publisher/graduate school.
- Appropriate credit for the requested material should be given as follows: "Reprinted (adapted) with permission from (COMPLETE REFERENCE CITATION). Copyright (YEAR) American Chemical Society." Insert appropriate information in place of the capitalized words.
- One-time permission is granted only for the use specified in your request. No additional uses are granted (such as derivative works or other editions). For any other uses, please submit a new request.

Title: Determination of Interfacial Mixing in Tapered Block Polymer Thin Films: Experimental and Theoretical Investigations

Author: Ming Luo, Jonathan R. Brown, Roddel A. Remy, et al

Publication: Macromolecules

Publisher: American Chemical Society

Date: Jul 1, 2016

PERMISSION/LICENSE IS GRANTED FOR YOUR ORDER AT NO CHARGE

This type of permission/license, instead of the standard Terms & Conditions, is sent to you because no fee is being charged for your order. Please note the following:

- Permission is granted for your request in both print and electronic formats, and translations.
- If figures and/or tables were requested, they may be adapted or used in part.
- Please print this page for your records and send a copy of it to your publisher/graduate school.
- Appropriate credit for the requested material should be given as follows: "Reprinted (adapted) with permission from (COMPLETE REFERENCE CITATION). Copyright (YEAR) American Chemical Society." Insert appropriate information in place of the capitalized words.
- One-time permission is granted only for the use specified in your request. No additional uses are granted (such as derivative works or other editions). For any other uses, please submit a new request.

BACK CLOSE WINDOW